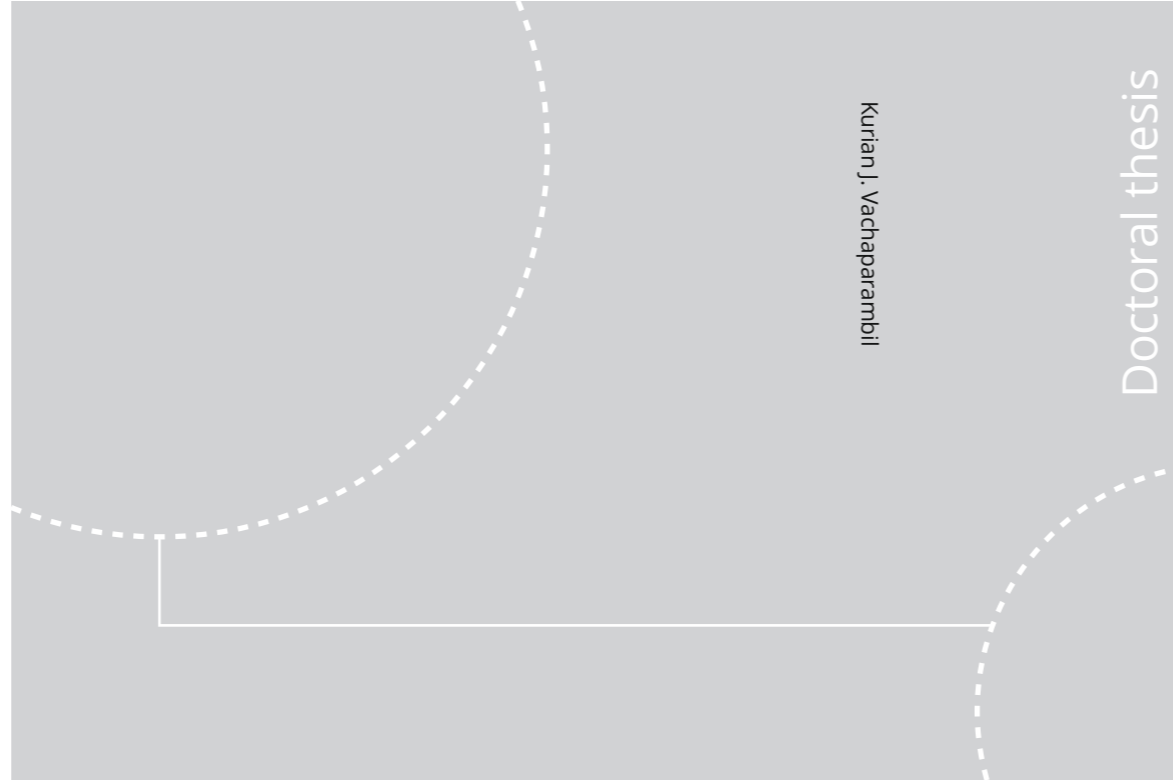


ISBN 978-82-326-5072-9 (printed ver.)  
ISBN 978-82-326-5073-6 (electronic ver.)  
ISSN 2703-8084 (online)  
ISSN 1503-8181 (printed ver.)



Doctoral theses at NTNU, 2020:363

Kurian J. Vachaparambil

# Interface resolved simulations of continuum scale electrochemical hydrogen evolution

Doctoral theses at NTNU, 2020:363

**NTNU**  
Norwegian University of Science and Technology  
Thesis for the Degree of  
Philosophiae Doctor  
Faculty of Natural Sciences  
Department of Materials Science and Engineering

 **NTNU**  
Norwegian University of  
Science and Technology

 NTNU

 **NTNU**  
Norwegian University of  
Science and Technology

Kurian J. Vachaparambil

# **Interface resolved simulations of continuum scale electrochemical hydrogen evolution**

Thesis for the Degree of Philosophiae Doctor

Trondheim, December 2020

Norwegian University of Science and Technology  
Faculty of Natural Sciences  
Department of Materials Science and Engineering



Norwegian University of  
Science and Technology

**NTNU**

Norwegian University of Science and Technology

Thesis for the Degree of Philosophiae Doctor

Faculty of Natural Sciences

Department of Materials Science and Engineering

© Kurian J. Vachaparambil

ISBN 978-82-326-5072-9 (printed ver.)

ISBN 978-82-326-5073-6 (electronic ver.)

ISSN 2703-8084 (online)

ISSN 1503-8181 (printed ver.)

Doctoral theses at NTNU, 2020:363

Printed by NTNU Grafisk senter

"He has made everything fall into place in its time."



This thesis is submitted to the Norwegian University of Science and Technology (NTNU) for partial fulfillment of the requirements for the degree of philosophiae doctor. The doctoral work has been carried out between September 2017 and August 2020 at the Department of Materials Science and Engineering, NTNU, Trondheim. The work has been supervised by Associate Professor Kristian Etienne Einarsrud.

The research was funded by the Department of Materials Science and Engineering, NTNU. The computational resources availed during the work was provided by NTNU HPC and UNINETT Sigma2 through grant NN9741K.

Kurian J. Vachaparambil  
Trondheim, December 2020.



## *Abstract*

An important aspect of improving the efficiency of water electrolysis is to remove the electrochemically generated hydrogen and oxygen bubbles. The evolution of these gases, which are associated with increased electrical resistance, are driven by electrochemical reactions causing supersaturation of the electrolyte which leads to bubble nucleation, growth, and eventual detachment from the electrode. Due to the different physics as well as the length and time scales associated with the process, referred to as the multiscale and multiphysics nature, predicting the bubble evolution using analytical models is challenging. As numerical modelling approaches, like Computational Fluid Dynamics (CFD), predicts the fluid flow based on the underlying governing equations, it can be used to study electrochemical bubble evolution.

The work undertaken during the PhD is primarily to develop and verify a multiphysics CFD framework based on the Volume of Fluid (VOF) method available in OpenFOAM<sup>®</sup> for continuum scale hydrogen bubbles. In the context of this work, continuum scale bubbles refers to bubble diameters which are larger than a few hundred micrometers. The VOF method is customized by adding the physics and numerical techniques relevant to treating electrochemical reactions, dissolved gas transport, charge transport, interfacial mass transfer and associated bubble growth (from a pre-existing submillimeter bubble). The proposed framework is developed incrementally, with each step corresponding to implementation and verification of a multiphysics module, eventually culminating in the fully coupled multiphysics framework. This modularized approach allows for verification of the implemented functionality with existing theoretical models and/or computational benchmarks.

The thesis, in essence, provides context to the undertaken research, review of the various modelling techniques used to treat the multiphysics nature of electrochemical hydrogen evolution and details of developed framework. In addition, the thesis also summarizes knowledge gained during the PhD about the solution procedure used in OpenFOAM<sup>®</sup> and the VOF method to enable knowledge dissemination for further research.





## *Acknowledgement*

First of all, I would like to express my gratitude to my supervisor, Kristian Etienne Einarsrud, for his support and guidance during this PhD. Thank you for all our discussions and prompt feedback on the manuscripts as well as taking the time to ensure that my PhD work went ahead even when you were away on paternity holidays. I am also grateful for your trust in me which allowed me to pursue my ideas.

I would also like to thank Associate professor Espen Sandnes as well as Professors Svein Sunde, Frode Seland, Andreas Erbe and Ann Mari Svensson, at the Department of Materials Science and Engineering, for taking the time to explain various aspects of electrochemistry and electrochemical hydrogen evolution. Additionally, I would also like to acknowledge the support provided by Tufan Arslan to setup and run the simulations on HPC.

Further, I would like to thank my office mates, both past and present, Alaa, Syed and Henrik, for the good conversations and sharing their knowledge/experience in electrochemistry. I have also been lucky enough to have met other PhDs and Postdocs with whom I have had many memorable moments from countless dinners and coffee breaks to hikes and road trips. I would like to thank Suresh, Varun and Hamid for proofreading parts of the thesis.

I am also very fortunate to have my family who stood by my side and got me till here. Finally, to the best thing that life has brought to me over the years, thank you Treesa for your understanding, wisdom, humor, patience and love.







# Contents



<b>I Introduction</b>	<b>21</b>
Hydrogen production via water electrolysis	23
Modelling electrochemical gas evolution	31
Goals, outline and contributions	35
<b>II Multiphysics modelling of electrochemical hydrogen evolution</b>	<b>39</b>
Overview of the underlying physics	41
Multiphase flows	49
Electrochemical reactions and bubble growth	55
<b>III Introduction to the numerical framework</b>	<b>61</b>
Overview of OpenFOAM <sup>®</sup> and the Finite Volume Method	63
Overview of the Volume of Fluid solver in OpenFOAM <sup>®</sup>	69
<b>IV Contributions</b>	<b>79</b>
Summary of paper A	83
Summary of paper B	87
Summary of paper C	89
Summary of paper D	95
Summary of paper E	99
Summary of paper F	103
<b>V Summary and final thoughts</b>	<b>109</b>
Conclusions	111
Topics for future research	113
Appendix A: Calculation of viscous terms	115

Appendix B: Calculation of source term for volume fraction advection	119
Appendix C: Computational resources	121
Bibliography	123
Appended paper A	141
Appended paper B	167
Appended paper C	175
Appended paper D	197
Appended paper E	207
Appended paper F	219

## List of Figures

- 1.1 Schematic of water electrolysis process in an alkaline electrolyzer. 24
- 1.2 Schematic of the non-uniform distribution of bubbles in the vicinity of a vertical electrode.  denotes the distance from the electrode where bubbles remain attached,  is the region when detached bubbles tends to form curtain, and  represents the bulk region. 26
- 2.1 Schematic of the multiscale nature and corresponding physics of electrochemical gas evolution. The abbreviations AS, MS and CS denotes the atomistic, meso and continuum scale physics with length and temporal scales ranging between 1 nm-1 m and  $10^{-15}$  s-1 s respectively [Taqieddin et al., 2018]. 31
- 2.2 Illustration of the multiphysics nature of electrochemical gas evolution. 33
- 2.3 Illustration of the multiphase modelling approaches where  represents the interface between the gas and liquid. 33
- 4.1 Illustration of homogeneous nucleation based on analogous graphics in Jones et al. 1999. 42
- 4.2 Illustration of heterogeneous nucleation mode based on analogous graphics in Jones et al. 1999. 43
- 4.3 Illustration of the pre-existing bubbles, whose radii is smaller than  $R_c$ , relevant in pseudo-classical nucleation mode based on analogous graphics in Jones et al. 1999. 43
- 4.4 Illustration of pre-existing bubbles, whose radii is larger or equal to  $R_c$ , relevant in non-classical nucleation mode based on analogous graphics in Jones et al. 1999. 44
- 4.5 Experimentally observed detachment of a hydrogen bubble during water electrolysis under a constant current density of  $7000\text{A}/\text{m}^2$  [Brussieux et al., 2011]. The smaller hydrogen bubbles in the figure are formed at the border of the electrode whereas the bigger bubbles (which are in the order of few millimeters) are at the center of the electrode. Reproduced from Brussieux et al. 2011 with permission from Elsevier. 45

4.6	Illustration of bubble on a microelectrode along with the contact angle (estimated in the liquid). At detachment, $\theta$ is equal to $\theta_{de}$ and footprint of the bubble is nearly the size of the electrode (of diameter in the order of few hundred micrometers) as observed in <a href="#">Fernández et al. 2014</a> .	45
7.1	Schematic of dividing the computational domain into small control volumes (cells).	64
7.2	Illustration of a control volume used in the calculation, highlighted in red, along with its neighbouring cell whose cell center is represented by $N$ and common face by $f$ .	64
8.1	Illustration of the volume fraction field produced by (a) Geometric and (b) Algebraic VOF methods with respect to the physical interface (represented by $\text{—}$ ).	75
9.1	Comparison of the predictions of the three surface tension models with the 2D benchmark data reported by <a href="#">Hysing et al. 2009</a> for TC1.	85
9.2	Comparison of the predictions of the three surface tension models with the 2D benchmark data reported by <a href="#">Hysing et al. 2009</a> for TC2.	85
9.3	Comparison of the predictions of the three surface tension models for the 2D capillary rise simulations.	86
11.1	Comparison of the temporal evolution of 2D bubble radius predicted by the proposed solver (based on driving force described in Eq.11.10d) with the approximate solution of Epstein–Plesset (Eq.11.11).	93
11.2	Comparison of the evolution of 2D bubble radius predicted by the proposed solver (based on driving force described using Fick's $1^{st}$ law and $Sh$ correlation) with analytical models like Eq.11.12 and Eq.11.13.	94
11.3	Comparison of the evolution of growth rate for a 2D bubble predicted by the proposed solver (based on driving force described using Fick's $1^{st}$ law and $Sh$ correlation), $\int \psi_0 dV$ , with analytical model based on Eq.11.13.	94
12.1	Comparison of the predicted bubble radius and normalized growth rate using driving forces described using Fick's $1^{st}$ law and $Sh$ correlations based 2D simulations with Extended Scriven model (with $\beta_{2D}$ ) for various levels of supersaturation: 2.5, 4.0 and 7.0.98	
13.1	Comparison of the spurious velocities (m/s) generated while modelling stationary 2D submillimeter bubbles at $t = 0.05s$ with interface (at $\alpha_1 = 0.5$ ) represented by the white contour.	100

- 13.2 The concentration of dissolved gas ( $\text{mol}/\text{m}^3$ ) around a 2D rising bubble (interface, at  $\alpha_1 = 0.5$ , is represented by white contour) modelled based on C-CST. 100
- 13.3 Illustration of the 2D cases, EC1 and EC2, considered to showcase the effect of electrode screening. EC1, represented by , considers a bubble of radius 1mm at the center of domain. EC2, represented by , considers two equal sized bubbles (semicircles with radii equal to 1mm) whose centers are 2.5mm and 6.5mm away from the bottom wall. 101
- 13.4 Comparison of the current density ( $\text{A}/\text{m}^2$ ) reduction with increase in void fraction of bubbles (in bulk) predicted by the simulations (for 2D and 3D) and Bruggermann's correlation. 102
- 14.1 The change in the dissolved gas concentration,  $C_i$ , ( $\text{mol}/\text{m}^3$ ) as a single 2D bubble evolves from the electrode with a contact angle equal to  $30^\circ$ . The white line represents the interface which is plotted at  $\alpha_1 = 0.5$ . 104
- 14.2 Comparison of the current normalized with current without any bubbles ( $I/I_0$ ), fraction of the volume of bubble with respect to the computational domain ( $f$ ), the bubble deformation in horizontal ( $\Delta x$ ) and vertical ( $\Delta y$ ) directions for a single 2D bubble evolving from an electrode with a contact angle of  $30^\circ$ . The vertical black line indicates the detachment of the bubble which in this case is around 1.69 ms. The red lines are equidistant at every 0.001 s to enable comparison between the plots. 105
- 14.3 Comparison of the current normalized with current without any bubbles ( $I/I_0$ ), fraction of the volume of bubble with respect to the computational domain ( $f$ ), the bubble deformation in horizontal ( $\Delta x$ ) and vertical ( $\Delta y$ ) directions for coalescence driven bubble evolution of two unequally sized 2D bubbles from an electrode with a contact angle of  $45^\circ$ . The vertical black line indicates the detachment of the bubble whereas the red lines are equidistant at every 0.0004 s to enable comparison between the plots. 106
- 14.4 The evolution of the interface and the concentration of the dissolved gas,  $C_i$ , ( $\text{mol}/\text{m}^3$ ) as the bubble coalescence and evolves from two equally sized 2D bubbles for a contact angle of  $45^\circ$ . The necking process (between 0 s-0.4 ms), propagation of deformation waves along the bubble interface which leads to the lifting of the bubble (between 0.6 ms-2 ms) and detachment as well as the oscillations of the bubble surface leading to elongation and flattening (2 ms-4 ms). The interface is plotted at  $\alpha_1 = 0.5$ . 107



- 14.5 The evolution of the interface and the concentration of the dissolved gas,  $C_i$ , ( $\text{mol}/\text{m}^3$ ) as the bubble coalescence and evolves from two unequally sized 2D bubbles for a contact angle of  $45^\circ$ . Note the necking process (between 0 s-0.2 ms), propagation of deformation waves along the bubble interface which leads to the lifting of the bubble (between 0.4 ms-1.2 ms) and detachment as well as the oscillations of the bubble surface leading to elongation and flattening (1.8 ms-3 ms). The interface is plotted at  $\alpha_1 = 0.5$ . 108
- 16.1 Comparing of the temporal change in bubble size and growth rate normalized by bubble radius predicted based on the source term used in  $\alpha_1$  advection equation using driving force computed based on  $Sh$  correlation in Eq.12.6 ( $\alpha_1 \nabla \cdot \vec{U}$  (□) and  $\alpha_1 \dot{m}/\rho$  (\*)) Fick's 1<sup>st</sup> law in Eq.6.15 ( $\alpha_1 \nabla \cdot \vec{U}$  (□) and  $\alpha_1 \dot{m}/\rho$  (\*)). Please note that these are 2D simulations and the points in the plots correspond to the bubble radius and growth rate at every 40 time steps taken by the solver. 120

## List of Tables

1.1	Comparison of half-cell reactions occurring at anode and cathode in alkaline (AEC), proton exchange membrane (PEMEC) and solid oxide (SOEC) electrolyzer cells, adapted from <a href="#">Chisholm and Cronin 2016</a> , <a href="#">Schmidt et al. 2017</a> .	24
1.2	Models for effective conductivity in heterogeneous media, see <a href="#">Zhao et al. 2019b</a> . $f$ is the void fraction of the bubbles (calculated as $V_b/(V_b + V_e)$ , where $V_b$ and $V_e$ are the total volumes occupied by bubble and electrolyte respectively) and $\Gamma_e$ is the conductivity of the pure electrolyte.	25
1.3	Comparison of alkaline (AEC), polymer electrolyte membrane (PEMEC) and solid oxide (SOEC) electrolyzer cells characteristics, adapted from <a href="#">Zeng and Zhang 2010</a> , <a href="#">Chisholm and Cronin 2016</a> , <a href="#">Schmidt et al. 2017</a> .	28
4.1	Thermodynamic properties of reactants and products during electrolysis of water at 298 K [ <a href="#">Haynes, 2011</a> ].	41
6.1	Few examples of various Sherwood number correlations available in literature.	59
8.1	Few examples of studies which used interFoam, both out-of-the-box and customized, to simulate multiphase flow scenarios.	69
10.1	Variation of capillary rise height with sharpening coefficients.	88
10.2	Time averaged spurious velocities, Laplace pressure and associated error (calculated as $(\Delta p_T - \overline{\Delta p_S})/\Delta p_T$ , where $p_T$ is equal to $\sigma/R$ ) while modelling a 2D submillimeter bubble.	88
13.1	Reduction of current due to the presence of bubble on the electrode.	101



# *Nomenclature*

## **Abbreviations**

AEC	Alkaline electrolyzer cell
C-CST	Compressive-continuum species transfer model
CFD	Computational fluid dynamics
CSF	Continuum surface force model
CST	Continuum species transfer model
FVM	Finite volume method
HER	Hydrogen evolution reaction
IR	Interface resolved methods
PEMEC	Proton exchange membrane electrolyzer cell
SOEC	Solid oxide electrolyzer cell
SSF	Sharp surface force model
VOF	Volume of fluid

## **Electrochemical symbols**

$e^-$	Electron
$H^+$	Hydrogen ion
$H_2$	Hydrogen
$H_2O$	Water
$O^{2-}$	Oxide ion
$O_2$	Oxygen
$OH^-$	Hydroxide ion

**Computational/physical parameters**

$\alpha$	Volume fraction
$\Delta G$	Gibbs free energy
$\eta$	Overpotential
$\Gamma$	Electrical conductivity
$\lambda$	Under-relaxation factor
$\mathcal{R}$	Universal gas constant
$S$	Source/sink term
$\mathfrak{R}$	Electrical resistance
$\mu, \nu$	Dynamic viscosity, kinematic viscosity
$\Phi$	Local electric potential
$\rho$	Density
$\sigma$	Surface tension
$\Theta$	Area fraction of electrode covered by bubble
$\theta$	Contact angle measured in the liquid phase
$\vec{n}$	Unit normal to the interface
$\vec{S}$	Surface area vector of the cell face
$\vec{U}$	Velocity vector
$A$	Total area of the electrode
$a(\cdot)$	Activity of a chemical species
$C$	Concentration
$D$	Diffusion coefficient
$E$	Applied potential
$E_{rev}$	Reversible potential
$f$	Void fraction of bubbles
$g, \vec{g}$	Acceleration due to gravity and its vector representation
$He_i$	Jump condition across the interface for species $i$
$i, \vec{i}$	Current density and its vector representation

$j$	Driving force for interfacial mass transfer
$n$	Number of electrons transferred during the electro-chemical reactions
$p$	Pressure
$Re$	Reynolds number
$S$	Supersaturation
$Sc$	Schmidt number
$Sh$	Sherwood number
$T$	Temperature
$z$	Charge of the ions
$F$	Faraday's constant
$R$	Bubble radius

#### Subscripts

$+/-$	Cations/Anions
1	In liquid phase
2	In gas phase
$a$	At anode
$b$	Used in Lagrangian tracking to denote individual bubbles
$c$	At cathode
$d$	Used to represent the dispersed phases
$de$	Detachment
$f$	Cell face
$i, j, k$	General indexes used in multiphase modelling
$N$	Neighbour cell centers
$P$	Owner cell center
$sat$	At saturation condition



## **Part I**

### **Introduction**





# Chapter 1:

## *Hydrogen production via water electrolysis*

### *Background and general overview*

With the push to reduce the dependence on fossil fuels, renewable energy resources (like wind and solar) are increasingly being used in power generation. Although technological advancements have improved the efficiency and reduced the cost of power generated from these renewable energy sources, they require storage solutions to mitigate the intermittencies in power generation [IRENA, 2017]. The various storage technologies used vary from chemical, electrochemical, mechanical, electrical, to thermal storage methods, see the review by Amrouche et al. [2016] for additional information.

Out of the proposed methods to store surplus renewable energy, the electrolysis of water to get hydrogen opens up possibilities to use the gas as an energy vector<sup>1</sup>. Due to the non-polluting nature of hydrogen combustion (which produces water), highest energy content (per unit mass) compared to other fuels and compatibility with fuel cells, hydrogen, if produced sustainably and economically, can replace fossil fuels which would reduce the environmental impact of the society, discussed in EU's strategic plan to be carbon-neutral by 2050 [European Commission, 2020], and eventually create a 'Hydrogen economy' [Scott, 2020].

In order to enable this transition, a decarbonized pathway to produce hydrogen is critical. Currently, the main methods, which accounts for nearly 95% of commercially produced hydrogen [Chisholm and Cronin, 2016], are based on steam-methane reforming<sup>2</sup> and partial oxidation reforming<sup>3</sup>, see Scott [2020]. An increasingly popular alternate way to produce hydrogen is via water electrolysis, which currently accounts for 5% of the hydrogen produced industrially [Scott, 2020]. Although water electrolysis, which is the process of splitting water into hydrogen and oxygen by supplying electrical energy, was

<sup>1</sup> Energy vector refers to the chemical substance or physical process that allows the transport of energy in order to enable its use at a later time by a consumer located away from the location of power generation [Orecchini, 2006]. Some of the most relevant present day examples of energy vectors are fossil fuels (example of chemical substance) and electricity (example of physical process), see Orecchini 2006

<sup>2</sup> Steam-methane reforming is an endothermic process that combines methane with steam to generate hydrogen, carbon dioxide and carbon monoxide, see Office of Energy Efficiency and Renewable Energy n.d..

<sup>3</sup> Partial oxidation reforming is an exothermic process that combines methane with oxygen to produce carbon monoxide, hydrogen and carbon dioxide, see Office of Energy Efficiency and Renewable Energy n.d..

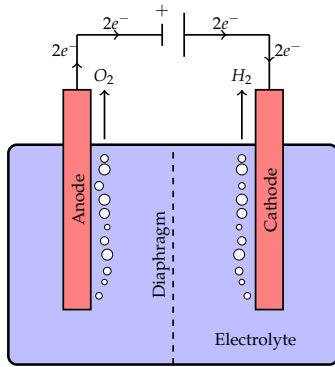
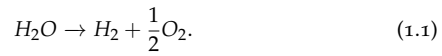


Figure 1.1: Schematic of water electrolysis process in an alkaline electrolyzer.

discovered in late 1700s [de Levie, 1999], it was not popular due to the high cost of electricity, which can account upto 75% of the cost of hydrogen generated [Scott, 2020]. With decreasing cost of electricity, especially generated from renewable energy, the sustainable production of hydrogen via water electrolysis can compete with less eco-friendly reforming methods used commercially today.

The water electrolysis is a process in which electrochemical reactions (driven by supplied electrical energy) at electrodes splits water into hydrogen and oxygen, which can be described as



A typical electrolyzer consists of electrodes, which are submerged in an ionic solution (known as the electrolyte), and separated by a membrane/diaphragm to prevent the explosive mixing of hydrogen and oxygen. The electrodes are the anode, where oxidation reactions occur, and the cathode, where reduction reactions occur, where oxygen and hydrogen evolves respectively, see Table.1.1. A schematic of the water electrolysis process is shown in Fig.1.1. Based on the type of electrolyte used, the water electrolysis system can be divided into alkaline (AEC), proton exchange membrane (PEMEC) and solid oxide (SOEC) electrolyzer cells, see Table.1.1. This process of converting water into hydrogen and oxygen has an efficiency of around 62-82% for AEC and PEMEC, used in commercial applications [Chisholm and Cronin, 2016].

	AEC	PEMEC	SOEC
Anodic reaction	$2OH^- \rightarrow H_2O + 2e^- + \frac{1}{2}O_2$	$H_2O \rightarrow 2H^+ + 2e^- + \frac{1}{2}O_2$	$O^{2-} \rightarrow 2e^- + \frac{1}{2}O_2$
Cathodic reaction	$2H_2O + 2e^- \rightarrow 2OH^- + H_2$	$2H^+ + 2e^- \rightarrow H_2$	$H_2O + 2e^- \rightarrow O^{2-} + H_2$

Table 1.1: Comparison of half-cell reactions occurring at anode and cathode in alkaline (AEC), proton exchange membrane (PEMEC) and solid oxide (SOEC) electrolyzer cells, adapted from Chisholm and Cronin 2016, Schmidt et al. 2017.

Ongoing fundamental research activities to further improve and optimize electrolyzers can be broadly divided based on the domain of investigation into electrochemical and bubble hydrodynamics. The electrochemical aspect delves predominantly into the development of durable [Siracusano et al., 2017] and cheap catalysts [Zhang et al., 2019, Khan et al., 2018] as well as understanding the reaction mechanism and kinetics [Shinagawa et al., 2015, Hu et al., 2019]. On the other hand, the research on bubble hydrodynamics focuses more on the physics and influence of bubble evolution (includes nucleation, growth and detachment) [Zhang and Zeng, 2012, Sakuma et al., 2014, Fernández et al., 2014, Baczyzmalski et al., 2017, Bashkatov et al., 2019]. Understanding the underlying physics provides invaluable knowledge which can be leveraged to enhance bubble detachment during water electrolysis, see

Darband et al. [2019]. Knowledge from both these research areas are crucial in developing strategies/materials to improve the efficiency of water electrolysis and improve the durability of the electrode materials [Brussieux et al., 2011, Kadyk et al., 2016].

Due to the ubiquitous nature of gas evolution during water electrolysis, fundamental understanding of the dynamic behaviour of these bubbles, especially the detachment, is critical in developing strategies to efficiently remove them and improve the performance of the water electrolyzer.

### Impact of electrochemical bubble evolution

In this section, a brief overview of the impact of bubble evolution in electrochemical systems is discussed. For a comprehensive description of the impact, including catalyst degradation and efficiency loss, interested readers may refer to works like Leistra and Sides [1987] or recent review works like Zhao et al. [2019b] and Angulo et al. [2020].

The losses introduced by electrochemical gas evolution during water electrolysis process can be quantified based on its effect on overpotential. The overpotential ( $\eta$ ), which is the difference between the potential applied ( $E$ ) and the reversible potential ( $E_{rev}$ )<sup>4</sup>, can be described as

$$\eta = E - E_{rev} = |\eta_{ohm}| + |\eta_s| + |\eta_C|, \quad (1.2)$$

where  $\eta_{ohm}$ ,  $\eta_s$  and  $\eta_C$  are the overpotentials associated with ohmic resistances in the system, electrochemical reactions and mass transfer at both the electrodes<sup>5</sup> [Leistra and Sides, 1987, Zeng and Zhang, 2010, Burheim, 2017]. As electrochemical systems can be run under potentiostatic (constant potential difference) or galvanostatic (constant current) conditions, bubble evolution would lead to fluctuations in current and overpotential respectively [Fernández et al., 2014, Yang et al., 2015].

<sup>4</sup>  $E_{rev}$  is the theoretical minimum potential that must be applied to start the electrochemical reaction, whose calculation is discussed further in Chapter 4.

<sup>5</sup> It should be pointed out that, in electrochemistry, the cathodic and anodic overpotentials are by convention represented by negative and positive values. In this thesis, to simplify the representation, the absolute value of these overpotentials are considered.

Reference	Correlation for effective conductivity ( $\Gamma_{e,b}$ )	Application
Maxwell 1873	$2(1-f)\Gamma_e/(2+f)$	For low void fraction and single size bubbles
Bruggeman 1935	$\Gamma_e(1-f)^{1.5}$	For polydispersed bubbles
Meredith and Tobias 1961	$8(2-f)(1-f)\Gamma_e/((4+f)(4-f))$	For two sizes of bubbles

The ohmic overpotential ( $\eta_{ohm}$ ) associated with bubble evolution are associated with adhered bubbles to the electrode surface and detached bubbles present in the bulk, as shown in Fig.1.2. When bubbles are

Table 1.2: Models for effective conductivity in heterogeneous media, see Zhao et al. 2019b.  $f$  is the void fraction of the bubbles (calculated as  $V_b/(V_b + V_e)$ , where  $V_b$  and  $V_e$  are the total volumes occupied by bubble and electrolyte respectively) and  $\Gamma_e$  is the conductivity of the pure electrolyte.

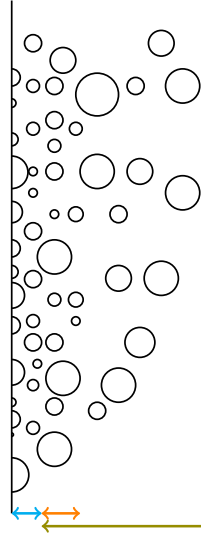
in the bulk of the electrolyte, the effective conductivity of the heterogeneous bubble-electrolyte medium ( $\Gamma_{e,b}$ ) can be estimated based on theoretical models, see Table.1.2.

Typically the detached bubbles from a vertical electrode tend to form curtains (see Fig.1.2) which causes an increase in resistance ( $\Delta R$ ) that is calculated as

$$\frac{\Delta \mathfrak{R}}{\mathfrak{R}_e} = \frac{H}{Y} \left( \frac{\Gamma_e}{\Gamma_{e,b}} - 1 \right), \quad (1.3)$$

where  $H$ ,  $Y$  and  $\mathfrak{R}_e$  are the bubble curtain thickness, inter-electrode distance and resistance introduced by the pure electrolyte respectively [Vogt and Kleinschrodt, 2003]. In Eq.1.3, when the inter-electrode distance ( $Y$ ) is small or when bubble curtain thickness is comparable to  $Y$ , the increase in resistance due to bubble curtain becomes more dominant.

Figure 1.2: Schematic of the non-uniform distribution of bubbles in the vicinity of a vertical electrode. ← denotes the distance from the electrode where bubbles remain attached, → is the region when detached bubbles tends to form curtain, and → represents the bulk region.



When bubbles are attached to the electrode they increase the ohmic resistance ( $\eta_{ohm}$ ) due to reduction of effective conductivity of the electrolyte as well as decrease in the electrode surface area in contact with the electrolyte [Sides and Tobias, 1980, Dukovic and Tobias, 1987, Yang et al., 2015]. The work by Sides and Tobias [1980] reported the ohmic resistance contribution from attached bubbles, whose diameters are a tenth of the inter-electrode gap and placed three bubble diameters apart from others, results in an increase in resistance by 1%. As the spacing between these attached bubbles decrease, the resistance becomes larger [Sides and Tobias, 1980, Dukovic and Tobias, 1987].

The surface overpotential ( $\eta_s$ ) is associated with the electrochemical

reaction at the electrode in contact with the electrolyte [Leistra and Sides, 1987], which can be described as<sup>6</sup>

$$|\eta_s| = \left| \frac{\mathcal{R}T}{\beta F} \ln i_0 - \frac{\mathcal{R}T}{\beta F} \ln \left( \frac{I}{A} \right) \right|, \quad (1.4)$$

where  $I$  is the current in the system,  $A$  is the electrode-electrolyte area<sup>7</sup>,  $i_0$  is the exchange current density which is unique to the catalyst used at the electrode,  $\beta$  is transfer coefficient of the reaction (usually set to 0.5) and  $\mathcal{R}T/(\beta F)$ , known as Tafel slope<sup>8</sup>, provides insight into the mechanism of the electrochemical reactions [Shinagawa et al., 2015, Anantharaj et al., 2018].

The Nernst equation relates the change in potential as a result of the variation of temperature and concentration. For example, the potential of cathode for HER during acidic water electrolysis is

$$E_c = E_c^0 - \frac{\mathcal{R}T}{nF} \ln \left( \frac{a(H_2)}{a(H^+)^2} \right), \quad (1.5a)$$

where  $n$  is equal to 2 for HER,  $E_c^0$  is the reversible potential of the  $H^+$  reduction reaction at cathode whereas  $a(H_2)$  and  $a(H^+)$  are the activities of  $H_2$  and  $H^+$  [Coutanceau et al., 2018]. Activities of a dissolved species  $x$ ,  $a(x)$ , can be written as  $\gamma_x C_x^*$  where  $C_x^*$  is the dimensionless molar concentration of  $x$  (normalized using concentration value measured at standard conditions like 1 atm) and  $\gamma_x$  is the corresponding activity coefficient [Kolasinski, 2016, Burheim, 2017]. As the activity coefficient is equal to unity for ideal solutions [Kolasinski, 2016, Burheim, 2017],  $a(H^+)$  is assumed to be constant between the supersaturated and saturated cases,  $a(H_2)/a(H_2)_{sat}$  can be written as  $C/C_{sat}$  and the change in  $E_c$  due to supersaturation of  $H_2$  can be calculated (assuming a reference state as the saturation condition which occurs away from the electrode) as

$$\begin{aligned} |\eta_c| &= |E_c - E_c|_{sat}| \\ &= \frac{\mathcal{R}T}{nF} \left| \ln \left( \frac{a(H_2)}{a(H_2)_{sat}} \right) \right| = \frac{\mathcal{R}T}{nF} \left| \ln \left( \frac{C}{C_{sat}} \right) \right|. \end{aligned} \quad (1.5b)$$

Due to the supersaturation<sup>9</sup> of the electrolyte near the electrode with dissolved gas produced from the electrochemical reactions, the associated concentration overpotential ( $|\eta_c|$ ) can be calculated based on Eq.1.5b, see Leistra and Sides [1987]. When bubbles are present at cathode, the interfacial mass transfer driven bubble growth would reduce the local supersaturation which has been observed to reduce  $\eta_c$  which subsequently lowers  $\eta$  [Dukovic and Tobias, 1987, Zhao et al., 2019a,b].

Apart from the impact on overpotential, electrochemical gas evolution also influences the mass transfer mechanisms due to the enhanced convection [Zhao et al., 2019b]. In the presence of static bubble, the dissolved gas has a developed concentration boundary layer at the interface due to the interfacial mass transfer but the radial growth of bubble and its detachment causes convection which results in the re-

<sup>6</sup> Eq.1.4 is commonly referred to as the Tafel equation which is widely used in electrochemical studies, see Shinagawa et al. 2015, Anantharaj et al. 2018 for more information.

<sup>7</sup> The area of the electrode exposed to electrolyte is equal to total area of electrode ( $A$ ) only when bubbles are absent. In the presence of the bubbles, the electrode in contact with electrolyte reduces to  $A(1 - \Theta)$ , where  $\Theta$  indicates the bubble coverage, see Leistra and Sides 1987.

<sup>8</sup> The negative and the positive sign of the Tafel slope is omitted for simpler representation. Please refer to Shinagawa et al. 2015, Anantharaj et al. 2018 for details of the Tafel slopes for anodic and cathodic reactions.

<sup>9</sup> The supersaturation of electrolyte with hydrogen due to electrochemical reactions as reported in literature are: 8-24 [Westerheide and Westwater, 1961], 1.5-19.9 [Glas and Westwater, 1964], and in the order of 100 [Shibata, 1963]. The difference in supersaturation reported in these studies have been attributed to the estimation based on measurements of bubble growth [Westerheide and Westwater, 1961, Glas and Westwater, 1964] and concentration overpotential [Shibata, 1963] which accounts for the dissolved gas away and at the electrode surface respectively [Vogt, 1980]. In comparison, more recent studies using smaller (micro/nano sized) cathodes during water electrolysis have reported supersaturation in the range of 300-400 [Yang et al., 2015, Chen and Luo, 2018].

distribution of the dissolved gas, see [Zhao et al., 2019b]. These modes of convection due to electrochemical gas evolution is further discussed in Chapter 4.

As the overall overpotential is a complex function of the fraction of the electrode covered by bubbles, size of the bubble as well as the distribution of the dissolved gas, see Eq.1.2, which varies as bubbles evolves,  $\eta$  and the overall resistance of the system also has temporal fluctuations. In experimental studies, the detachment of bubble from the electrode surface is observed to reduce the resistance of the system which results in increased current under potentiostatic conditions, see Yang et al. [2015], and decrease in overpotential under galvanostatic conditions, see Fernández et al. [2014]. As a result, the quick bubble detachment is critical for increasing the efficiency of water electrolysis, see Darband et al. 2019.

### *Broader context for the need to improve the efficiency of water electrolysis*

In order to make hydrogen produced from water electrolysis a viable and green energy vector, it has to be cheaper than the hydrogen generated commonly from natural gas and partial oxidation reforming, which costs around 1.5€/kg of hydrogen [European Commission, 2020]. With sharply reducing costs of generating electricity from renewable energy sources, especially wind and solar [IRENA, 2020], along with reducing cost of electrolyzers, see European Commission [2020], sustainably generated hydrogen currently costs around 2.5-5€/kg of hydrogen [European Commission, 2020]. The main

	Units	AEC	PEMEC	SOEC
Current density	A/cm <sup>2</sup>	0.1–0.4	0.6–2.0	0.3–2.0
Cell voltage	V	1.8–2.4	1.8–2.2	0.7–1.5
Operating pressure	bar	<30	<200	<25
Operating temperature	°C	60–80	50–80	650–1000
Production rate	m <sup>3</sup> /h †	<760	<40	<40
System energy consumption	kWh/m <sup>3</sup> †	4.5-6.6	4.2-6.6	>4.7
Capital system cost	€/kW ‡	1000–1200	1860–2320	>2000
Maturity (scale)	-	Commercial (large)	Commercial (small)	Demonstration (lab)

†m<sup>3</sup>/h represents the volume of hydrogen gas produced per hour.

† kWh/m<sup>3</sup> represents the electrical energy consumed to produce a cubic meter of hydrogen gas.

‡€/kW represents cost of constructing the system (in Euros) for unit kilo-watt (kW) of electrical energy consumed.

Table 1.3: Comparison of alkaline (AEC), polymer electrolyte membrane (PEMEC) and solid oxide (SOEC) electrolyzer cells characteristics, adapted from Zeng and Zhang 2010, Chisholm and Cronin 2016, Schmidt et al. 2017.

performance characteristics of the electrolyzers available today, i.e. AEC, PEMEC and SOEC, are summarized in Table. 1.3. For hydrogen

generated by water electrolysis (using energy from renewable energy sources) to replace or at least reduce the dependence on fossil fuels, its price should reduce to around 1.1-2.4€/kg, see [European Commission \[2020\]](#). In order to achieve this objective by 2030 as well as cut green house gas emissions by 50-55%, [European Commission \[2020\]](#) discusses a strategic roadmap of actions over the years to transition to a more hydrogen dependent economy and decarbonise different industries. The roadmap discusses the importance of "upscaling to larger size, more efficient and cost-effective electrolyzers in the range of gigawatts that, together with mass manufacturing capabilities and new materials, supply hydrogen to large consumers".

As bubble evolution is one of the source of losses in water electrolyzers, its quick detachment can yield an energy saving of around 10-25% [[Darband et al., 2019](#)]. This energy saving can be understood in terms of voltage efficiency, which is calculated based on Eq.1.2, as

$$\% \text{ (Voltage efficiency)} = \frac{E_{rev}}{E} \times 100 = \left(1 - \frac{\eta}{E}\right) \times 100, \quad (1.6)$$

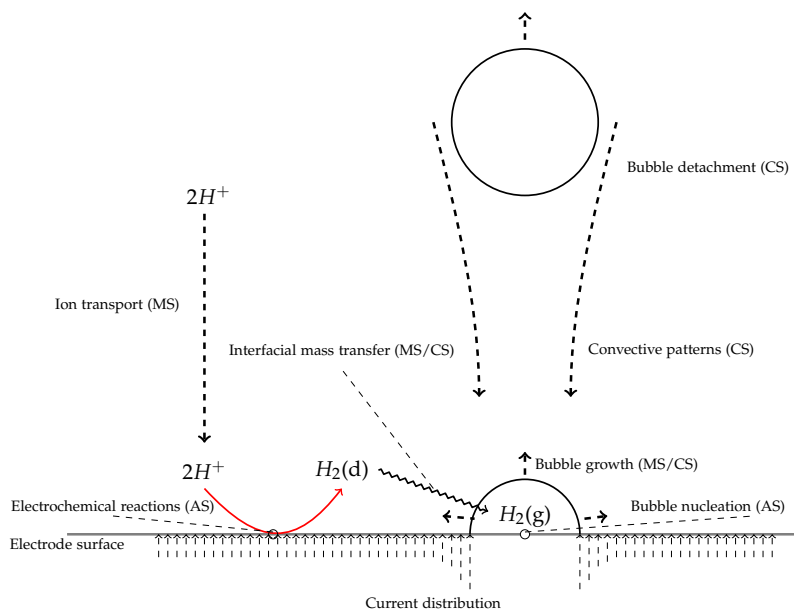
see [Zeng and Zhang \[2010\]](#). The voltage efficiency of the industrially used electrolyzers (AEC and PEMEC) is around 60-82% [[Schmidt et al., 2017](#)]. As the presence of bubbles increases  $\eta$ , its removal would result in reduction of the overpotential and increase the voltage efficiency of the system, based on Eq.1.6. Some of the practically used strategies to enhance the detachment of the bubbles in electrochemical systems are based on imposing ultrasonic, super gravity and external magnetic fields as well as developing superaerophobic surfaces, which has been reviewed in the recent work by [Darband et al. \[2019\]](#). So understanding the underlying physics that govern the bubble evolution is beneficial in developing newer and optimizing existing strategies to efficiently remove bubbles during water electrolysis.





## Chapter 2: Modelling electrochemical gas evolu- tion

In the previous chapter, the importance of understanding the bubble evolution, especially detachment, in improving the efficiency of water electrolysis is discussed. To create strategies to mitigate the losses introduced by bubble evolution, a fundamental understanding of bubble-electrode-electrolyte interface behaviour, which governs the detachment process, is critical.



Although experimental studies on bubble evolution, like [Yang et al. \[2018\]](#), [Fernández et al. \[2014\]](#), [Yang et al. \[2015\]](#), has shed light onto

Figure 2.1: Schematic of the multiscale nature and corresponding physics of electrochemical gas evolution. The abbreviations AS, MS and CS denotes the atomistic, meso and continuum scale physics with length and temporal scales ranging between  $1\text{ nm}-1\text{ m}$  and  $10^{-15}\text{ s}-1\text{ s}$  respectively [[Taqieddin et al., 2018](#)].

the existence of various hydrodynamic features in electrochemical systems and physics of phenomena, detailed visualization/measurement of the local flow parameters (and its temporal variations) can sometimes be difficult to obtain. For example, Particle Tracking Velocimetry (PTV) has been used to showcase the existence of Marangoni convection near electrochemical evolution of a single hydrogen bubble [Yang et al., 2018] but the tracer used in PTV method must be chosen such that these particles do not contaminate the flow or get absorbed at the liquid-gas interface [Ziegenhein et al., 2016] additionally this method is limited in its application to flows with large velocity gradients and high concentration of tracking particles [Cierpka et al., 2013, Cheminet et al., 2018]. On the other hand, numerical modelling of the phenomena can provide detailed information of spatial and temporal variation of the flow parameters that can provide insights into the dynamic nature of the bubble evolution which is invaluable in developing strategies to efficiently detach and remove these bubbles.

Due to the multiscale nature of electrochemical gas evolution, reviewed in Taqieddin et al. [2018] and illustrated in Fig.2.1, the spatial and temporal scales that are investigated determine the numerical approach used. For example, atomistic scale processes are typically investigated with molecular dynamics [Hofbauer and Frank, 2012] and density functional theory [Skúlason et al., 2010] simulations, whereas continuum scale processes like bubble evolution and interfacial mass transfer are usually studied using Computational Fluid Dynamics (CFD) [Catañeda et al., 2019]. To model mesoscale processes, like transport of ions, computational approaches based on Lattice Boltzmann Methods, which are applicable for atomistic to continuum scales, have been used in works like Gong and Cheng [2013], He and Li [2000]. As bubble growth and detachment, relevant in water electrolysis, are continuum scale phenomena, CFD can be used to study this process [Taqieddin et al., 2018].

The continuum scale CFD simulations that simulate electrochemical gas evolution must account for its multiphysics nature: the momentum transfer caused by the interaction between the phases (multiphase modelling), interfacial mass transfer along with the associated bubble growth, charge transport, electrochemical reactions and transport of dissolved gas. The complex and coupled interactions between the modules is summarized in Fig.2.2. The multiphase modelling approaches used to treat the interaction between the bubbles and liquid can be broadly categorized as dispersed phase and interface resolving methods. The dispersed phase modelling approaches require closure models to describe the momentum transfer between the phases because the dispersed phase [Sommerfeld, 2017], i.e. the bubbles, are not resolved as they are below the mesh resolution, see Fig.2.3. Addi-

tionally, these closure models typically rely on knowledge of the size of bubble at detachment as input, see Hreiz et al. [2015b]. On the other hand, interface resolving (IR) methods, like the Volume of Fluid (VOF) method, resolves the dynamic behaviour of the interface without any need to use approximations to describe the momentum transfer [Sommerfeld, 2017]. As a result IR approach, like the VOF method, can simulate bubble coalescence, detachment and deformation without the need for any approximations whereas dispersed modelling techniques requires models, like Fu and Ishii [2003], to account for the dynamic nature of bubble evolution. In multiphase simulations, dis-

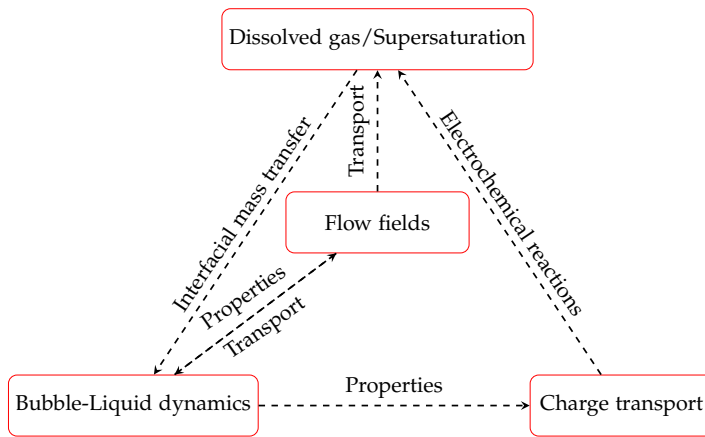
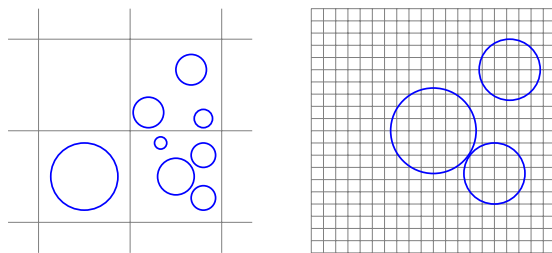


Figure 2.2: Illustration of the multiphysics nature of electrochemical gas evolution.

persed phase modelling approaches are typically used to study industrial scale systems where the larger flow patterns are more important and IR methods are used to study the behaviour of a few bubbles/the dynamic behaviour of interface in detail [Sommerfeld, 2017]. A few



(a) Dispersed phase modelling approach (b) Interface resolving approach

Figure 2.3: Illustration of the multiphase modelling approaches where — represents the interface between the gas and liquid.

examples of the application of IR based approaches are microfluidics

[Hoang et al., 2013], rising bubbles [Hysing, 2006, Klostermann et al., 2013], phase change processes [Samkhaniani and Ansari, 2016, Maes and Soulaire, 2020], as well as the growth and detachment process of bubbles in submerged orifice [Gerlach et al., 2006, Albadawi et al., 2013] and in multiphysics process like boiling [Georgoulas et al., 2017].

Although majority of works employ dispersed phase modelling to model electrochemical gas evolution, see Hreiz et al. [2015b], there has only been a limited application of IR approach to simulate this process. These IR approach based works vary in complexity with respect to the treated multiscale-multiphysics nature of the electrochemical gas evolution: Wang et al. [2011], Lafmejani et al. [2017], Zhang et al. [2020] accounted for just the multiphase modelling, Liu et al. [2016] simulated the interfacial mass transfer and bubble growth, and Einarsrud and Johansen [2012], Einarsrud et al. [2017], Sun et al. [2018] proposed a multiscale simulation framework but assumed that the larger bubbles (captured by interface resolved method) grow only via coalescence. In spite of the advances made by these studies, a full understanding of electrochemical gas evolution requires accounting for the coupled multiphysics and multiscale nature of the process which so far has received less attention, as noted in the recent review by Taqieddin et al. [2018]. Additionally, the CFD modelling of coalescence and detachment process during electrochemical bubble evolution has also not been well investigated, as discussed in the review by Taqieddin et al. [2017].

## Chapter 3:

### *Goals, outline and contributions*

#### *Research objectives and scope*

The main objective of this PhD is to develop a interface resolved framework, based on the Volume of Fluid (VOF) method, to treat the multiphysics nature of submillimeter sized hydrogen bubbles during water electrolysis. As the detailed understanding of the dynamics of interface is critical to elucidate the physics underlying the bubble growth and detachment, the proposed CFD framework would treat the interface dynamics, charge transport, electrochemical reactions, transport of dissolved gas as well as interfacial mass transfer and associated bubble growth. Continuum scale bubbles, in the context of this thesis, refers to bubbles with diameter in the order of a few hundred micrometers or larger which have been observed in experimental works like [Brussieux et al. \[2011\]](#), [Baczymalski et al. \[2017\]](#), [Yang et al. \[2018\]](#), [Bashkatov et al. \[2019\]](#). In order to develop the coupled multiphysics framework, based on the VOF approach, it is necessary to address the following questions:

- Is it possible to simulate submillimeter sized bubbles with the VOF method?
- How to simulate the transport of dissolved gas, interfacial mass transfer and associated bubble growth in VOF method?
- What are the physics relevant to developing a fully coupled framework for continuum scale electrochemical gas evolution?

The proposed framework is developed based on the assumption that the liquid and gas phases have constant density<sup>1</sup> and viscosity to simplify the simulations. The developed approach neglects the effect of temperature, like ohmic heating, and Marangoni [[Yang et al., 2018](#)] as well as natural [[Babu and Das, 2019](#)] convection.

Apart from the main objective stated earlier, the thesis also aims to present an overview of the physics relevant in electrochemical gas evo-

<sup>1</sup> For continuum scale bubbles treated in this thesis, the Laplace pressure in these spherical hydrogen bubbles, which can be calculated as  $2\sigma/R$  where  $\sigma$  is the surface tension (equal to 0.07 N/m) and  $R$  is the bubble radius, are typically around 140 Pa when  $R = 1000 \mu\text{m}$  and 700 Pa when  $R = 200 \mu\text{m}$ . The corresponding change in density, calculated based on the ideal gas law, is very small i.e. less than 1%.

lution and review relevant modelling approaches. In order to enable knowledge transfer and further advancements, the interface resolving approach employed in the proposed framework is also discussed. The multiphysics framework developed during the PhD is released together with this thesis (after the relevant papers are published) [Vacharambil, n.d.].

### *Outline of the thesis*

This thesis comprises of five parts, with each part subdivided into multiple chapters. An outline of the parts of the thesis are provided below:

#### *Part I: Introduction*

This part introduces the readers to the thesis topic, i.e. hydrogen production via water electrolysis, then describes the impact the bubbles have on the efficiency of the process as well as the importance of modelling the process. The objective and scope of the thesis is then stated.

#### *Part II: Multiphysics modelling of electrochemical hydrogen evolution*

This part of the thesis provides the readers with an overview of the relevant physics that underlie the evolution of hydrogen bubbles from the electrode surface during water electrolysis along with the numerical approaches required to tackle the multiphysics nature of the process. Although the goal of the thesis is to model hydrogen bubble evolution, modelling techniques reported in literature to simulate other processes, like gas evolution during aluminium reduction and pore-scale phenomena, has been included as they provide invaluable knowledge to achieve the project objectives.

#### *Part III: Introduction to the numerical framework*

This part of the thesis, the open source framework, i.e. OpenFOAM®, and the interface resolving method, i.e. interFoam, used to develop the proposed framework to simulate hydrogen bubble evolution are introduced. The thought behind adding this part was to summarize knowledge gain during the PhD about the implementation of interFoam, which is rather scattered in literature. This knowledge is relevant when customizing interFoam by adding new functionalities.

#### *Part IV: Contributions*

This part starts by highlighting the necessary tasks that must be addressed to develop the proposed framework by customizing inter-

Foam. Subsequently, the journal publications and conference proceedings submitted/published during the PhD duration are summarized to showcase the advances made towards developing the proposed framework during the PhD research.

*Part V: Final thoughts*

The final part of the thesis provides conclusions and highlights the possibilities for future work.

Following these parts of the thesis, appendices and bibliography along with the appended papers are provided.

*List of publications*

The thesis is written based on a collection of articles which has been submitted/published during the PhD. In addition to the journal publications and conference proceedings, conferences attended during the PhD have also been mentioned. In these works, Kurian J. Vachaparambil developed the solver, performed the simulations, evaluated and analyzed the results as well as wrote and submitted the manuscripts. The co-author in all these works, Kristian Etienne Einarsrud, has contributed by supervising, reviewing of the results, revising manuscripts and providing suggestions to increase the scientific level of the works.

*Primary works*

- Paper A: K.J. Vachaparambil & K.E. Einarsrud, Comparison of Surface Tension Models for the Volume of Fluid Method, *Processes*, 2019, 7, 542.<sup>2</sup> <sup>2</sup> Vachaparambil and Einarsrud 2019
- Paper B: K.J. Vachaparambil & K.E. Einarsrud, On sharp surface force model: effect of sharpening coefficient, Published in *Experimental and Computational Multiphase Flow*, 2020.<sup>3</sup> <sup>3</sup> Vachaparambil and Einarsrud 2020b
- Paper C: K.J. Vachaparambil & K.E. Einarsrud, Numerical simulation of bubble growth in a supersaturated solution, *Applied Mathematical Modelling*, 2020, 81, 690-710.<sup>4</sup> <sup>4</sup> Vachaparambil and Einarsrud 2020a
- Paper D: K.J. Vachaparambil & K.E. Einarsrud, Modeling interfacial mass transfer driven bubble growth in supersaturated solutions, *AIP Advances*, 2020, 10, 105024.<sup>5</sup> <sup>5</sup> Vachaparambil and Einarsrud 2020c
- Paper E: K.J. Vachaparambil & K.E. Einarsrud, On modelling electrochemical gas evolution using the Volume of Fluid method, Under peer-review in *14th International Conference on CFD in Oil & Gas, Metallurgical and Process Industries*.



Paper F: K.J. Vachaparambil & K.E. Einarsrud, Numerical simulation of continuum scale electrochemical hydrogen bubble evolution, Submitted to *Applied Mathematical Modelling*.

*Secondary works*

- K.J. Vachaparambil & K.E. Einarsrud, Hydrodynamics of electrochemical gas evolution. Presented at *NTNU Team Hydrogen Annual Workshop*, Trondheim, 2-3 December 2019.
- K.J. Vachaparambil & K.E. Einarsrud, Spurious velocities in the Volume of Fluid method: modeling a sub-millimeter bubble, Presented (poster) at *17th Multiphase Flow Conference and Short Course: Simulation, Experiment and Application*, Dresden, 11-15 November 2019.
- K.J. Vachaparambil & K.E. Einarsrud, Explanation of Bubble Nucleation Mechanisms: A Gradient Theory Approach, *Journal of The Electrochemical Society*, 2018, 165, E504.<sup>6</sup>
- K.J. Vachaparambil & K.E. Einarsrud, Analysis of Bubble Nucleation Mechanisms in Supersaturated Solutions: A Macroscopic Perspective, *ECS Meeting Abstracts*, 2018, MA2018-01 1366.<sup>7</sup>

<sup>6</sup> Vachaparambil and Einarsrud 2018b

<sup>7</sup> Vachaparambil and Einarsrud 2018a

## **Part II**

# **Multiphysics modelling of electrochemical hydrogen evolution**



## Chapter 4: Overview of the underlying physics

### Electrochemistry and thermodynamics

In order to understand the underlying electrochemical reactions that occur during water electrolysis, it is critical to understand the thermodynamics of the process. The overall electrochemical reaction of water electrolysis, Eq.1.1, involves generation of one mole of hydrogen and half mole of oxygen from a mole of water. The standard enthalpy of formation ( $H^0$ ) and molar entropy of the reactants and products ( $S^0$ ) corresponding to their physical state at standard operating conditions (pressure of 1 bar and 298 K) are tabulated in Table.4.1. The change in molar entropy due to reaction ( $\Delta S$ ) is calculated as  $S_{H_2}^0 + 0.5S_{O_2}^0 - S_{H_2O}^0$  to be  $0.16 \text{ kJmol}^{-1}\text{K}^{-1}$  and the corresponding change in enthalpy ( $\Delta H$ ) is  $285.8 \text{ kJmol}^{-1}$ . The Gibbs free energy ( $\Delta G$ ) for the reaction can be calculated as  $\Delta H - T\Delta S$  to be equal to  $237.12 \text{ kJmol}^{-1}$ , which shows that electrolysis of water is non-spontaneous and require external energy source.

	Units	$H_2O$ (l)	$H_2$ (g)	$O_2$ (g)
$H^0$	$\text{kJ mol}^{-1}$	-285.8	0	0
$S^0$	$\text{J mol}^{-1}\text{K}^{-1}$	70.0	130.7	205.2

Table 4.1: Thermodynamic properties of reactants and products during electrolysis of water at 298 K [Haynes, 2011].

Based on the calculated Gibbs free energy, the theoretical minimum voltage required for water splitting reaction, known as reversible potential for the reaction ( $E_{rev}$ ), can be calculated as

$$E_{rev} = \frac{\Delta G}{nF}, \quad (4.1)$$

where  $n$  and  $F$  are number of electrons transferred (equal to 2 for HER) and Faraday's constant, to be equal to  $1.23 \text{ V}$  [Coutanceau et al., 2018, Zeng and Zhang, 2010]. Use of higher temperature for electrolysis reduces  $E_{rev}$  as the contribution from  $T\Delta S$  increases with temperature,

as shown by [Coutanceau et al. \[2018\]](#). Due to the losses, described in Eq.1.2, the applied potential must be larger than  $E_{rev}$  to start electrochemical reactions, discussed in Table.1.1.

### Bubble nucleation

Due to the continuous electrochemical reactions, the electrolyte in the vicinity of the electrode ultimately becomes supersaturated. The supersaturation ratio ( $S$ ), which indicates the concentration of the dissolved gas that exceeds the saturation condition, is calculated as

$$S = \frac{C}{C_{sat}}, \quad (4.2)$$

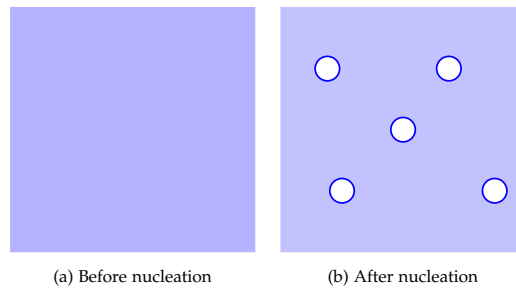
where  $C$  is the local concentration of dissolved gas and  $C_{sat}$  is the saturation concentration which is computed based on the Henry's law [[Henry and Banks, 1803](#)]. In the attempt to regain equilibrium, i.e.  $S = 1$ , the supersaturated electrolyte undergoes 'nucleation' which can occur via one of the four modes proposed by [Jones et al. \[1999\]](#). According to the 'classical theory', the minimum radii of the nucleated bubble is calculated as

$$R_c = \frac{2\sigma_0}{(S-1)P} \quad (4.3)$$

where  $P$  represents the pressure inside the bubble (including the Laplace pressure) and  $\sigma_0$  is the surface tension of the liquid-air interface at 1 atm, which for pure water is equal to 0.07198 N/m, [[Massoudi and King, 1974](#), [Lubetkin, 2003](#)]. These four nucleation modes, which provide a mechanistic description of the formation of these bubbles, are summarized below.

### Homogeneous nucleation

Figure 4.1: Illustration of homogeneous nucleation based on analogous graphics in [Jones et al. 1999](#).



In homogeneous nucleation, the formation of bubbles occurs randomly in the bulk as shown in Fig.4.1. This nucleation mode occurs at very high values of  $S$ , typically in the order of 100 [[Hemmingsen,](#)

1977]. The homogeneous nucleation is very difficult to observe experimentally, due to high supersaturation required [Liu, 2000]. For instance in electrochemical systems, supersaturation of electrolyte in the vicinity of the electrode would establish mass transport due to natural convection which would result in the redistribution of the dissolved gas [Babu and Das, 2019].

#### Heterogeneous nucleation

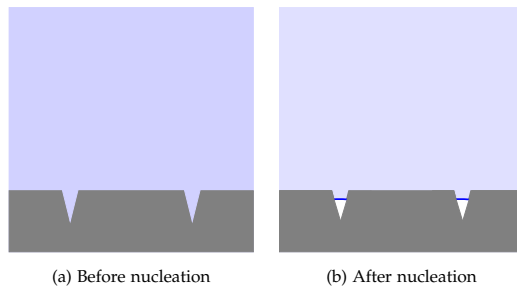


Figure 4.2: Illustration of heterogeneous nucleation mode based on analogous graphics in Jones et al. 1999.

The heterogeneous nucleation refers to the bubble formation that is aided by surface imperfections, as shown in Fig.4.2. The supersaturation required for this mode of bubble formation is lower than the homogeneous mode due to smaller nucleation energy requirement [Liu, 2000]. Once a bubble is formed via heterogeneous nucleation, a part of the bubble remains attached to the microstructure after the original bubble grows and detaches. The remaining bubble serves as a site for pseudo-classical and non-classical nucleation modes [Jones et al., 1999].

#### Pseudo-classical nucleation

Pseudo-classical nucleation uses pre-existing bubbles of radii smaller than the critical radius of nucleation, Eq.4.3, which are present on the microstructure at the surface or in the bulk, see Fig.4.3. Although classically speaking bubbles with radii below  $R_c$  shrink and disappear, these bubbles exist in supersaturated solutions due to the reduction on surface tension due to adsorption of gases at the interface [Lubetkin, 2003]. For example, the surface tension ( $\sigma$ ) of water due to adsorption of hydrogen under saturation condition can be written as

$$\sigma = \sigma_0 + bP, \quad (4.4)$$

where  $b$  is dependent of the adsorbed gas which in the case of  $H_2$  is equal to  $-0.0250 \text{ dyn}/(\text{cm}\cdot\text{atm})$  [Massoudi and King, 1974]. The

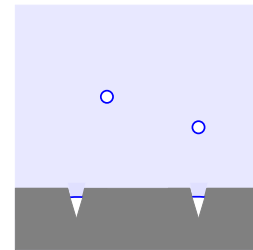


Figure 4.3: Illustration of the pre-existing bubbles, whose radii is smaller than  $R_c$ , relevant in pseudo-classical nucleation mode based on analogous graphics in Jones et al. 1999.

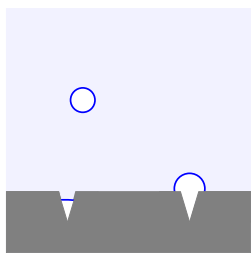


Figure 4.4: Illustration of pre-existing bubbles, whose radii is larger or equal to  $R_c$ , relevant in non-classical nucleation mode based on analogous graphics in Jones et al. 1999.

revised critical radius,  $R_c^*$  (which is smaller than  $R_c$ ), for nucleation can be estimated as

$$R_c^* = \frac{2(\sigma_0 + bP)}{(S-1)P} = \frac{2\sigma_0}{(S-1)P} + \frac{2b}{S-1}. \quad (4.5)$$

Apart from these bubbles, the stable nanobubbles, which has radii smaller than  $R_c$  [Attard, 2016], has also been observed to aid in bubble evolution [Hao et al., 2018]. Compared to heterogeneous nucleation, pseudo-classical mode requires lower supersaturation as the pre-existing bubble reduces the energy barrier [Jones et al., 1999].

#### *Non-classical nucleation*

The pre-existing bubbles, with radii  $\geq R_c$ , which are present on the surface imperfections and in the bulk (see Fig.4.4) can effectively reduce the nucleation energy required to zero [Jones et al., 1999]. This nucleation mode drives the cyclic evolution of bubbles, even at relatively low supersaturation levels ( $S \leq 8$ ) or low current densities (in the order of  $100 \text{ A/m}^2$ ), from the same site on the surface like observed during gas evolution during water electrolysis [Glas and Westwater, 1964, Brussieux et al., 2011].

#### *Bubble growth, coalescence and detachment*

Once a pre-existing bubble is available for the non-classical nucleation, the bubble grows and coalesce with adjacent bubbles. The evolution of the single bubble radius ( $R$ ) can be expressed empirically as

$$R = At^x, \quad (4.6)$$

where  $A$ ,  $x$  are the growth coefficient and time coefficient respectively. The value of  $x$  varies across three regimes of bubble growth: inertial controlled, diffusion controlled and direct injection [Matsushima et al., 2009, Sakuma et al., 2014, Zhao et al., 2019b]. The first regime is based on the work by Rayleigh [1917], characterized by  $x$  is equal to unity, is inertial controlled which can be understood as being limited by the displacement of the surrounding fluid, see Bejan and Kraus [2003]. This growth regime lasts only for fraction of a second and is typically observed in bubbles smaller than the 0.1 mm, see Matsushima et al. [2009], Sakuma et al. [2014]. In the second regime of bubble growth, which is diffusional mass transfer across the interface, is characterized by time coefficient equal to 0.5 [Scriven, 1959, Burman and Jameson, 1976]. In this regime, the wettability slightly influences the time coefficient, due to the dependence of the shape of the bubble on the contact angle [Sakuma et al., 2014]. The third regime, known as direct

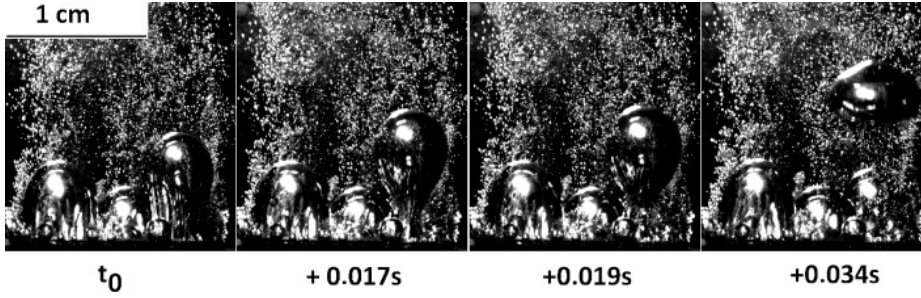


Figure 4.5: Experimentally observed detachment of a hydrogen bubble during water electrolysis under a constant current density of  $7000\text{A/m}^2$  [Brussieux et al., 2011]. The smaller hydrogen bubbles in the figure are formed at the border of the electrode whereas the bigger bubbles (which are in the order of few millimeters) are at the center of the electrode. Reproduced from Brussieux et al. 2011 with permission from Elsevier.

injection, which is characterized by  $x$  equal to  $1/3$  that corresponds to bubble growth controlled by the electrochemical reactions [Zhao et al., 2019b, Sakuma et al., 2014, Matsushima et al., 2009]. Apart from mass transfer driven bubble growth, adjacently growing bubbles can coalesce to form a larger bubble which has been observed in electrochemical systems [Westerheide and Westwater, 1961, Brussieux et al., 2011, Bashkatov et al., 2019].

Once the bubble is large enough the forces due to buoyancy and convection in electrolyte overcomes the anchoring force (related to the surface tension and wetting properties) and the bubble detaches, see Fig.4.5. Additionally, the convection induced by the coalescence of

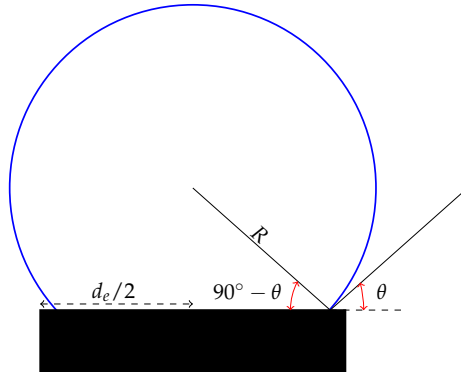


Figure 4.6: Illustration of bubble on a microelectrode along with the contact angle (estimated in the liquid). At detachment,  $\theta$  is equal to  $\theta_{de}$  and footprint of the bubble is nearly the size of the electrode (of diameter in the order of few hundred micrometers) as observed in Fernández et al. 2014.

bubbles has been proposed, in the recent numerical work by Zhang et al. [2020], to help in detachment of the merged bubble. A simple correlation for bubble radius at detachment ( $R_{de}$ ), derived in Fernández et al. [2014], is based on balance of surface tension and buoyancy forces of a spherical bubble at departure as

$$\frac{4}{3}\pi R_{de}^3 \Delta\rho g = 2\pi \frac{d_e}{2} \sigma \sin\theta_{de}, \quad (4.7a)$$



<sup>1</sup> Typically  $\Delta\rho$  is expressed as  $\Delta\rho \approx \rho_1$ , as the density of the bubble (in the order of  $10^0$  kg/m<sup>3</sup>) can be neglected in comparison to the density of the electrolyte (in the order of  $10^3$  kg/m<sup>3</sup>).

where  $\Delta\rho$  is the difference in the densities of the electrolyte and bubble<sup>1</sup>,  $g$  is the acceleration due to gravity,  $\theta_{de}$  is the contact angle at detachment and  $d_e$  is the diameter of the electrode, which in the case of Fernández et al. 2014 is approximately equal to the footprint of the bubble on the electrode. By rearranging the terms in the above equation and substituting  $\sin\theta_{de}$  as  $d_e/(2R_{de})$ , based on Fig.4.6, gives

$$R_{de} = \left( \frac{3d_e^2\sigma}{8g\Delta\rho} \right)^{1/4}, \quad (4.7b)$$

which has been shown to reasonably predict the hydrogen bubble detachment in the work by Fernández et al. [2014]. Another commonly used formulation, obtained empirically for boiling phenomena, used in literature to predict detachment size of bubbles in an electrochemical systems is

$$R_{de} = A\theta_{de}\sqrt{\frac{\sigma}{g\Delta\rho}}, \quad (4.8)$$

where  $A$  is dependent on the experiment, typically reported to be lower than unity [Brussieux et al., 2011, Vogt and Balzer, 2005]. Apart from this simple correlation, other works have used more complex approaches that considers the force balance to account for the effect of surface tension, buoyancy and other forces to predict detachment radius of the bubble, see Garcia-Navarro et al. [2019], Zhang and Zeng [2012], Taqieddin et al. [2017]. As larger current densities cause the evolution of more bubbles, Vogt and Balzer [2005] proposed a correlation to describe the dependence of bubble coverage of the electrode ( $\Theta$ ) on  $i$  (expressed in A/m<sup>2</sup>):  $\Theta = (i/i_{\Theta \rightarrow 1})^{0.3}$ , where  $i_{\Theta \rightarrow 1}$  corresponds to the current density when the electrode is completely covered by bubbles.

Once the bubble detaches, gas dissolved in the electrolyte is transported by the various transport modes (see review by Zhao et al. 2019b): diffusion of the reactant from fresh electrolyte after detachment (penetration model developed initially by Adam et al. [1971]), microconvection due to growth of an adhered bubble (developed by Stephan and Vogt [1979]) and the convection caused by swarm of rising bubbles (hydrodynamic model developed by Janssen and Hoogland [1970, 1973]). A recent work by Vogt and Stephan [2015] reported a global correlation to treat the transport associated with penetration, microconvection and wake (of detached bubble) modes. Apart from these classical convection modes, related to bubble evolution, which aids in the transport of the dissolved gas, recent experimental works by Yang et al. [2018] have reported the existence of Marangoni convection which generates strong vortex at the foot of the electrochemically generated hydrogen bubble. Additionally the spatial variations in density, due to gradients in temperature and supersaturation, produces natural

convection in electrochemical systems which is dominant when bubble evolution is negligible [Novev and Compton, 2018, Babu and Das, 2019]. These complex flow features, developed as a result of electrochemical gas evolution, results in redistribution of the dissolved gas which in turn influences further bubble evolution.



## Chapter 5:

# *Multiphase flows*

In this chapter an overview of both dispersed phase modelling and interface resolving (IR) methods, which were introduced in Chapter 2, is presented with emphasis on the latter.

### *Interface resolving methods*

IR methods are typically used when interface dynamics is the topic of investigation like during bubble growth and detachment. These IR methods are generally used to understand the flow physics and develop 'engineering type' correlations for momentum, heat and mass transfer for specific flow scenarios. The IR methods can broadly be divided into two approaches: interface tracking and capturing approaches. Interface tracking, like the moving mesh method, uses a boundary fitted mesh for each phase and are used typically to simulate mild deformation of interfaces, see [Tuković and Jasak \[2012\]](#). In interface capturing approaches, a fixed grid method that does not track the interface, reconstructs the interface from a scalar field which represents the phases [[Sommerfeld, 2017](#)]. Examples of popular interface capturing approaches are the Volume of Fluid (VOF) [[Deshpande et al., 2012a](#)], Phase Field [[Jamshidi et al., 2019](#), [Zhang et al., 2020](#)] and Level-Set [[Sussman et al., 1994](#)] methods. The phase field model relies on the evolution of the phase field parameter, which is computed based on Cahn-Hilliard equation, to describe the dynamics of the interfacial region of finite thickness [[Jamshidi et al., 2019](#)]. The thickness of the diffused nature of the interface is dependent on the user-defined value of capillary width which can introduce imbalance in mass if it is not small enough [[Yue et al., 2007](#)]. The level-set methods, which is based on the advection of a level-set parameter, relies on a reinitialization procedure to capture the interface accurately [[Sussman et al., 1994](#)]. Apart from the additional step required to reinitialize the level set function, the method as proposed by [Sussman et al. \[1994\]](#) has difficulties in conserving the mass, mainly due to numerical diffusion of

the solution [Yuan et al., 2018], but improvements to the method have addressed this, for example, using source terms [Yuan et al., 2018] and gradient-augmented level set methods [Nave et al., 2010]. The VOF method, which is based on the advection of a scalar volume fraction, in principle ensures mass conservation but to obtain a sharp interface it requires either an algebraic algorithm or sub-cell level reconstruction of the interface to render a sharp interface [Deshpande et al., 2012a]. Due to the relative ease to numerically implement and conserve mass, VOF is very commonly used to simulate multiphase flows [Deshpande et al., 2012a, Sommerfeld, 2017, Jamshidi et al., 2019] and is available in both commercial, such as ANSYS® Fluent® [ANSYS Inc., 2020] and FLOW-3D® [Flow Science Inc., 2019], and opensource, like OpenFOAM® [OpenFOAM, 2019], softwares.

*The Volume of Fluid method*

Proposed initially by Hirt and Nichols [1981], the Volume of Fluid (VOF) method uses a scalar known as volume fraction of liquid ( $\alpha_1$ ) to distinguish between the phases:

$$\alpha_1(\vec{x}, t) = \begin{cases} 0 & \text{(within gas or Phase 2)} \\ 0 < \alpha_1 < 1 & \text{(at the interface)} \\ 1 & \text{(within liquid or Phase 1)} \end{cases},$$

where  $\alpha_1$  can be understood to be a scalar field that represents the fraction of the volume occupied by liquid per unit grid volume. Similarly the volume fraction of the gas ( $\alpha_2$ ) can be calculated as  $1 - \alpha_1$ . The fluid properties like density and viscosity,  $\chi \in [\rho, \mu]$ , are determined as

$$\chi = \alpha_1 \chi_1 + \alpha_2 \chi_2. \tag{5.1}$$

The mass conservation of the phases can be written as

$$\nabla \cdot \vec{U} = \dot{m}, \tag{5.2}$$

where  $\dot{m}$  is a source term and  $\vec{U}$  is the single field description of velocity (shared by both phases). The advection equation for volume fraction of liquid is

$$\frac{\partial \alpha_1}{\partial t} + \nabla \cdot (\vec{U} \alpha_1) = \alpha_1 \dot{m}. \tag{5.3}$$

To capture the interface, which essentially is a discontinuous  $\alpha_1$  field, the advection of volume fraction is performed with either a computationally expensive geometric reconstruction method, to render a very sharp interface in one cell, or a computationally cheaper algebraic method, which produces a comparatively smeared interface (over 2

or 3 cells), described further in [Deshpande et al. \[2012a\]](#). The momentum equation for both phases is described using a single conservation equation:

$$\frac{\partial \rho \vec{U}}{\partial t} + \nabla \cdot (\rho \vec{U} \vec{U}) = -\nabla p + \nabla \cdot \mu (\nabla \vec{U} + \nabla \vec{U}^T) + \rho \vec{g} + \vec{F}_{ST}, \quad (5.4)$$

where  $\vec{F}_{ST}$  is the volumetric representation of the surface tension force which is typically modelled with the Continuum Surface Force approach, as proposed by [Brackbill et al. \[1992\]](#).

The VOF based approaches to study electrochemical gas evolution can be broadly divided based on the complexity into: (a) pure VOF, (b) multiphysics VOF, (c) hybrid VOF. Studies based on pure VOF, like [Wang et al. \[2011\]](#), [Lafmejani et al. \[2017\]](#), consider the multiphase nature of the phenomena by describing bubble evolution by using appropriate boundary conditions to account for bubble growth. The multiphysics VOF accounts for the works which treat some multiphysics relevant to electrochemical gas evolution, for example; [Liu et al. \[2016\]](#) simulated the growth and evolution of a hydrogen bubble due to interfacial mass transfer based on a Sherwood number correlation<sup>1</sup>. The hybrid VOF refers to works that account mainly for the multiscale nature of electrochemical gas evolution by simulating the larger bubbles with VOF and the sub-grid bubbles modelled using dispersed modelling approaches. For example, the works by [Sun et al. \[2018\]](#) and [Einarsrud and Johansen \[2012\]](#), [Einarsrud et al. \[2017\]](#) coupled sub-grid bubbles, modelled using a Lagrangian approach and population balance model respectively, to the VOF model to enable the growth of the larger bubble due to coalescence with the sub-grid bubbles. [Einarsrud and Johansen \[2012\]](#), [Einarsrud et al. \[2017\]](#) also treated the charge transport and the electrochemical reactions to estimate the growth of the sub-grid bubbles.

<sup>1</sup> The use of Sherwood number correlations to compute interfacial mass transfer is further described in Chapter 6.

### *Dispersed phase modelling*

As dispersed phase modelling approaches do not resolve the gas bubbles, the information lost about these dispersed bubbles are incorporated in the governing equations via closure terms for momentum and mass transfer. These closure terms are often flow scenario specific, for example the computation of drag force on a moving spherical bubble is dependent on Reynolds number of the associated flow and knowledge on the bubble size, see [Yeoh and Tu \[2010\]](#), [Liu et al. \[2018a\]](#), [Hreiz et al. \[2015b\]](#). Readers interested in the mathematics underlying the use of averaging technique to derive the governing equations for this approach should refer to books like [Drew and Passman \[1999\]](#) or [Yeoh and Tu \[2010\]](#). In this section, the final forms of the averaged

<sup>2</sup> To reduce complexity in representation, the averaged variable differs from the variables used in VOF by a different subscript, i.e.  $c$  and  $d$  for continuum and dispersed phases respectively.

governing equations<sup>2</sup> are provided along with a few examples of its applications to electrochemical gas evolution, see [Hreiz et al. \[2015b\]](#), [Catañeda et al. \[2019\]](#) for review.

### Euler-Euler

The averaged mass conservation equation can be described as

$$\frac{\partial}{\partial t}(\rho_k \alpha_k) + \nabla \cdot (\rho_k \alpha_k \vec{U}_k) = \dot{R}_k, \quad (5.5)$$

where  $\alpha_k$  is the averaged volume fraction and  $\dot{R}_k$  describes the source term of the dispersed ( $d$ ) or continuum ( $c$ ) phases based on  $k$ . The averaged momentum equation for the phase  $k$  is

$$\begin{aligned} \frac{\partial}{\partial t}(\rho_k \alpha_k \vec{U}_k) + \nabla \cdot (\rho_k \alpha_k \vec{U}_k \vec{U}_k) = & -\alpha_k \nabla p + \alpha_k \rho_k \vec{g} \\ & + \nabla \cdot \left[ \mu_k \alpha_k (\nabla \vec{U}_k + \nabla \vec{U}_k^T) \right] + \dot{R}_k \vec{U}_k + \vec{F}_k^{inter}, \end{aligned} \quad (5.6)$$

where  $p$  is the shared pressure between the phases,  $\mu_k$  is the sum of molecular and turbulent dynamic viscosities,  $\vec{F}_k^{inter}$  represents the momentum transfer between the phases and  $\dot{R}_k \vec{U}_k$  is the momentum due to mass sources. The momentum transfer between the phases typically accounts for

- Drag, which opposes the motion of bubbles in liquid [[Deen et al., 2001](#), [Yamoah et al., 2015](#)],
- Lift, which is experienced by bubbles due to rotation or shear flow [[Deen et al., 2001](#), [Yamoah et al., 2015](#)],
- Added/virtual mass, accounts for the the work required to accelerate the liquid as a result of the acceleration of the dispersed bubble [[Deen et al., 2001](#)],
- Wall lubrication, caused by the pressure difference experienced by the bubble as it travels close to the wall [[Yamoah et al., 2015](#)].
- Turbulent dispersion, accounts for the effect of turbulence on bubbles [[Liu et al., 2018a](#)],

which are calculated based on some degree of approximation [[Deen et al., 2001](#), [Yamoah et al., 2015](#), [Liu et al., 2018a](#)].

The application of Euler-Euler method to simulate electrochemical gas evolution during water electrolysis typically treat momentum transfer due to forces like drag, lift and turbulent dispersion but vary with respect to the assumption of bubble size used in the simulations. Works like [Liu et al. \[2018a\]](#), [Alexiadis et al. \[2012\]](#) and [Mat et al. \[2004\]](#) assume that the bubbles are of a constant size which leads to ignoring

the effects of bubble coalescence and breakup. In order to obtain the variations in bubble sizes, works like [Liu et al. \[2018b\]](#) and [Zhan et al. \[2018\]](#) coupled the Euler-Euler model with interfacial area concentration and population balance models, which relies on approximations to describe the coalescence and breakup of bubbles [[Wang et al., 2005](#), [Fu and Ishii, 2003](#)].

### Mixture

A simpler variant of the Euler-Euler approach, known as the Mixture model, is based on the approximation that complex interactions between the phases would cancel out if the mixture is considered, for instance  $\sum R_k = 0$  [[Sommerfeld, 2017](#)]. The governing equation for conservation of mass for the mixture of phases is

$$\frac{\partial}{\partial t}(\rho_m) + \nabla \cdot (\rho_m \vec{U}_m) = 0, \quad (5.7)$$

where the  $\rho_m$  and  $\vec{U}_m$  are defined in

$$\chi_m = \sum \alpha_k \chi_k \text{ where } \chi \in [\rho, \mu], \quad (5.8a)$$

$$\rho_m \vec{U}_m = \sum \alpha_k \rho_k \vec{U}_k. \quad (5.8b)$$

The momentum conservation equation for the mixture is

$$\begin{aligned} \frac{\partial}{\partial t}(\rho_m \vec{U}_m) + \nabla \cdot (\rho_m \vec{U}_m \vec{U}_m) = & -\nabla p + \rho_m \vec{g} \\ & + \nabla \cdot \left[ \mu_m (\nabla \vec{U}_m + \nabla \vec{U}_m^T) \right] - \nabla \cdot \sum \alpha_k \rho_k \vec{U}_{km} \vec{U}_{km}, \end{aligned} \quad (5.9)$$

where  $\vec{U}_{km} = \vec{U}_k - \vec{U}_m$  is the relative slip between the phase  $k$  (which represents continuous fluid ( $c$ ) and dispersed phase ( $d$ )) and the mixture [[Sommerfeld, 2017](#), [Sanyal et al., 1999](#)]. In the special case when  $\vec{U}_{km}$  is equal to zero, the approach is known as homogeneous mixture model [[Sommerfeld, 2017](#)]. Additionally, mixture model uses a conservation equation for the dispersed phase (represented by subscript  $d$ ) which is expressed as

$$\frac{\partial}{\partial t}(\rho_d \alpha_d) + \nabla \cdot (\rho_d \alpha_d \vec{U}_m) = \dot{R}_d - \nabla \cdot (\alpha_d \rho_d \vec{U}_{dm}), \quad (5.10)$$

where  $\dot{R}_d$  is the generation of the gas bubble at the electrode [[Sanyal et al., 1999](#)].

The mixture model has been used to simulate the electrochemical gas evolution during water electrolysis, with non-zero  $\vec{U}_{km}$  (which is modelled using closure terms that accounts for momentum transfer between phases) along with the assumption of constant size of bubbles, in works like [Wedin and Dahlkild \[2001\]](#), [Dahlkild \[2001\]](#), [Schillings et al. \[2015\]](#).



### Euler-Lagrange

In this approach, the Euler approach is used to treat the continuous fluid (represented by subscript  $c$ ) but the individual dispersed bubbles are computed using Lagrangian approach. The averaged continuity equation is described as

$$\frac{\partial}{\partial t}(\rho_c \alpha_c) + \nabla \cdot (\rho_c \alpha_c \vec{U}) = \dot{R}_c, \quad (5.11)$$

where  $\alpha_c$  and  $\vec{U}$  are the averaged volume fraction and the velocity of the continuous fluid respectively, and  $\dot{R}_c$  is the source term which accounts for the bubble growth, see [Taqieddin et al. \[2017\]](#), [Battistella et al. \[2018\]](#). The averaged momentum conservation equation for continuous phase can be described as

$$\begin{aligned} \frac{\partial}{\partial t}(\rho_c \alpha_c \vec{U}) + \nabla \cdot (\rho_c \alpha_c \vec{U} \vec{U}) = & -\alpha_c \nabla p + \alpha_c \rho_c \vec{g} \\ & + \nabla \cdot \left[ \mu_c \alpha_c (\nabla \vec{U} + \nabla \vec{U}^T) \right] + \vec{F}^{inter}, \end{aligned} \quad (5.12)$$

where  $\vec{F}^{inter}$  accounts for the momentum transfer between liquid and the Lagrangian bubbles and  $\mu_c$  accounts for both molecular as well as turbulent viscosities of the continuous phase [[Taqieddin et al., 2017](#), [Battistella et al., 2018](#)]. For the dispersed phase, which are treated in a Lagrangian approach, the velocity, position, volume and density of individual bubble are represented by  $\vec{v}_b$ ,  $\vec{x}_b$ ,  $V_b$  and  $\rho_b$  respectively. The Lagrangian tracking of the individual bubble is based on governing equations for particle velocity, position and volume as

$$\rho_b V_b \frac{d\vec{v}_b}{dt} = \sum \vec{F} - \rho_b \frac{dV_b}{dt} \vec{v}_b, \quad (5.13a)$$

$$\frac{d\vec{x}_b}{dt} = \vec{v}_b, \quad (5.13b)$$

$$\rho_b \frac{dV_b}{dt} = \dot{R}_b, \quad (5.13c)$$

where  $\dot{R}_b$  accounts for the bubble growth due to mass transfer and  $\sum \vec{F}$  accounts for net force acting on the bubble [[Taqieddin et al., 2017](#), [Battistella et al., 2018](#)].

The Euler-Lagrange based approach has been used in works like [Philippe et al. \[2005\]](#), [Hreiz et al. \[2015a\]](#) to simulate the bubble evolution during water electrolysis where the variations in the bubble size during evolution due to growth, coalescence and breakup are neglected. Similarly, the work by [Nierhaus et al. \[2009\]](#) simulated the effect of bubble evolution with polydispersed sizes in a rotating disk during water electrolysis.

## Chapter 6: Electrochemical reactions and bubble growth

### Charge transport and electrochemical reactions

In single phase flow, the flux of cations and anions in a bubble free electrolyte, can be described using the Nernst-Planck equation:

$$\vec{N}_{\pm} = -\frac{F}{RT}z_{\pm}C_{\pm}D_{\pm}\nabla\Phi - D_{\pm}\nabla C_{\pm} + C_{\pm}\vec{U}, \quad (6.1)$$

where the first, second and last terms represents the movement of the ions driven by potential difference, diffusion and convection respectively. In Eq.6.1,  $F$  is the Faraday's constant,  $RT$  is the product of the universal gas constant and temperature,  $z_{\pm}$  is the charge,  $D_{\pm}$  is the diffusion coefficient of the ions in the solution,  $\Phi$  is the potential applied at the electrodes and  $C_{\pm}$  is the concentration of the ions. The current density is calculated as

$$\vec{i} = Fz_{-}\vec{N}_{-} + Fz_{+}\vec{N}_{+}. \quad (6.2)$$

The governing equation for conservation of charge, known as Gauss' law (of the Maxwell's equations of electromagnetism), is

$$\nabla \cdot \vec{i} = 0. \quad (6.3)$$

In order to solve Eq.6.3, an additional transport equation of the anions and cations, based on Eq.6.1, in a single phase can be described using the Nernst-Planck equation as

$$\frac{\partial C_{\pm}}{\partial t} = \nabla \cdot \vec{N}_{\pm}. \quad (6.4)$$

As Eq.6.3 and Eq.6.4 are coupled, they are solved using a iterative methods with individual transport equation for each ions that is being modelled, see Litrico et al. [2017]. This approach is typically used in single phase flow applications like in electrochemical copper deposition [Litrico et al., 2017].

<sup>1</sup> The interfacial jump conditions for dissolved species is further discussed in Eq.6.10a and Eq.6.10b.

Due to the complexity in extending these ion transport equation for multiphase flows, whereas interfacial jump conditions<sup>1</sup> are relevant, a simpler alternative can be obtained by assuming electroneutrality which neglects the temporal and spatial gradients of  $C_{\pm}$ . This approximation allows Eq.6.2 to be simplified to get Ohm's law:

$$\vec{i} = -\Gamma_e \nabla \Phi, \quad (6.5)$$

where  $\Gamma_e$  describes the conductivity of the pure electrolyte, derived from Eq.6.1 and Eq.6.2 based on the assumptions used in this approach, as

$$\Gamma_e = \frac{F^2}{RT} (z_+^2 D_+ C_+ + z_-^2 D_- C_-). \quad (6.6)$$

In the presence of bubbles, which are insulating, the effective conductivity of the electrolyte is lower than  $\Gamma_e$ , which can be estimated using the correlations available to literature, see Table.1.2. When using interface resolving methods,  $\Gamma_e$  is replaced with  $\Gamma$  in Eq.6.5 and then combined with Eq.6.3 to get

$$\nabla \cdot (\Gamma \nabla \Phi) = 0, \quad (6.7)$$

where  $\Gamma$  can be computed as the arithmetic mean [Einarsrud and Johansen, 2012], analogous to Eq.5.1, and harmonic mean [Einarsrud et al., 2017], analogous to Eq.6.13, of the individual phase conductivities.

Once the current density ( $\vec{i}$ ) is known at the electrode surface, the electrochemical gas reaction can be modelled based on Faraday's law of electrolysis [Ehl and Ihde, 1954] as

$$R_h = \frac{|\vec{i}|}{nF}, \quad (6.8)$$

where  $R_h$  is the rate of production of dissolved gas per unit area and  $n$  is the number of electrons transferred for the reaction, which for the hydrogen evolution reaction (HER) is equal to two.

### *Dissolved gas transport*

For an incompressible single phase flow, the transport of the species, which does not modify the flow, can be written as

$$\frac{\partial C}{\partial t} + \nabla \cdot (\vec{U}C) = \nabla \cdot D \nabla C + \mathfrak{S}_c, \quad (6.9)$$

where  $\vec{U}$  is the velocity of the single phase,  $\mathfrak{S}_c$  is the source/sink term for the dissolved gas,  $C$  and  $D$  represents the molar concentration and diffusion coefficient of the dissolved species. When compared to single phase flows, the species transport in a two phase systems must account

for the jump conditions across the interface for the fluxes (Eq.6.10a) and concentration (Eq.6.10b):

$$\llbracket (-D_{i,j}\nabla C_{i,j}) \cdot \vec{n} \rrbracket = 0, \quad (6.10a)$$

$$C_{i,2} = He_i C_{i,1}, \quad (6.10b)$$

where the square brackets are used to represent the interfacial jump,  $D_{i,j}$  and  $C_{i,j}$  represent the diffusion coefficient and molar concentration of dissolved gas ( $i$ ) in phase  $j$  respectively,  $\vec{n}$  is the unit normal vector to the interface, and  $He_i$  is the non-dimensional partition coefficient that describes the concentration jump across the interface [Deising et al., 2016, Falcone and Marschall, 2017].

In order to satisfy the interface conditions, the governing equation that is used to describe the species transport in two phase systems can be categorized into single and two field approaches. The two field approach distinguishes between the species present in individual phases and computes the transport species for each phase as

$$\frac{\partial C_{i,j}}{\partial t} + \nabla \cdot (\vec{U}_j C_{i,j}) = \nabla \cdot D_{i,j} \nabla C_{i,j} + \mathcal{S}_i, \quad (6.11)$$

where  $\mathcal{S}_i$  is a source/sink term. Eq.6.11 is solved in each phase individually with the interfacial constraints, described in Eq.6.10a and Eq.6.10b, applied as boundary condition for both the phases, see Weber et al. [2017], Falcone and Marschall [2017].

The alternative to the two field approach is the single field model which treats the concentration in both phases and the interfacial conditions in a single unified governing equation. The single field approach proposed by Haroun et al. [2010], which was later called the Continuum Species Transfer (CST)<sup>2</sup> approach [Marschall et al., 2012, Deising et al., 2016], computes the distribution of dissolved species  $C_i$  (in both phases) based on

$$\frac{\partial C_i}{\partial t} + \nabla \cdot (\vec{U} C_i) = \nabla \cdot \left( \hat{D}_i \nabla C_i - \frac{1 - He_i}{\alpha_1 + \alpha_2 He_i} \hat{D}_i C_i \nabla \alpha_1 \right) + \mathcal{S}_i, \quad (6.12)$$

where  $\hat{D}_i$  is the harmonic mean of the diffusion coefficients of the species ( $D_{i,j}$ ) determined as

$$\hat{D}_i = \frac{D_{i,1} D_{i,2}}{D_{i,2} \alpha_1 + D_{i,1} \alpha_2}. \quad (6.13)$$

The CST approach has been used to simulate mass transfer in a liquid film [Haroun et al., 2010], bubbly flows [Deising et al., 2016, Marschall et al., 2012] and flow through porous media [Graveleau et al., 2017]. This approach has been shown to generate errors in predicting the interfacial jump when local convection, near the interface, is greater than

<sup>2</sup> Readers interested in the derivation of the CST approach should refer to Deising et al. 2016.

diffusion [Yang et al., 2017]. To address this numerical error reported by Yang et al. [2017], Maes and Soullaine [2018] proposed a Compressive Continuum Species Transfer (C-CST) model:

$$\begin{aligned} \frac{\partial C_i}{\partial t} + \nabla \cdot (\vec{U}C_i) = \nabla \cdot \left( \hat{D}_i \nabla C_i - \frac{1 - He_i}{\alpha_1 + \alpha_2 He_i} \hat{D}_i C_i \nabla \alpha_1 \right) \\ - \nabla \cdot \left( \frac{1 - He_i}{\alpha_1 + \alpha_2 He_i} \alpha_1 \alpha_2 \vec{U}_r C_i \right) + \mathcal{S}_i, \end{aligned} \quad (6.14)$$

where  $\vec{U}_r$  is compressive velocity used in algebraic VOF method, which will be discussed in Chapter 8.

Although both single and two field models can treat interfacial mass transfer and account for interfacial conditions, the latter (which is computationally more expensive) must be used along with VOF methods that use geometric reconstruction method (that produce very sharp interface) whereas the computationally cheaper former approach can be used with algebraic VOF methods in order to avoid artificial species transfer, see Deising et al. [2016].

### Supersaturation driven bubble growth

Due to the supersaturation of the liquid by the dissolved gas in the vicinity of the bubble, the mass transfer across the interface will result in the bubble growth. The driving force for the interfacial mass transfer can be computed by either using the phenomenological Fick's 1<sup>st</sup> law or case specific Sherwood number ( $Sh$ ) correlations.

The Fick's 1<sup>st</sup> law based approach, can be understood based on the interfacial jump condition described in Eq.6.10a which ensures that the amount of species  $i$  that is transferred across the interface is conserved. So the local driving force ( $j$ ) as a result of the presence of supersaturated liquid in the vicinity of interface can be computed as<sup>3</sup>

$$j = M_i D_{i,1} |\nabla C_i|, \quad (6.15)$$

where  $\nabla C_i$  the gradient of the concentration of the dissolved gas and  $M_i$  is the molar mass of dissolved species ( $i$ ). Due to the universality of Fick's 1<sup>st</sup> law, this approach can provide a generic approach to model supersaturation driven bubble growth given  $\nabla C_i$  is calculated accurately, which requires the concentration boundary layer to be well resolved.

Another commonly used approach, computes the local driving force ( $j$ ) using Sherwood number<sup>4</sup> ( $Sh$ ) based correlations as

$$j = M_i k (C_i - C_{sat}) = \frac{D_{i,1} Sh}{L} M_i (C_i - C_{sat}), \quad (6.16)$$

<sup>3</sup> Eq.6.15 is based on the assumption that the concentration gradient in the tangential direction to the interface is negligible. This approximation is used by Deising et al. 2016 to derive CST model, described in Eq.6.12.

<sup>4</sup>  $Sh$  is a dimensionless number which is defined as the ratio of convective to diffusive mass transfer.

where  $L$  is the characteristic length scale (specific to flow scenario),  $k$  is the mass transfer coefficient and Sherwood number correlation, according to Deising et al. [2018], can be expressed as <sup>5</sup>

$$Sh = 2 + aRe^b Sc^c \quad (6.17)$$

where  $Re$  and  $Sc$  are the Reynolds number<sup>6</sup> and Schmidt number<sup>7</sup> respectively. As  $Re$  and  $L$  are flow specific,  $Sh$  and the corresponding driving force ( $j$ ) are decided based on a priori knowledge of the phenomena. A few examples of  $Sh$  correlations reported in literature along with the applicable flow scenario is tabulated in Table.6.1. Readers interested in overview of  $Sh$  correlations available in literature can refer to works like Deising et al. [2018], Taqieddin et al. [2018] and Griffith [1960].

<sup>5</sup> In the limit  $Re \rightarrow 0$ , for a spherical particle/bubble in a stagnant fluid, Eq.6.17 reduces to  $Sh = 2$ , see Villadsen et al. 2011 for derivation.

<sup>6</sup>  $Re$  is a dimensionless number which is defined as the ratio of inertial to viscous forces, equal to  $U_\infty L / \nu_1$  where  $U_\infty$  is the characteristic velocity of the flow condition and  $\nu_1$  is the liquid kinematic viscosity.

<sup>7</sup>  $Sc$  is a dimensionless number which is defined as the ratio of kinematic viscosity of liquid to diffusion coefficient of the dissolved gas in liquid.

$Sh$ correlation	Applicable flow scenario	Reference
$Sh = 2 + 0.6515\sqrt{ReSc}$	For small mass transfer from spherical bubble in a creeping flow ( $Re \ll 1$ )	Bird et al. 2006
$Sh = \frac{2}{\sqrt{\pi}}\sqrt{ReSc}f(E)$ , where $f(E) = 0.524 + 0.88E - 0.49E^2 + 0.086E^3$ and $E$ is aspect ratio	For rising oblate bubbles, $500 < Re < 1000$ , $Sc > 100$ and $1 \leq E \leq 3$	Figuroa-Espinoza and Legendre 2010
$Sh = 2 + 0.6Re^{1/2}Sc^{1/3}$	Evaporation of droplets ( $0 \leq Re \leq 200$ )	Ranz and Marshall 1952

Table 6.1: Few examples of various Sherwood number correlations available in literature.

Although Fick's 1<sup>st</sup> law is universally applicable, this approach can at times be computationally expensive due to the need to resolve the concentration boundary layer. On the other hand, Sherwood number based correlations, which are computationally cheaper as the gradient calculation is circumvented, has limited applicability as they are valid for specific flow scenarios. Despite the pros and cons associated with each of these approaches, both Fick's 1<sup>st</sup> law [Maes and Soullaine, 2020] and  $Sh$  based correlation [Liu et al., 2016] has been used to model the change in the size of bubbles due to interfacial mass transfer.



## **Part III**

# **Introduction to the numerical framework**





## Chapter 7: *Overview of OpenFOAM<sup>®</sup> and the Finite Volume Method*

In order to simulate the multiphysics nature of electrochemical hydrogen evolution, the numerical framework used must be able to treat the relevant physics. As interface resolving modelling capabilities are already available in popular CFD codes, like ANSYS<sup>®</sup> Fluent<sup>®</sup> [ANSYS Inc., 2020], FLOW-3D<sup>®</sup> [Flow Science Inc., 2019] and OpenFOAM<sup>®</sup> [OpenFOAM, 2019], implementation of other numerical techniques and governing equations would require customization of the framework. In contrast to commercial CFD codes, like ANSYS<sup>®</sup> Fluent<sup>®</sup> [ANSYS Inc., 2020] and FLOW-3D<sup>®</sup> [Flow Science Inc., 2019], the open source nature of OpenFOAM<sup>®</sup> [OpenFOAM, 2019] allows the user to access the source code and modify it, which makes it an 'ideal starting point' to develop the proposed framework.

OpenFOAM<sup>®</sup> or Open Source Field Operation and Manipulation is a framework, written in C++, to develop applications to solve continuum mechanics (especially fluid dynamics related) problems [OpenFOAM, 2019]. This framework was initially developed by Weller et al. [1998] and subsequently released as open source code in 2004. The OpenFOAM<sup>®</sup> framework, out-of-the-box, provides a suite of solvers and utilities which can be used/customized by the users. The solvers are generic applications that can simulate a multitude of fluid flow scenarios like incompressible (icoFoam), compressible (rhoPimpleFoam), multiphase modelling based on interface resolved (interFoam) and dispersed phase (twoPhaseEulerFoam), combustion (fireFoam) and heat transfer (buoyantPimpleFoam) flows [Green Shields, 2019]. Utilities are used for pre/post processing like to generate/manipulate/import meshes, parallel processing and extract data from simulations [Green Shields, 2019]. The results from the simulations can be post-processed, by default, using ParaView [Kitware Inc., 2020], an open-source visualization application.

OpenFOAM<sup>®</sup> employs the finite volume method (FVM), which is

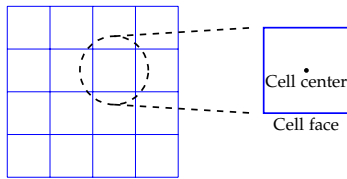


Figure 7.1: Schematic of dividing the computational domain into small control volumes (cells).

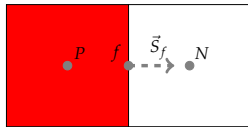


Figure 7.2: Illustration of a control volume used in the calculation, highlighted in red, along with its neighbouring cell whose cell center is represented by  $N$  and common face by  $f$ .

```

1 fvScalarMatrix CEqn
2 (
3     fvm::ddt(C)
4     + fvm::div(phi, C)
5     - fvm::laplacian(D, C)
6     - Gc
7 );
8 CEqn.solve();

```

Listing 7.1: Illustration of implementing the species transport equation in single phase flow.

a common method used in commercial CFD software like ANSYS® Fluent®, to solve the relevant governing equations. This method is based on dividing the computational domain into small control volumes based on the user defined mesh, then describing the governing equation on the control volume in its discretized form, which is then solved to obtain the solution. Each of these small control volumes have a cell center and faces, like shown in Fig.7.1. The implementation of finite volume method in OpenFOAM® uses a co-located approach to store the flow variables (like pressure and velocity) at the cell center. In order to address the ‘checker-board’ problem which arises from using the co-located approach [Versteeg and Malalasekera, 2007], OpenFOAM® employs a solution procedure that uses the values of the relevant flow variables at the cell face of the control volume, by interpolation.

In this chapter, the finite volume method, in OpenFOAM®, is illustrated using an example of governing equation of species transport in a single phase flow, Eq.6.9. This chapter is by no means a comprehensive description of the method but merely an overview to aid readers in understanding the settings and its implementation used while setting up simulations using this framework. For readers interested in understanding finite volume method and its implementation in OpenFOAM® can refer to books like Versteeg and Malalasekera [2007] and Holzmann [2017] respectively.

### Illustration of the Finite Volume Method in OpenFOAM®

Before going into FVM and the solution methodology, let us revisit the control volume. Each control volume has a cell center (denoted by  $P$ ) along with a volume of  $V$  and say a neighbouring cell (which has a cell center denoted by  $N$ ) with which it shares a common face (denoted by  $f$ ) whose surface area vector is represented by  $\vec{S}_f$ , as shown in Fig.7.2.

To show the solution methodology used by finite volume method, the governing equation for the species transport in a single phase flow with a source term ( $\mathcal{S}_c$ ), based on Eq.6.9, is written as

$$\frac{\partial C}{\partial t} + \nabla \cdot (\vec{U}C) = \nabla \cdot D\nabla C + \mathcal{S}_c. \quad (7.1)$$

In OpenFOAM®, the flow parameters, which are scalars (like  $C$ ) or vectors (like  $\vec{U}$ ), are both saved at cell centers using `volScalarField` and `volVectorField`, see OpenCFD [2020]. Compared to the flow parameters,  $D$  is defined as a `dimensionedScalar` which is ‘looked up’ during run time from the case files whereas the source term  $\mathcal{S}_c$ , which is defined as a `volScalarField` as `Gc` in Listing.7.1, is computed based on the relevant physics. For this example,  $\vec{U}$  in Eq.7.1 is assumed to

be a known vector field which can either be user defined or obtained at the previous time step.

The numerics behind running Listing.7.1 is presented briefly to illustrate the underlying idea of the finite volume method. Eq.7.1 is first integrated over the control volume and time to get

$$\int_t^{t+\delta t} \left[ \int_V \frac{\partial C}{\partial t} dV + \int_V \nabla \cdot (\vec{U}C) dV \right] dt = \int_t^{t+\delta t} \left[ \int_V \nabla \cdot (D\nabla C) dV + \int_V \mathfrak{S}_c dV \right] dt. \quad (7.2)$$

Using Gauss's theorem, the volume integrals of second and third terms in Eq.7.2 can be converted to surface integrals, based on control volume illustrated in Fig.7.2, as

$$\int_V \nabla \cdot (UC) dV = \int_S d\vec{S} \cdot (\vec{U}C) \approx \sum_f \vec{S}_f \cdot (\vec{U}_f C_f), \quad (7.3a)$$

$$\int_V \nabla \cdot (D\nabla C) dV = \int_S d\vec{S} \cdot (D\nabla C) \approx \sum_f \vec{S}_f \cdot (D_f \nabla_f C), \quad (7.3b)$$

where subscript  $f$  represents the interpolated value at the face. `phi`, used in Listing.7.1, corresponds to scalar volume flux field computed as  $\vec{U}_f \cdot \vec{S}_f$ . The central differencing method to obtain the interpolated value of  $C_f$  is

$$C_f = l_x C_P + (1 - l_x) C_N, \quad (7.3c)$$

where  $l_x$  is equal to  $\frac{|\vec{X}_f - \vec{X}_N|}{|\vec{X}_f - \vec{X}_N| + |\vec{X}_f - \vec{X}_P|}$  and  $\vec{X}_i$  represents the vector representing location of the cell centers ( $P$  and  $N$ ) and cell face ( $f$ ), see Rusche [2003].  $\nabla_f C$  is the cell face value of  $\nabla C$ . The term  $\vec{S}_f \cdot \nabla_f C$ , in Eq.7.3b, is calculated as

$$\vec{S}_f \cdot \nabla_f C = |\vec{S}_f| \frac{C_N - C_P}{|\vec{d}|}, \quad (7.3d)$$

where  $\vec{d}$  is calculated as  $\vec{X}_N - \vec{X}_P$  [Rusche, 2003]. It should be noted that Eq.7.3d is valid only when  $\vec{S}_f$  and  $\nabla_f C$  are parallel, which occurs in an orthogonal mesh. When a non-orthogonal mesh is used, i.e.  $\vec{S}_f \cdot \nabla_f C \neq |\vec{S}_f| (C_N - C_P) / |\vec{d}|$ , correction terms are used to ensure the accuracy of the term, see Rusche [2003]. The last term in Eq.7.2, volumetric integral of source term can be written as

$$\int_V \mathfrak{S}_c dV = \overline{\mathfrak{S}_c} V, \quad (7.4)$$

where  $\overline{\mathfrak{S}_c}$  is equal to  $(1/V) \int_V \mathfrak{S}_c dV$ . In order to solve Eq.7.1, initial and boundary conditions are required. The boundary conditions used in simulations can be broadly divided into the Dirichlet, which is implemented as `fixedValue`, and von Neumann, which is implemented

OpenFOAM<sup>®</sup> uses 'equation mimicking' to implement the governing equation, Eq.7.1, see Listing.7.1. To temporally implicitly and explicitly treat each term in the governing equation, these terms must be implemented using `fvm` and `fvc` namespaces respectively [OpenCFD, 2020]. Both these namespaces contains functions like `ddt`, `div` and `laplacian` to perform time derivative, divergence and laplacian operations respectively [OpenCFD, 2020].

as `fixedGradient`, conditions [Greenshields, 2019]. The implementation of boundary conditions are further described in Rusche [2003]. Finally, the volume integral of temporal term can be expressed based on Euler time stepping as

$$\int_V \frac{\partial C}{\partial t} dV = \frac{C_p^n - C_p^{n-1}}{\Delta t} V, \quad (7.5)$$

where  $n$  and  $n - 1$  represent the current and the previous time steps. The initial conditions required to solve the species transport equation corresponds to data at  $t = 0$ . Substituting Eq.7.3a, Eq.7.3b, Eq.7.4 and Eq.7.5 in Eq.7.2 gives

$$\int_t^{t+\Delta t} \left[ \frac{C_p^n - C_p^{n-1}}{\Delta t} V + \sum_f (\vec{S}_f \cdot \vec{U}_f) C_f \right] dt = \int_t^{t+\delta t} \left[ \sum_f \vec{S}_f \cdot (D_f \nabla_f C) + \overline{\Theta}_c V \right] dt. \quad (7.6)$$

The temporal treatment of the convective, diffusive and source terms in the above equation can be done implicitly (which uses values of  $C$  at  $n$  for spatial terms) or explicitly (which uses values of  $C$  at  $n - 1$  for the spatial terms). For implicit treatment of these terms, Eq.7.6 can be written as

$$\frac{C_p^n - C_p^{n-1}}{\Delta t} V + \sum_f (\vec{S}_f \cdot \vec{U}_f) C_f^n = \sum_f \vec{S}_f \cdot (D_f \nabla_f C^n) + \overline{\Theta}^n V. \quad (7.7)$$

The time step ( $\Delta t$ ) used by the solver is computed based on maximum Courant number, which must be set to be less than unity, or maximum time step constraint<sup>1</sup>. The source term,  $\overline{\Theta}^n V$ , is often written in a linearized form like  $(G_1 C_p^n + G_2) V$ , see Rusche [2003]. Substituting Eq.7.3c and Eq.7.3d in Eq.7.7 gives

$$\frac{C_p^n - C_p^{n-1}}{\Delta t} V + \sum_f (\vec{S}_f \cdot \vec{U}_f) (I_x C_p^n + (1 - I_x) C_N^n) = \sum_f \left( D_f |\vec{S}_f| (C_N^n - C_p^n) / |\vec{d}| \right) + (G_1 C_p^n + G_2) V. \quad (7.8)$$

The above equation can be rewritten as

$$\frac{V}{\Delta t} C_p^n - \frac{V}{\Delta t} C_p^{n-1} + \sum_f (\vec{S}_f \cdot \vec{U}_f) I_x C_p^n + \sum_f (\vec{S}_f \cdot \vec{U}_f) (1 - I_x) C_N^n = \sum_f \left( D_f |\vec{S}_f| C_N^n / |\vec{d}| \right) - \sum_f \left( D_f |\vec{S}_f| C_p^n / |\vec{d}| \right) + G_1 V C_p^n + G_2 V. \quad (7.9)$$

The above equation can be rearranged into the form, which considers multiple neighbouring cells and shared faces, of

$$a_P C_p^n + \sum_N a_N C_N^n = a_P, \quad (7.10)$$

<sup>1</sup>The time step taken by the solver ( $\Delta t$ ) can be summarized as  $\Delta t = \min(\Delta t_{Co}, \Delta t_{user})$ , see Greenshields 2019, where  $\Delta t_{user}$  is the user-defined maximum permissible time step and  $\Delta t_{Co}$  is the time step based on maximum Courant number ( $Co$ ) can be understood to satisfy

$$Co = \frac{|\vec{U}|}{\mathcal{X}} \Delta t_{Co},$$

where  $\mathcal{X}$  is the cell size in the direction of the flow velocity. Readers interested in the exact procedure employed in calculating the time step can refer to Berberović et al. 2009.

where  $\sum_N$  accounts for the multiple neighbouring cells for the control volume, whose cell center is denoted by  $P$ , and individual terms are defined as

$$a_P C_P^n = \frac{V}{\Delta t} C_P^n + \sum_f (\vec{S}_f \cdot \vec{U}_f) l_x C_P^n + \sum_f \left( D_f |\vec{S}_f| C_P^n / |\vec{d}| \right) - G_1 V C_P^n,$$

$$\sum_N a_N C_N^n = \sum_f (\vec{S}_f \cdot \vec{U}_f) (1 - l_x) C_N^n - \sum_f \left( D_f |\vec{S}_f| C_N^n / |\vec{d}| \right),$$

$$a_P = \frac{V}{\Delta t} C_P^{n-1} + G_2 V.$$

Please refer to Chapter 4 in [Versteeg and Malalasekera \[2007\]](#) for additional details about transforming a governing equation to linear equation, like [Eq.7.10](#). This linear algebraic equation can be written in matrix form as

$$[A][C] = [\mathfrak{A}] \quad (7.11)$$

where  $[C]$  is the column vector associated with the species concentration at the different cell centers in the domain,  $[\mathfrak{A}]$  is the column vector associated with  $a_P$  at various cell centers in the computational domain and matrix  $[A]$  consists of diagonal elements formed by  $a_P$  and off-diagonal elements based on  $a_N$ . Additional information about the matrix form of the system linear algebraic equation can be found in [Rusche \[2003\]](#).

Due to the computational cost in computing  $[C]$  directly as  $[A]^{-1}[\mathfrak{A}]$ , numerical approaches typically determines the solution using either direct or iterative methods [[Rusche, 2003](#)]. Direct methods solve the matrices in a finite number of matrix operations using algorithms, like LU decomposition or Gaussian Elimination [[Gentle, 1998](#)], which are computationally expensive for very large matrices [[Rusche, 2003](#)]. The iterative methods, on the other hand, calculate  $[C]$  based on the continuous improvement of an initial approximation until a convergence criteria is met [[Gentle, 1998](#), [Rusche, 2003](#)]. As iterative methods are computationally economical, most of the solvers available in OpenFOAM<sup>®</sup> are iterative [[Greenshields, 2019](#)]. The convergence criteria, used in iterative methods, is based on a reduction of scaled residual with iterations [[OpenCFD, 2020](#)]. The iterative procedure is stopped when the residuals obtained while solving the [Eq.7.11](#) becomes lower than the tolerance criteria specified by the user.

In order to improve the stability of computations, an under-relaxation factor can be used. OpenFOAM<sup>®</sup> allows the use of under-relaxation factors, set in `fvSolution`, to control the advancement of flow variables between iterations [[Greenshields, 2019](#)]. This operation can be applied either on a field or equation using under-relaxation factor ( $\lambda \in [0, 1]$ ), see [Greenshields \[2019\]](#). The under-relaxation of  $C$  field is

$$C^{new} = C^{n-1} + \lambda(C^n - C^{n-1}) \quad (7.12)$$

where superscript *new* is the updated field *C* [Rusche, 2003]. The field under-relaxation is implemented in OpenFOAM® as `C.relax()`. Setting a value of  $\lambda$  equal to zero, the field (*C*) does not get updated with iterations [Greenshields, 2019]. The under-relaxation of equation, for example Eq.7.10, can be expressed as described in Rusche [2003] as

$$\frac{a_p}{\lambda}C_p^n + \sum_N a_N C_N^n = a_p + \frac{1-\lambda}{\lambda}a_p C_p^{n-1}. \quad (7.13)$$

Under-relaxation of Eq.7.10, which is represented by Listing.7.1, is implemented in OpenFOAM® as `CEqn.relax()`. For transient simulations, when  $\lambda < 1$ , Eq.7.12 and Eq.7.13 would update the new solution based on values from the previous time step which would result in under-predicting the flow parameters which is being solved. On the contrary, when under-relaxation factor is used in steady-state simulations,  $n$  and  $n - 1$  would represent the iterations towards convergence [Rusche, 2003].

Further details of the numerical approach used by OpenFOAM® to solve partial differential equations can be found in Rusche [2003] or OpenCFD [2020].

## Chapter 8: Overview of the Volume of Fluid solver in OpenFOAM<sup>®</sup>

In order to simulate the phenomena of interest in this thesis, interFoam, the interface resolving method based on Volume of Fluid (VOF), available in OpenFOAM<sup>®</sup> 6 [OpenFOAM, 2019] which simulates the behaviour of two isothermal, immiscible and incompressible fluids is customized based on Fig.2.2. The interFoam solver was first implemented in the initial version of OpenFOAM<sup>®</sup> framework, proposed by Weller et al. [1998], during the 1990s by Ubbink [1997]. Since this initial implementation, interFoam has undergone various changes with respect to the implemented numerical methods. Due to the open source nature of the solver, it is very popular and has been used out-of-the-box and customized to successfully simulate a multitude of multiphase flow scenarios, see Table.8.1. Due to its widespread use and application specific verification in literature, a much needed review of the interFoam solver (included in older versions of OpenFOAM<sup>®</sup> framework) was performed by Rusche [2003], Deshpande et al. [2012a], which provided the knowledge foundation needed for this chapter of the thesis.

	Solver - interFoam	Application
Berberović et al. 2009	Out-of-the-box	Splashing
Deshpande et al. 2012b	Out-of-the-box	Jet impingement
Hoang et al. 2013	Modified surface tension model	Droplet/bubble microfluidics
Klostermann et al. 2013	Out-of-the-box	Rising bubbles
Samkhaniani and Ansari 2016	Added thermal energy transport equation and relevant phase change source terms	Bubble condensation
Maes and Soullaine 2020	Added species transport equation and relevant source terms	Shrinkage of rising bubble due to interfacial transfer of species

Table 8.1: Few examples of studies which used interFoam, both out-of-the-box and customized, to simulate multiphase flow scenarios.

In this chapter, the Volume of Fluid (VOF) method based solver



available in OpenFOAM<sup>®</sup> 6, `interFoam`, is discussed. The sections within this chapter delve into solution approach used in `interFoam` and the limitations of the solver.

### *Solving the advection of volume fraction*

As briefly presented in Chapter 5, the VOF approach uses a scalar called the volume fraction of liquid ( $\alpha_1$ ) which denotes the fraction of control volume occupied by the liquid phase.  $\alpha_1$  is equal to zero in the gas phase and unity in the liquid phase whereas  $0 < \alpha_1 < 1$  in the interface region. The volume fraction of the gas ( $\alpha_2$ ), which occupies the remaining region in the control volume, can be computed as  $1 - \alpha_1$ . The fluid properties, like density ( $\rho$ ) and dynamic viscosity ( $\mu$ ), are computed based on volume fraction weighted averaging, see Eq.5.1.

The governing equation that dictates the transport of volume fraction of liquid is

$$\frac{\partial \alpha_1}{\partial t} + \nabla \cdot (\vec{U}_1 \alpha_1) = 0, \quad (8.1)$$

which is essentially an advection equation for  $\alpha_1$  which is advected based on the velocity field in liquid phase ( $\vec{U}_1$ ). `interFoam` uses a single field description of the velocity field ( $\vec{U}$ ), which can be understood as

$$\vec{U} = \alpha_1 \vec{U}_1 + \alpha_2 \vec{U}_2, \quad (8.2)$$

where  $\vec{U}_1$  and  $\vec{U}_2$  are the velocity fields in liquid and gas phase respectively. The relative velocity between the phases ( $\vec{U}_r$ ) is computed as

$$\vec{U}_r = \vec{U}_1 - \vec{U}_2. \quad (8.3)$$

Combining  $\alpha_1 \times$ Eq.8.2 and  $\alpha_1(1 - \alpha_1) \times$ Eq.8.3 gives

$$\alpha_1 \vec{U} + \alpha_1(1 - \alpha_1) \vec{U}_r = \alpha_1 \vec{U}_1. \quad (8.4)$$

Eq.8.1 can be written as

$$\frac{\partial \alpha_1}{\partial t} + \nabla \cdot (\alpha_1 \vec{U}) + \nabla \cdot (\alpha_1(1 - \alpha_1) \vec{U}_r) = 0. \quad (8.5)$$

Eq.8.5, which is referred to as the interface compression approach, generates an interface which is smeared over 2-3 cells and it belongs to a class of VOF methods known as algebraic VOF [Deshpande et al., 2012a]. In the limit of very sharp interface, when  $\alpha_1(1 - \alpha_1) \vec{U}_r \rightarrow 0$ , Eq.8.5 reduces to

$$\frac{\partial \alpha_i}{\partial t} + \nabla \cdot (\alpha_1 \vec{U}) = 0. \quad (8.6)$$

Eq.8.6 is usually coupled with an algorithm to geometrically reconstruct the interface within a cell to preserve its sharpness, this approach belongs to a class of VOF approach known as the geometric

VOF, see Cifani et al. [2016]. The additional steps that is involved with reconstructing the interface in geometric VOF makes this approach more computationally expensive but they render a much sharper interface (in one cell). The VOF approach employed in interFoam uses an algebraic VOF method based on Eq.8.5.

When a single field formulation of velocity is used,  $\vec{U}_r$  is unknown and so it is numerically estimated as

$$\vec{U}_r = C_\alpha \left| \frac{\vec{U}_f \cdot \vec{S}_f}{|S_f|} \right| \vec{n}, \quad (8.7)$$

where  $\vec{n}$  is unit normal vector to the interface,  $\vec{U}_f$  is the interpolated value of the velocity at the cell face and  $C_\alpha$  is a user-defined value that determines the extent of the interface smearing [Deshpande et al., 2012a]. The associated scalar flux computed at the cell face, which is implemented in interFoam as shown in Listing.8.1, is calculated as  $\vec{U}_{r,f} \cdot \vec{S}_f$ , where  $\vec{U}_{r,f}$  is the value of  $\vec{U}_r$  at the cell face. Although  $C_\alpha$  can theoretically be set to any value,  $C_\alpha < 1$  renders a very smeared interface whereas  $C_\alpha > 1$  generates errors in interfacial curvature calculations which results in numerical artifacts in the simulations [Hoang et al., 2013, Cifani et al., 2016]. An optimal value of  $C_\alpha$ , equal to unity, which generates a reasonably sharp interface and reduces numerical errors is recommended for multiphase simulations [Hoang et al., 2013, Greenshields, 2019].

```
surfaceScalarField phic(mixture.cAlpha()*mag(phi/mesh.magSf()));
```

Listing 8.1: Code snippet from alphaEqn.H, from the interFoam source code, in which flux associated with  $\vec{U}_r$  is calculated.

```

1  if (nAlphaSubCycles > 1)
2  {
3      .
4      .
5      .
6      for
7      (
8          subCycle<volScalarField> alphaSubCycle(alpha1, nAlphaSubCycles);
9          !(++alphaSubCycle).end();
10     )
11     {
12         #include "alphaEqn.H"
13         rhoPhiSum += (runTime.deltaT()/totalDeltaT)*rhoPhi;
14     }
15     rhoPhi = rhoPhiSum;
16 }
17 else
18 {
19     #include "alphaEqn.H"
20 }
```

Listing 8.2: Code snippet to showcase the sub-cycling algorithm used to solve the volume fraction advection equation in alphaEqnSubCycle.H.

Eq.8.5 is solved using semi-implicit Multidimensional Universal Limiter with Explicit Solution (MULES) algorithm, which is enabled by

setting MULESCorr to ‘yes’, to ensure the boundedness of  $\alpha_1$  (between zero and one) [Greenshields, 2014]. The semi-implicit MULES involves solving Eq.8.5 by a implicit predictor and explicit corrector method, see Greenshields [2014]. The interFoam solver allows to sub-cycle Eq.8.5 which allows for smaller temporal increments between the time steps of  $n - 1$  and  $n$  [Greenshields, 2019]. It should be noted that, the sub-cycling, uses  $\vec{U}$  values based on  $n - 1$  time step, as velocity is computed after  $\alpha_1$  is determined. These intermediate time steps are based on the user-defined value of nAlphaSubCycles [Greenshields, 2019]. Based on nAlphaSubCycles the number of sub-cycling is decided, see Listing.8.2. When nAlphaSubCycles  $> 1$ , each sub-cycle is associated with a time step ( $\Delta t_{subc}$ ) which is computed as  $\Delta t_{subc} = \Delta t / N_{subc}$ , where  $N_{subc}$  is the user defined nAlphaSubCycles, otherwise  $\Delta t_{subc} = \Delta t$ . If  $N_{subc} > 1$ , then Eq.8.5 is solved using semi-implicit MULES, in line 12 of Listing.8.2, for each sub-cycle. If  $N_{subc} \leq 1$ , Eq.8.5 is directly computed using semi-implicit MULES in line 19 of Listing.8.2.

### Computing the velocity field: Pressure-velocity coupling

The pressure ( $p$ ) can be rewritten as in terms of a modified pressure term ( $p_{rgh}$ ), defined as  $p_{rgh} = p - \rho \vec{g} \cdot \vec{x}$ . The use of  $p_{rgh}$  instead of  $p$  allows for simpler pressure boundary condition [Rusche, 2003]. As the modified pressure is used, this must be accounted for in the momentum equation (Eq.5.4), which uses gradient of pressure, by

$$-\nabla p_{rgh} = -\nabla p + \vec{g} \cdot \vec{x} \nabla \rho + \rho \vec{g} \quad (8.8)$$

<sup>1</sup> See Appendix A for further details of the reformulation of the viscous terms.

The viscous terms in Eq.5.4,  $\nabla \cdot \mu (\nabla \vec{U} + \nabla \vec{U}^T)$ , is reformulated<sup>1</sup> to a numerically efficient  $(\nabla \cdot (\mu \nabla \vec{U}) + \nabla \vec{U} \cdot \nabla \mu)$ , as reported by [Rusche, 2003, Deshpande et al., 2012a, Deising et al., 2016]. Substituting these simplifications to Eq.5.4 gives the momentum equation as used in interFoam:

$$\frac{\partial \rho \vec{U}}{\partial t} + \nabla \cdot (\rho \vec{U} \vec{U}) = -\nabla p_{rgh} + \left( \nabla \cdot (\mu \nabla \vec{U}) + \nabla \vec{U} \cdot \nabla \mu \right) - \vec{g} \cdot \vec{x} \nabla \rho + \sigma \kappa \nabla \alpha_1, \quad (8.9)$$

where the last term treats the surface tension force based on the Continuum Surface Force model proposed by Brackbill et al. [1992] using interfacial curvature ( $\kappa$ ) and surface tension ( $\sigma$ ). Eq.8.9 can be integrated over a control volume, and divergence terms can be converted to surface intergrals using Gauss’ theorem to get

$$\int_V \frac{\partial \rho \vec{U}}{\partial t} dV + \int_S (\rho \vec{U} \vec{U}) \cdot d\vec{S} = - \int_V \nabla p_{rgh} dV - \int_V \vec{g} \cdot \vec{x} \nabla \rho dV + \int_S (\mu_1 \nabla \vec{U}_1) \cdot d\vec{S} + \int_V \nabla \vec{U}_1 \cdot \nabla \mu dV + \int_V \sigma \kappa \nabla \alpha_1 dV. \quad (8.10)$$

The solution to the momentum equation is obtained by iteratively correcting a predicted velocity field using the pressure correction step in the Pressure Implicit with Splitting of Operators (PISO) algorithm [Issa, 1986]. These iterations are indicated using the superscript  $m$ . At first iteration  $m = 0$  is known from the field values known at time step  $n - 1$ . The first step of the PISO algorithm, based on Issa [1986], Deshpande et al. [2012a], is to calculate a predicted velocity field ( $\vec{U}^*$ ) using the temporal, convective and viscous terms of the momentum equation:

$$\frac{\partial \rho \vec{U}}{\partial t} + \nabla \cdot (\rho \vec{U} \vec{U}) = \left( \nabla \cdot (\mu \nabla \vec{U}) + \nabla \vec{U} \cdot \nabla \mu \right) \quad (8.11)$$

which is implemented in interFoam as shown in Listing.8.3. The vis-

```

1 fvVectorMatrix UEqn
2 (
3     fvm::ddt(rho, U)
4     + fvm::div(rhoPhi, U)
5     + MRF.DDt(rho, U)
6     + turbulence->divDevRhoReff(rho, U)
7     ==
8     fvOptions(rho, U)
9 );
    
```

Listing 8.3: Code snippet of the UEqn.H where interFoam constructs descriptized from of Eq.8.11 which is used, in PISO algorithm, to compute pressure and corrected velocity fields.

cus terms,  $\nabla \cdot (\mu \nabla \vec{U})$  and  $\nabla \vec{U} \cdot \nabla \mu$ , which are accounted via line 6 in Listing.8.3, are treated implicitly and explicitly respectively [Deshpande et al., 2012a, Deising et al., 2016]. The descriptized form of Eq.8.11 can be converted to a form similar to Eq.7.10:

$$A_P \vec{U}_P^* + \sum_N A_N \vec{U}_N^{m-1} = \mathfrak{A}_P, \quad (8.12)$$

where subscript  $P$  and  $N$  represents the value stored at the owner' cell center and neighbour' cell center respectively. The exact formulation of the matrices  $A_P$ ,  $A_N$  and  $H$  can be found in the work by Deshpande et al. [2012a]. For ease of writing, Eq.8.12 can be expressed as  $A_P \vec{U}_P^* = H$ , where  $H = \mathfrak{A}_P - \sum_N A_N \vec{U}_N^{m-1}$ . The predicted velocity can be computed as  $\vec{U}_P^* = H/A_P$ . The flux ( $\vec{U}_f^* \cdot \vec{S}_f$ ), at the cell face, associated with predicted velocity,  $\vec{U}_P^*$ , can be computed as

$$\vec{U}_f^* \cdot \vec{S}_f = \left( \frac{H}{A_P} \right)_f \cdot \vec{S}_f \quad (8.13)$$

The next step in PISO algorithm is to include the effects of gravity and surface tension, whose values at current time ( $n$ ) is known as

volume fraction equation is solved before PISO algorithm:

$$\begin{aligned} \vec{U}_f^* \cdot \vec{S}_f = & \left( \frac{H}{A_p} \right)_f \cdot \vec{S}_f + \left( \frac{(\sigma\kappa)^n}{A_p} \right)_f \nabla_f \alpha_1^n \cdot \vec{S}_f \\ & - \left( \frac{(\vec{g} \cdot \vec{x})^n}{A_p} \right)_f \nabla_f \rho^n \cdot \vec{S}_f, \end{aligned} \quad (8.14)$$

where  $\nabla_f \alpha_1$  and  $\nabla_f \rho$  are the cell face values of gradient of volume fraction of liquid and density respectively. Eq.8.14 corresponds to line

Listing 8.4: Illustration how interFoam adds the fluxes associated with gravity and surface tension to the predicted velocity. This code snippet is obtained from pEqn.H.

```

1 surfaceScalarField phig
2 (
3   (
4     mixture.surfaceTensionForce() - ghf*fv::snGrad(rho)
5     ) * rAUf * mesh.magSf()
6   );
7 phiHbyA += phig;

```

7 of Listing.8.4. The surface tension force, based on Brackbill et al. [1992], is computed<sup>2</sup> in line 4 of Listing.8.4. In order to compute  $\vec{U}_f^m \cdot \vec{S}_f$ , the contribution of pressure must be accounted in Eq.8.14:

$$\begin{aligned} \vec{U}_f^m \cdot \vec{S}_f = & \left( \frac{H}{A_p} \right)_f \cdot \vec{S}_f + \left( \frac{(\sigma\kappa)^n}{A_p} \right)_f \nabla_f \alpha_1^n \cdot \vec{S}_f \\ & - \left( \frac{(\vec{g} \cdot \vec{x})^n}{A_p} \right)_f \nabla_f \rho^n \cdot \vec{S}_f - \left( \frac{\nabla p_{rgh}^m}{A_p} \right)_f \cdot \vec{S}_f, \end{aligned} \quad (8.16)$$

<sup>2</sup> The surface tension model, proposed by Brackbill et al. 1992 is used by `mixture.surfaceTensionForce()`. This function is part of the `interfaceProperties.C` in `transportModels`. The surface tension force is computed as

$$\vec{F}_{CSF} = \sigma \kappa \nabla \alpha_1, \quad (8.15a)$$

where  $\kappa$  is the local interfacial curvature which is determined as

$$\kappa = -\nabla \cdot \vec{n}, \quad (8.15b)$$

where  $\vec{n}$  is the unit normal to the interface which is computed as

$$\vec{n} = \frac{\nabla \alpha_1}{|\nabla \alpha_1| + \delta}, \quad (8.15c)$$

where  $\delta$  is a stabilization value used to prevent denominator from becoming zero, and then corrected for the effect of contact angle at the wall boundaries.

which can be written as

$$\vec{U}_f^m \cdot \vec{S}_f = \vec{U}_f^* \cdot \vec{S}_f - \left( \frac{\nabla p_{rgh}^m}{A_p} \right)_f \cdot \vec{S}_f. \quad (8.17)$$

To compute  $p_{rgh}$ , the continuity equation,  $\nabla \cdot \vec{U}^m = 0$  whose discretized form is  $\sum \vec{U}_f^m \cdot \vec{S}_f = 0$ , is imposed on Eq.8.17 to get a pressure-correction equation:

$$\sum \left( \frac{\nabla p_{rgh}^m}{A_p} \right)_f \cdot \vec{S}_f = \sum \vec{U}_f^* \cdot \vec{S}_f, \quad (8.18)$$

which is implemented in interFoam as shown in Listing.8.5. The  $\vec{U}_f^m \cdot \vec{S}_f$  is calculated by correcting the predicted flux using Eq.8.17 and implemented in the source code as shown in Listing.8.6. The final step of the PISO algorithm is to calculate the velocity field stored at the cell center by reconstructing the vectors from the volumetric flux at cell face, see Deshpande et al. [2012a]. The steps from calculating a predicted velocity (in Eq.8.11) to reconstructing the velocity vectors from face values

```
fvScalarMatrix p_rghEqn
(
    fvm::laplacian(rAUf, p_rgh) == fvc::div(phiHbyA)
);
```

Listing 8.5: Code snippet from pEqn.H, from the interFoam source code, in which the pressure ( $p_{rgh}$ ) is computed based on Eq.8.18.

of flux are iteratively computed until both velocity and pressure satisfy both continuity and momentum equations. The number of predictor-corrector iterations is set by user in `nCorrectors`, typically to two or three [Greenshields, 2019]. At the end of the iterative procedure, when the both pressure and velocity fields have converged, the values at the final iteration are set to the new time advanced fields at  $n$ .

```
phi = phiHbyA - p_rghEqn.flux();
```

Listing 8.6: Code snippet from pEqn.H which corrects the predicted flux based on Eq.8.17.

### Limitations of the Volume of Fluid method in OpenFOAM®

As discussed previously, interFoam employs interface capturing based on the interface compression approach, Eq.8.5, which belongs to the algebraic class that produces an interface which is smeared across two-three cells. Although this approach is easier to implement and computationally cheaper, it provides an approximate rendering of the interface when compared to a more accurate and sharp interface obtained from geometric VOF approach which employs sub-grid level reconstruction of the interface, see Fig.8.1.

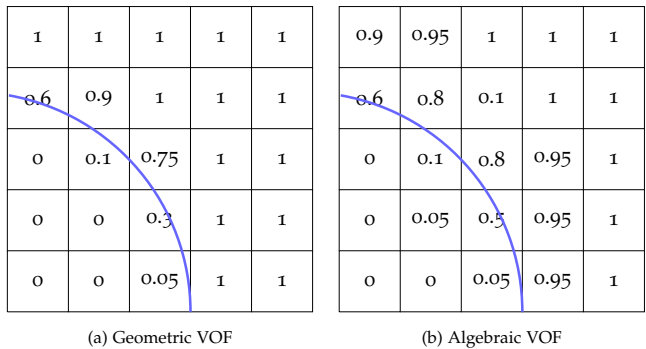


Figure 8.1: Illustration of the volume fraction field produced by (a) Geometric and (b) Algebraic VOF methods with respect to the physical interface (represented by ).

In VOF methods, due to the discontinuous change of  $\alpha_1$  between the phases, the interfacial curvature and normal which are computed based on second and first order derivatives of  $\alpha_1$  in Eq.8.15b and Eq.8.15c are subject to numerical errors [Cifani et al., 2016]. These

<sup>3</sup>For a 2D static bubble, the pressure jump in the bubble as described by the Laplace-Young equation is computed as  $\Delta p = \sigma/R$ , where  $R$  is the radius of the 2D bubble.

<sup>4</sup>Capillary number ( $Ca$ ), is a dimensionless number, which is determined as ratio of viscous forces to surface tension force. Smaller values of  $Ca$  represents flow scenarios in which surface tension is dominant.

numerical errors are associated with surface tension calculations and cause the associated pressure jump across the interface to converge to a value which is different from the analytical solution of the Laplace–Young equation<sup>3</sup> [Deshpande et al., 2012a]. Another source of these numerical errors is the inconsistent force discretization [Deshpande et al., 2012a]. These numerical errors, which are important when simulating surface tension dominant flows [Deshpande et al., 2012a], generate nonphysical flow near the interface which are commonly referred to as spurious velocities/currents [Klostermann et al., 2013, Raeini et al., 2012, Hoang et al., 2013, Samkhaniani and Ansari, 2016]. Spurious velocities adversely affect the accuracy of the simulations by altering the heat and mass transfer across the interface [Samkhaniani and Ansari, 2016], as well as cause nonphysical flows that can induce ‘random walk’ of a bubble or droplet [Hoang et al., 2013]. The effect of these spurious velocities has been reported to increase with smaller Capillary<sup>4</sup> number [Deshpande et al., 2012a, Hoang et al., 2013]. As a result of these spurious velocities, interFoam cannot simulate bubbles which are smaller than a millimeter, see Deshpande et al. [2012a], Jamshidi et al. [2019].

By interpolating the flow variables, which are stored at cell center, to obtain the corresponding cell face values and performing gradient calculations at the cell face, interFoam ensures consistent discretization of pressure gradient, gravitational, surface tension force and velocity flux, see Eq.8.16 and Eq.8.18. Despite the consistent discretization, the convergence criterion used to determine  $p_{rgh}$ , in Eq.8.18, introduces some force imbalance which can be reduced by setting a very low (in the order of  $10^{-20}$ ) tolerance [Deshpande et al., 2012a]. The balance between the forces, which would result in negligible amount of spurious velocities if errors associated with computing interfacial curvature are negligible, has been showcased for interFoam by using a static bubble whose radius of curvature was imposed [Deshpande et al., 2012a].

The main source of spurious velocities in interFoam is associated with errors in curvature calculations, as shown in the work by Deshpande et al. [2012a]. In geometric VOF methods, which produce the interface within a cell, the errors associated in calculating interfacial curvature based on Eq.8.15b is circumvented by using more advanced formulations to determine  $\kappa$ , which is based on the sub-cell level geometric representation of the interface (see Renardy and Renardy [2002] and Guo et al. [2015]). Although spurious velocities has been observed even when geometric reconstruction of the interface is used, geometric VOF methods are far superior to algebraic VOF methods as the spurious velocities generated as several order of magnitude lower [Renardy and Renardy, 2002, Guo et al., 2015]. Due to the complexity in implementing geometric VOF methods and added computational overhead

of interface reconstruction [Gerlach et al., 2006], works like Raeini et al. [2012] and Hoang et al. 2013 have attempted to address spurious velocities by implementing ‘different’ surface tension models which are used with algebraic VOF methods. These methods typically employ a smoothed  $\alpha_1$  to compute  $\kappa$ , there by reducing the errors associated with the first and second order differentiation of  $\alpha_1$ , to reduce spurious velocities by few orders of magnitude when compared to the out-of-the-box interFoam [Raeini et al., 2012, Hoang et al., 2013].

As discussed in Chapter 8, the solution algorithm in interFoam first solves the advection of  $\alpha_1$ , then momentum and continuity equations are solved together using PISO algorithm. The advection of  $\alpha_1$  is based on the velocity at the previous time step, see Eq.8.5. This means that the surface tension force, used in the momentum equation, is computed based on the advected  $\alpha_1$  from Eq.8.5, as shown in Eq.8.14. This would lead to the surface tension force remaining constant during the PISO algorithm as the velocity field gets updated and  $\alpha_1$  is not correspondingly advected. This is known as the explicit treatment of the surface tension model. The explicit treatment of surface tension force imposes time step constraint to prevent the growth of the generated spurious velocities, Brackbill et al. [1992],

$$\Delta t < \sqrt{\frac{\rho_{avg}(\Delta x)^3}{2\pi\sigma}}, \quad (8.19)$$

where  $\rho_{avg}$  is the average of the fluid densities and  $\Delta x$  is the grid spacing. Another time step constraint, based on the work by Galusinski and Vigneaux [2008], dependent on the average dynamic viscosity of the phases ( $\mu_{avg}$ ) is

$$\Delta t \leq \frac{1}{2} \left( C_2 \tau_\mu + \sqrt{(C_2 \tau_\mu)^2 + 4C_1 \tau_\rho^2} \right), \quad (8.20)$$

where  $C_1$  and  $C_2$  are constants,  $\tau_\mu$  and  $\tau_\rho$  are time scales which are defined as  $\mu_{avg} \Delta x / \sigma$  and  $\sqrt{\rho_{avg}(\Delta x)^3 / \sigma}$ . The work by Deshpande et al. [2012a] proposed a additional constraint on time step (for interFoam) along with Eq.8.20 to control the evolution of spurious velocities as

$$\Delta t \leq \max(C_2 \tau_\mu, 10C_1 \tau_\rho). \quad (8.21)$$

Deshpande et al. [2012a] also reported that, for interFoam,  $C_1$  and  $C_2$  (used in Eq.8.20 and Eq.8.21) are equal to 0.01 and 10 respectively. These time step constraints increase the computational overhead, especially for ‘fine’ meshes, for example a mesh resolution equal to 1  $\mu\text{m}$  and  $\rho_{avg} / \sigma$  around 1000  $\text{s}^2 / \text{m}^3$  gives  $\Delta t < 1.2 \times 10^{-8}$  s (computed based on Eq.8.19). One of ways to ease this time step constraint is by implicitly treating the surface tension term, which was hypothesized



by Brackbill et al. [1992], as shown in works like Hysing [2006] and Raessi et al. [2009].

## **Part IV**

# **Contributions**



To achieve the PhD objective, which is to develop an interface resolved framework to simulate the electrochemical evolution of continuum scale hydrogen bubbles, customization of `interFoam` is paramount. In order to achieve this goal, a modularized approach is undertaken during the PhD to incrementally develop the framework which can be summarized as

**1. Surface tension modelling, spurious velocities and simulating submillimeter bubbles**

Due to the presence of spurious velocities, discussed in Chapter 8, bubbles simulated with `interFoam` are typically larger than a millimeter, see [Deshpande et al. \[2012a\]](#), [Jamshidi et al. \[2019\]](#). The objective of this task is to reduce spurious velocities, in the algebraic VOF method used to compute the advected interface in the framework, by implementing a different surface tension model instead of the Continuum Surface Force model available in `interFoam`. Additionally, the implemented surface tension model should be able to reliably simulate bubbles whose diameters are below one millimeter. This work is reported in papers A and B.

**2. Interfacial mass transfer and associated bubble growth**

Although modelling of interfacial mass transfer in `interFoam` has been an active topic of investigation (see Chapter 6), it has not been coupled to the associated bubble growth except in [Liu et al. \[2016\]](#) who employed a  $Sh$  based correlation. In this module, a VOF based framework to simulate supersaturation driven bubble growth is developed. This work has been reported in papers C and D. It should be pointed out that while paper C was undergoing peer-review, [Maes and Soulaine \[2020\]](#) reported a `interFoam` based framework which simulated the shrinking of a rising bubble due to interfacial mass transfer using a single field formulation of dissolved species transport.

**3. Framework for continuum scale electrochemical hydrogen evolution**

Papers E and F, developed during this module, delves into implementing the multiphysics relevant to simulate continuum scale electrochemical hydrogen evolution which was summarized in Fig.2.2.

The chapters in this part provides summaries of the six papers developed during the PhD in order to highlight the advances made towards addressing the project objective. Please note that this part of the thesis contains just summaries of the papers, so readers interested in details like the convergence, implemented governing equations and mass/dissolved gas conservation should refer to the appended papers.



## Chapter 9: Summary of paper A

### Comparison of Surface Tension Models for the Volume of Fluid Method

K.J. Vachaparambil & K.E. Einarsrud, *Processes*, 2019, 7, 542.<sup>1</sup>

<sup>1</sup> Vachaparambil and Einarsrud 2019

#### *Context to the work*

Spurious velocities produced during VOF simulations affect the accuracy of simulations, so it is critical to address them.

Two approaches that has been reported to reduce spurious velocities, by a few orders of magnitude, when using algebraic VOF approach, like the interface compression implemented in OpenFOAM® [Deshpande et al., 2012a], are based on Raeini et al. [2012] and Hoang et al. [2013] who reformulated the surface tension calculation to obtain variants of the Continuum Surface Force (CSF) model [Brackbill et al., 1992] known as the Sharp Surface Force (SSF) model and Smoothed CSF model respectively. Both these models are easy to implement and do not need the computationally expensive interface reconstruction method when compared to the geometric VOF method and they have been used to simulate a variety of surface tension dominant flows:

- The SSF model has been used to simulate capillary rise [Raeini et al., 2012] and interfacial mass transfer [Maes and Soullaine, 2018];
- The Smoothed CSF model has been used to simulate bubble/droplet microfluidics [Hoang et al., 2013] and bubble condensation [Samkhaniani and Ansari, 2016].

#### *Objective*

The primary objective of the paper is to implement both SSF (as proposed by Raeini et al. [2012]) and Smoothed CSF (as proposed by Hoang et al. [2013]) surface tension models in interFoam. The ability of these models were compared to the out-of-the-box interFoam (which uses CSF model) to capture surface tension dominant flows

and quantify the spurious velocities generated during the simulations. Apart from these, the influence of the under-relaxation factors and maximum time step constraints on the spurious velocities are investigated.

#### *Overview of implemented surface tension models*

The Continuum Surface Force model, proposed by Brackbill et al. [1992], is the default surface tension model available in interFoam which is computed based on Eq.8.15a, Eq.8.15b and Eq.8.15c (which is corrected for contact angle at wall boundary conditions).

The Smoothed CSF model, proposed by Hoang et al. [2013], employ a smoothened  $\alpha_1$  in order to compute the unit normal to the interface which is corrected to account for the contact angle and then used to compute the interfacial curvature. This smoothening procedure used on  $\alpha_1$  reduces the discontinuous nature of the volume fraction field which allows for a less error prone first and second order derivative calculations which reduces spurious velocities [Hoang et al., 2013].

The Sharp Surface Force model, proposed by Raeini et al. [2012], is more complex compared to the other two models. The first step is to smoothen  $\alpha_1$ , then estimate the unit normal to the interface (which is corrected for the contact angle conditions). After which the initial estimate to interfacial curvature is computed. The second step involves smoothening the interfacial curvature away from the interface. The final step involves sharpening  $\alpha_1$  to get  $\alpha_{sh}$ :

$$\alpha_{sh} = \frac{1}{1 - C_{sh}} \left[ \min \left( \max \left( \alpha_1, \frac{C_{sh}}{2} \right), 1 - \frac{C_{sh}}{2} \right) - \frac{C_{sh}}{2} \right], \quad (9.1)$$

<sup>2</sup> In this paper,  $C_{sh}$  is set to 0.5 for capillary rise and rising bubble simulations and 0.98 for static bubble simulations.

where  $C_{sh}$  is the sharpening coefficient<sup>2</sup>. The sharpened volume fraction of liquid ( $\alpha_{sh}$ ) and final estimate of curvature ( $\kappa_{final}$ ) is used to compute the surface tension force which is represented as

$$\vec{F}_{st} = \sigma \kappa_{final} \nabla \alpha_{sh}. \quad (9.2)$$

#### *Main results*

The three surface tension models are compared on its ability to simulate two-dimensional cases of rising bubbles and capillary rise along with the static bubble of diameter equal to 5 mm.

RISING BUBBLES simulated consisted of two cases (TC1 and TC2) which was proposed by Hysing et al. [2009] as a computational benchmark. The cases TC1 and TC2 differed in the Capillary number ( $Ca$ ), i.e. equal to 0.286 and 3.571 respectively. The predictions from the three surface tension models were compared to the benchmark with respect

to the reported data for bubble morphology and rise velocities. As shown in Fig.9.1 and Fig.9.2 the surface tension models provide reasonable agreement to the rising bubble benchmark for both cases. The deviations in the bubble morphologies and rise velocities observed in TC1 and TC2 from the computational benchmark can be attributed to the spurious velocities, as discussed by Klostermann et al. [2013].

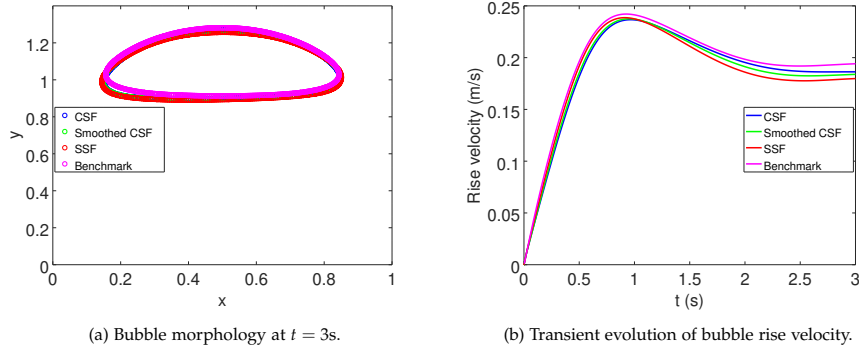


Figure 9.1: Comparison of the predictions of the three surface tension models with the 2D benchmark data reported by Hysing et al. 2009 for TC1.

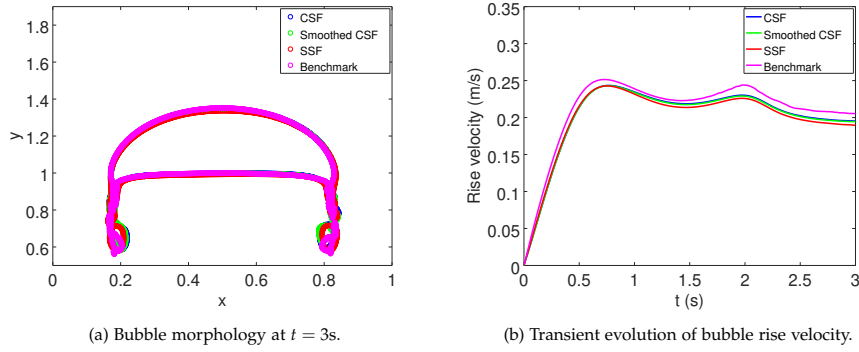


Figure 9.2: Comparison of the predictions of the three surface tension models with the 2D benchmark data reported by Hysing et al. 2009 for TC2.

CAPILLARY RISE height ( $h_b$ ) for the liquid rising between two parallel vertical plates can be obtained analytically as

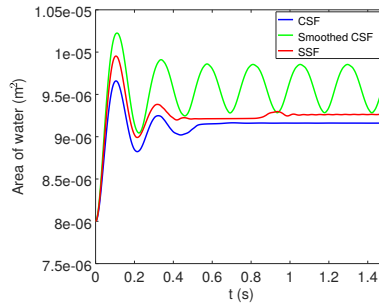
$$h_b = \frac{2\sigma\cos\theta}{\Delta\rho|\vec{g}|a}, \quad (9.3)$$

where  $a$  is the distance between the plates and  $\theta$  is the contact angle at the side walls which is equal to  $45^\circ$  [Bullard and Garboczi, 2009]. For



the computational settings used in the simulations,  $h_b$  equal to 9.9mm and  $a$  is equal to one millimeter. The capillary rise height predicted by SSF and CSF had an error of 6.5% and 7.6% respectively but the Smoothed CSF model did not converge to a steady state solution (due to spurious velocities), as shown in Fig.9.3.

Figure 9.3: Comparison of the predictions of the three surface tension models for the 2D capillary rise simulations.



STATIC BUBBLES are an ideal way to study spurious velocities as theoretically the velocity in the domain must be zero. The fluid properties used in the stationary bubble simulations are  $\rho_1 = 1000 \text{ kg/m}^3$ ,  $\rho_2 = 1 \text{ kg/m}^3$ ,  $\nu_1 = 10^{-6} \text{ m}^2/\text{s}$ ,  $\nu_2 = 1.48 \times 10^{-5} \text{ m}^2/\text{s}$  and  $\sigma = 0.07 \text{ N/m}$ . The static bubble, with a diameter of 5 mm, has been reliably simulated with all three surface tension models. For meshes, which resolve bubble diameter with 40-60 cells (which is practically used in VOF simulations [Samkhaniani and Ansari, 2016]), Smoothed CSF and SSF models predicted the Laplace pressure in the bubble with an error around 9% whereas CSF model had a slightly larger error (around 13%). Spurious velocities developed with SSF and Smoothed CSF models were one-twentieth and one-tenth of the spurious velocities developed during the static bubble simulation using CSF model. When using the CSF model, finer mesh resulted in larger spurious velocities whereas for Smoothed CSF and SSF models these numerical artifacts did not increase.

When no under-relaxation is used in the solution algorithm, the use of time step constraint due to the explicit treatment of surface tension as reported by Deshpande et al. [2012a] (Eq.8.20 and Eq.8.21) seems to reduce spurious velocities for both Smoothed CSF and SSF but it had no significant effect on CSF model when compared to the simulations run with Brackbill et al. [1992] (Eq.8.19).

The use of an under-relaxation factor equal to 0.9 resulted in reliable simulations for stationary bubbles. However, this approach cannot be used for transient cases, as it can lead to under predicting the flow variables (as shown in Eq.7.12 and Eq.7.13).

## Chapter 10: Summary of paper B

### On sharp surface force model: effect of sharpening coefficient

K.J. Vachaparambil & K.E. Einarsrud, Published in *Experimental and Computational Multiphase Flow*, 2020.<sup>1</sup>

<sup>1</sup> Vachaparambil and Einarsrud 2020b

#### Context to the work

Due to the existence of spurious velocities in interFoam, which is shown in paper A, reliably simulating bubbles less than a millimeter in diameter is difficult, see [Jamshidi et al. \[2019\]](#). To be able to study continuum scale electrochemical gas evolution, which were observed in experimental works like [Brussieux et al. \[2011\]](#), [Baczyzmalski et al. \[2017\]](#), [Yang et al. \[2018\]](#), [Bashkatov et al. \[2019\]](#), it is necessary to resolve bubbles in the order of hundreds of micrometer. Additionally, these bubbles evolve from an electrode surface where the wetting condition at the electrode also plays a role in the bubble detachment [[Zhang and Zeng, 2012](#)].

#### Objective

The objective of the paper is to show that using an appropriate choice of sharpening coefficient ( $C_{sh}$ ) used in the SSF model, Eq.9.2, can reduce spurious velocities which can enable two-dimensional simulations of millimeter and submillimeter sized bubble as well as simulate wetting dependent phenomena like capillary rise. For the simulations, the effect of  $0 \leq C_{sh} \leq 0.5$  is investigated for these 2D cases.

#### Main results

It should be pointed out the all the simulations in this paper are based on the time step constraint proposed by [Deshpande et al. \[2012a\]](#) which was also investigated in paper A. The fluid properties used in the stationary bubble and capillary rise simulations are  $\rho_1 = 1000 \text{ kg/m}^3$ ,  $\rho_2 = 1 \text{ kg/m}^3$ ,  $\nu_1 = 10^{-6} \text{ m}^2/\text{s}$ ,  $\nu_2 = 1.48 \times 10^{-5} \text{ m}^2/\text{s}$  and  $\sigma =$

0.07 N/m. For the 2D capillary rise simulation, gravity of  $10 \text{ m}^2/\text{s}$  is enabled while for stationary 2D millimeter and submillimeter bubble simulations it is set to zero.

CAPILLARY RISE simulations consider the distance between the two parallel side walls to be 1 mm with a contact angle of  $45^\circ$ . The results, tabulated in Table.10.1, show that the SSF model is approximately able to predict the capillary rise height quite well for the range of sharpening coefficient considered in the simulation. The spurious velocities are observed to be largest when using sharpening coefficient equal to zero, see Table.10.1.

Table 10.1: Variation of capillary rise height with sharpening coefficients.

$C_{sh}$	$U_{sc} _{t=1.5s}^\ddagger$ (m/s)	$h_S$ (mm)	Error <sup>†</sup>
0.0	0.1810	9.36	0.056
0.1	0.0098	9.30	0.062
0.2	0.0097	9.34	0.057
0.3	0.0050	9.30	0.061
0.4	0.0041	9.31	0.061
0.5	0.0031	9.26	0.065

<sup>†</sup> Error =  $(h_b - h_S)/h_b$  where  $h_b$  is calculated based on Eq.9.3.

<sup>‡</sup>  $U_{sc}$  is the measure of spurious velocities which is calculated as  $\max(|\vec{U}|)$ .

STATIC BUBBLE SIMULATIONS consider bubbles with a radius equal to 2.5 mm, referred to as millimeter sized bubbles, and 0.25 mm, which are referred to as submillimeter bubbles, in the absence of gravity. For the case of millimeter sized bubble, the static bubble is obtained for  $0 \leq C_{sh} \leq 0.5$  but spurious velocities decreased with larger values of  $C_{sh}$  and the error in predicted Laplace pressure in the bubble is around 8 %-9 %. The submillimeter bubble can be reliably simulated only using  $C_{sh} \leq 0.3$ , see Table.10.2.

Table 10.2: Time averaged spurious velocities, Laplace pressure and associated error (calculated as  $(\Delta p_T - \bar{\Delta p}_S)/\Delta p_T$ , where  $p_T$  is equal to  $\sigma/R$ ) while modelling a 2D submillimeter bubble.

$C_{sh}$	$\bar{U}_{sc}^\ddagger$ (m/s)	$\bar{\Delta p}_S^\dagger$ (Pa)	Error
0.0	0.061	254.285	0.092
0.1	0.039	254.294	0.092
0.2	0.028	255.350	0.088
0.3	0.011	255.279	0.088
0.4	Bubble numerically drifts from the original position		
0.5	Bubble numerically drifts from the original position		

<sup>‡</sup>  $\bar{U}_{sc}$  is the time averaged spurious velocities.

<sup>†</sup>  $\bar{\Delta p}_S$  is the time averaged predicted Laplace pressure in the bubble.

## Chapter 11: Summary of paper C

### **Numerical simulation of bubble growth in a supersaturated solution**

K.J. Vachaparambil & K.E. Einarsrud, *Applied Mathematical Modelling*, 2020, 81, 690-710.<sup>1</sup>

<sup>1</sup> Vachaparambil and Einarsrud 2020a

#### *Context to the work*

As discussed in Chapter 6, VOF based modelling of interfacial mass transfer, in the OpenFOAM<sup>®</sup> framework, has been an active topic of investigation, see Eq.6.12 and Eq.6.14, but the associated change in bubble volume has not been coupled to the proposed frameworks, see Haroun et al. [2010], Deising et al. [2016], Marschall et al. [2012] and Maes and Soullaine [2018]. Although an attempt to simulate this phenomena was reported by Liu et al. [2016], their work computed the driving force for bubble growth based on the flow scenario specific  $Sh$  based correlation, see Chapter 6. This paper is an attempt to address this issue.

#### *Objective*

The objective of the paper is to develop a framework, based on interFoam, to simulate the growth of a bubble in the presence of a supersaturated solution. In order to achieve this objective, interFoam, described in Chapter 8, is modified to treat the relevant source terms to account for the growth of the bubble which is coupled to the transport of dissolved gas and the driving force for interfacial mass transfer based on local supersaturation. The effect of modelling driving force for bubble growth computed based on both Fick's 1<sup>st</sup> law and  $Sh$  based correlations are also investigated.

#### *Overview of developed framework*

This section provides an overview of the framework discussed in papers C and D along with some additional notes.

The first step of the developed framework is to solve for the volume fraction of fluid  $\alpha_1$ , based on the interface compression approach, using

$$\frac{\partial \alpha_1}{\partial t} + \nabla \cdot (\alpha_1 \vec{U}) + \nabla \cdot (\alpha_1 (1 - \alpha_1) \vec{U}_r) = \dot{S}_\alpha. \quad (11.1)$$

The term on the right hand side of the above equation is associated with the bubble growth and is calculated as  $\dot{S}_\alpha = \alpha_1 \nabla \cdot \vec{U}$ . As demonstrated in appendix B, this formulation of the source term is equivalent to  $\dot{S} = \alpha_1 \dot{m} / \rho$ , where  $\dot{m}$  is computed as described in Eq.11.5. Eq.11.1 is computed based on the semi-implicit Multidimensional Universal Limiter with Explicit Solution (MULES) method, described in Greenshields [2014]. It should be noted that the semi-implicit MULES uses a predictor-corrector algorithm which results in the source term expressed in implicit and explicit formulations.

The concentration of the dissolved gas over the saturation condition (represented<sup>2</sup> by  $C_i$ ) is used to calculate the driving force based on Eq.6.15 and Eq.6.16. This assumption leads to saturation concentration being represented by  $C_i = 0 \text{ mol/m}^3$  and the driving forces is implemented as

- Fick's 1<sup>st</sup> law:  $j = M_i D_{i,1} |\nabla C_i|$ , where  $D_{i,1}$  is the diffusion coefficient of the dissolved gas in the liquid,
- Sh correlation:  $j = D_{i,1} Sh M_i C_i / L$ , where

$$Sh = 2 + 0.6515 \sqrt{Re Sc}, \quad (11.2)$$

which is derived for small mass transfer rates from bubble in a creeping flow, see Bird et al. [2006]. The characteristic velocity and length scale ( $L$ ), used to compute  $Re$  and  $j$ , are calculated as rate of change of bubble radius and bubble diameter respectively.

The source terms are computed based on the approach initially developed by Hardt and Wondra [2008] and then adapted to interFoam by Kunkelmann and Stephan [2009], Kunkelmann [2011] for temperature driven phase change processes<sup>3</sup>. Once driving force  $j$  is computed, by Fick's 1<sup>st</sup> law or based on  $Sh$  correlation, the local mass transfer rate  $\psi_0$  is computed at the liquid side of the interface as

$$\psi_0 = N j \alpha_1 |\nabla \alpha_1|, \quad (11.3)$$

where  $N$  is a normalization factor [Hardt and Wondra, 2008].  $\psi_0$  is then smeared based on

$$D \Delta t \nabla^2 \psi = \psi - \psi_0, \quad (11.4)$$

where  $D \Delta t$  is a user defined value [Hardt and Wondra, 2008]. Using the value of  $\psi$ , the source terms for continuity equation ( $\dot{m}$ ) is shifted

<sup>2</sup>Please note the  $C_i$  used in this part are different from the concentration field used in Chapter 6.

<sup>3</sup>The approach developed by Hardt and Wondra 2008 is in principle independent of the employed interface capturing method which allows it to be used on both geometric and algebraic VOF methods.

away from the interface to the pure gas phase by applying a heavyside function which uses a volume fraction cutoff of  $10^{-3}$ , this procedure, further described in Kunkelmann [2011], results in the redistribution of  $\dot{m}$  in the region where  $\alpha_1 < 10^{-3}$ . Shifting the source term for continuity equation, allows the interface to be advected only based on the velocity field and not influenced by the source term [Kunkelmann, 2011]. The source term for the continuity equation is calculated as

$$\dot{m} = A\alpha_2\psi, \quad (11.5)$$

where  $A$  is another normalization factor [Hardt and Wondra, 2008]. In order to ensure the disappearance of dissolved gas at the interface, the sink term for the dissolved gas transport is computed as

$$S_i = -\frac{N\alpha_1(j|\nabla\alpha_1|)}{M_i}, \quad (11.6)$$

which is applied to the liquid side of the interface.

In the next step, the continuity equation, with source term calculated in Eq.11.5,

$$\nabla \cdot \vec{U} = \frac{\dot{m}}{\rho}, \quad (11.7)$$

is solved together with the momentum equation,

$$\frac{\partial \rho \vec{U}}{\partial t} + \nabla \cdot (\rho \vec{U} \vec{U}) = -\nabla p_{rgh} + \left( \nabla \cdot (\mu \nabla \vec{U}) + \nabla \vec{U} \cdot \nabla \mu \right) - \vec{g} \cdot \vec{x} \nabla \rho + \vec{F}_{ST}, \quad (11.8)$$

using PISO scheme (described in Chapter 8). The surface tension force implemented in Eq.11.8 is the Sharp Surface Force (SSF) model as reported in papers A and B. Finally, the transport of the dissolved gas is computed based on the C-CST model proposed by [Maes and Soulaire, 2018] and sink term calculated using Eq.11.6 as

$$\begin{aligned} \frac{\partial C_i}{\partial t} + \nabla \cdot (\vec{U} C_i) = \nabla \cdot \left( \hat{D}_i \nabla C_i - \frac{1 - He_i}{\alpha_1 + \alpha_2 He_i} \hat{D}_i C_i \nabla \alpha_1 \right) \\ - \nabla \cdot \left( \frac{1 - He_i}{\alpha_1 + \alpha_2 He_i} \alpha_1 \alpha_2 \vec{U}_r C_i \right) + S_i, \end{aligned} \quad (11.9)$$

where  $He_i$  describes the concentration jump across the interface<sup>4</sup>, see Eq.6.10b.

### Main results

The proposed model is compared to well known analytical models, Epstein and Plesset [1950] and Scriven [1959], to describe diffusion controlled growth of bubbles due to supersaturation. Epstein and Plesset

<sup>4</sup>Due to the single field  $C_i$  used in C-CST model,  $He_i$  should be set to a small value to simulate the dissolved gas in addition to obtaining the saturation concentration at the interface, see papers C and D for detailed discussion.

Consider a two dimensional growing bubble, whose radius at any give time is denoted by  $R$ , from a pre-existing bubble (of radius  $R_0$ ). Its growth can be described as

$$\rho_2 \left( 2\pi R \frac{dR}{dt} \right) = 2\pi R j, \quad (11.10a)$$

where  $R$  is the radius of the bubble and  $j$  is calculated as the driving force. Eq.11.10a can be written as

$$\rho_2 \left( \frac{dR}{dt} \right) = M_i k \Delta C_i, \quad (11.10b)$$

where  $k = (D_{i,1}/2R)(2 + 0.6515\sqrt{ReSc})$ , based on Eq.11.2 and  $\Delta C_i$  represents the bulk concentration over the saturation condition. When the convection caused by bubble growth is neglected, i.e.  $Re = 0$ , the above equation can be written as

$$\rho_2 \left( \frac{dR}{dt} \right) = M_i \frac{D_{i,1}}{R} \Delta C_i, \quad (11.10c)$$

which can be integrated in time to obtain Eq.11.11. The corresponding driving force can be written as

$$j = \frac{D_{i,1}}{R} M_i \Delta C_i. \quad (11.10d)$$

[1950] derived an 'approximate solution' which describes the temporal evolution of the bubble radius when the effects of bubble convection is neglected. This assumption was subsequently addressed by Scriven [1959] who derived an asymptotic solution of the change in bubble radius time based on the assumption of radially uniform growth of bubble in an unbounded medium (referred for simplicity as Scriven). As Scriven [1959] does not account for the initial growth phase, the work by Hashemi and Abedi [2007] reported an extension to the Scriven [1959] to account for the diffusive growth from a pre-existing bubble (referred to as Extended Scriven). As these models are derived for spherical bubbles, its equivalent for two-dimensional bubbles which are treated in the simulations are derived in the appended paper C.

WHEN CONVECTION IS NEGLECTED, the increase in bubble radius with time can be determined analytically:

$$\left( \frac{R}{R_0} \right)^2 = 1 + \frac{2M_i D_{i,1} (\Delta C_i)}{\rho_2 R_0^2} t, \quad (11.11)$$

where  $\Delta C_i$  is set as equal to  $200.64 \text{ mol/m}^3$ , which corresponds to supersaturation ratio of seven, as used in the simulations. Eq.11.11 is the approximate solution derived by Epstein-Plesset [Epstein and Plesset, 1950]. The driving force for the simulations is set to Eq.11.10d as it is used to derive Eq.11.11. The predictions using the proposed solver and Eq.11.11 agree well, see Fig.11.1.

WHEN CONVECTION IS CONSIDERED, the asymptotic solution of bubble growth in a supersaturated solution, as proposed by Scriven [1959], is given by

$$R_{Scriven} = 2\beta \sqrt{D_{i,1} t}, \quad (11.12)$$

where  $\beta$  is the growth parameter. Based on the work by Hashemi and Abedi [2007], an Extended Scriven model that modifies Eq.11.12 to account for the growth from a pre-existing bubble of radius  $R_0$  can be described as

$$R_{Scriven-ext} = 2\beta \sqrt{D_{i,1} \left( t + \frac{R_0^2}{4D_{i,1}\beta^2} \right)}. \quad (11.13)$$

Previous works by Wang et al. [2016], Jones et al. [1999], reported an analytical expression to determine  $\beta$  for a spherical bubble as

$$\beta_{3D} = \frac{a + \sqrt{a^2 + 2a}}{2}, \quad (11.14)$$

where  $a$  is equal to  $M_i \Delta C_i / \rho_2$ . An equivalent expression for growth parameter for two dimensional bubble growth driven by supersatura-

tion is

$$\beta_{2D} = \frac{a + \sqrt{a^2 + 4a}}{2\sqrt{2}}, \quad (11.15)$$

where  $a$  is defined based on Eq.11.14. The derivation of Eq.11.15, which is based on Wang et al. [2016], is included in the appendix of the appended paper C. For the simulations in this paper,  $\beta_{3D}$  and  $\beta_{2D}$  are equal to 5.3346 and 4.0509 respectively. The comparison of proposed solver using Fick's 1<sup>st</sup> law and  $Sh$  correlation with Eq.11.12 and Eq.11.13 based on 2D and 3D formulations of  $\beta$  is shown in Fig.11.2. The predictions from the proposed framework using Fick's 1<sup>st</sup> law provides a reasonable agreement to the analytical model when using  $\beta_{2D}$ . The framework when using  $Sh$  correlation, described in Eq.11.2, seems to under-predict the bubble radius. The difference in the predictive ability between the models can be explained by the evolution of growth rate, see Fig.11.3. The large initial growth rate (compared to the analytical model) when using Fick's 1<sup>st</sup> law in the proposed framework is due to the lack of concentration boundary layer in the distribution of the dissolved gas used to initialize the simulation. Due to the uniform initialization used, during the first time step, the gradient at the interface would be larger but with time the concentration boundary layer develops, as dissolved gas is removed from the liquid, then the predicted growth rates matches the analytical model as observed in Fig.11.3.

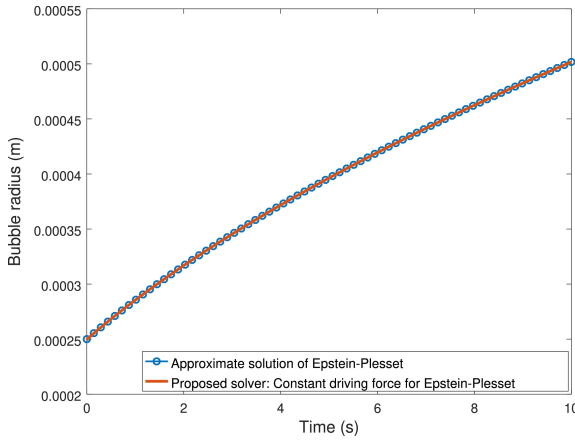


Figure 11.1: Comparison of the temporal evolution of 2D bubble radius predicted by the proposed solver (based on driving force described in Eq.11.10d) with the approximate solution of Epstein-Plesset (Eq.11.11).

PARAMETRIC STUDIES on the influence of  $He_i$  (in Eq.11.9) shows that using a value of  $10^{-4}$  can reasonably predict the transport of dissolved gas. Similarly,  $D\Delta t$  (in Eq.11.4) equal to a value of  $10^{-6}$  m<sup>2</sup> seems to



provide a solution which is independent of the user-defined parameter.

Another notable result in the paper is that spurious velocities generated when simulating the growth of a bubble (with surface tension treated but gravity neglected) reduces the growth rate by removing the dissolved gas away from the interface.

Figure 11.2: Comparison of the evolution of 2D bubble radius predicted by the proposed solver (based on driving force described using Fick's 1<sup>st</sup> law and  $Sh$  correlation) with analytical models like Eq.11.12 and Eq.11.13.

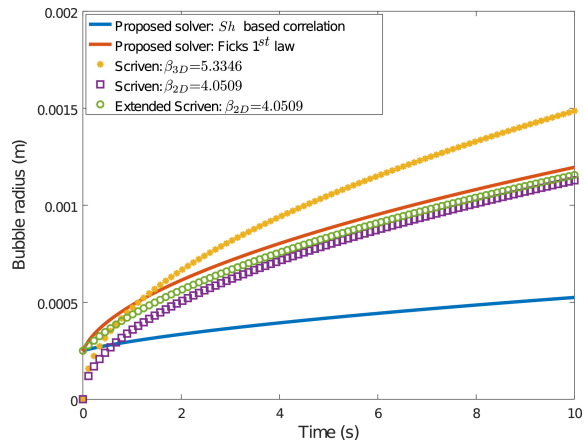
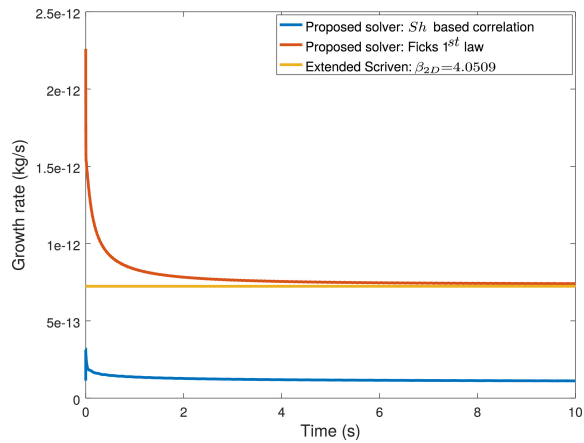


Figure 11.3: Comparison of the evolution of growth rate for a 2D bubble predicted by the proposed solver (based on driving force described using Fick's 1<sup>st</sup> law and  $Sh$  correlation),  $\int \psi_0 dV$ , with analytical model based on Eq.11.13.



## Chapter 12: Summary of paper D

### Modeling interfacial mass transfer driven bubble growth in supersaturated solutions

K.J. Vachaparambil & K.E. Einarsrud, *AIP Advances*, 2020, 10, 105024.<sup>1</sup>

<sup>1</sup> Vachaparambil and Einarsrud 2020c

#### *Context to the work and objectives*

Despite the universal applicability of Fick's 1<sup>st</sup> law to describe the interfacial mass transfer and bubble growth, application oriented simulation of the processes, like Liu et al. [2016], tend to rely on  $Sh$  correlations. In paper C, the Sherwood number correlation used,  $Sh = 2 + 0.6515\sqrt{ReSc}$ , under-predicts the bubble growth but the Fick's 1<sup>st</sup> law (due to the lack of concentration boundary layer in the initialized dissolved gas distribution) predicted a large initial growth rate. This raised the following questions:

- Which  $Sh$  correlation can describe the analytical bubble growth derived by Scriven [1959] and later extended by Hashemi and Abedi [2007] ?
- Is the framework proposed in paper C valid for a range of supersaturation levels?

The objective of this paper is to answer these questions.

#### *Derivation of a new driving force based on $Sh$ correlation for bubble growth*

This derivation is based on the work by Burman and Jameson [1976], who derived an analytical expression for  $Sh$ , based on bulk supersaturation, to describe the bubble growth by Scriven [1959]. For the 2D bubble, the growth rate can be expressed as

$$\rho_2 \frac{dV}{dt} = jA, \quad (12.1)$$

where  $V$  is the volume of the bubble which is equal to  $\pi R^2 h$ ,  $A$  is the surface area of the bubble which is computed as  $2\pi R h$  and the driving force is calculated as  $j = M_i k C_i$ , where  $h$  is the unit cell thickness used to define 2D domains in OpenFOAM® which is set equal to one micrometer. Substituting the expression for  $V, A$  and  $j$  into the above equation gives

$$\rho_2 \frac{dR}{dt} = M_i k C_i. \quad (12.2)$$

The rate of change of the radius can be calculated based on Eq.11.13 as

$$\frac{dR}{dt} = \frac{2\beta^2 D_{i,1}}{R}. \quad (12.3)$$

Substituting Eq.12.3 in Eq.12.2 to get

$$\frac{2\beta^2 D_{i,1}}{R} = \frac{M_i k C_i}{\rho_2}. \quad (12.4)$$

The above equation can be rearranged and multiplied with two on both sides to get

$$k = \frac{D_{i,1}}{2R} \frac{4\beta^2 \rho_2}{M_i C_i}, \quad (12.5)$$

and the corresponding  $Sh$  is defined as

$$Sh = \frac{4\beta^2 \rho_2}{M_i C_i}. \quad (12.6)$$

#### Simulation setup

In the framework proposed in paper C, the following driving force for interfacial mass transfer are implemented:

- Fick's 1<sup>st</sup> law:  $j = M_i D_{i,1} |\nabla C_i|$ ,
- $Sh$  correlation 1:  $j = D_{i,1} Sh M_i C_i / L$  where

$$Sh = 2 + 0.6515 \sqrt{Re Sc}, \quad (12.7)$$

which is derived for small mass transfer rates from bubble in a creeping flow, see Bird et al. [2006]. The characteristic velocity and length scale ( $L$ ) used to compute  $Re$  and  $j$  are calculated as rate of change of bubble radius and bubble diameter respectively.

- $Sh$  correlation 2: Based on  $k$  defined in Eq.12.5, the corresponding driving force can be written as  $j = M_i C_i k$ .

The 2D simulations are initialized with a uniform distribution of dissolved gas in the liquid phase at three different concentrations (over saturation concentration) equal to  $50.16 \text{ mol/m}^3$ ,  $100.32 \text{ mol/m}^3$  and  $200.64 \text{ mol/m}^3$  which correspond to supersaturation ( $S$ ) equal to 2.5, 4 and 7 respectively. By substituting the relevant values into the analytical solution, Eq.11.15, these three levels of supersaturation yields growth coefficient ( $\beta_{2D}$ ) equal to 1.3230, 2.2632 and 4.0509.

### *Main results*

As the different driving forces for interfacial mass transfer results in various growth rates, which is also observed in paper C, it is important to account for the variation of bubble size. This can be accounted by calculating growth rate per unit area of the interface, discussed in the mesh convergence studies performed in paper C. In the case of two dimensional bubble, as the surface area of the bubble is proportional to radius, the growth rate normalized with bubble radius can be used to compare the simulations.

The driving force based on  $Sh$  correlation 1 consistently under-predicts the normalized growth rate and bubble radius in the three supersaturation levels considered in the simulations, see Fig.12.1. On the other hand, the driving force based on  $Sh$  correlation 2 provides a very good agreement with the analytical predictions of bubble radius and normalized growth rate, see Fig.12.1. Interestingly, driving force using Fick's 1<sup>st</sup> law has a larger deviation from the analytical solution for smaller supersaturation which can be explained as a result of the higher initial growth rate due to the initialized concentration distribution of the dissolved gas. The bubble radius growth rate reaches the values predicted by the analytical model once the concentration boundary layer is developed and bubble growth is diffusion limited. The higher initial growth rates leads to quicker increase in the bubble size which causes the discrepancy observed in Fig.12.1.

The results show that it is necessary to choose the  $Sh$  correlation carefully to simulate a flow scenario. If the  $Sh$  correlations are not available or the flow scenario cannot be described by a single correlation, it is preferable to use Fick's 1<sup>st</sup> law to compute the driving force. The simulations also show the importance of having a resolved concentration boundary layer even at  $t = 0$  s when using Fick's 1<sup>st</sup> law.

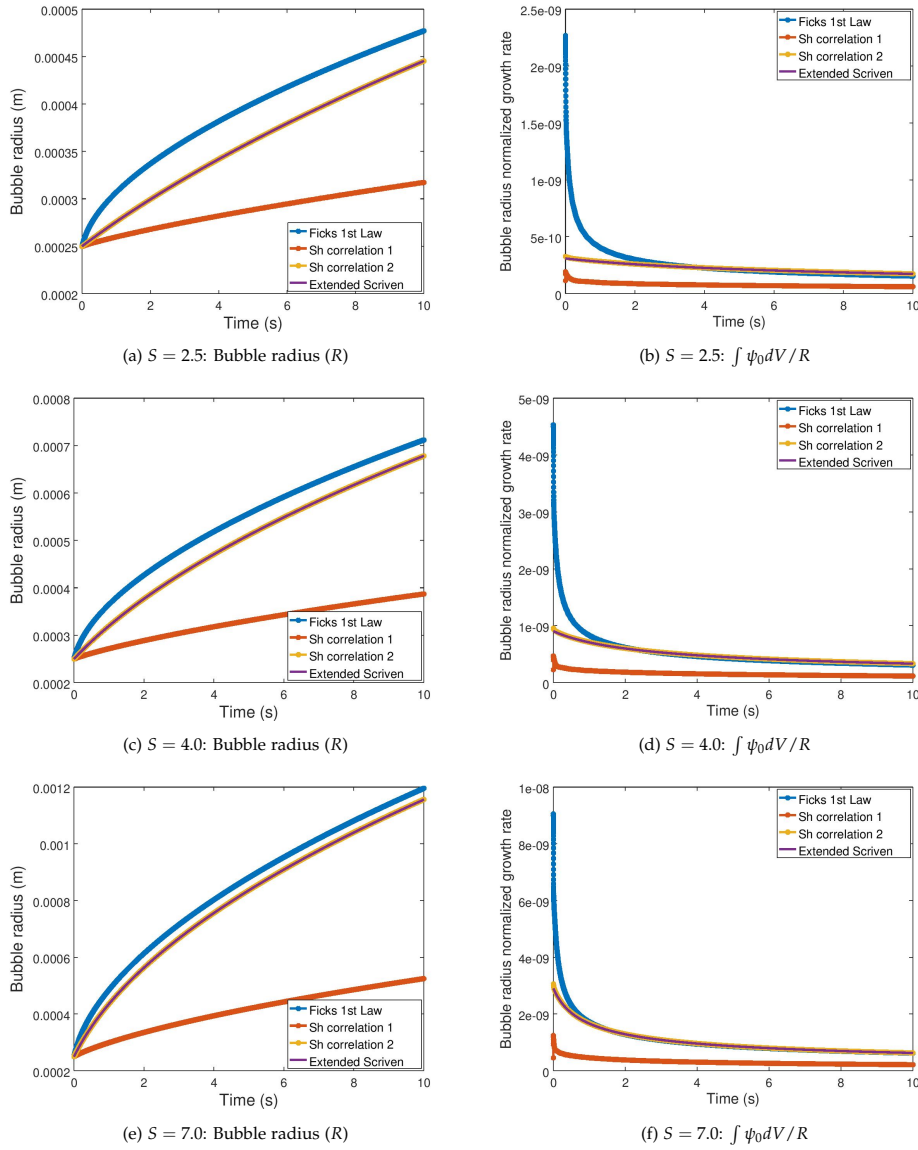


Figure 12.1: Comparison of the predicted bubble radius and normalized growth rate using driving forces described using Fick's 1<sup>st</sup> law and  $Sh$  correlations based 2D simulations with Extended Scriven model (with  $\beta_{2D}$ ) for various levels of supersaturation: 2.5, 4.0 and 7.0.

## Chapter 13:

### Summary of paper E

#### **On modelling electrochemical gas evolution using the Volume of Fluid method**

K.J. Vachaparambil & K.E. Einarsrud, Under-peer review in *14th International Conference on Computational Fluid Dynamics In the Oil & Gas, Metallurgical and Process Industries (CFD2020)*, Trondheim.

#### *Objective*

In this paper, the multiphysics modules, summarized in Fig.2.2, required to simulate continuum scale electrochemical gas evolution is described and validated in a decoupled approach.

#### *Main results - decoupled multiphysics modules and their verification*

SUBMILLIMETER BUBBLES of diameter  $500 \mu\text{m}$ , which are present in the bulk and on the surface, are simulated using sharpening coefficient equal to 0.3 in Sharp Surface Force model, implemented in paper A and B. The results showed that both the cases were reliably simulated by SSF model, see Fig.13.1.

TRANSPORT OF THE DISSOLVED GAS is performed by implementing the Compressive species transport (C-CST) equation, which is Eq.11.9 without the source/sink term, in interFoam. The interfacial condition which describes the concentration jump across the interface ( $He_i$ ), see Eq.6.10b, is set to  $10^{-4}$  based on parametric study performed in paper C. In order to verify that the transport of the dissolved gas is simulated accurately, a qualitative check is performed for the case of rising bubble through a region of supersaturation. As the bubble rises up through the supersaturated region, the dissolved gas get advected without numerically diffusing into the bubble, see Fig.13.2

SUPERSATURATION DRIVEN BUBBLE GROWTH is simulated based on

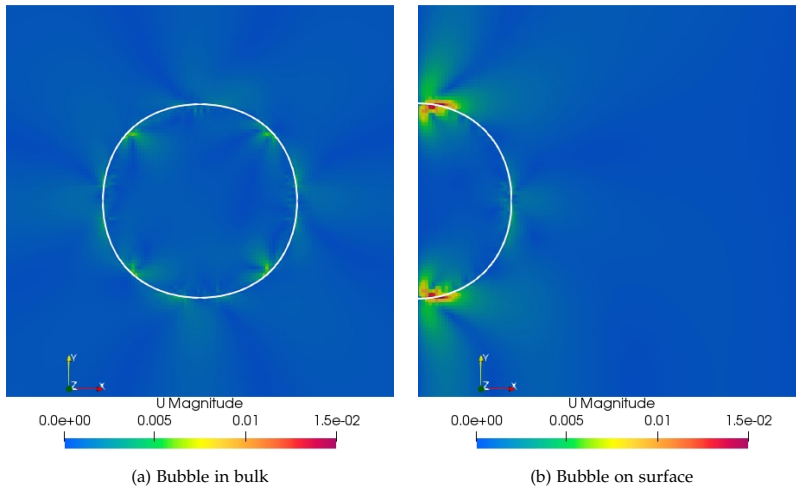


Figure 13.1: Comparison of the spurious velocities (m/s) generated while modelling stationary 2D submillimeter bubbles at  $t = 0.05$ s with interface (at  $\alpha_1 = 0.5$ ) represented by the white contour.

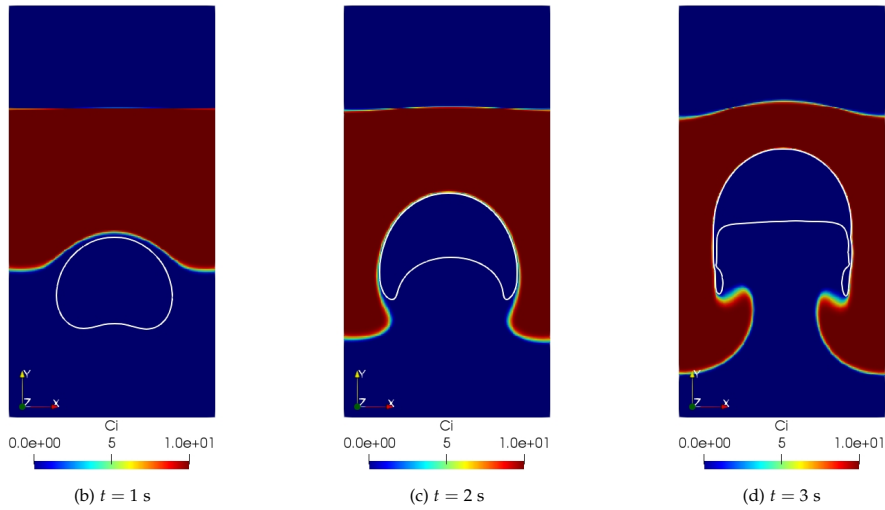


Figure 13.2: The concentration of dissolved gas ( $\text{mol/m}^3$ ) around a 2D rising bubble (interface, at  $\alpha_1 = 0.5$ , is represented by white contour) modelled based on C-CST.

the proposed framework in paper C and D, and validated against the analytical bubble growth predicted by Hashemi and Abedi [2007], Scriven [1959] in Eq.11.13. Due to the initialized uniform concentration of the dissolved gas, the initial growth rate is larger than theory but it reduces to the analytical predictions once the concentration boundary layer is established, which has been reported in both papers C and D.

CHARGE TRANSPORT is simulated using the Gauss' law (one of the four Maxwell's equations of electromagnetism), see Eq.6.3 and current density described based on Ohm's law, see Eq.6.5, to get a governing equation for charge conservation:  $\nabla \cdot \Gamma \nabla \Phi = 0$ , where  $\Gamma$  is the arithmetic mean of the electrical conductivities of the phases. Under constant potential difference, the current can be obtained as  $\sum \vec{i} \cdot \vec{S}$ , where  $\vec{S}$  is the surface area vector of individual mesh at the boundary. The verification of this module is performed based on two stationary scenarios in which both gravity and surface tension effects are neglected, but the bubble is located in the bulk or on the electrode surface.

The first scenario indicates the change in current when the bubble is present on the electrode and in the bulk which are denoted by EC1 and EC2, see Fig.13.3. When bubble is present on the surface, apart from the ohmic resistance the bubble also reduces the area of electrode in contact with electrolyte which results in larger resistance than when equivalent bubble is in the bulk. As a result when bubble leaves the surface the current increases which is observed in EC1 and EC2, see Table.13.1.

Case	$1 - \Theta$	Area of 2D bubbles (m <sup>2</sup> )	Current (A)
EC1	1	$3.16 \times 10^{-6}$	$9.384 \times 10^{-7}$
EC2	0.6	$3.16 \times 10^{-6}$	$9.306 \times 10^{-7}$

Please note that  $1 - \Theta$ , which represents the fraction of the electrode area in contact with electrolyte, is different from the notation used in paper E.

The second scenario describes the current obtained when the bubbles are in the bulk, in this case, 11 three dimensional and 9 two dimensional simulations in which the bubbles are initialized with random sizes and location in the bulk are simulated. The predictions of the current density<sup>1</sup> is verified by comparing against the equivalent theoretical solution obtained using the correlation for effective conductivity proposed by Bruggeman [1935], see Table.1.2. The 3D simulations agrees reasonably well with the theoretical solution but two dimensional simulations, as expected, predicts a lower current density, see Fig.13.4.

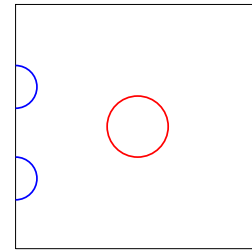


Figure 13.3: Illustration of the 2D cases, EC1 and EC2, considered to showcase the effect of electrode screening. EC1, represented by ●, considers a bubble of radius 1mm at the center of domain. EC2, represented by ◐, considers two equal sized bubbles (semicircles with radii equal to 1mm) whose centers are 2.5mm and 6.5mm away from the bottom wall.

Table 13.1: Reduction of current due to the presence of bubble on the electrode.

<sup>1</sup> Current density is calculated as the current at the boundary divided by the total area of the electrode surface.



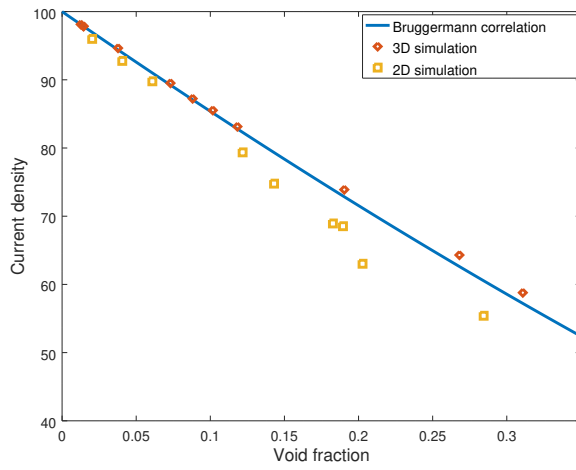


Figure 13.4: Comparison of the current density ( $A/m^2$ ) reduction with increase in void fraction of bubbles (in bulk) predicted by the simulations (for 2D and 3D) and Bruggemann's correlation.

## Chapter 14: Summary of paper F

### Numerical simulation of continuum scale electrochemical hydrogen bubble evolution

K.J. Vachaparambil & K.E. Einarsrud, Submitted to *Applied Mathematical Modelling*.

#### Objective

In paper E, the various modules relevant to developing a coupled multiphysics framework were presented and discussed. In this paper, these individual modules are integrated into a single framework to study the multiphysics nature of continuum scale electrochemical gas evolution.

#### Overview of the developed framework

This section provides an overview of the framework, based on some simplifications<sup>1</sup>, discussed in paper F.

The advection of the volume fraction of fluid ( $\alpha_1$ ), based on the interface compression approach, is solved as

$$\frac{\partial \alpha_1}{\partial t} + \nabla \cdot (\alpha_1 \vec{U}) + \nabla \cdot (\alpha_1 (1 - \alpha_1) \vec{U}_r) = \alpha_1 \nabla \cdot \vec{U}. \quad (14.1)$$

The term on the right hand side of Eq.14.1 is the source term associated with the bubble growth, see paper C. Once  $\alpha_1$  is computed, the volume fraction of bubble ( $\alpha_2$ ) is computed as  $\alpha_2 = 1 - \alpha_1$ .

The driving force for interfacial mass transfer is then computed based on the Fick's 1<sup>st</sup> law as

$$j = M_i D_{i,1} |\nabla C_i|, \quad (14.2)$$

where  $M_i$  is the molar mass of the dissolved hydrogen ( $i$ ) and  $D_{i,1}$  is the diffusion coefficient of the dissolved hydrogen in the electrolyte. Then the local mass transfer rate ( $\psi_0$ ) is computed at the liquid side of the interface based on Eq.11.3.  $\psi_0$  is then smeared using Eq.11.4

<sup>1</sup> The simplifications used in the proposed framework are

- Bubble evolution is assumed to occur only at the cathode whereas the anode is assumed to not effect the flow.
- Flow is isothermal and laminar.
- Density and viscosity of liquid and gas is constant.
- The interface is assumed to be always at saturation concentration which does not change as the bubble evolves.
- The changes in current, under constant potential difference, is a result of shielding the electrode and ohmic resistance of the bubbles. The effects of surface and concentration overpotentials are not treated.

to obtain  $\psi$ . The source for the continuity equation and sink term for the dissolved gas transport are computed as Eq.11.5 and Eq.11.6 respectively.

The continuity, Eq.11.7, and momentum, Eq.11.8, equations are solved together with PISO algorithm. The surface tension is treated using the Sharp Surface Force (SSF) model as implemented in papers A and B.

The change transport is computed based on Gauss's law as

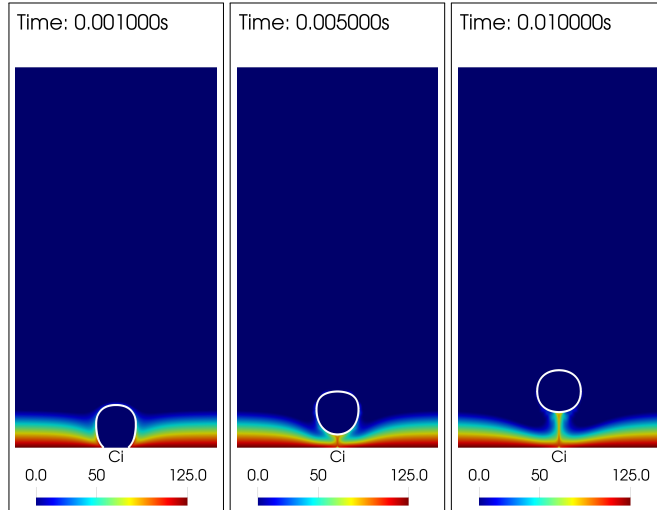
$$\nabla \cdot \vec{i} = 0 \quad (14.3)$$

where  $\vec{i}$ , the current density vector, is written in terms on Ohm's law as  $\vec{i} = -\Gamma \nabla \Phi$  and  $\Gamma$  is the arithmetic mean of the electrical conductivities of the phases. The transport of the dissolved hydrogen is then computed based on Eq.11.9.

The electrochemical reactions are accounted through boundary condition at the electrode via Faraday's law of electrolysis as  $\partial_n C_i = |\vec{i}| \alpha_1 / (nFD_{i,1})$ , where  $n$  is the number of electrons transferred for the electrochemical reaction to produce hydrogen (equal to 2),  $F$  is the Faraday's constant (equal to 96485 As/mol) and  $D_{i,1}$  is the diffusion coefficient of dissolved hydrogen in the liquid.

### Main results

Figure 14.1: The change in the dissolved gas concentration,  $C_i$ , ( $\text{mol}/\text{m}^3$ ) as a single 2D bubble evolves from the electrode with a contact angle equal to  $30^\circ$ . The white line represents the interface which is plotted at  $\alpha_1 = 0.5$ .



VERIFICATION of the proposed framework is based on bubble growth in a uniformly supersaturated solution predicted by Hashemi and

Abedi [2007], Scriven [1959] and qualitative analysis of the variation in current based on static bubble simulations.

SINGLE BUBBLE EVOLUTION from a horizontal electrode shows that when submillimeter sized bubbles are initialized on the surface, the difference between the initialized contact angle and the wetting condition at the electrode causes the detachment. As the bubble rises up the dissolved gas is also transported, see Fig.14.1. Due to the stronger hydrophilic nature of the electrode at smaller contact angles<sup>2</sup>, detachment time of the bubble in the case of contact angle equal to  $15^\circ$  is smaller than when it is  $30^\circ$ . As the bubble detaches and rises up, the surface of the bubble undergoes deformation, i.e. it flattens and then gets elongated, see Fig.14.2b-c. When the bubble is flatter, the projected area of the bubble on the electrode is larger which reduces the current<sup>3</sup>, see Fig.14.2. Larger rise velocity of the bubble, results in a more deformed bubble, as a result of the shape dictated by drag and surface tension, which reduces the current. Interestingly, although the growth of the bubble does not result in substantial changes to detachment time or rise velocity it effects the current but it is only noticeable when the bubble deformations are damped. Once the bubble has detached, the current is observed to decrease as the bubble rises up from the electrode due to the increase in the effective length experienced by the current path lines (until the bubble reaches half the distance between the electrodes).

<sup>2</sup> When the contact angle of  $45^\circ$  is used, although the bubble is deformed, it did not detach from the surface.

<sup>3</sup> The current at the electrode is computed as the dot product between the local current density and surface area vector of the individual mesh face at the boundary, i.e.  $I = \sum \vec{i} \cdot \vec{S}$ .

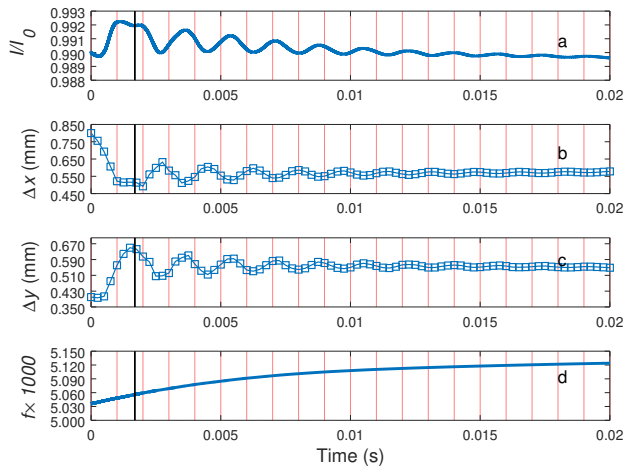
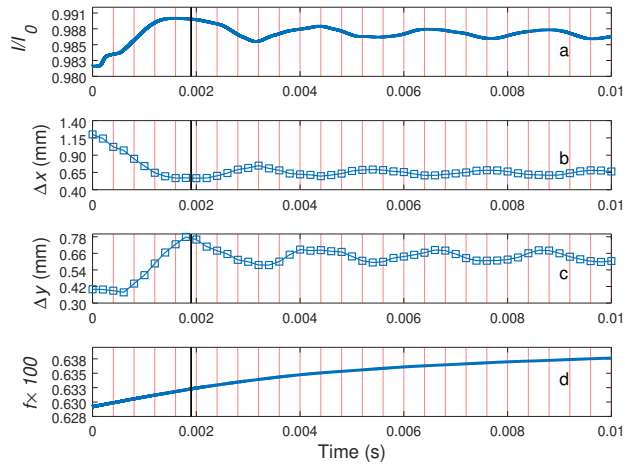


Figure 14.2: Comparison of the current normalized with current without any bubbles ( $I/I_0$ ), fraction of the volume of bubble with respect to the computational domain ( $f$ ), the bubble deformation in horizontal ( $\Delta x$ ) and vertical ( $\Delta y$ ) directions for a single 2D bubble evolving from an electrode with a contact angle of  $30^\circ$ . The vertical black line indicates the detachment of the bubble which in this case is around 1.69 ms. The red lines are equidistant at every 0.001 s to enable comparison between the plots.

COALESCENCE DRIVEN BUBBLE EVOLUTION considers the two bubbles which are equally and unequally sized as shown in Fig.14.4 and Fig.14.5 respectively. The simulations show that coalescence driven bubble evolution consists of three different regimes: necking, propagation of deformation waves, and detachment/deformation of the rising bubble which has also been observed experimentally in [Moreno Soto et al. \[2018\]](#), see Fig.14.4. The propagation of the deformation waves are symmetric during the coalescence of two equally sized bubbles but in the case of non-uniform bubble sizes these deformation waves are observed to travel towards the smaller bubble, see Fig.14.5. The propagation of the deformation wave causes the quicker detachment as well as the translation of the bubble along the electrode as observed in Fig.14.5. A large increase in the current is observed as a result of the bubble detachment due to coalescence, see Fig.14.3, when compared to single bubble detachment (where the effect of bubble deformation and its rising are significant), see Fig.14.2 and Fig.14.3. This large increase in current is a result of the larger decrease in the fraction of electrode covered by the bubble, see Fig.14.2b and Fig.14.3b. These simulations suggests coalescence as the primary mechanism of bubble detachment, at least for continuum scale bubbles, when compared to bubble growth due to interfacial mass transfer.

Figure 14.3: Comparison of the current normalized with current without any bubbles ( $I/I_0$ ), fraction of the volume of bubble with respect to the computational domain ( $f$ ), the bubble deformation in horizontal ( $\Delta x$ ) and vertical ( $\Delta y$ ) directions for coalescence driven bubble evolution of two unequally sized 2D bubbles from an electrode with a contact angle of  $45^\circ$ . The vertical black line indicates the detachment of the bubble whereas the red lines are equidistant at every 0.0004 s to enable comparison between the plots.



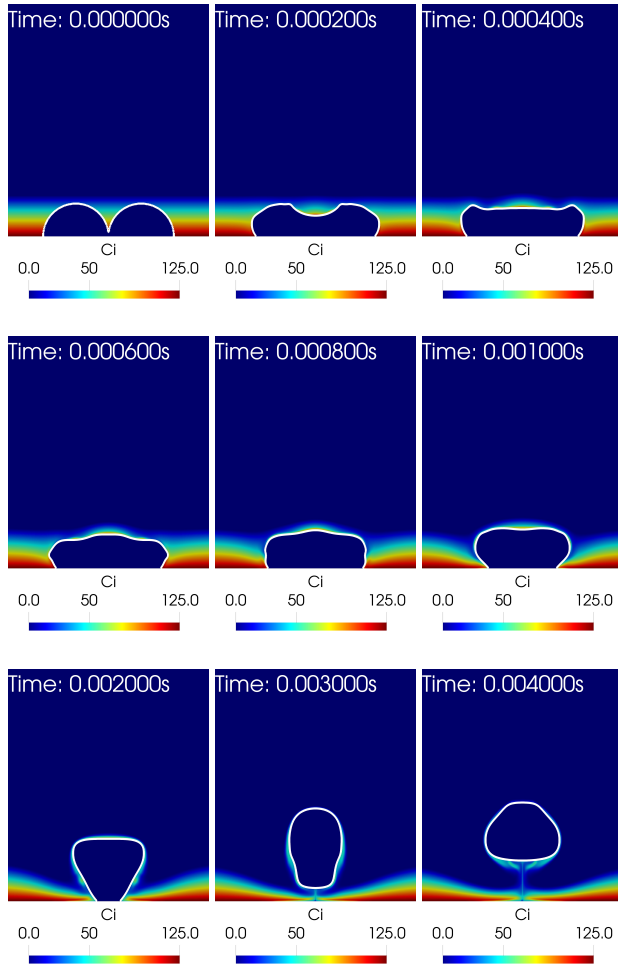
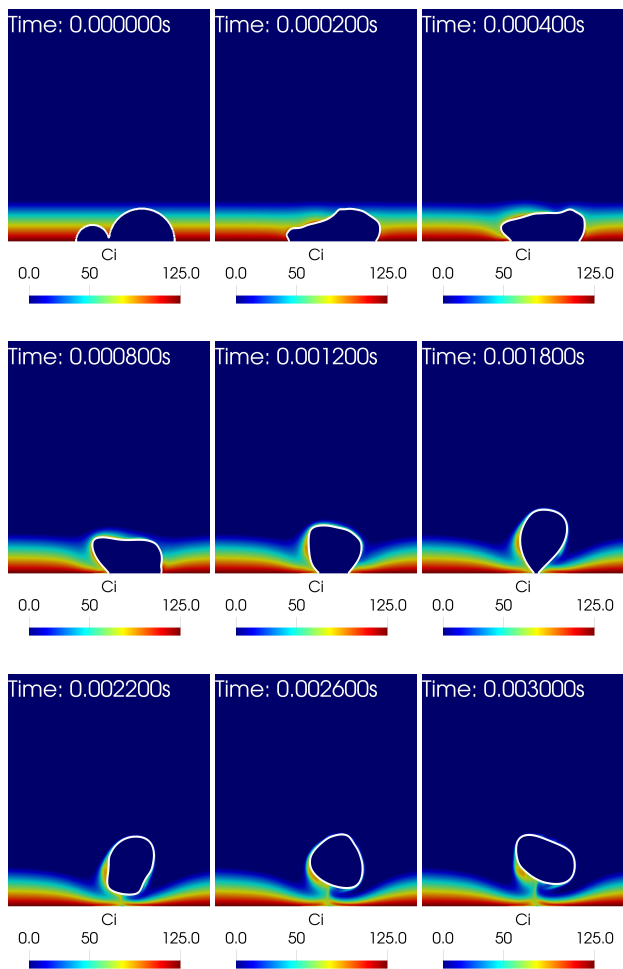


Figure 14.4: The evolution of the interface and the concentration of the dissolved gas,  $C_i$ , (mol/m<sup>3</sup>) as the bubble coalescence and evolves from two equally sized 2D bubbles for a contact angle of  $45^\circ$ . The necking process (between 0 s-0.4 ms), propagation of deformation waves along the bubble interface which leads to the lifting of the bubble (between 0.6 ms-2 ms) and detachment as well as the oscillations of the bubble surface leading to elongation and flattening (2 ms-4 ms). The interface is plotted at  $\alpha_1 = 0.5$ .

Figure 14.5: The evolution of the interface and the concentration of the dissolved gas,  $C_i$ , ( $\text{mol}/\text{m}^3$ ) as the bubble coalescence and evolves from two unequally sized 2D bubbles for a contact angle of  $45^\circ$ . Note the necking process (between 0 s-0.2 ms), propagation of deformation waves along the bubble interface which leads to the lifting of the bubble (between 0.4 ms-1.2 ms) and detachment as well as the oscillations of the bubble surface leading to elongation and flattening (1.8 ms-3 ms). The interface is plotted at  $\alpha_1 = 0.5$ .



## **Part V**

# **Summary and final thoughts**





## Chapter 15: Conclusions

The thesis delves into the development of a VOF based multiphysics framework to study the evolution of continuum scale electrochemical hydrogen bubbles. As understanding the physics of electrochemical gas evolution is crucial to building a new modelling framework, Part II summarizes the various fundamental aspects of how hydrogen evolution occurs during water electrolysis as well as the review of numerical methods available in literature to treat the various multiphysics modules. Part III of the thesis is a summary of the knowledge gained about the numerical method and its associated implementation in OpenFOAM® and interFoam source code. The idea of having this chapter is to share the knowledge about OpenFOAM® and interFoam to enable further development. Part IV discusses the modularized approach undertaken to develop the framework:

- **Surface tension modelling, spurious velocities and modelling sub-millimeter bubbles:** The Sharp Surface Force (SSF), proposed by [Raeini et al. \[2012\]](#), is implemented in interFoam. The implemented surface tension model is compared against out-of-the-box interFoam (which uses the Continuum Surface Force model by [Brackbill et al. \[1992\]](#)) and the commonly used the Smoothed CSF (as proposed by [Hoang et al. \[2013\]](#)). The results show that the SSF model reduces the spurious velocities by almost an order of magnitude and can reliably simulate two-dimensional capillary rise and rising bubble simulations. Tuning the user defined value of sharpening coefficient in SSF model, i.e.  $C_{sh} \leq 0.3$ , has been shown to lower spurious velocities enough to reliably simulate a 2D submillimeter bubble of diameter equal to 500  $\mu\text{m}$ .
- **Interfacial mass transfer and associated bubble growth:** This module focused on developing a novel framework to model the supersaturation driven bubble growth. This entailed implementing dissolved gas transport using C-CST model, proposed by [Maes and Soullaine \[2018\]](#); source/sink terms for governing equations for the

continuity and transport of dissolved gas equation, which is based on the approach developed by [Hardt and Wondra \[2008\]](#) and [Kunkelmann \[2011\]](#) and similarly a source term for the volume fraction advection equation (as shown in Eq.11.1); and finally the driving force which is simulated using either the universally valid Fick's 1<sup>st</sup> law or the flow specific *Sh* correlations. This framework is validated using 2D analytical models of bubble growth in supersaturated solutions. The driving force computed based on a *Sh* correlation, if available for a specific flow scenario, can reasonably simulate the process without having to resolve concentration gradients like in Fick's 1<sup>st</sup> law. The simulations showed that for processes like electrochemical gas evolution, which has complex flow fields associated with bubble growth and detachment which cannot be captured by a single *Sh* correlation, Fick's 1<sup>st</sup> law based approach provides a more realistic prediction.

- Framework for continuum scale electrochemical hydrogen evolution:** In this final module a coupled multiphysics framework based on Volume of Fluid method is developed. The multiphysics included are charge transport based on Gauss' law and Ohm's law, supersaturation driven bubble growth based on Fick's 1<sup>st</sup> law (developed in the previous task) and electrochemical reaction, which is treated via boundary condition, based on the Faraday's law of electrolysis. The developed framework when used to simulate continuum scale hydrogen bubble evolution showed that the detached bubble undergoes surface deformations which causes the current to fluctuate. The effect of growth of the bubble on the rise velocity and detachment time is negligible but the associated reduction in current is noticeable only when the bubble deformations has damped. Coalescence of bubbles occurs via three stages: necking, the propagation of deformation waves and the detachment as well as surface deformation of the rising bubble. The propagation of the deformation waves during coalescence influences the detachment process. The framework also predicts the increase in current due to bubble detachment. These simulations suggest that coalescence as a primary mechanism for bubble detachment, atleast at continuum scales which were of interest in this work, when compared to the interfacial mass transfer driven bubble growth.

## Chapter 16:

### *Topics for future research*

Although the framework developed in this thesis can simulate multi-physics aspect of the evolution of a continuum scale hydrogen bubble and the associated impact, this framework needs further advancements to be applied to an industrial scale water electrolyzer. Some of the avenues for further advances to the proposed framework are:

1. Although the framework developed in this thesis in principle is applicable for 3D simulations, further simulations are needed to confirm this.
2. Although Sharp Surface Force model generated less spurious velocities when compared to the Continuum Surface Force model, these numerical artifacts still influences interfacial mass transfer. Future works could implement a geometric VOF method<sup>1</sup> which uses an sub-cell interface reconstruction to reduce these spurious velocities.
3. As observed in paper F, the inconsistent contact angle of the initialized bubble and the wetting condition at the electrode results in inducing momentum which causes bubble detachment. In order to address this problem, it is important to consider the multiscale nature of the process where sub-micrometer bubbles, grow by interfacial mass transfer and coalescence to reach continuum length scales. In order to capture these range of length scales, interface resolved methods can be coupled to dispersed phase modelling approaches like done in works like [Einarsrud and Johansen \[2012\]](#), [Einarsrud et al. \[2017\]](#) and [Sun et al. \[2018\]](#).
4. The proposed framework considers only the ohmic and shielding effects of the bubble, further advancements can take into account the consequences of surface and concentration overpotentials which were discussed in Chapter 1 or refer to [Leistra and Sides \[1987\]](#).
5. As water electrolysis can be operated under both potentiostatic or galvanostatic conditions, the framework can be extended to gal-

<sup>1</sup> Please note that the latest version of OpenFOAM<sup>®</sup>, i.e. version 8, has released libraries to enable geometric VOF based interface capturing, see [Green-shields 2020](#).

vanostatic conditions to determine the effect of electrochemical gas evolution on the observed overpotential.

6. Additional developments could also treat Marangoni and natural convection which have been observed during electrochemical gas evolution, see [Yang et al. \[2018\]](#), [Babu and Das \[2019\]](#).
7. Further advances to the framework to enable its eventual use in optimizing industrial scale electrolyzers involve reducing the computational requirement like by the implicit treatment of the surface tension term in the solution algorithm, see [Chapter 8](#), to remove the time step constraint. Another potential end use to the multiscale-multiphysics framework is to develop correlation for mass transfer which can be used as closure models in the computationally cheaper dispersed phase modelling as well as the prediction of bubble size at detachment.
8. Last but not the least, in order to validate the numerical framework, its predictions must be compared to experiments. Some of the possible parameters which could be used for comparison are the bubble detachment radius and potential/current fluctuations associated with bubble evolution.

## Appendix A: Calculation of viscous terms

The velocity vector ( $\vec{U}$ ) can be written as

$$\vec{U} = \begin{pmatrix} u \\ v \\ w \end{pmatrix}.$$

The corresponding gradient of velocity  $\nabla\vec{U}$  can be computed as

$$\nabla\vec{U} = \begin{pmatrix} \frac{\partial u}{\partial x} & \frac{\partial u}{\partial y} & \frac{\partial u}{\partial z} \\ \frac{\partial v}{\partial x} & \frac{\partial v}{\partial y} & \frac{\partial v}{\partial z} \\ \frac{\partial w}{\partial x} & \frac{\partial w}{\partial y} & \frac{\partial w}{\partial z} \end{pmatrix},$$

see Lai et al. [2010], Kundu et al. [2016]. The transpose of  $\nabla\vec{U}$ , i.e.  $\nabla\vec{U}^T$ , is equal to

$$\nabla\vec{U}^T = \begin{pmatrix} \frac{\partial u}{\partial x} & \frac{\partial v}{\partial x} & \frac{\partial w}{\partial x} \\ \frac{\partial u}{\partial y} & \frac{\partial v}{\partial y} & \frac{\partial w}{\partial y} \\ \frac{\partial u}{\partial z} & \frac{\partial v}{\partial z} & \frac{\partial w}{\partial z} \end{pmatrix}.$$

The viscous stress, i.e.  $\nabla \cdot \mu(\nabla \vec{U} + \nabla \vec{U}^T)$ , can be calculated as

$$\begin{aligned} & \nabla \cdot \mu(\nabla \vec{U} + \nabla \vec{U}^T) \\ &= \begin{pmatrix} \frac{\partial}{\partial x} \\ \frac{\partial}{\partial y} \\ \frac{\partial}{\partial z} \end{pmatrix} \cdot \left[ \mu \begin{pmatrix} \frac{\partial u}{\partial x} & \frac{\partial u}{\partial y} & \frac{\partial u}{\partial z} \\ \frac{\partial v}{\partial x} & \frac{\partial v}{\partial y} & \frac{\partial v}{\partial z} \\ \frac{\partial w}{\partial x} & \frac{\partial w}{\partial y} & \frac{\partial w}{\partial z} \end{pmatrix} + \mu \begin{pmatrix} \frac{\partial u}{\partial x} & \frac{\partial v}{\partial x} & \frac{\partial w}{\partial x} \\ \frac{\partial u}{\partial y} & \frac{\partial v}{\partial y} & \frac{\partial w}{\partial y} \\ \frac{\partial u}{\partial z} & \frac{\partial v}{\partial z} & \frac{\partial w}{\partial z} \end{pmatrix} \right], \\ &= \begin{pmatrix} \frac{\partial}{\partial x} \\ \frac{\partial}{\partial y} \\ \frac{\partial}{\partial z} \end{pmatrix} \cdot \begin{pmatrix} \mu \left( \frac{\partial u}{\partial x} + \frac{\partial u}{\partial x} \right) & \mu \left( \frac{\partial v}{\partial x} + \frac{\partial u}{\partial y} \right) & \mu \left( \frac{\partial w}{\partial x} + \frac{\partial u}{\partial z} \right) \\ \mu \left( \frac{\partial u}{\partial y} + \frac{\partial v}{\partial x} \right) & \mu \left( \frac{\partial v}{\partial y} + \frac{\partial v}{\partial y} \right) & \mu \left( \frac{\partial w}{\partial y} + \frac{\partial v}{\partial z} \right) \\ \mu \left( \frac{\partial u}{\partial z} + \frac{\partial w}{\partial x} \right) & \mu \left( \frac{\partial v}{\partial z} + \frac{\partial w}{\partial y} \right) & \mu \left( \frac{\partial w}{\partial z} + \frac{\partial w}{\partial z} \right) \end{pmatrix}, \\ &= \begin{pmatrix} \frac{\partial}{\partial x} \left( \mu \left( \frac{\partial u}{\partial x} + \frac{\partial u}{\partial x} \right) \right) + \frac{\partial}{\partial y} \left( \mu \left( \frac{\partial v}{\partial x} + \frac{\partial u}{\partial y} \right) \right) + \frac{\partial}{\partial z} \left( \mu \left( \frac{\partial w}{\partial x} + \frac{\partial u}{\partial z} \right) \right) \\ \frac{\partial}{\partial x} \left( \mu \left( \frac{\partial u}{\partial y} + \frac{\partial v}{\partial x} \right) \right) + \frac{\partial}{\partial y} \left( \mu \left( \frac{\partial v}{\partial y} + \frac{\partial v}{\partial y} \right) \right) + \frac{\partial}{\partial z} \left( \mu \left( \frac{\partial w}{\partial y} + \frac{\partial v}{\partial z} \right) \right) \\ \frac{\partial}{\partial x} \left( \mu \left( \frac{\partial u}{\partial z} + \frac{\partial w}{\partial x} \right) \right) + \frac{\partial}{\partial y} \left( \mu \left( \frac{\partial v}{\partial z} + \frac{\partial w}{\partial y} \right) \right) + \frac{\partial}{\partial z} \left( \mu \left( \frac{\partial w}{\partial z} + \frac{\partial w}{\partial z} \right) \right) \end{pmatrix}. \end{aligned}$$

The matrix can expanded using chain rule and it can be rearranged as:

$$\begin{aligned} & \nabla \cdot \mu(\nabla \vec{U} + \nabla \vec{U}^T) = \\ & \begin{pmatrix} \frac{\partial \mu}{\partial x} \frac{\partial u}{\partial x} + \mu \frac{\partial^2 u}{\partial x^2} + \frac{\partial \mu}{\partial y} \frac{\partial u}{\partial y} + \mu \frac{\partial^2 u}{\partial y^2} + \frac{\partial \mu}{\partial z} \frac{\partial u}{\partial z} + \mu \frac{\partial^2 u}{\partial z^2} \\ \frac{\partial \mu}{\partial x} \frac{\partial v}{\partial x} + \mu \frac{\partial^2 v}{\partial x^2} + \frac{\partial \mu}{\partial y} \frac{\partial v}{\partial y} + \mu \frac{\partial^2 v}{\partial y^2} + \frac{\partial \mu}{\partial z} \frac{\partial v}{\partial z} + \mu \frac{\partial^2 v}{\partial z^2} \\ \frac{\partial \mu}{\partial x} \frac{\partial w}{\partial x} + \mu \frac{\partial^2 w}{\partial x^2} + \frac{\partial \mu}{\partial y} \frac{\partial w}{\partial y} + \mu \frac{\partial^2 w}{\partial y^2} + \frac{\partial \mu}{\partial z} \frac{\partial w}{\partial z} + \mu \frac{\partial^2 w}{\partial z^2} \end{pmatrix} \\ & + \begin{pmatrix} \frac{\partial \mu}{\partial x} \frac{\partial u}{\partial x} + \mu \frac{\partial^2 u}{\partial x^2} + \frac{\partial \mu}{\partial y} \frac{\partial v}{\partial x} + \mu \frac{\partial^2 v}{\partial x \partial y} + \frac{\partial \mu}{\partial z} \frac{\partial w}{\partial x} + \mu \frac{\partial^2 w}{\partial x \partial z} \\ \frac{\partial \mu}{\partial x} \frac{\partial u}{\partial y} + \mu \frac{\partial^2 u}{\partial x \partial y} + \frac{\partial \mu}{\partial y} \frac{\partial v}{\partial y} + \mu \frac{\partial^2 v}{\partial y^2} + \frac{\partial \mu}{\partial z} \frac{\partial w}{\partial y} + \mu \frac{\partial^2 w}{\partial y \partial z} \\ \frac{\partial \mu}{\partial x} \frac{\partial u}{\partial z} + \mu \frac{\partial^2 u}{\partial x \partial z} + \frac{\partial \mu}{\partial y} \frac{\partial v}{\partial z} + \mu \frac{\partial^2 v}{\partial y \partial z} + \frac{\partial \mu}{\partial z} \frac{\partial w}{\partial z} + \mu \frac{\partial^2 w}{\partial z^2} \end{pmatrix}. \end{aligned}$$

The above matrices can be further rearranged as

$$\begin{aligned} \nabla \cdot \mu (\nabla \vec{U} + \nabla \vec{U}^T) &= \begin{pmatrix} \frac{\partial}{\partial x} \left( \mu \frac{\partial u}{\partial x} \right) + \frac{\partial}{\partial y} \left( \mu \frac{\partial u}{\partial y} \right) + \frac{\partial}{\partial z} \left( \mu \frac{\partial u}{\partial z} \right) \\ \frac{\partial}{\partial x} \left( \mu \frac{\partial v}{\partial x} \right) + \frac{\partial}{\partial y} \left( \mu \frac{\partial v}{\partial y} \right) + \frac{\partial}{\partial z} \left( \mu \frac{\partial v}{\partial z} \right) \\ \frac{\partial}{\partial x} \left( \mu \frac{\partial w}{\partial x} \right) + \frac{\partial}{\partial y} \left( \mu \frac{\partial w}{\partial y} \right) + \frac{\partial}{\partial z} \left( \mu \frac{\partial w}{\partial z} \right) \end{pmatrix} \\ &+ \begin{pmatrix} \frac{\partial \mu}{\partial x} \frac{\partial u}{\partial x} + \frac{\partial \mu}{\partial y} \frac{\partial v}{\partial x} + \frac{\partial \mu}{\partial z} \frac{\partial w}{\partial x} \\ \frac{\partial \mu}{\partial x} \frac{\partial u}{\partial y} + \frac{\partial \mu}{\partial y} \frac{\partial v}{\partial y} + \frac{\partial \mu}{\partial z} \frac{\partial w}{\partial y} \\ \frac{\partial \mu}{\partial x} \frac{\partial u}{\partial z} + \frac{\partial \mu}{\partial y} \frac{\partial v}{\partial z} + \frac{\partial \mu}{\partial z} \frac{\partial w}{\partial z} \end{pmatrix} + \begin{pmatrix} \mu \frac{\partial^2 u}{\partial x^2} + \mu \frac{\partial^2 v}{\partial x \partial y} + \mu \frac{\partial^2 w}{\partial x \partial z} \\ \mu \frac{\partial^2 u}{\partial x \partial y} + \mu \frac{\partial^2 v}{\partial y^2} + \mu \frac{\partial^2 w}{\partial y \partial z} \\ \mu \frac{\partial^2 u}{\partial x \partial z} + \mu \frac{\partial^2 v}{\partial y \partial z} + \mu \frac{\partial^2 w}{\partial z^2} \end{pmatrix}, \end{aligned}$$

which can be written as

$$\begin{aligned} \nabla \cdot \mu (\nabla \vec{U} + \nabla \vec{U}^T) &= \begin{pmatrix} \frac{\partial}{\partial x} \left( \mu \frac{\partial u}{\partial x} \right) + \frac{\partial}{\partial y} \left( \mu \frac{\partial u}{\partial y} \right) + \frac{\partial}{\partial z} \left( \mu \frac{\partial u}{\partial z} \right) \\ \frac{\partial}{\partial x} \left( \mu \frac{\partial v}{\partial x} \right) + \frac{\partial}{\partial y} \left( \mu \frac{\partial v}{\partial y} \right) + \frac{\partial}{\partial z} \left( \mu \frac{\partial v}{\partial z} \right) \\ \frac{\partial}{\partial x} \left( \mu \frac{\partial w}{\partial x} \right) + \frac{\partial}{\partial y} \left( \mu \frac{\partial w}{\partial y} \right) + \frac{\partial}{\partial z} \left( \mu \frac{\partial w}{\partial z} \right) \end{pmatrix} \\ &+ \begin{pmatrix} \frac{\partial \mu}{\partial x} \frac{\partial u}{\partial x} + \frac{\partial \mu}{\partial y} \frac{\partial v}{\partial x} + \frac{\partial \mu}{\partial z} \frac{\partial w}{\partial x} \\ \frac{\partial \mu}{\partial x} \frac{\partial u}{\partial y} + \frac{\partial \mu}{\partial y} \frac{\partial v}{\partial y} + \frac{\partial \mu}{\partial z} \frac{\partial w}{\partial y} \\ \frac{\partial \mu}{\partial x} \frac{\partial u}{\partial z} + \frac{\partial \mu}{\partial y} \frac{\partial v}{\partial z} + \frac{\partial \mu}{\partial z} \frac{\partial w}{\partial z} \end{pmatrix} + \begin{pmatrix} \mu \frac{\partial}{\partial x} \left( \frac{\partial u}{\partial x} + \frac{\partial v}{\partial y} + \frac{\partial w}{\partial z} \right) \\ \mu \frac{\partial}{\partial y} \left( \frac{\partial u}{\partial x} + \frac{\partial v}{\partial y} + \frac{\partial w}{\partial z} \right) \\ \mu \frac{\partial}{\partial z} \left( \frac{\partial u}{\partial x} + \frac{\partial v}{\partial y} + \frac{\partial w}{\partial z} \right) \end{pmatrix}. \end{aligned}$$

Using the conservation of mass for incompressible fluids, i.e.  $\nabla \cdot \vec{U} = 0$ , the last matrix reduces to zero and the remaining matrices can be written as

$$\nabla \cdot \mu (\nabla \vec{U} + \nabla \vec{U}^T) = \nabla \cdot (\mu \nabla \vec{U}) + \nabla \vec{U} \cdot \nabla \mu.$$





## Appendix B: Calculation of source term for volume fraction advection

The  $\alpha_1$  advection can be obtained from continuity equation:

$$\begin{aligned} \nabla \cdot \vec{U} &= \frac{\dot{m}}{\rho}, \\ \frac{\partial}{\partial t}(\alpha_1 + \alpha_2) + \nabla \cdot (\alpha_1 \vec{U} + \alpha_2 \vec{U}) &= \frac{\dot{m}}{\rho}(\alpha_1 + \alpha_2). \end{aligned} \quad (16.1)$$

The advection of liquid volume fraction is

$$\frac{\partial \alpha_1}{\partial t} + \nabla \cdot (\alpha_1 \vec{U}) = \frac{\dot{m}}{\rho} \alpha_1, \quad (16.2)$$

which can be rewritten based on interface compression as

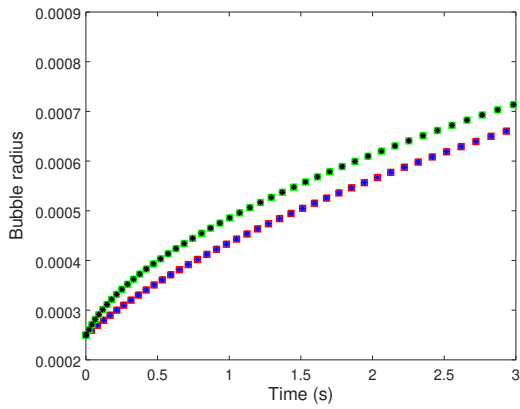
$$\frac{\partial \alpha_1}{\partial t} + \nabla \cdot (\alpha_1 \vec{U}) + \nabla \cdot (\alpha_1(1 - \alpha_1) \vec{U}_r) = \frac{\dot{m}}{\rho} \alpha_1, \quad (16.3)$$

where the term on the right hand side of the equation is the source term associated with the bubble growth. Based on the continuity equation, the above equation can be written as

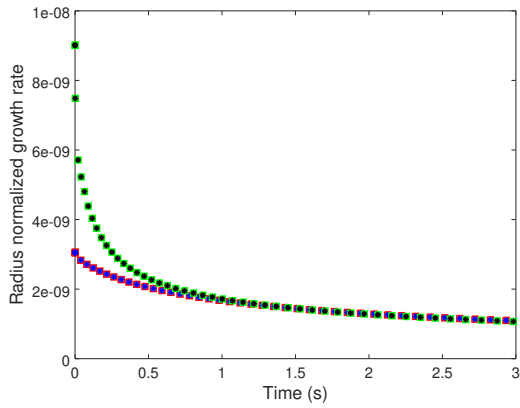
$$\frac{\partial \alpha_1}{\partial t} + \nabla \cdot (\alpha_1 \vec{U}) + \nabla \cdot (\alpha_1(1 - \alpha_1) \vec{U}_r) = \alpha_1 \nabla \cdot \vec{U}, \quad (16.4)$$

which is formulation used in the proposed framework.

In order to investigate the effect of computing  $\alpha_1$  based on Eq.16.3 and Eq.16.4, the bubble growth from a pre-existing bubble in the bulk of a uniformly supersaturated ( $C_i$  is equal to 200.64 mol/m<sup>3</sup> at  $t = 0$ s), analogous to the case discussed in paper C, is simulated based on driving force computed based on  $Sh$  correlation, Eq.12.6, and Fick's 1<sup>st</sup> law, Eq.6.15. The result shows that the temporal evolution of bubble radius and growth rate predicted based on Eq.16.3 and Eq.16.4 using  $Sh$  correlation and Fick's 1<sup>st</sup> law based driving forces are nearly identical as seen in Fig.16.1.



(a) Evolution of bubble radius (m).



(b) Evolution of bubble radius normalized growth rate ( $\text{kgm}^{-1}\text{s}^{-1}$ ).

Figure 16.1: Comparing of the temporal change in bubble size and growth rate normalized by bubble radius predicted based on the source term used in  $\alpha_1$  advection equation using driving force computed based on  $Sh$  correlation in Eq.12.6 ( $\alpha_1 \nabla \cdot \vec{U}$  ( $\square$ ) and  $\alpha_1 \dot{m}/\rho$  ( $*$ )) Fick's 1<sup>st</sup> law in Eq.6.15 ( $\alpha_1 \nabla \cdot \vec{U}$  ( $\square$ ) and  $\alpha_1 \dot{m}/\rho$  ( $*$ )). Please note that these are 2D simulations and the points in the plots correspond to the bubble radius and growth rate at every 40 time steps taken by the solver.

## *Appendix C: Computational resources*

The simulations discussed in this thesis were mainly run on two High Performance Computing (HPC) systems:

- Idun, which is a computing platform for NTNU, see [NTNU HPC Group n.d.](#) for more information,
- Fram, which is a cluster that belongs to the Norwegian national e-infrastructure (provided by UNINETT Sigma2), see [Uninett Sigma2 n.d.](#) for more information.

In order to provide an overview of the computational cost associated with running interface resolved multiphysics simulations discussed in this thesis, resources and CPU time used for two illustrative cases are described below.

- Supersaturation driven bubble growth, described in paper D which considered a domain of  $3\text{ cm} \times 3\text{ cm}$  and meshed by  $4000 \times 4000$  cells (corresponding to a mesh resolution of  $7.5 \times 10^{-6}\text{ m}$ ), was run on  $5 \times 32$  cores (on Fram). The simulation case with supersaturation of seven took 20 hours whereas case with supersaturation equal to 2.5 took around 5 hours to complete. It should be noted that the choice of the iterative solver used to obtain  $\psi$  (by smearing  $\psi_0$  based on Eq. 11.4) has been observed to substantially influence the simulation time, see appendix b of appended paper D for further discussion.
- Electrochemical evolution of hydrogen bubble, described in paper F which considered a domain of  $10\text{ mm} \times 5\text{ mm}$  which was meshed by  $1600 \times 800$  cells (corresponding to a mesh resolution of  $6.25 \times 10^{-6}\text{ m}$ ), was run on  $5 \times 32$  cores (on Fram) and took about 12 hours to complete.



## Bibliography

- E. Adam, J. Venczel, and E. Schalch. Stofftransport bei der elektrolyse mit gasrührung. *Chemie Ingenieur Technik*, 43(4):202–215, 1971. DOI: 10.1002/cite.330430418.
- A. Albadawi, D. Donoghue, A. Robinson, D. Murray, and Y. De-lauré. On the analysis of bubble growth and detachment at low capillary and bond numbers using volume of fluid and level set methods. *Chemical Engineering Science*, 90:77 – 91, 2013. DOI: <https://doi.org/10.1016/j.ces.2012.12.004>.
- A. Alexiadis, M. P. Dudukovic, P. Ramachandran, A. Cornell, J. Wanggård, and A. Bokkers. Transition to pseudo-turbulence in a narrow gas-evolving channel. *Theoretical and Computational Fluid Dynamics*, 26(6):551–564, Dec 2012. DOI: 10.1007/s00162-011-0248-4.
- S. O. Amrouche, D. Rekioua, T. Rekioua, and S. Bacha. Overview of energy storage in renewable energy systems. *International Journal of Hydrogen Energy*, 41(45):20914 – 20927, 2016. DOI: <https://doi.org/10.1016/j.ijhydene.2016.06.243>.
- S. Anantharaj, S. R. Ede, K. Karthick, S. Sam Sankar, K. Sangeetha, P. E. Karthik, and S. Kundu. Precision and correctness in the evaluation of electrocatalytic water splitting: revisiting activity parameters with a critical assessment. *Energy & Environmental Science*, 11:744–771, 2018. DOI: 10.1039/C7EE03457A.
- A. Angulo, P. van der Linde, H. Gardeniers, M. Modestino, and D. F. Rivas. Influence of bubbles on the energy conversion efficiency of electrochemical reactors. *Joule*, 4(3):555 – 579, 2020. DOI: <https://doi.org/10.1016/j.joule.2020.01.005>.
- ANSYS Inc. *ANSYS Fluent - CFD Software*, 2020. URL <http://www.ansys.com/products/fluids/ansys-fluent>.
- P. Attard. Pinning down the reasons for the size, shape, and stability of nanobubbles. *Langmuir*, 32(43):11138–11146, 2016. DOI: 10.1021/acs.langmuir.6b01563.

- R. Babu and M. K. Das. Experimental studies of natural convective mass transfer in a water-splitting system. *International Journal of Hydrogen Energy*, 44(29):14467 – 14480, 2019. DOI: <https://doi.org/10.1016/j.ijhydene.2019.04.043>.
- D. Baczyzmański, F. Karnbach, G. Mutschke, X. Yang, K. Eckert, M. Uhlemann, and C. Cierpka. Growth and detachment of single hydrogen bubbles in a magnetohydrodynamic shear flow. *Physical Review Fluids*, 2:093701, Sep 2017. DOI: 10.1103/PhysRevFluids.2.093701.
- A. Bashkatov, S. S. Hossain, X. Yang, G. Mutschke, and K. Eckert. Oscillating hydrogen bubbles at Pt microelectrodes. *Physical Review Letters*, 123:214503, 2019. DOI: 10.1103/PhysRevLett.123.214503.
- A. Battistella, S. S. C. Aelen, I. Roghair, and M. Van Sint Annaland. Euler–Lagrange modeling of bubbles formation in supersaturated water. *ChemEngineering*, 2(3), 2018. DOI: 10.3390/chemengineering2030039.
- A. Bejan and A. Kraus. *Heat Transfer Handbook*. Number v. 1 in Heat Transfer Handbook. Wiley, 2003. URL [https://books.google.no/books?id=d4cgNG\\_IUq8C](https://books.google.no/books?id=d4cgNG_IUq8C).
- E. Berberović, N. P. van Hinsberg, S. Jakirlić, I. V. Roisman, and C. Tropea. Drop impact onto a liquid layer of finite thickness: Dynamics of the cavity evolution. *Physical Review E*, 79:036306, Mar 2009. DOI: 10.1103/PhysRevE.79.036306.
- R. Bird, W. Stewart, and E. Lightfoot. *Transport Phenomena*. Wiley International edition. Wiley, 2006. URL <https://books.google.no/books?id=L5FnNlIaGfcC>.
- J. Brackbill, D. Kothe, and C. Zemach. A continuum method for modeling surface tension. *Journal of Computational Physics*, 100(2):335 – 354, 1992. DOI: [https://doi.org/10.1016/0021-9991\(92\)90240-Y](https://doi.org/10.1016/0021-9991(92)90240-Y).
- D. A. G. Bruggeman. Berechnung verschiedener physikalischer konstanten von heterogenen substanzen. i. dielektrizitätskonstanten und leitfähigkeiten der mischkörper aus isotropen substanzen. *Annalen der Physik*, 416(7):636–664, 1935. DOI: 10.1002/andp.19354160705.
- C. Brussieux, P. Viers, H. Roustan, and M. Rakib. Controlled electrochemical gas bubble release from electrodes entirely and partially covered with hydrophobic materials. *Electrochimica Acta*, 56(20):7194 – 7201, 2011. DOI: <https://doi.org/10.1016/j.electacta.2011.04.104>.

- J. W. Bullard and E. J. Garboczi. Capillary rise between planar surfaces. *Physical Review E*, 79:011604, Jan 2009. DOI: 10.1103/PhysRevE.79.011604.
- O. S. Burheim. Chapter 6 - electrochemical energy storage. In O. S. Burheim, editor, *Engineering Energy Storage*, pages 75 – 110. Academic Press, 2017. DOI: <https://doi.org/10.1016/B978-0-12-814100-7.00006-7>.
- J. Burman and G. Jameson. Diffusional mass transfer to a growing bubble. *Chemical Engineering Science*, 31(5):401 – 403, 1976. DOI: [https://doi.org/10.1016/0009-2509\(76\)80011-5](https://doi.org/10.1016/0009-2509(76)80011-5).
- L. F. Catañeda, F. F. Rivera, T. Pérez, and J. L. Nava. Mathematical modeling and simulation of the reaction environment in electrochemical reactors. *Current Opinion in Electrochemistry*, 16:75 – 82, 2019. DOI: <https://doi.org/10.1016/j.coelec.2019.04.025>.
- A. Cheminet, J.-F. Krawczynski, and P. Druault. Particle image reconstruction for particle detection in particle tracking velocimetry. *Measurement Science and Technology*, 29(12):125202, nov 2018. DOI: 10.1088/1361-6501/aae9c2.
- Q. Chen and L. Luo. Correlation between gas bubble formation and hydrogen evolution reaction kinetics at nanoelectrodes. *Langmuir*, 34(15):4554–4559, 2018. DOI: 10.1021/acs.langmuir.8b00435.
- G. Chisholm and L. Cronin. Chapter 16 - hydrogen from water electrolysis. In T. M. Letcher, editor, *Storing Energy*, pages 315 – 343. Elsevier, Oxford, 2016. DOI: <https://doi.org/10.1016/B978-0-12-803440-8.00016-6>.
- C. Cierpka, B. Lütke, and C. J. Kähler. Higher order multi-frame particle tracking velocimetry. *Experiments in Fluids*, 54:1533, 2013. DOI: <https://doi.org/10.1007/s00348-013-1533-3>.
- P. Cifani, W. Michalek, G. Priems, J. Kuerten, C. van der Geld, and B. Geurts. A comparison between the surface compression method and an interface reconstruction method for the vof approach. *Computers & Fluids*, 136:421 – 435, 2016. DOI: <https://doi.org/10.1016/j.compfluid.2016.06.026>.
- C. Coutanceau, S. Baranton, and T. Audichon. Chapter 3 - hydrogen production from water electrolysis. In C. Coutanceau, S. Baranton, and T. Audichon, editors, *Hydrogen Electrochemical Production, Hydrogen Energy and Fuel Cells Primers*, pages 17 – 62. Academic Press, 2018. DOI: <https://doi.org/10.1016/B978-0-12-811250-2.00003-0>.



- A. A. Dahlkild. Modelling the two-phase flow and current distribution along a vertical gas-evolving electrode. *Journal of Fluid Mechanics*, 428:249–272, 2001. DOI: 10.1017/S002211200002639.
- G. B. Darband, M. Aliofkhaezai, and S. Shanmugam. Recent advances in methods and technologies for enhancing bubble detachment during electrochemical water splitting. *Renewable and Sustainable Energy Reviews*, 114:109300, 2019. DOI: <https://doi.org/10.1016/j.rser.2019.109300>.
- R. de Levie. The electrolysis of water. *Journal of Electroanalytical Chemistry*, 476(1):92 – 93, 1999. DOI: [https://doi.org/10.1016/S0022-0728\(99\)00365-4](https://doi.org/10.1016/S0022-0728(99)00365-4).
- N. Deen, T. Solberg, and B. Hjertager. Large eddy simulation of the gas-liquid flow in a square cross-sectioned bubble column. *Chemical Engineering Science*, 56(21):6341 – 6349, 2001. DOI: [https://doi.org/10.1016/S0009-2509\(01\)00249-4](https://doi.org/10.1016/S0009-2509(01)00249-4).
- D. Deising, H. Marschall, and D. Bothe. A unified single-field model framework for volume-of-fluid simulations of interfacial species transfer applied to bubbly flows. *Chemical Engineering Science*, 139: 173 – 195, 2016. DOI: <https://doi.org/10.1016/j.ces.2015.06.021>.
- D. Deising, D. Bothe, and H. Marschall. Direct numerical simulation of mass transfer in bubbly flows. *Computers & Fluids*, 172:524 – 537, 2018. DOI: <https://doi.org/10.1016/j.compfluid.2018.03.041>.
- S. S. Deshpande, L. Anumolu, and M. F. Trujillo. Evaluating the performance of the two-phase flow solver interFoam. *Computational Science & Discovery*, 5(1):014016, nov 2012a. DOI: 10.1088/1749-4699/5/1/014016.
- S. S. Deshpande, M. F. Trujillo, X. Wu, and G. Chahine. Computational and experimental characterization of a liquid jet plunging into a quiescent pool at shallow inclination. *International Journal of Heat and Fluid Flow*, 34:1 – 14, 2012b. DOI: <https://doi.org/10.1016/j.ijheatfluidflow.2012.01.011>.
- D. A. Drew and S. L. Passman. *Averaged Equations*, pages 121–130. Springer New York, New York, NY, 1999. DOI: 10.1007/0-387-22637-0\_12.
- J. Dukovic and C. W. Tobias. The influence of attached bubbles on potential drop and current distribution at gas-evolving electrodes. *Journal of The Electrochemical Society*, 134(2):331–343, 1987. DOI: 10.1149/1.2100456.

- R. G. Ehl and A. J. Ihde. Faraday's electrochemical laws and the determination of equivalent weights. *Journal of Chemical Education*, 31(5): 226, 1954. DOI: 10.1021/ed031p226.
- K. E. Einarsrud and S. T. Johansen. Modelling of bubble behaviour in aluminium reduction cells. *Progress in Computational Fluid Dynamics, an International Journal*, 12(2-3):119–130, 2012. DOI: 10.1504/PCFD.2012.047455.
- K. E. Einarsrud, I. Eick, W. Bai, Y. Feng, J. Hua, and P. J. Witt. Towards a coupled multi-scale, multi-physics simulation framework for aluminium electrolysis. *Applied Mathematical Modelling*, 44:3 – 24, 2017. DOI: <https://doi.org/10.1016/j.apm.2016.11.011>.
- P. S. Epstein and M. S. Plesset. On the stability of gas bubbles in liquid-gas solutions. *The Journal of Chemical Physics*, 18(11):1505–1509, 1950. DOI: 10.1063/1.1747520.
- European Commission. A hydrogen strategy for a climate-neutral Europe, 2020. URL [https://ec.europa.eu/energy/sites/ener/files/hydrogen\\_strategy.pdf](https://ec.europa.eu/energy/sites/ener/files/hydrogen_strategy.pdf). Online; accessed 13 July 2020.
- M. Falcone and H. Marschall. Explicit radial-basis-function-based finite-difference method for interfacial mass-transfer problems. *Chemical Engineering & Technology*, 40(8):1385–1390, 2017. DOI: 10.1002/ceat.201600536.
- D. Fernández, P. Maurer, M. Martine, J. M. D. Coey, and M. E. Möbius. Bubble formation at a gas-evolving microelectrode. *Langmuir*, 30(43): 13065–13074, 2014. DOI: 10.1021/la500234r.
- B. Figueroa-Espinoza and D. Legendre. Mass or heat transfer from spheroidal gas bubbles rising through a stationary liquid. *Chemical Engineering Science*, 65(23):6296 – 6309, 2010. DOI: <https://doi.org/10.1016/j.ces.2010.09.018>.
- Flow Science Inc. *FLOW-3D, Version 12.0*. Santa Fe, NM, 2019. URL <https://www.flow3d.com/>.
- X. Fu and M. Ishii. Two-group interfacial area transport in vertical air–water flow: I. mechanistic model. *Nuclear Engineering and Design*, 219(2):143 – 168, 2003. DOI: [https://doi.org/10.1016/S0029-5493\(02\)00285-6](https://doi.org/10.1016/S0029-5493(02)00285-6).
- C. Galusinski and P. Vignaux. On stability condition for bifluid flows with surface tension: Application to microfluidics. *Journal of Computational Physics*, 227(12):6140 – 6164, 2008. DOI: <https://doi.org/10.1016/j.jcp.2008.02.023>.

- J. Garcia-Navarro, M. Schulze, and K. Friedrich. Detecting and modeling oxygen bubble evolution and detachment in proton exchange membrane water electrolyzers. *International Journal of Hydrogen Energy*, 44(50):27190 – 27203, 2019. DOI: <https://doi.org/10.1016/j.ijhydene.2019.08.253>.
- J. E. Gentle. *Solution of Linear Systems*, pages 87–121. Springer New York, New York, NY, 1998. DOI: 10.1007/978-1-4612-0623-1\_3.
- A. Georgoulas, M. Andredaki, and M. Marengo. An enhanced vof method coupled with heat transfer and phase change to characterise bubble detachment in saturated pool boiling. *Energies*, 10(3), 2017. DOI: 10.3390/en10030272.
- D. Gerlach, G. Tomar, G. Biswas, and F. Durst. Comparison of volume-of-fluid methods for surface tension-dominant two-phase flows. *International Journal of Heat and Mass Transfer*, 49(3):740 – 754, 2006. DOI: <https://doi.org/10.1016/j.ijheatmasstransfer.2005.07.045>.
- J. Glas and J. Westwater. Measurements of the growth of electrolytic bubbles. *International Journal of Heat and Mass Transfer*, 7(12):1427 – 1443, 1964. DOI: [https://doi.org/10.1016/0017-9310\(64\)90130-9](https://doi.org/10.1016/0017-9310(64)90130-9).
- S. Gong and P. Cheng. Lattice boltzmann simulation of periodic bubble nucleation, growth and departure from a heated surface in pool boiling. *International Journal of Heat and Mass Transfer*, 64:122 – 132, 2013. DOI: <https://doi.org/10.1016/j.ijheatmasstransfer.2013.03.058>.
- M. Graveleau, C. Soulaire, and H. A. Tchelepi. Pore-scale simulation of interphase multicomponent mass transfer for subsurface flow. *Transport in Porous Media*, 120(2):287–308, Nov 2017. DOI: 10.1007/s11242-017-0921-1.
- C. Greenshields. Interface capturing in openfoam, 2020. URL <https://cfd.direct/openfoam/free-software/multiphase-interface-capturing/>. Online; accessed 25 July 2020.
- C. J. Greenshields. OpenFOAM 2.3.0: Multiphase Modelling : Predictor-Corrector Semi-Implicit MULES, 2014. URL <https://openfoam.org/release/2-3-0/multiphase/>. Online; accessed 13 July 2020.
- C. J. Greenshields. OpenFOAM User Guide version 7, 2019. URL <http://foam.sourceforge.net/docs/Guides-a4/OpenFOAMUserGuide-A4.pdf>. Online; accessed 13 July 2020.

- R. Griffith. Mass transfer from drops and bubbles. *Chemical Engineering Science*, 12(3):198 – 213, 1960. DOI: [https://doi.org/10.1016/0009-2509\(60\)85006-3](https://doi.org/10.1016/0009-2509(60)85006-3).
- Z. Guo, D. F. Fletcher, and B. S. Haynes. Implementation of a height function method to alleviate spurious currents in cfd modelling of annular flow in microchannels. *Applied Mathematical Modelling*, 39(16):4665 – 4686, 2015. DOI: <https://doi.org/10.1016/j.apm.2015.04.022>.
- R. Hao, Y. Fan, M. D. Howard, J. C. Vaughan, and B. Zhang. Imaging nanobubble nucleation and hydrogen spillover during electrocatalytic water splitting. *Proceedings of the National Academy of Sciences*, 115(23):5878–5883, 2018. DOI: [10.1073/pnas.1800945115](https://doi.org/10.1073/pnas.1800945115).
- S. Hardt and F. Wondra. Evaporation model for interfacial flows based on a continuum-field representation of the source terms. *Journal of Computational Physics*, 227(11):5871 – 5895, 2008. DOI: <https://doi.org/10.1016/j.jcp.2008.02.020>.
- Y. Haroun, D. Legendre, and L. Raynal. Volume of fluid method for interfacial reactive mass transfer: Application to stable liquid film. *Chemical Engineering Science*, 65(10):2896 – 2909, 2010. DOI: <https://doi.org/10.1016/j.ces.2010.01.012>.
- S. J. Hashemi and J. Abedi. Advances in modeling of new phase growth. *Energy & Fuels*, 21(4):2147–2155, 2007. DOI: [10.1021/ef060643l](https://doi.org/10.1021/ef060643l).
- W. Haynes. *CRC Handbook of Chemistry and Physics*. CRC Handbook of Chemistry and Physics. CRC Press, 2011. URL <https://books.google.no/books?id=pYPRBQAAQBAJ>.
- X. He and N. Li. Lattice boltzmann simulation of electrochemical systems. *Computer Physics Communications*, 129(1):158 – 166, 2000. DOI: [https://doi.org/10.1016/S0010-4655\(00\)00103-X](https://doi.org/10.1016/S0010-4655(00)00103-X).
- E. A. Hemmingsen. Spontaneous formation of bubbles in gas-supersaturated water. *Nature*, 267(5607):141–142, 1977. DOI: [10.1038/267141a0](https://doi.org/10.1038/267141a0).
- W. Henry and J. Banks. Iii. experiments on the quantity of gases absorbed by water, at different temperatures, and under different pressures. *Philosophical Transactions of the Royal Society of London*, 93:29–274, 1803. DOI: [10.1098/rstl.1803.0004](https://doi.org/10.1098/rstl.1803.0004).
- C. Hirt and B. Nichols. Volume of fluid (vof) method for the dynamics of free boundaries. *Journal of Computational Physics*, 39(1):201 – 225, 1981. DOI: [https://doi.org/10.1016/0021-9991\(81\)90145-5](https://doi.org/10.1016/0021-9991(81)90145-5).

- D. A. Hoang, V. van Steijn, L. M. Portela, M. T. Kreutzer, and C. R. Kleijn. Benchmark numerical simulations of segmented two-phase flows in microchannels using the volume of fluid method. *Computers & Fluids*, 86:28–36, 2013. DOI: <https://doi.org/10.1016/j.compfluid.2013.06.024>.
- F. Hofbauer and I. Frank. Electrolysis of water in the diffusion layer: First-principles molecular dynamics simulation. *Chemistry – A European Journal*, 18(1):277–282, 2012. DOI: 10.1002/chem.201002094.
- T. Holzmann. *Mathematics, Numerics, Derivations and OpenFOAM®*. Holzmann CFD, 2017. URL [www.holzmann-cfd.de](http://www.holzmann-cfd.de).
- R. Hreiz, L. Abdelouahed, D. Fünfschilling, and F. Lopicque. Electrogenerated bubbles induced convection in narrow vertical cells: Piv measurements and euler–lagrange cfd simulation. *Chemical Engineering Science*, 134:138 – 152, 2015a. DOI: <https://doi.org/10.1016/j.ces.2015.04.041>.
- R. Hreiz, L. Abdelouahed, D. Fünfschilling, and F. Lopicque. Electrogenerated bubbles induced convection in narrow vertical cells: A review. *Chemical Engineering Research and Design*, 100:268 – 281, 2015b. DOI: <https://doi.org/10.1016/j.cherd.2015.05.035>.
- C. Hu, L. Zhang, and J. Gong. Recent progress made in the mechanism comprehension and design of electrocatalysts for alkaline water splitting. *Energy & Environmental Science*, 12:2620–2645, 2019. DOI: 10.1039/C9EE01202H.
- S. Hysing. A new implicit surface tension implementation for interfacial flows. *International Journal for Numerical Methods in Fluids*, 51(6): 659–672, 2006. DOI: 10.1002/flid.1147.
- S. Hysing, S. Turek, D. Kuzmin, N. Parolini, E. Burman, S. Ganesan, and L. Tobiska. Quantitative benchmark computations of two-dimensional bubble dynamics. *International Journal for Numerical Methods in Fluids*, 60(11):1259–1288, 2009. DOI: 10.1002/flid.1934.
- IRENA. *Electricity Storage and Renewables: Costs and Markets to 2030*. International Renewable Energy Agency, Abu Dhabi, 2017.
- IRENA. *Renewable Power Generation Costs in 2019*. International Renewable Energy Agency, Abu Dhabi, 2020.
- R. Issa. Solution of the implicitly discretised fluid flow equations by operator-splitting. *Journal of Computational Physics*, 62(1):40–65, 1986. DOI: [https://doi.org/10.1016/0021-9991\(86\)90099-9](https://doi.org/10.1016/0021-9991(86)90099-9).

- F. Jamshidi, H. Heimel, M. Hasert, X. Cai, O. Deutschmann, H. Marschall, and M. Wörner. On suitability of phase-field and algebraic volume-of-fluid openfoam® solvers for gas–liquid microfluidic applications. *Computer Physics Communications*, 236:72 – 85, 2019. DOI: <https://doi.org/10.1016/j.cpc.2018.10.015>.
- L. Janssen and J. Hoogland. The effect of electrolytically evolved gas bubbles on the thickness of the diffusion layer. *Electrochimica Acta*, 15(6):1013 – 1023, 1970. DOI: [https://doi.org/10.1016/0013-4686\(70\)80041-X](https://doi.org/10.1016/0013-4686(70)80041-X).
- L. Janssen and J. Hoogland. The effect of electrolytically evolved gas bubbles on the thickness of the diffusion layer—ii. *Electrochimica Acta*, 18(8):543 – 550, 1973. DOI: [https://doi.org/10.1016/0013-4686\(73\)85016-9](https://doi.org/10.1016/0013-4686(73)85016-9).
- S. Jones, G. Evans, and K. Galvin. Bubble nucleation from gas cavities — a review. *Advances in Colloid and Interface Science*, 80(1):27 – 50, 1999. DOI: [https://doi.org/10.1016/S0001-8686\(98\)00074-8](https://doi.org/10.1016/S0001-8686(98)00074-8).
- T. Kadyk, D. Bruce, and M. Eikerling. How to enhance gas removal from porous electrodes? *Scientific Reports*, 6:38780, 2016. DOI: <https://doi.org/10.1038/srep38780>.
- M. A. Khan, H. Zhao, W. Zou, Z. Chen, W. Cao, J. Fang, J. Xu, L. Zhang, and J. Zhang. Recent progresses in electrocatalysts for water electrolysis. *Electrochemical Energy Reviews*, 1:483–530, 2018. DOI: <https://doi.org/10.1007/s41918-018-0014-z>.
- Kitware Inc. *ParaView*, 2020. URL <https://www.paraview.org/>.
- J. Klostermann, K. Schaake, and R. Schwarze. Numerical simulation of a single rising bubble by vof with surface compression. *International Journal for Numerical Methods in Fluids*, 71(8):960–982, 2013. DOI: 10.1002/flid.3692.
- K. Kolasinski. *Physical Chemistry: How Chemistry Works*. Wiley, 2016. URL <https://books.google.no/books?id=5EskDQAAQBAJ>.
- P. K. Kundu, I. M. Cohen, and D. R. Dowling. Chapter 2 - cartesian tensors. In P. K. Kundu, I. M. Cohen, and D. R. Dowling, editors, *Fluid Mechanics (Sixth Edition)*, pages 49 – 76. Academic Press, Boston, sixth edition edition, 2016. URL <http://www.sciencedirect.com/science/article/pii/B9780124059351000022>.
- C. Kunkelmann. *Numerical Modeling and Investigation of Boiling Phenomena*. PhD thesis, Technische Universität, Darmstadt, May 2011. URL <http://tuprints.ulb.tu-darmstadt.de/2731/>.

- C. Kunkelmann and P. Stephan. Cfd simulation of boiling flows using the volume-of-fluid method within openfoam. *Numerical Heat Transfer, Part A: Applications*, 56(8):631–646, 2009. DOI: 10.1080/10407780903423908.
- S. S. Lafmejani, A. C. Olesen, and S. K. Kær. Vof modelling of gas–liquid flow in pem water electrolysis cell micro-channels. *International Journal of Hydrogen Energy*, 42(26):16333 – 16344, 2017. DOI: <https://doi.org/10.1016/j.ijhydene.2017.05.079>.
- W. M. Lai, D. Rubin, and E. Krempf. Chapter 2 - tensors. In W. M. Lai, D. Rubin, and E. Krempf, editors, *Introduction to Continuum Mechanics (Fourth Edition)*, pages 3 – 68. Butterworth-Heinemann, Boston, fourth edition edition, 2010. URL <http://www.sciencedirect.com/science/article/pii/B9780750685603000025>.
- J. A. Leistra and P. J. Sides. Voltage components at gas evolving electrodes. *Journal of The Electrochemical Society*, 134(10):2442–2446, 1987. DOI: 10.1149/1.2100218.
- G. Litrico, C. B. Vieira, E. Askari, and P. Proulx. Strongly coupled model for the prediction of the performances of an electrochemical reactor. *Chemical Engineering Science*, 170:767 – 776, 2017. DOI: <https://doi.org/10.1016/j.ces.2016.12.060>.
- C.-L. Liu, Z. Sun, G.-M. Lu, and J.-G. Yu. Hydrodynamic characteristics of the two-phase flow field at gas-evolving electrodes: numerical and experimental studies. *Royal Society Open Science*, 5(5):171255, 2018a. DOI: 10.1098/rsos.171255.
- H. Liu, L.-m. Pan, and J. Wen. Numerical simulation of hydrogen bubble growth at an electrode surface. *The Canadian Journal of Chemical Engineering*, 94(1):192–199, 2016. DOI: 10.1002/cjce.22378.
- L. Liu, W. Cai, Y. Chen, and Y. Wang. Fluid dynamics and mass transfer study of electrochemical oxidation by cfd prediction and experimental validation. *Industrial & Engineering Chemistry Research*, 57(18):6493–6504, 2018b. DOI: 10.1021/acs.iecr.7b04226.
- X. Y. Liu. Heterogeneous nucleation or homogeneous nucleation? *The Journal of Chemical Physics*, 112(22):9949–9955, 2000. DOI: 10.1063/1.481644.
- S. D. Lubetkin. Why is it much easier to nucleate gas bubbles than theory predicts? *Langmuir*, 19(7):2575–2587, 2003. DOI: 10.1021/la0266381.
- J. Maes and C. Soulaine. A new compressive scheme to simulate species transfer across fluid interfaces using the volume-of-fluid

- method. *Chemical Engineering Science*, 190:405 – 418, 2018. DOI: <https://doi.org/10.1016/j.ces.2018.06.026>.
- J. Maes and C. Soulaine. A unified single-field volume-of-fluid-based formulation for multi-component interfacial transfer with local volume changes. *Journal of Computational Physics*, 402:109024, 2020. DOI: <https://doi.org/10.1016/j.jcp.2019.109024>.
- H. Marschall, K. Hinterberger, C. Schüler, F. Habla, and O. Hinrichsen. Numerical simulation of species transfer across fluid interfaces in free-surface flows using openfoam. *Chemical Engineering Science*, 78: 111 – 127, 2012. DOI: <https://doi.org/10.1016/j.ces.2012.02.034>.
- R. Massoudi and A. D. King. Effect of pressure on the surface tension of water. adsorption of low molecular weight gases on water at 25.deg. *The Journal of Physical Chemistry*, 78(22):2262–2266, 1974. DOI: 10.1021/j100615a017.
- M. D. Mat, K. Aldas, and O. J. Ilegbusi. A two-phase flow model for hydrogen evolution in an electrochemical cell. *International Journal of Hydrogen Energy*, 29(10):1015 – 1023, 2004. DOI: <https://doi.org/10.1016/j.ijhydene.2003.11.007>. Fuel Cells.
- H. Matsushima, D. Kiuchi, Y. Fukunaka, and K. Kuribayashi. Single bubble growth during water electrolysis under microgravity. *Electrochemistry Communications*, 11(8):1721 – 1723, 2009. DOI: <https://doi.org/10.1016/j.elecom.2009.07.009>.
- J. Maxwell. *A Treatise on Electricity and Magnetism*. Number v. 1 in A Treatise on Electricity and Magnetism. Clarendon Press, 1873. URL <https://books.google.no/books?id=gokfAQAAAJ>.
- R. E. Meredith and C. W. Tobias. Conductivities in emulsions. *Journal of The Electrochemical Society*, 108(3):286–290, 1961. DOI: 10.1149/1.2428064.
- Á. Moreno Soto, T. Maddalena, A. Fraters, D. van der Meer, and D. Lohse. Coalescence of diffusively growing gas bubbles. *Journal of Fluid Mechanics*, 846:143–165, 2018.
- J.-C. Nave, R. R. Rosales, and B. Seibold. A gradient-augmented level set method with an optimally local, coherent advection scheme. *Journal of Computational Physics*, 229(10):3802 – 3827, 2010. DOI: <https://doi.org/10.1016/j.jcp.2010.01.029>.
- T. Nierhaus, H. V. Parys, S. Dehaeck, J. van Beeck, H. Deconinck, J. Deconinck, and A. Hubin. Simulation of the two-phase flow hydrodynamics in an IRDE reactor. *Journal of The Electrochemical Society*, 156(9):P139, 2009. DOI: 10.1149/1.3155423.



- J. K. Novev and R. G. Compton. Natural convection effects in electrochemical systems. *Current Opinion in Electrochemistry*, 7:118 – 129, 2018. DOI: <https://doi.org/10.1016/j.coelec.2017.09.010>.
- NTNU HPC Group. *Idun*, n.d. URL <https://www.hpc.ntnu.no/idun>. Online; accessed 3 November 2020.
- Office of Energy Efficiency and Renewable Energy. Hydrogen Production: Natural Gas Reforming, n.d. URL <https://www.energy.gov/eere/fuelcells/hydrogen-production-natural-gas-reforming>. Online; accessed 13 July 2020.
- OpenCFD. OpenFOAM®: Open source CFD : Documentation, 2020. URL <https://www.openfoam.com/documentation/guides/latest/doc/index.html>. Online; accessed 27 July 2020.
- OpenFOAM. The OpenFOAM Foundation, 2019. URL <https://openfoam.org/>.
- F. Orecchini. The era of energy vectors. *International Journal of Hydrogen Energy*, 31(14):1951 – 1954, 2006. DOI: <https://doi.org/10.1016/j.ijhydene.2006.01.015>.
- M. Philippe, H. Jérôme, B. Sebastien, and P. Gérard. Modelling and calculation of the current density distribution evolution at vertical gas-evolving electrodes. *Electrochimica Acta*, 51(6):1140 – 1156, 2005. DOI: <https://doi.org/10.1016/j.electacta.2005.06.007>.
- A. Q. Raeini, M. J. Blunt, and B. Bijeljic. Modelling two-phase flow in porous media at the pore scale using the volume-of-fluid method. *Journal of Computational Physics*, 231(17):5653 – 5668, 2012. DOI: <https://doi.org/10.1016/j.jcp.2012.04.011>.
- M. Raessi, M. Bussmann, and J. Mostaghimi. A semi-implicit finite volume implementation of the csf method for treating surface tension in interfacial flows. *International Journal for Numerical Methods in Fluids*, 59(10):1093–1110, 2009. DOI: 10.1002/flid.1857.
- W. E. Ranz and W. R. Marshall. Evaporation from drops. *Chem.Eng.Prog.*, 48(4):173–180, 1952.
- L. Rayleigh. Viii. on the pressure developed in a liquid during the collapse of a spherical cavity. *The London, Edinburgh, and Dublin Philosophical Magazine and Journal of Science*, 34(200):94–98, 1917. DOI: 10.1080/14786440808635681.
- Y. Renardy and M. Renardy. Prost: A parabolic reconstruction of surface tension for the volume-of-fluid method. *Journal of Computational Physics*, 183(2):400 – 421, 2002. DOI: <https://doi.org/10.1006/jcph.2002.7190>.

- H. Rusche. *Computational fluid dynamics of dispersed two-phase flows at high phase fractions*. PhD thesis, Imperial College London (University of London), 2003. URL <http://hdl.handle.net/10044/1/8110>.
- G. Sakuma, Y. Fukunaka, and H. Matsushima. Nucleation and growth of electrolytic gas bubbles under microgravity. *International Journal of Hydrogen Energy*, 39(15):7638 – 7645, 2014. DOI: <https://doi.org/10.1016/j.ijhydene.2014.03.059>.
- N. Samkhaniani and M. Ansari. Numerical simulation of bubble condensation using cf-vof. *Progress in Nuclear Energy*, 89:120 – 131, 2016. DOI: <https://doi.org/10.1016/j.pnucene.2016.02.004>.
- J. Sanyal, S. Vásquez, S. Roy, and M. Dudukovic. Numerical simulation of gas–liquid dynamics in cylindrical bubble column reactors. *Chemical Engineering Science*, 54(21):5071 – 5083, 1999. DOI: [https://doi.org/10.1016/S0009-2509\(99\)00235-3](https://doi.org/10.1016/S0009-2509(99)00235-3).
- J. Schillings, O. Doche, and J. Deseure. Modeling of electrochemically generated bubbly flow under buoyancy-driven and forced convection. *International Journal of Heat and Mass Transfer*, 85:292 – 299, 2015. DOI: <https://doi.org/10.1016/j.ijheatmasstransfer.2015.01.121>.
- O. Schmidt, A. Gambhir, I. Staffell, A. Hawkes, J. Nelson, and S. Few. Future cost and performance of water electrolysis: An expert elicitation study. *International Journal of Hydrogen Energy*, 42(52):30470 – 30492, 2017. DOI: <https://doi.org/10.1016/j.ijhydene.2017.10.045>.
- K. Scott. Chapter 1 introduction to electrolysis, electrolysers and hydrogen production. In *Electrochemical Methods for Hydrogen Production*, pages 1–27. The Royal Society of Chemistry, 2020. DOI: 10.1039/9781788016049-00001.
- L. Scriven. On the dynamics of phase growth. *Chemical Engineering Science*, 10(1):1 – 13, 1959. DOI: [https://doi.org/10.1016/0009-2509\(59\)80019-1](https://doi.org/10.1016/0009-2509(59)80019-1).
- S. Shibata. The concentration of molecular hydrogen on the platinum cathode. *Bulletin of the Chemical Society of Japan*, 36(1):53–57, 1963. DOI: 10.1246/bcsj.36.53.
- T. Shinagawa, A. T. Garcia-Esparza, and K. Takanabe. Insight on tafel slopes from a microkinetic analysis of aqueous electrocatalysis for energy conversion. *Scientific Reports*, 5(13801), 2015. DOI: 10.1038/srep13801.
- P. J. Sides and C. W. Tobias. Primary potential and current distribution around a bubble on an electrode. *Journal of The Electrochemical Society*, 127(2):288–291, 1980. DOI: 10.1149/1.2129657.

- S. Siracusano, N. Hodnik, P. Jovanovic, F. Ruiz-Zepeda, M. Šala, V. Baglio, and A. S. Aricò. New insights into the stability of a high performance nanostructured catalyst for sustainable water electrolysis. *Nano Energy*, 40:618 – 632, 2017. DOI: <https://doi.org/10.1016/j.nanoen.2017.09.014>.
- E. Skúlason, V. Tripkovic, M. E. Björketun, S. Gudmundsdóttir, G. Karlberg, J. Rossmeisl, T. Bligaard, H. Jónsson, and J. K. Nørskov. Modeling the electrochemical hydrogen oxidation and evolution reactions on the basis of density functional theory calculations. *The Journal of Physical Chemistry C*, 114(42):18182–18197, 2010. DOI: 10.1021/jp1048887.
- M. Sommerfeld. *Numerical Methods for Dispersed Multiphase Flows*, pages 327–396. Springer International Publishing, Cham, 2017. DOI: 10.1007/978-3-319-60282-0\_6.
- K. Stephan and H. Vogt. A model for correlating mass transfer data at gas evolving electrodes. *Electrochimica Acta*, 24(1):11 – 18, 1979. DOI: [https://doi.org/10.1016/0013-4686\(79\)80033-X](https://doi.org/10.1016/0013-4686(79)80033-X).
- M. Sun, B. Li, and L. Li. A multi-scale mathematical model of growth and coalescence of bubbles beneath the anode in an aluminum reduction cell. *Metallurgical and Materials Transactions B*, 49(5):2821–2834, Oct 2018. DOI: 10.1007/s11663-018-1311-y.
- M. Sussman, P. Smereka, and S. Osher. A level set approach for computing solutions to incompressible two-phase flow. *Journal of Computational Physics*, 114(1):146 – 159, 1994. DOI: <https://doi.org/10.1006/jcph.1994.1155>.
- A. Taqieddin, R. Nazari, L. Rajic, and A. Alshawabkeh. Review—physicochemical hydrodynamics of gas bubbles in two phase electrochemical systems. *Journal of The Electrochemical Society*, 164(13):E448–E459, 2017. DOI: 10.1149/2.1161713jes.
- A. Taqieddin, M. R. Allshouse, and A. N. Alshawabkeh. Editors' choice—critical review—mathematical formulations of electrochemically gas-evolving systems. *Journal of The Electrochemical Society*, 165(13):E694–E711, 2018. DOI: 10.1149/2.0791813jes.
- Z. Tuković and H. Jasak. A moving mesh finite volume interface tracking method for surface tension dominated interfacial fluid flow. *Computers & Fluids*, 55:70 – 84, 2012. DOI: <https://doi.org/10.1016/j.compfluid.2011.11.003>.
- O. Ubbink. *Numerical prediction of two fluid systems with sharp interfaces*. PhD thesis, Imperial College London (University of London), 1997. URL <http://hdl.handle.net/10044/1/8604>.

- Uninett Sigma2. *HPC and storage hardware*, n.d. URL <https://www.sigma2.no/systems#fram>. Online; accessed 3 November 2020.
- K. J. Vachaparambil. CSECGEFoam: Continuum scale electrochemical gas evolution solver on OpenFOAM, n.d. URL <https://github.com/kurianjv/CSECGEFoam>.
- K. J. Vachaparambil and K. E. Einarsrud. Analysis of bubble nucleation mechanisms in supersaturated solutions: A macroscopic perspective. *ECS Meeting Abstracts*, MA2018-01 1366, 2018a. DOI: 10.1149/ma2018-01/21/1366.
- K. J. Vachaparambil and K. E. Einarsrud. Explanation of bubble nucleation mechanisms: A gradient theory approach. *Journal of The Electrochemical Society*, 165(10):E504–E512, 2018b. DOI: 10.1149/2.1031810jes.
- K. J. Vachaparambil and K. E. Einarsrud. Comparison of surface tension models for the volume of fluid method. *Processes*, 7(8):542, 2019. DOI: 10.3390/pr7080542.
- K. J. Vachaparambil and K. E. Einarsrud. Numerical simulation of bubble growth in a supersaturated solution. *Applied Mathematical Modelling*, 81:690 – 710, 2020a. DOI: <https://doi.org/10.1016/j.apm.2020.01.017>.
- K. J. Vachaparambil and K. E. Einarsrud. On sharp surface force model: Effect of sharpening coefficient. *Experimental and Computational Multiphase Flow*, Jun 2020b. DOI: 10.1007/s42757-020-0063-5.
- K. J. Vachaparambil and K. E. Einarsrud. Modeling interfacial mass transfer driven bubble growth in supersaturated solutions. *AIP Advances*, 10(10):105024, 2020c. DOI: 10.1063/5.0020210.
- H. Versteeg and W. Malalasekera. *An Introduction to Computational Fluid Dynamics: The Finite Volume Method*. Pearson Education Limited, 2007. URL <https://books.google.no/books?id=RvBZ-UmpGzIC>.
- J. Villadsen, J. Nielsen, and G. Lidén. *Bioreaction Engineering Principles*. SpringerLink : Bücher. Springer US, 2011. URL [https://books.google.no/books?id=Sq2VJ3D\\_Q0wC](https://books.google.no/books?id=Sq2VJ3D_Q0wC).
- H. Vogt. On the supersaturation of gas in the concentration boundary layer of gas evolving electrodes. *Electrochimica Acta*, 25(5):527 – 531, 1980. DOI: [https://doi.org/10.1016/0013-4686\(80\)87052-6](https://doi.org/10.1016/0013-4686(80)87052-6).
- H. Vogt and R. Balzer. The bubble coverage of gas-evolving electrodes in stagnant electrolytes. *Electrochimica Acta*, 50(10):2073 – 2079, 2005. DOI: <https://doi.org/10.1016/j.electacta.2004.09.025>.

- H. Vogt and H.-D. Kleinschrodt. Ohmic interelectrode voltage drop in alumina reduction cells. *Journal of Applied Electrochemistry*, 33: 563–569, 2003. DOI: 10.1023/A:1024959807438.
- H. Vogt and K. Stephan. Local microprocesses at gas-evolving electrodes and their influence on mass transfer. *Electrochimica Acta*, 155:348 – 356, 2015. DOI: <https://doi.org/10.1016/j.electacta.2015.01.008>.
- T. Wang, J. Wang, and Y. Jin. Population balance model for gas–liquid flows: Influence of bubble coalescence and breakup models. *Industrial & Engineering Chemistry Research*, 44(19):7540–7549, 2005. DOI: 10.1021/ie0489002.
- Y. Wang, L. Zhang, and X. Zuo. Simulation of the fluid flow-related phenomena in the electrolyte of an aluminum electrolysis cell. *Metallurgical and Materials Transactions B*, 42(5):1051–1064, Oct 2011. DOI: 10.1007/s11663-011-9531-4.
- Y. Wang, X. Hu, Z. Cao, and L. Guo. Investigations on bubble growth mechanism during photoelectrochemical and electrochemical conversions. *Colloids and Surfaces A: Physicochemical and Engineering Aspects*, 505:86 – 92, 2016. DOI: <https://doi.org/10.1016/j.colsurfa.2016.01.004>.
- P. S. Weber, H. Marschall, and D. Bothe. Highly accurate two-phase species transfer based on ale interface tracking. *International Journal of Heat and Mass Transfer*, 104:759 – 773, 2017. DOI: <https://doi.org/10.1016/j.ijheatmasstransfer.2016.08.072>.
- R. Wedin and A. A. Dahlkild. On the transport of small bubbles under developing channel flow in a buoyant gas-evolving electrochemical cell. *Industrial & Engineering Chemistry Research*, 40(23):5228–5233, 2001. DOI: 10.1021/ie001073u.
- H. G. Weller, G. Tabor, H. Jasak, and C. Fureby. A tensorial approach to computational continuum mechanics using object-oriented techniques. *Computers in Physics*, 12(6):620–631, 1998. DOI: 10.1063/1.168744.
- D. E. Westerheide and J. W. Westwater. Isothermal growth of hydrogen bubbles during electrolysis. *AIChE Journal*, 7(3):357–362, 1961. DOI: 10.1002/aic.690070303.
- S. Yamoah, R. Martínez-Cuenca, G. Monrós, S. Chiva, and R. Macián-Juan. Numerical investigation of models for drag, lift, wall lubrication and turbulent dispersion forces for the simulation of gas–liquid two-phase flow. *Chemical Engineering Research and Design*, 98:17 – 35, 2015. DOI: <https://doi.org/10.1016/j.cherd.2015.04.007>.

- L. Yang, M. J. Nieves-Remacha, and K. F. Jensen. Simulations and analysis of multiphase transport and reaction in segmented flow microreactors. *Chemical Engineering Science*, 169:106 – 116, 2017. DOI: <https://doi.org/10.1016/j.ces.2016.12.003>.
- X. Yang, F. Karnbach, M. Uhlemann, S. Odenbach, and K. Eckert. Dynamics of single hydrogen bubbles at a platinum microelectrode. *Langmuir*, 31(29):8184–8193, 2015. DOI: [10.1021/acs.langmuir.5b01825](https://doi.org/10.1021/acs.langmuir.5b01825).
- X. Yang, D. Baczymalski, C. Cierpka, G. Mutschke, and K. Eckert. Marangoni convection at electrogenerated hydrogen bubbles. *Physical Chemistry Chemical Physics*, 20:11542–11548, 2018. DOI: [10.1039/C8CP01050A](https://doi.org/10.1039/C8CP01050A).
- G. H. Yeoh and J. Tu. Chapter 2 - governing equations and boundary conditions. In G. H. Yeoh and J. Tu, editors, *Computational Techniques for Multiphase Flows*, pages 21 – 94. Butterworth-Heinemann, Oxford, 2010. DOI: <https://doi.org/10.1016/B978-0-08-046733-7.00002-3>.
- H.-Z. Yuan, C. Shu, Y. Wang, and S. Shu. A simple mass-conserved level set method for simulation of multiphase flows. *Physics of Fluids*, 30(4):040908, 2018. DOI: [10.1063/1.5010152](https://doi.org/10.1063/1.5010152).
- P. Yue, C. Zhou, and J. J. Feng. Spontaneous shrinkage of drops and mass conservation in phase-field simulations. *Journal of Computational Physics*, 223(1):1 – 9, 2007. DOI: <https://doi.org/10.1016/j.jcp.2006.11.020>.
- K. Zeng and D. Zhang. Recent progress in alkaline water electrolysis for hydrogen production and applications. *Progress in Energy and Combustion Science*, 36(3):307 – 326, 2010. DOI: <https://doi.org/10.1016/j.pecs.2009.11.002>.
- S. Zhan, J. Wang, Z. Wang, and J. Yang. Computational fluid dynamics-population balance model simulation of effects of cell design and operating parameters on gas-liquid two-phase flows and bubble distribution characteristics in aluminum electrolysis cells. *JOM*, 70(2): 229–236, Feb 2018. DOI: [10.1007/s11837-017-2636-8](https://doi.org/10.1007/s11837-017-2636-8).
- D. Zhang and K. Zeng. Evaluating the behavior of electrolytic gas bubbles and their effect on the cell voltage in alkaline water electrolysis. *Industrial & Engineering Chemistry Research*, 51(42):13825–13832, 2012. DOI: [10.1021/ie301029e](https://doi.org/10.1021/ie301029e).
- R. Zhang, P. E. Pearce, Y. Duan, N. Dubouis, T. Marchandier, and A. Grimaud. Importance of water structure and catalyst–electrolyte interface on the design of water splitting catalysts. *Chemistry of Materials*, 31(20):8248–8259, 2019. DOI: [10.1021/acs.chemmater.9b02318](https://doi.org/10.1021/acs.chemmater.9b02318).

- Z. Zhang, W. Liu, and M. L. Free. Phase-field modeling and simulation of gas bubble coalescence and detachment in a gas-liquid two-phase electrochemical system. *Journal of The Electrochemical Society*, 167(1): 013532, jan 2020. DOI: 10.1149/2.0322001jes.
- X. Zhao, R. Ranaweera, and L. Luo. Highly efficient hydrogen evolution of platinum via tuning the interfacial dissolved-gas concentration. *Chemical Communications*, 55:1378–1381, 2019a. DOI: 10.1039/C8CC08803A.
- X. Zhao, H. Ren, and L. Luo. Gas bubbles in electrochemical gas evolution reactions. *Langmuir*, 35(16):5392–5408, 2019b. DOI: 10.1021/acs.langmuir.9b00119.
- T. Ziegenhein, M. Garcon, and D. Lucas. Particle tracking using micro bubbles in bubbly flows. *Chemical Engineering Science*, 153:155 – 164, 2016. DOI: <https://doi.org/10.1016/j.ces.2016.07.024>.

## *Appended paper A*

### **Comparison of Surface Tension Models for the Volume of Fluid Method**

Kurian J. Vachaparambil and Kristian Etienne Einarsrud  
Published in *Processes*

There is a typo in Eq.12, which deals with the contact angle correction of interface normal ( $\hat{n}$ ), in the *Processes* paper. The equation should actually read  $\hat{n} = \hat{n}_w \cos\theta + \hat{t}_w \sin\theta$ .





Article

# Comparison of Surface Tension Models for the Volume of Fluid Method

Kurian J. Vachaparambil \*  and Kristian Etienne Einarsrud

Department of Materials Science and Engineering, Norwegian University of Science and Technology (NTNU), 7491 Trondheim, Norway

\* Correspondence: kurian.j.vachaparambil@ntnu.no; Tel.: +47-45517425

Received: 24 July 2019; Accepted: 13 August 2019; Published: 15 August 2019

**Abstract:** With the increasing use of Computational Fluid Dynamics to investigate multiphase flow scenarios, modelling surface tension effects has been a topic of active research. A well known associated problem is the generation of spurious velocities (or currents), arising due to inaccuracies in calculations of the surface tension force. These spurious currents cause nonphysical flows which can adversely affect the predictive capability of these simulations. In this paper, we implement the Continuum Surface Force (CSF), Smoothed CSF and Sharp Surface Force (SSF) models in OpenFOAM. The models were validated for various multiphase flow scenarios for Capillary numbers of  $10^{-3}$ – $10$ . All the surface tension models provide reasonable agreement with benchmarking data for rising bubble simulations. Both CSF and SSF models successfully predicted the capillary rise between two parallel plates, but Smoothed CSF could not provide reliable results. The evolution of spurious current were studied for millimetre-sized stationary bubbles. The results shows that SSF and CSF models generate the least and most spurious currents, respectively. We also show that maximum time step, mesh resolution and the under-relaxation factor used in the simulations affect the magnitude of spurious currents.

**Keywords:** surface tension modelling; VOF; rising bubbles; capillary rise

## 1. Introduction

For a comprehensive understanding of flow physics in multiphase systems, which is ubiquitous in both nature and technological processes, consideration of surface tension is important. For instance, the break down of a fluid jet into droplets is used to form droplets in inkjets [1] and lab-on-chip devices [2] while the thinning and breakdown dynamics of non-Newtonian fluid filaments is critical in its application in jetting [3,4]. Flow scenarios such as underground water flows [5], oil recovery [6] and paper-based microfluidics [7] are examples of flow through porous media where dominance of surface tension may produce a capillary rise. The detachment diameter of the bubble [8,9] and shape of rising bubble [10] during bubble evolution in champagne, boiling and electrochemical gas evolution is dependent on surface tension, as is the droplet size produced during atomisation of fuels [11], spraying [12,13] and growth of a bubble in confined geometries [14]. The effect of surface tension is also important in events such as nucleation of bubbles [15,16] and droplets [17].

Due to the importance and complex nature of multiphase flows, numerical simulations, especially computational fluid dynamics (CFD), are commonly used to study and understand these processes. The CFD strategies used to model multiphase flows can broadly be divided into four categories: Euler–Euler (EE), Euler–Lagrange (EL), interface tracking and capturing methods. The EE approach assumes that phases are interpenetrating, which is efficient when modelling large-scale industrial processes [18,19], while EL tracks the dispersed phases individually, which can be computationally expensive [20,21]. As both EE and EL approaches do not resolve the complete interactions between

the phases, they require so called “closure laws” (see [18–21]). Interface tracking methods, such as the moving mesh method, use a separate boundary-fitted moving mesh for each phase [22]. Although interface tracking methods are quite accurate, they are typically used to model bubble or droplets with mild-moderate deformations [22,23] but to handle complex interface deformations these methods require a global or local re-meshing [24]. Interface capturing methods use a fixed grid with functions to capture the interface such as the Volume Of Fluid method (VOF) [25], level-set [26] and diffuse interface methods [27]. Other methods available in the literature employ a hybrid interface tracking-capturing approach, such as the immersed boundary [28] and front tracking method [29]. Due to its ability to conserve mass (both level-set [30] and phase-field [31] models have difficulties in conserving mass), robustness and ability to produce reasonably sharp interfaces VOF is very popular in multiphase simulations [32–57] and implemented in both commercial (ANSYS Fluent<sup>®</sup> and Flow-3D<sup>®</sup>) and open source (OpenFOAM<sup>®</sup>) CFD packages.

Due to the popularity of open source CFD packages, this paper predominantly delves into the VOF formulation and reported development in interFoam, which is the VOF-based solver available in OpenFOAM<sup>®</sup>. In the VOF method, a scalar function representing the volume fraction of phases in the computational cells is advected. The advection of the volume fraction equation is done using specific discretisation schemes, such as the interface compression method [58], to prevent the excessive smearing of the interface thickness. Apart from interface compression method, recent work has explored reconstruction of interface using techniques such as the isoAdvector method [59,60] and piece wise linear interface calculation (PLIC) algorithm [61]. Although the VOF approach in theory produces a sharp interface, the “real” VOF, which is implemented in solvers such as interFoam, produces a non-sharp interface, which stretches over a few computational cells. This non-sharp nature of the volume fraction leads to errors in the calculated curvature which generates spurious currents that is quantified in the work by Harvie et al. [62], appearing as vortices around the interface (see [63,64]). The presence of these spurious currents introduces non-physical velocities near the interface, which can increase the interfacial mass transfer while modelling condensation [32] and evaporation [57] scenarios and adversely effects the accuracy of simulations. In the literature, spurious currents in VOF methods can be reduced by the following approaches:

- force balance, which is achieved by discretising the surface tension and pressure forces at the same location [65];
- accurate calculation of the curvature (see Table 1); and
- choosing the appropriate time step for the solver (see [63]).

**Table 1.** An overview of improved curvature calculations and surface tension models developed for VOF method.

Publication	Remarks
Brackbill et al. [66]	Introduced the Continuum Surface Force (CSF) and density scaled CSF models. These methods are very common due to its relatively straightforward implementation in a VOF framework.
Ubbink [67]	Proposed using a smoothed volume fraction to calculate curvature (referred to as “Smoothed CSF” in this paper). Using a smoothed volume fraction to compute the curvature instead of non-smoothed volume fraction in CSF model reduced spurious current up to one order of magnitude [56]. This method has been used in modelling condensing bubbles [32] and droplets in microfluidic devices [56]. A similar smoothing of $\alpha_1$ was proposed by Heyns and Oxtoby [68].
Sussman and Puckett [69]	Developed a fully coupled level-set VOF (CLSVOF) method which combines the mass conservativeness of VOF method with smoothness of the level-set function to reduce spurious currents. The CLSVOF method has been used to applications such as splashing droplets [45], flow through microfluidic devices [46], wave breaking [47] and droplet evaporation [43]. Another variant of coupled level set approach is the simple coupled level-set VOF (S-CLSVOF) proposed by Albadawi et al. [70].
Raessi et al. [71]	Proposed a method to calculate $\kappa$ based on advected normals. The spurious currents were lower than CSF (within the same order) while modelling cases such as stationary bubble, rising bubble and Rayleigh–Taylor instability [71].
Renardy and Renardy [72]	Introduced parabolic reconstruction of surface tension (PROST) algorithm which uses a least-squares fit of the interface to a quadratic surface. The spurious current produced by the algorithm is lower by two orders of magnitude compared to CSF [72]. The model was used to simulate droplet deformation including breakup [48,72].
Cifani et al. [61]	Implemented piecewise linear interface calculation (PLIC) algorithm (proposed by Youngs [73]) to reconstruct the interface in interFoam and managed to reduce spurious currents.
Pilliod and Puckett [74]	Developed an efficient least squares volume-of-fluid interface reconstruction algorithm (ELIVRA) which reconstructs the interface using a least square method to fit the interface to a linear surface.
Popinet [75]	Proposed calculating curvature using height functions. Use of height functions have reduced spurious current (slightly outperformed PROST algorithm [75]) and has been shown to model flow in microchannels [49], rising bubble [34,44] and other multiphase flows [50].
Raeini et al. [76]	Introduced a sharp surface force formulation to calculate the capillary force, which is then filtered to reduce the spurious currents (known as FSF model). Neglecting the filtering terms in the FSF model provides a sharp surface formulation of surface tension known as SSF, which is described in [42]. The SSF has been reported to be reduce the spurious currents by two to three orders in comparison to CSF [42]. The FSF model has been reported to provide periodic bursts in the velocity fields but lower spurious current than SSF [42]. The approach has been used to model bubbles in microfluidic devices [51] and flow through porous media [52].
Denner et al. [77]	Proposed the use of artificial viscosity model, which applies artificial shear stress in the tangential direction to interface, to dampen the spurious currents. The model has been used to model rising bubble and capillary instability of a water jet [77].
Lafaurie et al. [78]	Proposed an alternative to the CSF model, known as the Continuum Surface Stress (CSS) model, determines surface tension as divergence of stress tensor without relying on complex curvature calculations. Due to imbalance in the surface tension and pressure, CSS model can also produce spurious currents [35] which has reported to be in the same order as CSF [72]. CSS model has been used to model static droplets and rising bubbles [35], but it does not provide reliable results for falling films [41].

To analyse the force balance (described in [65]), Deshpande et al. [63] evaluated interFoam and showed that there is no imbalance in the surface tension and pressure forces due to inconsistent discretisation. However, the iterative process, which is used to solve pressure equation, introduces an imbalance which is related to the user defined tolerance level of the solution [63]. An overview of literature that provides an improved estimate of the interface curvature and surface tension modelling approaches is provided in Table 1. The improved representation of the interface (which aids in accurate calculation of the interface curvature) is provided by coupled level-set VOF (CLSVOF) method, height functions and interface reconstruction algorithms (like piecewise linear interface calculation (PLIC), parabolic reconstruction of surface tension (PROST) and efficient least squares volume-of-fluid interface reconstruction (ELIVRA) algorithms), whereas the other methods discussed in Table 1 provide alternative approaches to model surface tension. To ensure that spurious currents do not grow over time, a stability condition, proposed by Brackbill et al. [66], for explicit treatment of surface tension is

$$\Delta t < \sqrt{\frac{\rho_{avg}(\Delta x)^3}{2\pi\sigma}}, \quad (1)$$

where  $\Delta x$ ,  $\sigma$  and  $\rho_{avg}$  are grid spacing, surface tension and average of density of both phases, respectively. As proposed by Galusinski and Vigneaux [79], a comprehensive constraint on the time step must consider the effect of both density and viscosity which can be expressed as

$$\Delta t \leq \frac{1}{2} \left( C_2 \tau_\mu + \sqrt{(C_2 \tau_\mu)^2 + 4C_1 \tau_\rho^2} \right), \quad (2)$$

where  $\tau_\mu$  and  $\tau_\rho$  are time scales which are defined as  $\mu_{avg} \Delta x / \sigma$  and  $\sqrt{\rho_{avg}(\Delta x)^3 / \sigma}$ , where  $\mu_{avg}$  is the average dynamic viscosity between the phases, respectively. An evaluation of interFoam, by Deshpande et al. [63], proposed that time step should satisfy

$$\Delta t \leq \max(C_2 \tau_\mu, 10C_1 \tau_\rho), \quad (3)$$

along with the time step constraint discussed in Equation (2). Deshpande et al. [63] also calculated the values of  $C_1$  and  $C_2$  for interFoam to be equal to 0.01 and 10, respectively. Further details of the numerical methods used to model surface tension is available in the recent review work by Popinet [80].

In the literature, comparison between surface tension models is often done for a specific of flow phenomenon and at times a static scenario is used to quantify the spurious currents. Some examples of flow phenomena used to compare surface tension models are rising bubbles whose diameters are in the order of few millimetres [33–35], translating and rotating bubbles [64], oscillating droplets or bubbles [34], stagnant bubbles or droplets [34,35,39,64], Rayleigh–Taylor instability [37,38], Taylor bubbles [64], falling films [41], droplet splashing [38,39], capillary rise [42] and bubble evolution [37,40]. These typically compare the CSF model with height functions [33,34,64], PROST [37], PLIC [42], CLSVOF and its variants [37–40,64], FSF and SSF [42], and CSS [35,41] models. Although the flow scenarios that are used to compare surface tension models are diverse, they can be broadly categorised based on the dominance of surface tension in the flow using the Capillary number ( $Ca$ ), which is defined as the ratio of viscous to surface tension forces in the system. Flow phenomena such as capillary rise and stationary bubbles are examples of low values of  $Ca$  whereas flows with larger values of  $Ca$  include rising bubbles and falling films.

During processes such as gas evolution during electrochemical reactions and boiling, nucleated bubbles grow by mass transfer across the interface [15,16] or coalescence [8], but once the bubble detaches it may deform as it rises up and/or interacts with other bubbles [53]. Other complex processes, such as splashing, involve droplet spreading on a surface which is accompanied by formation of secondary smaller droplets at the rim [81]. To reliably model these processes, surface tension models must be able to accurately handle flow scenarios with both small and large capillary numbers.

In literature, the work by Hoang et al. [56] implemented the Smoothed CSF approach to model the steady motion of bubbles in a straight two-dimensional channel, the formation of bubbles in two- and three-dimensional T-junctions, and the breakup of droplets in three-dimensional T-junctions. A study by Heyns and Oxtoby [68] implemented a selection of surface tension modelling approaches (e.g., the CSF, a variant of Smoothed CSF and a force-balanced higher-resolution artificial compressive formulation) to model a stationary bubble. To the best of the authors' knowledge, a recent study by Yamamoto et al. [36] is the only one of its kind where different surface tension models (i.e., S-CLSVOF, density scaled S-CLSVOF and CSF) are compared based on a variety of processes with various capillary numbers (e.g., rising bubbles, capillary rise, capillary wave and thermocapillary flows).

In this study, we implemented three different surface tension models, namely CSF [66], Smoothed CSF [67] and SSF [76], in interFoam available in OpenFOAM 6. To investigate the capability of the surface tension models to handle various flow scenarios, we used two benchmark cases:

- two-dimensional rising bubbles (proposed by Hysing et al. [54], Klostermann et al. [55]); and
- two-dimensional capillary rise.

These two benchmark cases were selected due to their relevance in a variety of processes. To compare the spurious currents generated by the surface tension models, a stationary bubble was simulated. For practical applications, the time step constraint can substantially increase the computational time, thus the temporal development of the spurious currents with the surface tension models were also examined. Furthermore, the evolution of spurious currents with mesh resolution and under-relaxation factor used for the simulations was also investigated. In the interest of knowledge dissemination, the solvers and the test cases (implemented in OpenFOAM 6) discussed in the paper are available in the Supplementary Materials.

## 2. Numerical Model

### 2.1. Governing Equations

The VOF approach (developed by Hirt and Nichols [25]) denotes the individual phases using a scalar function called volume fraction, represented as

$$\alpha_1(\vec{x}, t) = \begin{cases} 0 & \text{(within Phase 2 or gas)} \\ 0 < \alpha_1 < 1 & \text{(at the interface)} \\ 1 & \text{(within Phase 1 or liquid),} \end{cases} \quad (4)$$

where  $\alpha_1$  is the volume fraction of liquid. The fluid properties such as density ( $\rho$ ) and viscosity ( $\mu$ ) in a control volume are calculated as

$$\chi = \chi_1 \alpha_1 + \chi_2 \alpha_2 \text{ where } \chi \in [\rho, \mu], \quad (5)$$

where  $\chi_1$  and  $\chi_2$  represent the fluid property of liquid and gas phase, respectively.

Considering the fluids to be incompressible, isothermal and immiscible, the VOF approach solves a single set of continuity and momentum equation for the whole domain. The continuity equation is written as

$$\nabla \cdot \vec{U} = 0, \quad (6)$$

where  $\vec{U}$  is the fluid velocity. The momentum equation is

$$\frac{\partial \rho \vec{U}}{\partial t} + \nabla \cdot (\rho \vec{U} \vec{U}) = -\nabla p + \rho \vec{g} + \nabla \cdot \mu (\nabla \vec{U} + \nabla \vec{U}^T) + \vec{F}_{st}, \quad (7)$$

where last term represents the surface tension forces, the second last term is the viscous term,  $\vec{g}$  is the acceleration due to gravity and  $p$  is the pressure. Advection of the volume fraction of liquid ( $\alpha_1$ ) is implemented in interFoam as

$$\frac{\partial \alpha_1}{\partial t} + \nabla \cdot (\alpha_1 \vec{U}) + \nabla \cdot (\alpha_1 (1 - \alpha_1) \vec{U}_r) = 0, \quad (8)$$

where the third term is an artificial compression term used to sharpen the interface [58,61]. The artificial compression term uses a relative velocity ( $\vec{U}_r$ ) defined as

$$\vec{U}_r = C_\alpha \left| \frac{\phi}{S_f} \right| \vec{n}_f, \quad (9)$$

where  $\phi$ ,  $S_f$ ,  $C_\alpha$  and  $\vec{n}_f$  are the velocity flux, face surface area, an adjustable compression factor and unit normal vector to the interface, respectively. In the literature,  $C_\alpha$  can be set between 0 and 4, where  $C_\alpha$  equal to zero and one correspond to the case of no and moderate compression, respectively [56]. The increase in the value of  $C_\alpha$  sharpens the interface but increases the magnitude of spurious currents (see [51,56]). To model practical flow scenarios using interFoam, the value of  $C_\alpha$  is generally set to unity [32,63].

## 2.2. Surface Tension Models

This section introduces the three surface tension models: CSF, Smoothed CSF and SSF.

### 2.2.1. The Continuum Surface Force (CSF) Model

Proposed by Brackbill et al. [66], the CSF model provides a volumetric representation of surface tension, represented as

$$\vec{F}_{st} = \sigma \kappa \nabla \alpha_1, \quad (10)$$

where  $\sigma$  is the surface tension and  $\kappa$  is the curvature, defined in Equation (13). The unit normal vector at the interface is calculated as

$$\hat{n} = \frac{\nabla \alpha_1}{|\nabla \alpha_1| + \delta}, \quad (11)$$

where  $\delta$  is a small non-zero term to ensure that the denominator does not become zero.  $\delta$  is calculated as  $10^{-8} / \left( \frac{\sum_N V_i}{N} \right)^{1/3}$ , where  $N$  is the number of computational cells and  $\sum_N V_i$  provides the sum of the volumes of individual cells (represented by  $i$ ). Once  $\hat{n}$  is calculated, it is corrected to account for wall adhesion through

$$\hat{n} = \hat{n}_w \cos \theta + \hat{t}_w \sin \theta \quad (12)$$

where  $\theta$  is the contact angle of the gas-liquid interface at the walls (measured in the liquid phase), and  $\hat{n}_w$  and  $\hat{t}_w$  are unit vectors that are normal and tangential to the wall, respectively [82]. The curvature of the interface is then calculated as

$$\kappa = -\nabla \cdot \hat{n}. \quad (13)$$

### 2.2.2. The Smoothed CSF Model

The Smoothed CSF model (by Ubbink [67]) proposed modifying CSF by modifying the calculation of curvature of interface by using a smoothed volume fraction of liquid ( $\alpha_1$ ).

The smoothed volume fraction field is calculated using a smoother proposed by Lafaurie et al. [78], which has been implemented in the literature [32,56] and is represented as

$$\tilde{\alpha}_1 = \frac{\sum_{f=1}^N \langle \alpha_1 \rangle_{c \rightarrow f} S_f}{\sum_{f=1}^N S_f}, \quad (14)$$

where the indices  $c$  and  $f$  are the cell and face centre indices, respectively.  $\langle \alpha_1 \rangle_{c \rightarrow f}$  represents the interpolation of  $\alpha_1$  from cell to face centre. The smoothening of volume fraction, done using Equation (14), is applied twice to obtain a smooth volume fraction field, which is used in Equation (15). Implementation of Equation (14) in interFoam is done using the subroutine developed in the work by [56]. Based on the smoothed volume fraction field, the unit normal to the interface is calculated as

$$\tilde{n} = \frac{\nabla \tilde{\alpha}_1}{|\nabla \tilde{\alpha}_1| + \delta}, \quad (15)$$

which is then corrected for wall adhesion (based on Equation (12)). The curvature of the interface is then calculated as

$$\tilde{\kappa} = -\nabla \cdot \tilde{n}. \quad (16)$$

The surface tension can be represented using the modified curvature ( $\tilde{\kappa}$  in Equation (16)), which can be represented as

$$\vec{F}_{st} = \sigma \tilde{\kappa} \nabla \alpha_1. \quad (17)$$

### 2.2.3. The Sharp Surface Force (SSF) Model

In the SSF model, proposed by Raeini et al. [76], smoothened and sharpened volume fraction fields are used to calculate curvature and gradient of volume fraction.

The smoothened volume fraction ( $\alpha_s$ ) is calculated based on interpolating the cell-centred values of  $\alpha_1$  to the cell faces using a three consecutive smoothening steps described using Equations (18a)–(18c)

$$\alpha_{s1} = \mathcal{C} \langle \langle \alpha_1 \rangle_{c \rightarrow f} \rangle_{f \rightarrow c} + (1 - \mathcal{C}) \alpha_1, \quad (18a)$$

$$\alpha_{s2} = \mathcal{C} \langle \langle \alpha_{s1} \rangle_{c \rightarrow f} \rangle_{f \rightarrow c} + (1 - \mathcal{C}) \alpha_{s1}, \quad (18b)$$

$$\alpha_s = \mathcal{C} \langle \langle \alpha_{s2} \rangle_{c \rightarrow f} \rangle_{f \rightarrow c} + (1 - \mathcal{C}) \alpha_{s2}, \quad (18c)$$

where  $\mathcal{C}$  is set equal to 0.5. The unit normal to the interface is then calculated as

$$\hat{n}_s = \frac{\nabla \alpha_s}{|\nabla \alpha_s| + \delta}, \quad (19)$$

which is then corrected for wall adhesion (based on Equation (12)). The curvature ( $\kappa_s$ ) is calculated using Equation (19) as

$$\kappa_s = -\nabla \cdot \hat{n}_s. \quad (20)$$

The interface curvature is smoothed by using a three step procedure, which can be broadly summarised into Equations (21a), (21c), and (21d). The first step involves smoothening the curvature calculated in Equation (20) as

$$\kappa_{f1} = \left( 2\sqrt{\alpha_c(1-\alpha_c)} \right) \kappa_s + \left( 1 - 2\sqrt{\alpha_c(1-\alpha_c)} \right) \kappa_s^* \quad (21a)$$

where  $\alpha_c$  is defined as  $\min(1, \max(\alpha_1, 0))$  and

$$\kappa_s^* = \frac{\langle \langle w \kappa_s \rangle_{c \rightarrow f} \rangle_{f \rightarrow c}}{\langle \langle w \rangle_{c \rightarrow f} \rangle_{f \rightarrow c}}, \quad w = \sqrt{\alpha_c(1-\alpha_c) + 10^{-3}}. \quad (21b)$$



The second step further smoothens the curvature (calculated in Equation (21a)) as

$$\kappa_{f2} = \left(2\sqrt{\alpha_c(1-\alpha_c)}\right)\kappa_s + \left(1-2\sqrt{\alpha_c(1-\alpha_c)}\right)\kappa_{s2}^*, \text{ where } \kappa_{s2}^* = \frac{\langle \langle w\kappa_{f1} \rangle_{c \rightarrow f} \rangle_{f \rightarrow c}}{\langle \langle w \rangle_{c \rightarrow f} \rangle_{f \rightarrow c}}. \quad (21c)$$

The final step calculates the the final curvature as

$$\kappa_{final} = \frac{\langle w\kappa_{f2} \rangle_{c \rightarrow f}}{\langle w \rangle_{c \rightarrow f}}. \quad (21d)$$

The surface tension is then given as

$$\vec{F}_{st} = \sigma\kappa_{final}\nabla\alpha_{sh}, \quad (22)$$

where  $\alpha_{sh}$  is a sharpened volume fraction of liquid defined in Equation (23).

$$\alpha_{sh} = \frac{1}{1-C_{sh}} \left[ \min\left(\max\left(\alpha_1, \frac{C_{sh}}{2}\right), 1 - \frac{C_{sh}}{2}\right) - \frac{C_{sh}}{2} \right], \quad (23)$$

where  $C_{sh}$  is a sharpening coefficient. A value of  $C_{sh}=0$  reduces  $\alpha_{sh}$  to  $\alpha_1$ , whereas  $C_{sh}=1$  provides sharp representation of the interface (which is numerically unstable). We used  $C_{sh}=0.98$  for static cases and  $C_{sh}=0.5$  for dynamic cases.

### 3. Solver Settings

To simplify the treatment of pressure boundary condition and density change across the interface, interFoam uses  $p_{rgh}$  which is defined as  $p - \rho\vec{g} \cdot \vec{x}$ , where  $\rho\vec{g} \cdot \vec{x}$  is the hydrostatic component of pressure [58]. The volume fraction evolution equation (Equation (8)) is solved using the Multidimensional Universal Limiter with Explicit Solution (MULES) algorithm, which preserves the boundedness of volume fraction [61,63]. Once volume fraction is solved, the continuity equation (Equation (6)) and momentum equation (Equation (7)) are solved using the Pressure Implicit with Splitting of Operator (PISO) algorithm [83]. In PISO, a predicted velocity is updated using a pressure correction procedure to advance velocity and pressure fields in time [58,63]. To understand the implementation and solution algorithm of the governing equations (Equations (6)–(8)) in interFoam, please refer to the work by Rusche [58] or Deshpande et al. [63]. The discretisation schemes, solvers and others parameters used to solve the governing equations for all the simulations discussed in this paper are presented in Tables 2–4, respectively. Under-relaxation factors, if set to less than unity, cause damping of the solution, which can lead to longer computational time for the solution reach to a steady state value. In flow scenarios where there is no steady state solution, using an under-relaxation factor can lead to erroneous results due to under-prediction of the flow variables. We used an under-relaxation factor in the solver equal to one for dynamic cases and 0.9 for static cases. The effect of using an under relaxation factor of one on static cases is also investigated.

**Table 2.** Discretisation schemes.

Modeling Term	Keyword	Scheme	Remarks
Time derivatives	ddtSchemes	Euler	First order implicit method (see [84])
Divergence term	$\nabla \cdot (\rho \vec{U} \vec{U})$	vanLeerV	Modified vanLeer for vector fields (see [84])
	$\nabla \cdot (\vec{U} \alpha_1)$	vanLeer	See [85]
	$\nabla \cdot (\vec{U}_c \alpha_1 (1 - \alpha_1))$	interfaceCompression	See [63]
Gradient term	gradSchemes	linear	Operator with $\nabla$ (see [84])
Laplacian term	laplacianSchemes	linear corrected	Operator with $\nabla^2$ (see [84])
Others	snGradSchemes	corrected	Surface normal gradients (see [84])
	interpolationSchemes	linear	Interpolates values (see [84])

**Table 3.** Solvers used for the discretised equation.

Equation	Linear Solver	Smoother/Preconditioner	Tolerance
Pressure correction equation	PCG	DIC	$10^{-20}$ (based on [63])
Momentum equation	smoothSolver	symGaussSeidel	$10^{-12}$
Volume fraction equation	smoothSolver	symGaussSeidel	$10^{-12}$

**Table 4.** Other parameters used in solving the discretised equations.

Parameter	Value	Notes
nAlphaCorr	2	Number of $\alpha_1$ correction [55]; typically set equal to 1 or 2 for time-dependent flows [86].
nAlphaSubCycles	1	Represents the number of sub-cycles within $\alpha_1$ equation [84].
cAlpha ( $C_\alpha$ )	1	Used for interface compression in Equation (9).
MULESCorr	yes	Switches on semi-implicit MULES [87].
nLimiterIter	3	Number of MULES iterations over the limiter [87].
momentumPredictor	no	Controls solving of the momentum predictor; typically set to 'no' for multiphase and low Reynolds number flows [84].
minIter	1	Minimum number of iterations used in momentum calculation.
nOuterCorrectors	1	PISO algorithm is selected by setting this parameter equal to unity (in PIMPLE algorithm) [84].
nCorrectors	3	The number of times the PISO algorithm solves the pressure and momentum equation in each step; usually set to 2 or 3 [84].
nNonOrthogonalCorrectors	0	Used when meshes are non-orthogonal [84].

#### 4. Validation: Benchmark Test Cases

##### 4.1. Two Dimensional Rising Bubbles

Due to the computational overhead of modelling a three-dimensional rising bubble, we model the buoyancy driven motion of a single bubble as proposed by Hysing et al. [54], Klostermann et al. [55]. The work by Hysing et al. [54] reported benchmarking data such as the bubble shape, rising velocity and circularity for two cases. These benchmarking data are produced based on numerical simulations using codes such as TP2D, FreeLIFE and MoonNMD [54]. In the work by Klostermann et al. [55], the benchmark proposed by Hysing et al. [54] was used to evaluate the VOF solver in OpenFOAM® (i.e., interFoam) for various meshes.

The computational domain used for the simulation is a rectangle of dimensions 1 m  $\times$  2 m where the bubble of diameter 0.5 m was initialised such that the centre of the bubble is at a distance of 0.5 m from the bottom and side walls. As mesh convergence could not be achieved perfectly in previous works [36,55], we used a uniform grid 160  $\times$  320 for the simulations, corresponding to the fine mesh

used in [54]. The pressure boundary conditions used in the simulations were zero gradient on the side and bottom walls, and a Dirichlet condition (equal to zero) at the top wall. The volume fraction of fluid used a zero gradient boundary condition on all walls. The velocity boundary conditions used for the simulations were no slip on top and bottom walls, but slip condition was implemented for the side walls. The fluid properties associated with the test cases, which are abbreviated as TC1 and TC2, are tabulated in Table 5. The maximum Courant number used by the solver was set equal to 0.01 and maximum time step permitted was based on Equations (2) and (3). The test cases are distinguished based on Reynolds ( $Re$ ), Eötvös ( $Eo$ ) and Capillary ( $Ca$ ) numbers, which are defined as

$$Re = \frac{U_g L}{\nu_1}, Eo = \frac{\rho_1 U_g^2 L}{\sigma}, Ca = \frac{Eo}{Re} \quad (24)$$

with  $L$  and  $U_g$  being the characteristic length scale (equal to 0.5 m) and characteristic velocity (defined as  $\sqrt{|\bar{g}|L}$ ), respectively. The bubble shape was obtained at  $\alpha_1 = 0.5$  and rising velocity was calculated based on bubble volume averaged vertical component of the velocity vector [54,55]. For validation, we used the data reported by Klostermann et al. [55] and Hysing et al. [54] (for the predictions by the FreeLIFE solver, which is referred to as 'Benchmark' in this paper) for a uniform grid of  $160 \times 320$ .

**Table 5.** Physical parameters used for the rising bubble simulations (see [54]).

Cases	$\rho_1$ (kg/m <sup>3</sup> )	$\rho_2$ (kg/m <sup>3</sup> )	$\nu_1$ (m <sup>2</sup> /s)	$\nu_2$ (m <sup>2</sup> /s)	$\sigma$ (N/m)	$\bar{g}$ (m/s <sup>2</sup> )*	$Re$	$Eo$	$Ca$
TC1	1000	100	$10^{-2}$	$10^{-2}$	24.5	(0 −0.98 0)	35	10	0.286
TC2	1000	1	$10^{-2}$	$10^{-1}$	1.96	(0 −0.98 0)	35	125	3.571

\* $\bar{g}$  is the reduced gravity as described in [54].

The first test case, TC1, corresponds to the case where surface tension effects are dominant [55]. The temporal evolution of the bubble as predicted by the various surface tension models is compared in Figure 1. Due to the stronger surface tension effects, the interface deforms into an ellipsoidal bubble (see Figure 2). The bubble shape (at  $t = 3$  s) predicted by CSF model provides a slightly better agreement to the benchmark data compared to the other surface tension models. The surface tension models also tend to underpredict the position of the bubble at  $t = 3$  s. This underprediction could be attributed to the lower rising velocity (see Figure 3), which has also been reported in previous studies using OpenFOAM [36,54,55]. Although bubble shape and rising velocity provide an overview of the capability of the surface tension models, the quantification of the errors associated with the models was based on the maximum rising velocity ( $V_{max}$ ) and the time at which the  $V_{max}$  occurred (tabulated in Table 6). The benchmarking data show that SSF model provides a better agreement to the data reported by Hysing et al. [54] (absolute error is less than 2%) and Klostermann et al. [55] (absolute error is nearly 1.5%) in comparison to the other models.

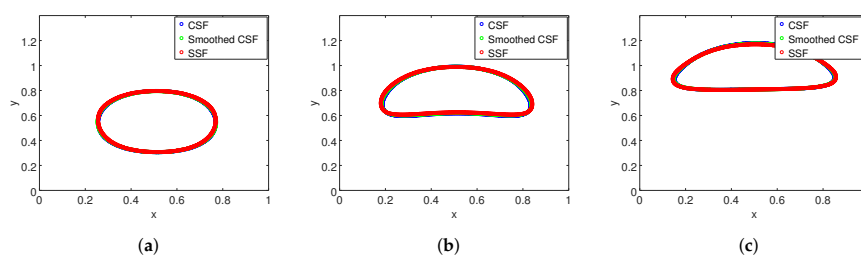


**Figure 1.** Temporal evolution of the bubble for TC1: (a)  $t = 0.5$  s; (b)  $t = 1.5$  s; and (c)  $t = 2.5$  s.

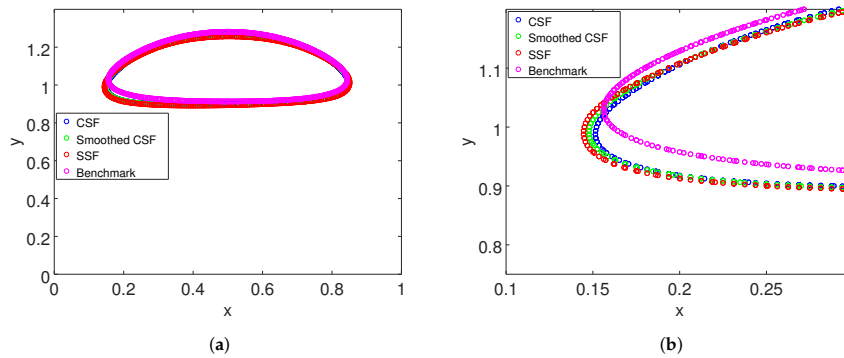


Figure 2. Validation Bubble shape for TC1 at  $t = 3$  s: (a) bubble morphology; and (b) detailed.

Table 6. Benchmark quantities for TC1.

Parameter	CSF	Smoothed CSF	SSF	[55]	Benchmark ([54])
$V_{max}$	0.2366	0.2375	0.2386	0.2365	0.2419
$t(V_{max})$	0.9632	0.9491	0.9104	0.9219	0.9270

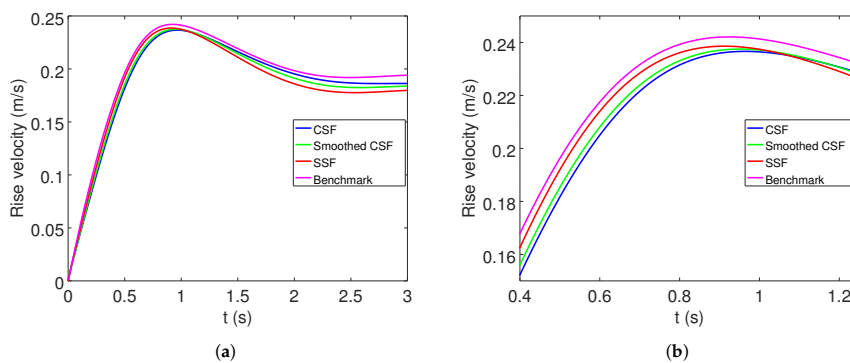


Figure 3. Validation Bubble rising velocity for TC1: (a) temporal changes of bubble rising velocity; and (b) detailed.

The other test case, TC2, corresponds to a case where the surface tension effects are lower [55]. This results in larger deformation of interface as the bubble evolves (see Figure 4) and eventually forms a skirted bubble that has thin filaments that breaks down into smaller droplets (see Figure 5). Comparing the surface tension models to the benchmark for final bubble shape shows that the models agree quite well (see Figure 5) but there is a difference between the models with respect to the prediction of the skirted part of the bubble (see Figure 5b). Figure 6 shows that the surface tension models in comparison to the benchmark data under-predicts the rise velocity. Comparing with the benchmark, the SSF model provides the closest agreement for  $V_{max1}$  (absolute error is nearly 3.5% [54] and less than 0.1% for [55]) and  $t(V_{max1})$  (absolute error is nearly 3–3.5% for both [54,55]) (see Table 7). On the other hand, CSF model agrees with the benchmarking data for  $V_{max2}$  (absolute error is nearly 5.7% [54] and 0% for [55]) and  $t(V_{max2})$  (absolute error is nearly 0.6% for both [54,55]) (see Table 7).

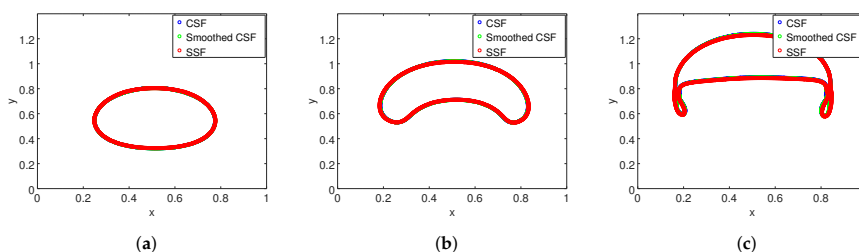


Figure 4. Temporal evolution of the bubble for TC2: (a)  $t = 0.5$  s; (b)  $t = 1.5$  s; and (c)  $t = 2.5$  s.

Table 7. Benchmark quantities for TC2.

Parameter	CSF	Smoothed CSF	SSF	[55]	Benchmark ([54])
$V_{max1}$	0.2434	0.2429	0.2427	0.2431	0.2514
$t(V_{max1})$	0.7663	0.7637	0.7502	0.7250	0.7281
$V_{max2}$	0.2302	0.2290	0.2260	0.2302	0.2440
$t(V_{max2})$	1.9721	1.9700	1.9729	1.9594	1.9844

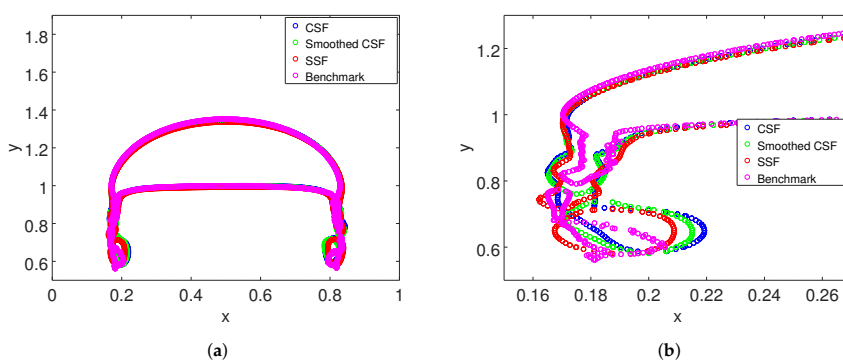


Figure 5. Validation Bubble shape for TC2 at  $t = 3$  s: (a) bubble morphology; and (b) detailed.

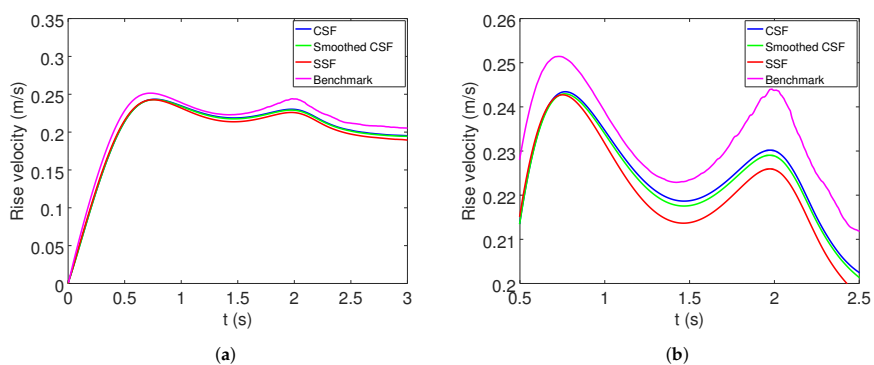


Figure 6. Validation Bubble rising velocity for TC2: (a) temporal changes of bubble rising velocity; and (b) detailed.

In the previous work by Klostermann et al. [55], the spurious currents were reported to be the reason for the error between the benchmark ([54]) and their simulations (for both TC1 and TC2). Thus, the differences in the predictions, for the rising bubble simulations, between the three surface tension models considered in this paper and their departure from the benchmark can also be attributed to spurious currents generated by these models (which is discussed below). For TC2, the larger variation between the surface tension models after the first peak in the transient evolution of the rise velocity (see Figure 6) can be attributed to the differences in the shapes of filament or satellite droplets (based on the work of Yamamoto et al. [36]). Interestingly, there are also some differences in the predictions by the CSF model (for both TC1 and TC2) and the data reported by Klostermann et al. [55], which could be attributed to the difference in the solver settings (e.g., the discretisation schemes, linear solvers and number of iterations) and/or the variations within the different versions of OpenFOAM. The influence of the discretisation schemes on the predicting the flow variables has been previously investigated in [88,89] but further investigation into the effects of other solver settings (e.g., the choice of linear solver and number of iterations) on the solution is required to quantify its effect. As OpenFOAM gets updated, some of the functionalities and/or the algorithms are modified, for example, the artificial interface compression term used in advection of  $\alpha_1$  (defined in Equation (9)) is computed differently in the older versions of the software (see [55]). To the best knowledge of the authors, no study has reported a comparison of the performance of various versions of OpenFOAM for specific flow scenarios. These settings, especially discretisation schemes and interface compression algorithms, would effect the generation and evolution of spurious currents, which could be the potential source of the discrepancy between our simulations and the data reported in literature.

#### 4.2. Two-Dimensional Capillary Rise

The rise of liquid through a narrow tube or between two parallel plates, which occurs as a consequence of the wetting of the walls by the liquid, is known as capillary rise. As the liquid rises, it reaches a point of equilibrium when the vertical component of the force exerted by surface tension is balanced by the gravitational force acting on the risen liquid column. This equilibrium point (for liquid rising between two vertical parallel plates) is denoted using a height ( $h_b$ ), which can be analytically calculated as

$$h_b = \frac{2\sigma\cos\theta}{\Delta\rho|\bar{g}|a}, \quad (25)$$

where  $\Delta\rho$  is the difference between densities of liquid and gas, and  $a$  is the distance between the plates [90].

To study capillary rise, we used a rectangular domain of dimensions 1 mm  $\times$  20 mm, where  $a$  (defined in Equation (25)) is equal to 1 mm, with a uniform mesh of 20  $\times$  400. This mesh resolution provided the most accurate prediction of capillary rise for the same computational domain while using CSF model in the previous work by Yamamoto et al. [36]. The boundary conditions for velocity field imposes a no slip boundary condition for the walls and pressure based condition (applied to both inlet and outlet) that computes inlet velocity based on the patch-face normal component of the internal-cell velocity and outflow using the zero gradient condition. The volume fraction field uses a zero gradient condition at walls (with a contact angle of 45°) and outlet, along with a Dirichlet condition (equal to one) at inlet. The boundary condition for pressure uses a Dirichlet condition (equal to zero) at inlet and outlet whereas the walls use a Neumann boundary condition. The materials properties used for the simulations are described in Table 8. The initial volume fraction of liquid in the domain is set such that the liquid–gas interface is at a height of 8 mm from the bottom surface. The maximum time step (which satisfies both Equations (2) and (3)) and maximum Courant number were set equal to 3.5  $\mu$ s and 0.1, respectively.

**Table 8.** Physical parameters used for the capillary rise simulations.

$\rho_1(\text{kg/m}^3)$	$\rho_2(\text{kg/m}^3)$	$v_1(\text{m}^2/\text{s})$	$v_2(\text{m}^2/\text{s})$	$\sigma(\text{N/m})$	$\vec{g}(\text{m/s}^2)^*$	$Ca$
1000	1	$10^{-6}$	$1.48 \times 10^{-5}$	0.07	(0 −10 0)	0.0014

\*This value of  $\vec{g}$  is used to study capillary rise by Yamamoto et al. [36].

Once the interface position stabilised (see Figure 7), the capillary height  $h_{b,calc}$  was calculated approximately from the volume fraction field as

$$h_{b,calc} = \frac{\int_S \alpha_1 dS}{a}, \quad (26)$$

where the numerator is the area occupied by the liquid in the computational domain [36]. The capillary rise height calculated from the simulations is compared to the analytically derived  $h_b$  (which was determined to be 9.9 mm using Equation (25)) in Table 9.

**Table 9.** Errors associated with the surface tension models on prediction of capillary rise.

Surface Tension Model	$h_{b,calc}$ (mm)	$E(h) = (h_{b,calc} - h_b)/h_b$
CSF	9.16	−0.076
Smoothed CSF	Capillary height did not stabilise during simulations (see Figure 7)	
SSF	9.26	−0.065

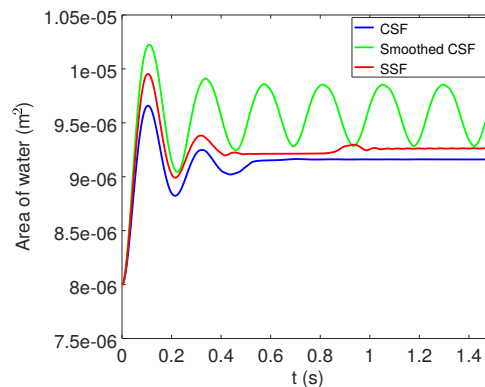
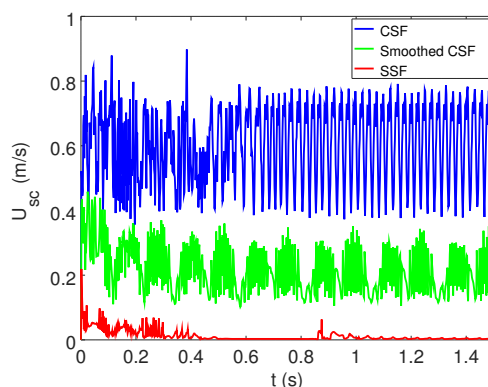
**Figure 7.** Evolution of the water column during capillary rise.

Table 9 shows that SSF model provides a better prediction of the capillary rise height compared to CSF model. A previous work by Yamamoto et al. [36] reported an error of 7.7% for a capillary rise model using the CSF model. Interestingly, the Smoothed CSF model could not provide a reliable capillary rise prediction due to the oscillation of the water column (see Figure 7). This discrepancy can be explained based on the evolution of the spurious currents ( $U_{sc}$  defined in Equation (27)), which are plotted in Figure 8. The magnitude of spurious currents ( $U_{sc}$ ) generated in the simulations was computed at each time step as

$$U_{sc} = \max(|\vec{U}|). \quad (27)$$

The periodic growth and decay of the spurious currents in the Smoothed CSF model (see Figure 8) results in the unrealistic motion of the interface whereas the CSF model which has much larger magnitude of spurious currents is much more periodic (see Figure 8), which reduces the net motion of the liquid–gas interface. Compared to CSF and Smoothed CSF models, the spurious current evolution in the SSF model is lowered by nearly two orders of magnitude (see Figure 8).



**Figure 8.** Evolution of spurious currents during the capillary rise simulations. It is worth pointing out that the figure is plotted using data extracted at every 500th point from the dataset obtained from simulations in order to reduce the rendering time of the image but care has been taken to showcase the larger temporal variations of  $U_{sc}$ .

### 5. Analysis: Spurious Current

To study the spurious currents generated during the simulations, we simulated a stationary bubble where the effect of gravity was neglected. A bubble of diameter  $2R$  was set at the centre of a square domain of dimensions  $4R \times 4R$ . The properties of the two phases and other physical parameters used for the simulations described in this section are tabulated in Table 10. For these simulations, the boundaries were assigned the Dirichlet condition, equal to 101325 Pa, for pressure and zero gradient condition for both  $\alpha_1$  and  $\vec{U}$ . The simulations were run until an end time of 0.05 s to ensure that initial transients (if any) were eliminated with maximum time step calculated based on Equations (2) and (3) along with maximum Courant number of 0.1.

**Table 10.** Physical parameters used for the simulations in the analysis of spurious current.

$\rho_1(\text{kg/m}^3)$	$\rho_2(\text{kg/m}^3)$	$\nu_1(\text{m}^2/\text{s})$	$\nu_2(\text{m}^2/\text{s})$	$\sigma(\text{N/m})$	$\vec{g}(\text{m/s}^2)$
1000	1	$10^{-6}$	$1.48 \times 10^{-5}$	0.07	(0 0 0)

The accuracy of the surface tension models was calculated based on the following parameters: Laplace pressure, magnitude of spurious currents and mass imbalance. For a two-dimensional bubble, the Laplace pressure can be calculated using the Young–Laplace equation as

$$\Delta p'_c = \frac{\sigma}{R}. \quad (28)$$

The Laplace pressure inside the bubble was calculated from the simulation as

$$\Delta p_c = \frac{\int_V \alpha_2 p dV}{\int_V \alpha_2 dV} - p_0, \quad (29)$$

where  $p_0$  is the operating pressure (which was equal to 101325 Pa). The mean error associated with the Laplace pressure calculated by the various surface tension models was determined as

$$\bar{E}(\Delta p_c) = \frac{\overline{\Delta p_c} - \Delta p'_c}{\Delta p'_c}, \quad (30)$$



where the overbar represents the time averaged variables.

### 5.1. Stagnant Bubble of Few Millimetres

In this test case, we modelled a bubble with a radius of 2.5 mm using fluid properties described in Table 10 and under-relaxation factor of 0.9. The computations were performed using a uniform structured grid. The total number of mesh elements and maximum time step (which satisfies both Equations (2) and (3)) used in the simulations are described in Table 11.

**Table 11.** Details of mesh and the associated maximum time step calculated based on Equations (2) and (3) used for stationary bubble simulations.

Mesh	Mesh Resolution (mm <sup>2</sup> )	Total Number of Cells	$R/\delta x^*$	Maximum Time Step (s)
M0	$0.5 \times 0.5$	400	5	$9 \times 10^{-5}$
M1	$0.25 \times 0.25$	1600	10	$3 \times 10^{-5}$
M2	$0.125 \times 0.125$	6400	20	$1 \times 10^{-5}$
M3	$0.083 \times 0.083$	14400	30	$6 \times 10^{-6}$

\* $R/\delta x$  is the ratio of the radius of the bubble and the cell size.

To understand how spurious currents occur with various surface tension models,  $U_{sc}$  is plotted at  $t = 0.05$  s for the grid described by M3 in Figure 9. In the surface tension models considered in this study, the spurious currents occur around the interface but their magnitudes are much larger in the bubble than outside. To quantify the spurious currents from the simulations, the magnitude of spurious currents and capillary pressure are tabulated in Table 12. The spurious currents generated by the surface tension models tends to reduce with finer meshes for both SSF and Smoothed CSF. On the other hand, the increase in spurious current for CSF can be explained based on the dependence on the mesh size ( $\Delta x$ ) is given by

$$C_{\Delta x} \sim \sqrt{\frac{\sigma}{\rho \Delta x}}, \quad (31)$$

where  $C_{\Delta x}$  is the magnitude of the spurious velocities (studied for CSF model [63,66]). Equation (31) indicates that smaller mesh sizes result in larger values of spurious currents for CSF model. As shown in Table 12, the Laplace pressure predicted by the surface tension models does not perfectly match  $\Delta p'_c$  but both Smoothed CSF and SSF provides a better prediction in comparison to CSF.

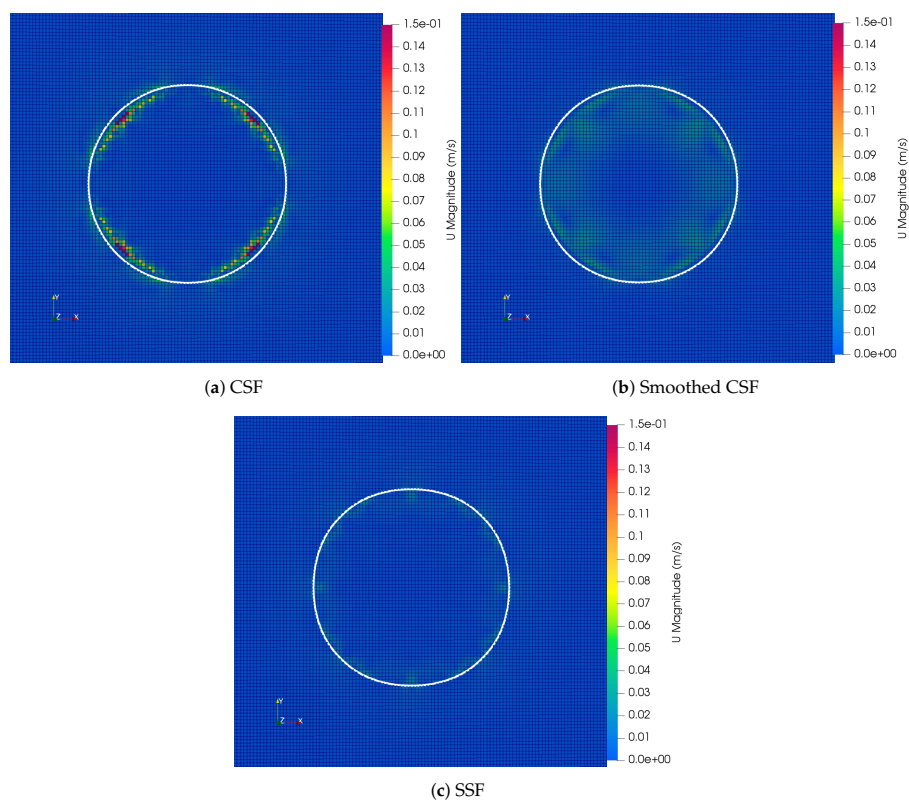


**Figure 9.** Comparison of spurious current generated by surface tension models at  $t = 0.05$  s using M3 mesh. The gas–liquid interface in the domain is represented using a contour (in white) that is plotted at  $\alpha_1 = 0.5$ .

**Table 12.** Comparison of spurious currents based on mesh and surface tension models (using an under-relaxation factor of 0.9).

Surface Tension Model	Mesh	$\overline{U}_{sc}$	$Ca = \frac{\rho_1 v_1 \overline{U}_{sc}}{\sigma}$	$\overline{\Delta p_c}$	$\overline{E}(\Delta p_c)$	Mass Imbalance
CSF	M0	0.133	0.002	22.29	−0.20	0
	M1	0.171	0.002	23.03	−0.18	0
	M2	0.174	0.002	24.06	−0.14	0
	M3	0.189	0.003	24.77	−0.12	0
Smoothed CSF	M0	0.096	0.001	24.12	−0.14	0
	M1	0.088	0.001	25.14	−0.10	0
	M2	0.062	0.001	25.19	−0.10	0
	M3	0.049	0.001	26.09	−0.07	0
SSF	M0	0.045	0.001	23.95	−0.14	0
	M1	0.087	0.001	25.12	−0.10	0
	M2	0.036	0.001	25.88	−0.08	0
	M3	0.041	0.001	25.55	−0.09	0

### 5.2. Effect of Time Step

The two time step constraints were from Brackbill et al. [66] (Equation (1)) and Deshpande et al. [63] (Equations (2) and (3)). To study the effect of time step constraint, the simulations used a bubble of 2.5 mm with the M3 mesh (see Table 11) and fluid properties described in Table 10 using an under-relaxation factor of 0.9. The maximum time steps ( $\Delta t$ ) used for the simulations are 25  $\mu\text{s}$  (based on [66]) and 6  $\mu\text{s}$  (based on [63]).

The temporal evolution of  $U_{sc}$  is compared for the surface tension models in Figure 10. Using the time step dictated by Deshpande et al. [63], the spurious currents generated by the CSF model are reduced by less than half in comparison to when time step constraint proposed by Brackbill et al. [66] was used. The other models show an absolute difference in the mean spurious current of nearly 7% and 6%, respectively, for the time step constraints (see Table 13).

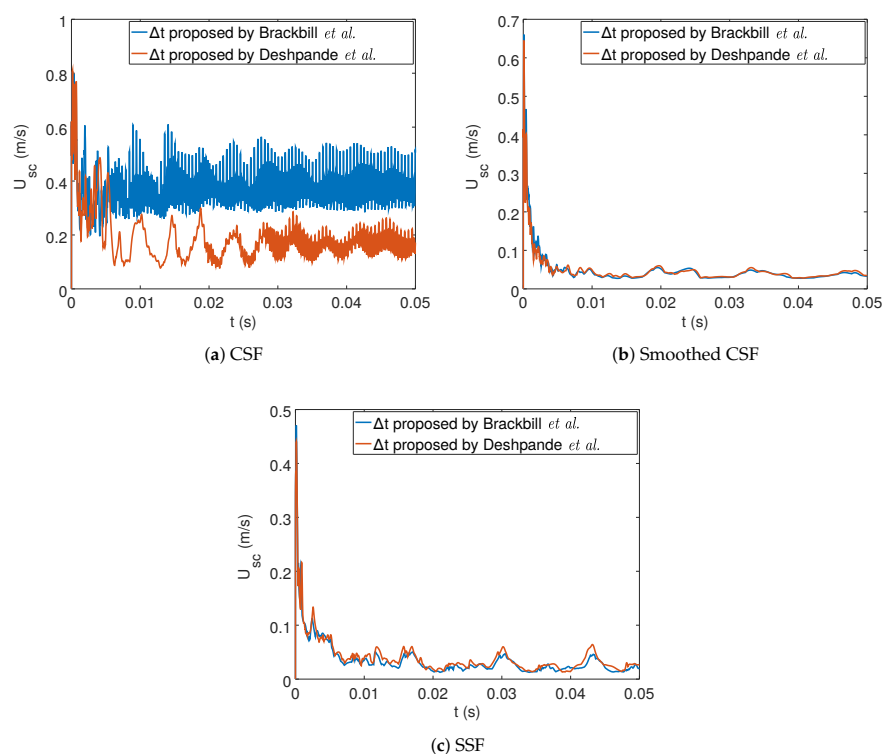


Figure 10. Evolution of spurious currents for various surface tension models.

Table 13. Comparison of spurious currents for the time stepping constraints based on M3 mesh and surface tension models (while using an under-relaxation factor of 0.9).

Surface Tension Model	$\overline{U_{sc}}$ based on Brackbill et al. [66]	$\overline{U_{sc}}$ based on Deshpande et al. [63]
CSF	0.395950	0.189170
Smoothed CSF	0.052188	0.048619
SSF	0.038550	0.040984

### 5.3. Effect of Under-Relaxation Factor

To understand the effect of under-relaxation factor, we considered a case which used an under-relaxation factor of unity for modelling the stationary bubble of 2.5 mm with M3 mesh. Table 14 provides a summary of the spurious current and the Laplace pressure in the bubble. Comparison of the results from under-relaxation factor of 0.9 (see Table 12) and 1 (see Table 14) shows that spurious currents generated by Smoothed CSF model is substantially larger when using a larger under-relaxation factor (nearly twice). The SSF model provides the least amount of spurious currents for both the under-relaxation factors and the CSF model generates larger spurious currents with larger mesh density (as described by Equation (31)). It is also worth pointing out that the evolution of spurious currents for the time step constraints provide marginally higher spurious currents for CSF model (0.1% using the time step constraint by Equation (1)) but the Smoothed CSF and SSF models show a spurious current reduction by nearly 10% and 11%, respectively (see Table 15). Based on the evolution of spurious currents based on time step constraint, the SSF model generates the least spurious current when compared to Smoothed CSF and CSF models.

**Table 14.** Comparison of spurious currents based on mesh and surface tension models (using no under-relaxation and time step dictated by Deshpande et al. [63]).

Surface Tension Model	Mesh	$\overline{U}_{sc}$	$Ca = \frac{\rho v_1 \overline{U}_{sc}}{\sigma}$	$\overline{\Delta p_c}$	$\overline{E}(\Delta p_c)$	Mass Imbalance
CSF	M0	0.158	0.002	22.27	−0.20	0
	M1	0.279	0.004	23.09	−0.18	0
	M2	0.510	0.007	24.34	−0.13	0
	M3	0.723	0.010	24.47	−0.13	0
Smoothed CSF	M0	0.154	0.002	24.02	−0.14	0
	M1	0.122	0.002	24.97	−0.11	0
	M2	0.104	0.001	25.21	−0.10	0
	M3	0.075	0.001	26.03	−0.07	0
SSF	M0	0.042	0.001	24.07	−0.14	0
	M1	0.065	0.001	24.86	−0.11	0
	M2	0.033	0.000	26.04	−0.07	0
	M3	0.036	0.001	25.64	−0.08	0

**Table 15.** Comparison of spurious currents for the time stepping constraints based on M3 mesh and surface tension models (while providing no under-relaxation to the flow variables).

Surface Tension Model	$\overline{U}_{sc}$ based on Brackbill et al. [66]	$\overline{U}_{sc}$ based on Deshpande et al. [63]
CSF	0.722930	0.723390
Smoothed CSF	0.082800	0.075458
SSF	0.040016	0.035903

## 6. Conclusions

In the study, we successfully implemented CSF, Smoothed CSF and SSF models in OpenFOAM and compared them based on their ability to simulate a two-dimensional stationary bubble, rising bubbles and capillary rise. The flow scenarios modelled corresponds to a variety of capillary numbers (in the order of  $10^{-3}$ , 0.1 and 1), which is relevant in various industrial processes. The numerical simulations show that:

- For a stationary bubble with a 2.5 mm radius, CSF and SSF models generate the most and least amount of spurious currents, respectively. For the finest mesh used, Smoothed CSF and SSF models reduce spurious currents by nearly one-tenth and one-twentieth of the CSF model (when no under-relaxation factor is used), respectively. When using a lower under-relaxation

factor (for the finest mesh), Smoothed CSF and SSF models reduce the spurious currents by approximately one-fourth of the CSF model.

- The time step constraints proposed by Brackbill et al. [66] and Deshpande et al. [63] show that spurious currents generated by the CSF is significantly reduced while using a lower under-relaxation factor. In Smoothed CSF and SSF models, when using the same under-relaxation factor, the time step constraint slightly reduces the spurious currents by 6–7%. Interestingly, when no under-relaxation is used, the CSF model generates marginally larger (nearly 0.1%) spurious currents with the time step constraint proposed by Deshpande et al. [63], but other models show a reduction in spurious current by less than 10%.
- The Laplace pressure in the bubbles predicted by Smoothed CSF and SSF is more accurate with an error of 7–9% for the higher mesh densities than CSF model with negligible imbalance in mass of the phases.
- Although using a lower under-relaxation factor reduces the spurious currents and predicts the Laplace pressure in the stationary bubble (for all the surface tension models considered) quite reasonably, it can adversely effect the accuracy of dynamic cases such as rising bubbles by underestimating the flow variables.
- Using a higher mesh density results in larger spurious currents for CSF model but they are reduced for both Smoothed CSF and SSF models for the static case considered.
- The effect of mesh resolution was studied only for the stationary bubble in this work. For the case of rising bubbles, previous works [36,55], using the CSF model, reported challenges in achieving a mesh independent solution. Similarly, for capillary rise using the CSF model, Yamamoto et al. [36] reported an increasing error when using a finer mesh. The meshes used in this paper correspond to the finest grid (used in FreeLIFE solver) implemented by Hysing et al. [54] and the grid that provided a most accurate model for capillary rise in the work by Yamamoto et al. [36]. We expect similar effects of mesh resolution for both Smoothed CSF and SSF models for dynamic cases, as they are variants of the same formulation. The quantification of these errors will be treated in future work.
- Rising bubbles were successfully modelled using the surface tension models and validated based on the final bubble shape and rising velocities proposed by Hysing et al. [54] and Klostermann et al. [55].
- Modelling the capillary rise with SSF was shown to provide a more accurate representation than the CSF model. Interestingly, the Smoothed CSF could not reliably simulate capillary rise due to spurious currents.

Although the surface tension models considered in this study did not eliminate spurious currents entirely, the comparison provides insights into the limitations of these models. Based on the simulations done in this study, the SSF model seems to provide a versatile surface tension formulation that generates small spurious currents and provides a more accurate representation of various processes in comparison to the standard CSF model.

**Supplementary Materials:** The following are available online at <https://www.mdpi.com/2227-9717/7/8/542/s1>.

**Author Contributions:** K.J.V. built the models, ran the simulations, post-processed and analysed the results, and wrote the manuscript. K.E.E. contributed in supervising, reviewing of the results and revising manuscript.

**Funding:** We would also like to thank the Department of Material Science and Engineering, NTNU, for funding this research.

**Acknowledgments:** The authors would like to thank the OpenFOAM community (both developers and contributors). We would also like to thank the reviewers whose comments improved the manuscript.

**Conflicts of Interest:** The authors declare no conflict of interest. The funding organisation had no role in the design of the study; in the collection, analyses, or interpretation of data; in the writing of the manuscript, or in the decision to publish the results.

## References

1. Basaran, O.A.; Gao, H.; Bhat, P.P. Nonstandard inkjets. *Annu. Rev. Fluid Mech.* **2013**, *45*, 85–113. [[CrossRef](#)]
2. Clark, I.C.; Abate, A.R. Microfluidic bead encapsulation above 20 kHz with triggered drop formation. *Lab Chip* **2018**, *18*, 3598–3605. [[CrossRef](#)] [[PubMed](#)]
3. Jomy Vachaparambil, K. An Analytical and Numerical Study of Droplet Formation and Break-off for Jetting of Dense Suspensions. Master's Thesis, KTH, School of Engineering Sciences (SCI), Mechanics, Stockholm, Sweden, 2016.
4. Valette, R.; Hachem, E.; Khalloufi, M.; Pereira, A.; Mackley, M.; Butler, S. The effect of viscosity, yield stress, and surface tension on the deformation and breakup profiles of fluid filaments stretched at very high velocities. *J. Non-Newton. Fluid Mech.* **2019**, *263*, 130–139. [[CrossRef](#)]
5. Høst-Madsen, J.; Jensen, K.H. Laboratory and numerical investigations of immiscible multiphase flow in soil. *J. Hydrol.* **1992**, *135*, 13–52. [[CrossRef](#)]
6. Muggerridge, A.; Cockin, A.; Webb, K.; Frampton, H.; Collins, I.; Moulds, T.; Salino, P. Recovery rates, enhanced oil recovery and technological limits. *Philos. Trans. Royal Soc. A Math. Phys. Eng. Sci.* **2014**, *372*, 20120320. [[CrossRef](#)] [[PubMed](#)]
7. Osborn, J.L.; Lutz, B.; Fu, E.; Kauffman, P.; Stevens, D.Y.; Yager, P. Microfluidics without pumps: reinventing the T-sensor and H-filter in paper networks. *Lab Chip* **2010**, *10*, 2659–2665. [[CrossRef](#)] [[PubMed](#)]
8. Brussieux, C.; Viers, P.; Roustan, H.; Rakib, M. Controlled electrochemical gas bubble release from electrodes entirely and partially covered with hydrophobic materials. *Electrochimica Acta* **2011**, *56*, 7194–7201. [[CrossRef](#)]
9. Guan, P.; Jia, L.; Yin, L.; Tan, Z. Effect of bubble contact diameter on bubble departure size in flow boiling. *Exp. Heat Transf.* **2016**, *29*, 37–52. [[CrossRef](#)]
10. Clift, R.; Grace, J.; Weber, M. *Bubbles, Drops, and Particles*; Dover Civil and Mechanical Engineering Series; Dover Publications: Mineola, NY, USA, 2005.
11. Vuorinen, V.A.; Hillamo, H.; Kaario, O.; Nuutinen, M.; Larmi, M.; Fuchs, L. Effect of droplet size and atomization on spray formation: A priori study using large-eddy simulation. *Flow Turbul. Combust.* **2011**, *86*, 533–561. [[CrossRef](#)]
12. Hilz, E.; Vermeer, A.W. Spray drift review: The extent to which a formulation can contribute to spray drift reduction. *Crop Prot.* **2013**, *44*, 75–83. [[CrossRef](#)]
13. Bouffard, J.; Kaster, M.; Dumont, H. Influence of process variable and physicochemical properties on the granulation mechanism of mannitol in a fluid bed top spray granulator. *Drug Dev. Ind. Pharm.* **2005**, *31*, 923–933. [[CrossRef](#)] [[PubMed](#)]
14. Gallino, G.; Gallaire, F.; Lauga, E.; Michelin, S. Physics of Bubble-Propelled Microrockets. *Adv. Funct. Mater.* **2018**, *28*, 1800686. [[CrossRef](#)]
15. Vachaparambil, K.J.; Einarsrud, K.E. Analysis of bubble nucleation mechanisms in supersaturated solutions: A macroscopic perspective. *Meet. Abstr.* **2018**, *MA2018-01*, 1366.
16. Vachaparambil, K.J.; Einarsrud, K.E. Explanation of bubble nucleation mechanisms: A gradient theory approach. *J. Electrochem. Soc.* **2018**, *165*, E504–E512. [[CrossRef](#)]
17. Xu, W.; Lan, Z.; Peng, B.; Wen, R.; Ma, X. Heterogeneous nucleation capability of conical microstructures for water droplets. *RSC Adv.* **2015**, *5*, 812–818. [[CrossRef](#)]
18. Alexiadis, A.; Dudukovic, M.; Ramachandran, P.; Cornell, A.; Wanggård, J.; Bokkers, A. Liquid–gas flow patterns in a narrow electrochemical channel. *Chem. Eng. Sci.* **2011**, *66*, 2252–2260. [[CrossRef](#)]
19. Gupta, A.; Roy, S. Euler–Euler simulation of bubbly flow in a rectangular bubble column: Experimental validation with Radioactive Particle Tracking. *Chem. Eng. J.* **2013**, *225*, 818–836. [[CrossRef](#)]
20. Shams, E.; Finn, J.; Apte, S.V. A numerical scheme for Euler–Lagrange simulation of bubbly flows in complex systems. *Int. J. Numer. Methods Fluids* **2011**, *67*, 1865–1898. [[CrossRef](#)]
21. Legendre, D.; Zevenhoven, R. A numerical Euler–Lagrange method for bubble tower CO<sub>2</sub> dissolution modeling. *Chem. Eng. Res. Des.* **2016**, *111*, 49–62. [[CrossRef](#)]
22. Tuković, Ž.; Jasak, H. A moving mesh finite volume interface tracking method for surface tension dominated interfacial fluid flow. *Comput. Fluids* **2012**, *55*, 70–84. [[CrossRef](#)]
23. Charin, A.; Tuković, Ž.; Jasak, H.; Silva, L.; Lage, P. A moving mesh interface tracking method for simulation of liquid–liquid systems. *J. Comput. Phys.* **2017**, *334*, 419–441. [[CrossRef](#)]

24. Menon, S.; Mooney, K.G.; Stapf, K.; Schmidt, D.P. Parallel adaptive simplicial re-meshing for deforming domain CFD computations. *J. Comput. Phys.* **2015**, *298*, 62–78. [[CrossRef](#)]
25. Hirt, C.; Nichols, B. Volume of fluid (VOF) method for the dynamics of free boundaries. *J. Comput. Phys.* **1981**, *39*, 201–225. [[CrossRef](#)]
26. Chang, Y.; Hou, T.; Merriman, B.; Osher, S. A Level Set Formulation of Eulerian Interface Capturing Methods for Incompressible Fluid Flows. *J. Comput. Phys.* **1996**, *124*, 449–464. [[CrossRef](#)]
27. Jacqmin, D. Calculation of Two-Phase Navier–Stokes Flows Using Phase-Field Modeling. *J. Comput. Phys.* **1999**, *155*, 96–127. [[CrossRef](#)]
28. Peskin, C.S. Flow patterns around heart valves: A numerical method. *J. Comput. Phys.* **1972**, *10*, 252–271. [[CrossRef](#)]
29. Pivello, M.; Villar, M.; Serfaty, R.; Roma, A.; Silveira-Neto, A. A fully adaptive front tracking method for the simulation of two phase flows. *Int. J. Multiph. Flow* **2014**, *58*, 72–82. [[CrossRef](#)]
30. Cubos-Ramírez, J.; Ramírez-Cruz, J.; Salinas-Vázquez, M.; Vicente-Rodríguez, W.; Martínez-Espinosa, E.; Lagarza-Cortes, C. Efficient two-phase mass-conserving level set method for simulation of incompressible turbulent free surface flows with large density ratio. *Comput. Fluids* **2016**, *136*, 212–227. [[CrossRef](#)]
31. Yue, P.; Zhou, C.; Feng, J.J. Spontaneous shrinkage of drops and mass conservation in phase-field simulations. *J. Comput. Phys.* **2007**, *223*, 1–9. [[CrossRef](#)]
32. Samkhaniani, N.; Ansari, M. Numerical simulation of bubble condensation using CF-VOF. *Prog. Nucl. Energy* **2016**, *89*, 120–131. [[CrossRef](#)]
33. Baltussen, M.; Kuipers, J.; Deen, N. A critical comparison of surface tension models for the volume of fluid method. *Chem. Eng. Sci.* **2014**, *109*, 65–74. [[CrossRef](#)]
34. Patel, H.; Kuipers, J.; Peters, E. Computing interface curvature from volume fractions: A hybrid approach. *Comput. Fluids* **2018**, *161*, 74–88. [[CrossRef](#)]
35. Jafari, A.; Shirani, E.; Ashgriz, N. An improved three-dimensional model for interface pressure calculations in free-surface flows. *Int. J. Comput. Fluid Dyn.* **2007**, *21*, 87–97. [[CrossRef](#)]
36. Yamamoto, T.; Okano, Y.; Dost, S. Validation of the S-CLSVOF method with the density-scaled balanced continuum surface force model in multiphase systems coupled with thermocapillary flows. *Int. J. Numer. Methods Fluids* **2017**, *83*, 223–244. [[CrossRef](#)]
37. Gerlach, D.; Tomar, G.; Biswas, G.; Durst, F. Comparison of volume-of-fluid methods for surface tension-dominant two-phase flows. *Int. J. Heat Mass Transf.* **2006**, *49*, 740–754. [[CrossRef](#)]
38. Yokoi, K. A practical numerical framework for free surface flows based on CLSVOF method, multi-moment methods and density-scaled CSF model: Numerical simulations of droplet splashing. *J. Comput. Phys.* **2013**, *232*, 252–271. [[CrossRef](#)]
39. Yokoi, K. A density-scaled continuum surface force model within a balanced force formulation. *J. Comput. Phys.* **2014**, *278*, 221–228. [[CrossRef](#)]
40. Ningegowda, B.; Premachandran, B. A coupled level set and volume of fluid method with multi-directional advection algorithms for two-phase flows with and without phase change. *Int. J. Heat Mass Transf.* **2014**, *79*, 532–550. [[CrossRef](#)]
41. Albert, C.; Raach, H.; Bothe, D. Influence of surface tension models on the hydrodynamics of wavy laminar falling films in volume of fluid-simulations. *Int. J. Multiph. Flow* **2012**, *43*, 66–71. [[CrossRef](#)]
42. Pavuluri, S.; Maes, J.; Doster, F. Spontaneous imbibition in a microchannel: analytical solution and assessment of volume of fluid formulations. *Microfluid. Nanofluid.* **2018**, *22*, 90. [[CrossRef](#)]
43. Gumulya, M.; Utikar, R.P.; Pareek, V.; Mead-Hunter, R.; Mitra, S.; Evans, G.M. Evaporation of a droplet on a heated spherical particle. *Chem. Eng. J.* **2015**, *278*, 309–319. [[CrossRef](#)]
44. Gumulya, M.; Joshi, J.B.; Utikar, R.P.; Evans, G.M.; Pareek, V. Bubbles in viscous liquids: Time dependent behaviour and wake characteristics. *Chem. Eng. Sci.* **2016**, *144*, 298–309. [[CrossRef](#)]
45. Li, D.; Duan, X. Numerical analysis of droplet impact and heat transfer on an inclined wet surface. *Int. J. Heat Mass Transf.* **2019**, *128*, 459–468. [[CrossRef](#)]
46. Sontti, S.G.; Atta, A. Formation characteristics of Taylor bubbles in power-law liquids flowing through a microfluidic co-flow device. *J. Ind. Eng. Chem.* **2018**, *65*, 82–94. [[CrossRef](#)]
47. Wang, Z.; Yang, J.; Koo, B.; Stern, F. A coupled level set and volume-of-fluid method for sharp interface simulation of plunging breaking waves. *Int. J. Multiph. Flow* **2009**, *35*, 227–246. [[CrossRef](#)]

48. Khismatullin, D.; Renardy, Y.; Renardy, M. Development and implementation of VOF-PROST for 3D viscoelastic liquid–liquid simulations. *J. Non-Newton. Fluid Mech.* **2006**, *140*, 120–131. [[CrossRef](#)]
49. Guo, Z.; Fletcher, D.F.; Haynes, B.S. Implementation of a height function method to alleviate spurious currents in CFD modelling of annular flow in microchannels. *Appl. Math. Model.* **2015**, *39*, 4665–4686. [[CrossRef](#)]
50. Fuster, D.; Agbaglah, G.; Josserand, C.; Popinet, S.; Zaleski, S. Numerical simulation of droplets, bubbles and waves: State of the art. *Fluid Dyn. Res.* **2009**, *41*, 065001. [[CrossRef](#)]
51. Aboukhedr, M.; Georgoulas, A.; Marengo, M.; Gavaises, M.; Vogiatzaki, K. Simulation of micro-flow dynamics at low capillary numbers using adaptive interface compression. *Comput. Fluids* **2018**, *165*, 13–32. [[CrossRef](#)]
52. Raeini, A.Q.; Blunt, M.J.; Bijeljic, B. Direct simulations of two-phase flow on micro-CT images of porous media and upscaling of pore-scale forces. *Adv. Water Resour.* **2014**, *74*, 116–126. [[CrossRef](#)]
53. Liu, Q.; Palm, B. Numerical study of bubbles rising and merging during convective boiling in micro-channels. *Appl. Therm. Eng.* **2016**, *99*, 1141–1151. [[CrossRef](#)]
54. Hysing, S.; Turek, S.; Kuzmin, D.; Parolini, N.; Burman, E.; Ganesan, S.; Tobiska, L. Quantitative benchmark computations of two-dimensional bubble dynamics. *Int. J. Numer. Methods Fluids* **2009**, *60*, 1259–1288. [[CrossRef](#)]
55. Klostermann, J.; Schaake, K.; Schwarze, R. Numerical simulation of a single rising bubble by VOF with surface compression. *Int. J. Numer. Methods Fluids* **2013**, *71*, 960–982. [[CrossRef](#)]
56. Hoang, D.A.; van Steijn, V.; Portela, L.M.; Kreutzer, M.T.; Kleijn, C.R. Benchmark numerical simulations of segmented two-phase flows in microchannels using the Volume of Fluid method. *Comput. Fluids* **2013**, *86*, 28–36. [[CrossRef](#)]
57. Hardt, S.; Wondra, F. Evaporation model for interfacial flows based on a continuum-field representation of the source terms. *J. Comput. Phys.* **2008**, *227*, 5871–5895. [[CrossRef](#)]
58. Rusche, H. Computational Fluid Dynamics of Dispersed Two-Phase Flows at High Phase Fractions. Ph.D. Thesis, Imperial College London (University of London), London, UK, 2003.
59. Roenby, J.; Bredmose, H.; Jasak, H. A computational method for sharp interface advection. *Royal Soc. Open Sci.* **2016**, *3*, 160405. [[CrossRef](#)] [[PubMed](#)]
60. Scheufler, H.; Roenby, J. Accurate and efficient surface reconstruction from volume fraction data on general meshes. *J. Comput. Phys.* **2019**, *383*, 1–23. [[CrossRef](#)]
61. Cifani, P.; Michalek, W.; Priems, G.; Kuerten, J.; van der Geld, C.; Geurts, B. A comparison between the surface compression method and an interface reconstruction method for the VOF approach. *Comput. Fluids* **2016**, *136*, 421–435. [[CrossRef](#)]
62. Harvie, D.; Davidson, M.; Rudman, M. An analysis of parasitic current generation in volume of fluid simulations. *Appl. Math. Model.* **2006**, *30*, 1056–1066. [[CrossRef](#)]
63. Deshpande, S.S.; Anumolu, L.; Trujillo, M.F. Evaluating the performance of the two-phase flow solver interFoam. *Comput. Sci. Discov.* **2012**, *5*, 014016. [[CrossRef](#)]
64. Abadie, T.; Aubin, J.; Legendre, D. On the combined effects of surface tension force calculation and interface advection on spurious currents within Volume of Fluid and Level Set frameworks. *J. Comput. Phys.* **2015**, *297*, 611–636. [[CrossRef](#)]
65. Francois, M.M.; Cummins, S.J.; Dendy, E.D.; Kothe, D.B.; Sicilian, J.M.; Williams, M.W. A balanced-force algorithm for continuous and sharp interfacial surface tension models within a volume tracking framework. *J. Comput. Phys.* **2006**, *213*, 141–173. [[CrossRef](#)]
66. Brackbill, J.; Kothe, D.; Zemach, C. A continuum method for modeling surface tension. *J. Comput. Phys.* **1992**, *100*, 335–354. [[CrossRef](#)]
67. Ubbink, O. Numerical Prediction of Two Fluid Systems with Sharp Interfaces. Ph.D Thesis, Imperial College London (University of London), London, UK, 1997.
68. Heyns, J.A.; Oxtoby, O.F. Modelling surface tension dominated multiphase flows using the VOF approach. In Proceedings of 6th European Conference on Computational Fluid Dynamics, Barcelona, Spain, 20–25 July 2014.
69. Sussman, M.; Puckett, E.G. A coupled level set and volume-of-fluid method for computing 3D and axisymmetric incompressible two-phase flows. *J. Comput. Phys.* **2000**, *162*, 301–337. [[CrossRef](#)]



70. Albadawi, A.; Donoghue, D.; Robinson, A.; Murray, D.; Delauré, Y. Influence of surface tension implementation in volume of fluid and coupled volume of fluid with level set methods for bubble growth and detachment. *Int. J. Multiph. Flow* **2013**, *53*, 11–28. [[CrossRef](#)]
71. Raessi, M.; Mostaghimi, J.; Bussmann, M. A volume-of-fluid interfacial flow solver with advected normals. *Comput. Fluids* **2010**, *39*, 1401–1410. [[CrossRef](#)]
72. Renardy, Y.; Renardy, M. PROST: A Parabolic Reconstruction of Surface Tension for the Volume-of-Fluid Method. *J. Comput. Phys.* **2002**, *183*, 400–421. [[CrossRef](#)]
73. Youngs, D. Time-dependent multi-material flow with large fluid distortion. In *Numerical Methods for Fluid Dynamics*; Morton, K.W., Baines, M.J., Eds.; Academic Press: New York, USA, 1982, pp. 273–285.
74. Pilliod, J.E.; Puckett, E.G. Second-order accurate volume-of-fluid algorithms for tracking material interfaces. *J. Comput. Phys.* **2004**, *199*, 465–502. [[CrossRef](#)]
75. Popinet, S. An accurate adaptive solver for surface-tension-driven interfacial flows. *J. Comput. Phys.* **2009**, *228*, 5838–5866. [[CrossRef](#)]
76. Raeni, A.Q.; Blunt, M.J.; Bijeljic, B. Modelling two-phase flow in porous media at the pore scale using the volume-of-fluid method. *J. Comput. Phys.* **2012**, *231*, 5653–5668. [[CrossRef](#)]
77. Denner, F.; Evrard, F.; Serfaty, R.; van Wachem, B.G. Artificial viscosity model to mitigate numerical artefacts at fluid interfaces with surface tension. *Comput. Fluids* **2017**, *143*, 59–72. [[CrossRef](#)]
78. Lafaurie, B.; Nardone, C.; Scardovelli, R.; Zaleski, S.; Zanetti, G. Modelling merging and fragmentation in multiphase flows with SURFER. *J. Comput. Phys.* **1994**, *113*, 134–147. [[CrossRef](#)]
79. Galusinski, C.; Vigneaux, P. On stability condition for bifluid flows with surface tension: Application to microfluidics. *J. Comput. Phys.* **2008**, *227*, 6140–6164. [[CrossRef](#)]
80. Popinet, S. Numerical models of surface tension. *Annu. Rev. Fluid Mech.* **2018**, *50*, 49–75. [[CrossRef](#)]
81. Wang, Y.; Dandekar, R.; Bustos, N.; Poulain, S.; Bourouiba, L. Universal rim thickness in unsteady sheet fragmentation. *Phys. Rev. Lett.* **2018**, *120*, 204503. [[CrossRef](#)] [[PubMed](#)]
82. Saha, A.A.; Mitra, S.K. Effect of dynamic contact angle in a volume of fluid (VOF) model for a microfluidic capillary flow. *J. Colloid Interface Sci.* **2009**, *339*, 461–480. [[CrossRef](#)] [[PubMed](#)]
83. Issa, R. Solution of the implicitly discretised fluid flow equations by operator-splitting. *J. Comput. Phys.* **1986**, *62*, 40–65. [[CrossRef](#)]
84. Greenshields, C.J. *OpenFOAM User Guide*; Version 6; The OpenFOAM Foundation: London, UK.
85. Van Leer, B. Towards the ultimate conservative difference scheme. II. Monotonicity and conservation combined in a second-order scheme. *J. Comput. Phys.* **1974**, *14*, 361–370. [[CrossRef](#)]
86. Maki, K. Ship Resistance Simulations with OpenFOAM. In Proceedings of the 6th OpenFOAM Workshop: The Pennsylvania State University, State College, PA, USA, 13–16 June 2011.
87. Greenshields, C. OpenFOAM 2.3.0: Multiphase Modelling. 2014. Available online: <https://openfoam.org/release/2-3-0/multiphase/> (accessed on 12 August 2019).
88. Song, B.; Liu, G.R.; Lam, K.Y.; Amano, R.S. On a higher-order bounded discretization scheme. *Int. J. Numer. Methods Fluids* **2000**, *32*, 881–897. [[CrossRef](#)]
89. Min, T.; Yoo, J.Y.; Choi, H. Effect of spatial discretization schemes on numerical solutions of viscoelastic fluid flows. *J. Non-Newton. Fluid Mech.* **2001**, *100*, 27–47. [[CrossRef](#)]
90. Bullard, J.W.; Garboczi, E.J. Capillary rise between planar surfaces. *Phys. Rev. E* **2009**, *79*, 011604. [[CrossRef](#)] [[PubMed](#)]



## *Appended paper B*

### **On sharp surface force model: Effect of sharpening coefficient**

Kurian J. Vachaparambil and Kristian Etienne Einarsrud

Published in *Experimental and Computational Multiphase Flow*



## On sharp surface force model: Effect of sharpening coefficient

Kurian J. Vachaparambil (✉), Kristian Etienne Einarsrud

Department of Materials Science and Engineering, Norwegian University of Science and Technology, 7491 Trondheim, Norway

### Abstract

Amongst the multitude of approaches available in literature to reduce spurious velocities in Volume of Fluid approach, the Sharp Surface Force (SSF) model is increasingly being used due to its relative ease to implement. The SSF approach relies on a user-defined parameter, the sharpening coefficient, which determines the extent of the smeared nature of interface used to determine the surface tension force. In this paper, we use the SSF model implemented in OpenFOAM® to investigate the effect of this sharpening coefficient on spurious velocities and accuracy of dynamic, i.e., capillary rise, and static bubble simulations. Results show that increasing the sharpening coefficient generally reduces the spurious velocities in both static and dynamic cases. Although static millimeter sized bubbles were simulated with the whole range of sharpening coefficients, sub-millimeter sized bubbles show nonphysical behavior for values larger than 0.3. The accuracy of the capillary rise simulations has been observed to change non-linearly with the sharpening coefficient. This work illustrates the importance of using an optimized value of the sharpening coefficient with respect to spurious velocities and accuracy of the simulation.

### Keywords

OpenFOAM®  
spurious velocities  
two-phase flows  
Volume of Fluid

### Article History

Received: 6 January 2020

Revised: 6 March 2020

Accepted: 7 March 2020

### Research Article

© The Author(s) 2020

### 1 Introduction

Modelling surface tension dominant multiphase flows is relevant in a multitude of industrial processes like lab-on-chip, atomization, and boiling. One of the main approach to capture the interface dynamics is the Volume of Fluid method which uses the advection of scalar volume fraction based on algebraic (interface compression) or geometric (piecewise linear interface calculation or PLIC) reconstruction algorithms in order to preserve the sharpness of interfacial region (Cifani et al., 2016). The VOF based solver available in OpenFOAM®, interFoam, which generates an interface which is smeared over a few computational cells uses the interface compression method due to its relative simplicity (Deshpande et al., 2012).

In the VOF approach used in interFoam, the volume fraction field is used to determine curvature and corresponding surface tension force based on models like the widely used Continuum Surface Force (CSF) approach (Brackbill et al., 1992). Due to the smeared nature of the interface, the curvature and the pressure jump across the interface obtained from the simulations do not match the theoretical value which generates spurious velocities

(Deshpande et al., 2012). These spurious velocities introduce nonphysical flows near the interface which may cause the bubble to numerically drift as well as alter the heat/mass transfer coefficients in supersaturation and temperature driven phase change processes (Samkhaniani and Ansari, 2016; Saufi et al., 2019; Vachaparambil and Einarsrud, 2020). The works by Popinet (2018) and Deshpande et al. (2012) have reviewed the various approaches reported to mitigate these effects, namely: improved curvature estimation, force balance between surface tension and pressure gradient (for static cases), time step constraint when surface tension is calculated explicitly and temporally implicit approach to estimate surface tension.

Amongst the approaches proposed, the Sharp Surface Force model, developed by Raeini et al. (2012), estimates surface tension based on a smoothed interface curvature and a sharpened interface region defined using a user defined sharpening coefficient ( $C_{sh}$ ). This model, which is relatively simple to implement compared to height function based approach (Pavuluri et al., 2018), has been shown to reduce spurious velocities in comparison to commonly used CSF model (Pavuluri et al., 2018; Vachaparambil and Einarsrud, 2019a). The SSF model,

✉ kurian.j.vachaparambil@ntnu.no, kurian\_jomy@hotmail.com

using  $C_{sh} \in [0, 0.5]$ , has been used to simulate dynamic cases like rising bubbles (Vachaparambil and Einarsrud, 2019a), microfluidic T-junction (Soh et al., 2016), microchannels (Pavuluri et al., 2018), capillary rise (Raeini et al., 2012; Vachaparambil and Einarsrud, 2019a), interfacial mass transfer (Maes and Soulaire, 2018), and bubble growth (Vachaparambil and Einarsrud, 2020) whereas when modelling static cases, like stationary millimeter sized bubble,  $C_{sh}$  is set equal to 0.98 (Vachaparambil and Einarsrud, 2019a). The choice of the value  $C_{sh}$  used in the simulations is often heuristic and to the best knowledge of the authors there has not been a systematic attempt to quantify the effect of this user-defined parameter.

In this paper, we investigate the effect of the sharpening coefficient used in the SSF model, as developed on OpenFOAM<sup>®</sup> 6 by Vachaparambil and Einarsrud (2019a), to model two dimensional dynamic cases like capillary rise and static cases like millimeter and sub-millimeter bubbles. All the simulations discussed in this work use the sharpening coefficient typically used in simulating practical flow scenarios, i.e.,  $0 \leq C_{sh} \leq 0.5$  (based on the values used in Raeini et al. (2012), Soh et al. (2016), Maes and Soulaire (2018), Pavuluri et al. (2018), Vachaparambil and Einarsrud (2019a), Vachaparambil and Einarsrud (2020)).

## 2 Governing equations

The volume fraction ( $\alpha_i$ ) used in VOF method is a scalar field that is zero in gas phase, unity in the liquid phase, and  $0 < \alpha_i < 1$  at the interface. The interface dynamics is captured based on the advection of  $\alpha_i$  as

$$\frac{\partial \alpha_i}{\partial t} + \nabla \cdot (U \alpha_i) + \nabla \cdot (\alpha_i (1 - \alpha_i) U_r) = 0 \quad (1)$$

where  $U$  is the velocity in both phases and the third term is the interface compression term that acts in the interfacial region to prevent excessive smearing using  $U_r$  which is defined as

$$U_r = C_\alpha \left| \frac{\phi}{S_f} \right| \mathbf{n} \quad (2)$$

where  $C_\alpha$ ,  $\phi$ ,  $S_f$ , and  $\mathbf{n}$  represent adjustable compression factor (set equal to unity as recommended by Greenshields (2019)), volumetric flux across the cell face, cell face surface area, and unit normal to interface respectively (Deshpande et al., 2012). The fluid properties like density ( $\rho$ ) and viscosity ( $\mu$ ) are calculated as

$$\chi = \chi_1 \alpha_1 + \chi_2 \alpha_2, \text{ where } \chi \in [\rho, \mu] \quad (3)$$

where  $\alpha_2 = 1 - \alpha_1$ . The mass conservation of the incom-

pressible phases is described using continuity equation as

$$\nabla \cdot U = 0 \quad (4)$$

The momentum equation is written based on a modified pressure ( $p_{rgh}$ ), defined as  $p_{rgh} = p - \rho \mathbf{g} \cdot \mathbf{x}$ , as

$$\begin{aligned} \frac{\partial \rho U}{\partial t} + \nabla \cdot \rho U U &= -\nabla p_{rgh} - \mathbf{g} \cdot \mathbf{x} \nabla \rho \\ &+ \nabla \cdot \mu (\nabla U + \nabla U^T) + F_{ST} \end{aligned} \quad (5)$$

where  $F_{ST}$  is the surface tension modelled based on SSF described in Vachaparambil and Einarsrud (2019a) and Raeini et al. (2012). Initially, a smoothed volume fraction is obtained using a three consecutive smoothing steps ( $i = 1, 2, 3$ ) as

$$\alpha_{i+1}^s = C \langle \alpha_i^s \rangle_{c-f} + (1 - C) \alpha_i^s \quad (6)$$

where  $\alpha_i^s = \alpha_i$ ,  $C$  is equal to 0.5, and  $\langle \alpha_i \rangle_{c-f}$  represents the interpolation of  $\alpha_i$  from cell center to face. The unit normal to the smoothed interface is calculated and corrected for the effects of contact angle, see Vachaparambil and Einarsrud (2019a). Subsequently an initial estimate of curvature is calculated as

$$\kappa_1 = -\nabla \cdot \frac{\nabla \alpha_1^s}{|\nabla \alpha_1^s| + \delta} \quad (7)$$

where  $\delta$ , defined as  $10^{-8} / \left( \frac{\sum_N V_i}{N} \right)^{1/3}$ , is used to prevent denominator from becoming zero. The curvature is smoothed using a two step procedure ( $i=1, 2$ ) as

$$\kappa_{i+1}^s = 2\sqrt{A} \kappa_i + (1 - 2\sqrt{A}) \frac{\langle w \kappa_i^s \rangle_{c-f}}{\langle w \rangle_{c-f}} \quad (8)$$

where  $\kappa_i^s = \kappa_i$ ,  $w = \sqrt{A + 0.001}$ , and  $A = \min(1, \max(\alpha_1, 0))(1 - \min(1, \max(\alpha_1, 0)))$ . The final curvature is calculated as

$$\kappa_{\text{final}} = \frac{\langle w \kappa_2^s \rangle_{c-f}}{\langle w \rangle_{c-f}} \quad (9)$$

The surface tension is estimated based on  $F_{ST} = \sigma \kappa_{\text{final}} \cdot \nabla \alpha_{sh}$ , where  $\alpha_{sh}$  is

$$\alpha_{sh} = \frac{1}{1 - C_{sh}} \left[ \min(\max(\alpha_1, \frac{C_{sh}}{2}), 1 - \frac{C_{sh}}{2}) - \frac{C_{sh}}{2} \right] \quad (10)$$

where  $C_{sh}$  is the sharpening coefficient which when equal to zero produces  $\alpha_{sh}$  that is equivalent to  $\alpha_1$ . Due to the coupled nature of Eq. (4) and Eq. (5), these equations are solved by Pressure-Implicit with Splitting of Operators (PISO) algorithm (Deshpande et al., 2012). PISO algorithm involves estimation of a predicted velocity that is used to

calculate pressure, using pressure correction equation, which is used to update the velocity in an iterative manner (Deshpande et al., 2012). In order to reduce spurious velocities, the force balance between pressure gradient, surface tension, and gravitational force due to discretization is ensured by calculating the gradients at cell faces as described in Deshpande et al. (2012). However the iterative procedure used to solve  $p_{\text{rgh}}$ , i.e., the PISO algorithm, converges based on a user defined tolerance (Deshpande et al., 2012). This tolerance, required to calculate  $p_{\text{rgh}}$ , introduces a force imbalance between surface tension, gravitational force, and pressure gradient which can be reduced by setting a very low convergence criterion, like  $10^{-20}$  used in Table 1, as recommended by Deshpande et al. (2012).

### 3 Computational domain and solver settings

The governing equations are discretized using first and second order methods in time and space respectively, see Vachaparambil and Einarsrud (2019a), and solved based on methods described in Table 1. Other numerical settings like the sub-cycling of volume fraction equation and momentum predictor, which are relevant in solving the governing equations, are set based on OpenFOAM® default settings/recommendations for simulating multiphase flows which has also been used in Vachaparambil and Einarsrud (2019a). The simulations are run with no under-relaxation factor and maximum time step is calculated as

$$\Delta t \leq \frac{1}{2} \left( C_2 \tau_\mu + \sqrt{(C_2 \tau_\mu)^2 + 4C_1 \tau_p^2} \right)$$

$$\text{and } \Delta t \leq \max(C_2 \tau_\mu, 10C_1 \tau_p) \quad (11)$$

where  $C_1 = 0.01$ ,  $C_2 = 10$ ,  $\tau_\mu = \mu_{\text{avg}} \Delta x / \sigma$ , and  $\tau_p = \sqrt{\rho_{\text{avg}} (\Delta x)^3 / \sigma}$ .  $\mu_{\text{avg}}$  and  $\rho_{\text{avg}}$  are defined as the average dynamic viscosity and density between the phases and  $\Delta x$  is the mesh resolution used in the simulations (Deshpande et al., 2012; Vachaparambil and Einarsrud, 2019a).

The fluid properties used in the both capillary rise and stationary bubble simulations are  $\rho_1 = 1000 \text{ kg/m}^3$ ,  $\rho_2 = 1 \text{ kg/m}^3$ ,  $\nu_1 = 10^{-6} \text{ m}^2/\text{s}$ ,  $\nu_2 = 1.48 \times 10^{-5} \text{ m}^2/\text{s}$ , and  $\sigma = 0.07 \text{ N/m}$ . The capillary rise simulations use  $|\mathbf{g}|$  equal to  $10 \text{ m/s}^2$  whereas stationary bubble simulations neglect gravity (Yamamoto et al., 2017; Vachaparambil and Einarsrud, 2019a).

The computational domain used for the capillary rise simulations is  $20 \text{ mm} \times 1 \text{ mm}$  and meshed with a hexahedral grid of  $400 \times 20$ . This mesh is chosen based on the work by Yamamoto et al. (2017) that investigated the

**Table 1** Solvers used for the discretized equation (Greenshields, 2019)

Equation	Linear solver	Smoother/preconditioner	Tolerance
Pressure correction equation	PCG	GAMG	$10^{-20}$
Momentum equation	smoothSolver	symGaussSeidel	$10^{-10}$
Volume fraction equation	smoothSolver	symGaussSeidel	$10^{-10}$

effect of grid resolution on the accuracy of the capillary rise simulations. The boundary conditions used for  $\alpha_1$  is zero gradient at the outlet, Dirichlet condition equal to one at inlet, and zero gradient with a constant contact angle of  $45^\circ$  at the side boundaries. The modified pressure ( $p_{\text{rgh}}$ ) uses Dirichlet condition, equal to zero, at inlet and outlet but the side walls are assigned the zero gradient condition. The boundary conditions for  $\mathbf{U}$  at side boundaries are set as no slip whereas the inlet and outlet are assigned a pressure-inlet outlet velocity condition (Greenshields, 2019). The simulations are initialized with liquid column at a height of  $8 \text{ mm}$  (from the inlet) in the computational domain. These simulations are run until  $1.5 \text{ s}$  which is enough to reach steady capillary rise height with maximum time step, calculated based on Eq. (11), equal to  $3.5 \mu\text{s}$ .

In order to model a stationary bubble of radius  $R$ , which is initialized at the center of a square computational domain of dimensions  $4R \times 4R$ , gravity is neglected. The four boundaries are assigned zero gradient condition for  $\mathbf{U}$  and  $\alpha_1$  but the  $p_{\text{rgh}}$  employs a Dirichlet condition equal to the operating pressure (equal to  $101,325 \text{ Pa}$ ). The bubbles modelled in this work are a millimeter sized bubble of radius equal to  $2.5 \text{ mm}$  and a sub-millimeter bubble of radius equal to  $0.25 \text{ mm}$ . These simulations are run until  $0.05 \text{ s}$  and the corresponding time step constraints based on the mesh resolution are discussed in Section 4.2 and Section 4.3.

## 4 Results and discussions

In order compare the results from the dynamic and static simulations, spurious velocities, denoted by  $U_{\text{sc}}$ , are calculated as  $\max(|\mathbf{U}|)$ . The time averaging of an arbitrary parameter  $\Phi$  and spurious velocities are represented as with an over bar as  $\bar{\Phi}$  and  $\bar{U}_{\text{sc}}$  respectively.

### 4.1 Capillary rise

For 2D capillary rise, the equilibrium height ( $h_T$ ) at which when gravitational force balance the vertical component of surface tension force for a liquid column rising between two parallel plates can be theoretical calculated as

$$h_T = \frac{2\sigma \cos\theta}{\Delta\rho |\mathbf{g}| t} \quad (12)$$

where  $\theta$ ,  $t$ , and  $\Delta\rho$  are the contact angle, distance between parallel plates (equal to 1 mm), and difference between densities of the phases respectively (Bullard and Garboczi, 2009).  $h_T$ , based on Eq. (12), is equal to 9.91 mm and the capillary rise height from the simulations is calculated as

$$h_s = \frac{\int_s \alpha_i dS}{t} \quad (13)$$

where the numerator represents the area of the liquid in the computational domain.

The capillary rise from the simulations is compared to Eq. (12) in Table 2. The temporal evolution of the capillary rise heights and spurious velocities ( $U_{sc}$ ) are plotted in Fig. 1 and Fig. 2 respectively. Although  $h_s$  obtained from the simulations stabilize after the initial transients, the capillary rise height obtained with  $C_{sh} = 0.3$  oscillates slightly, by approximately  $9.30 \pm 0.009$  mm, as shown in Fig. 1. This oscillation in the interface position, using  $C_{sh} = 0.3$ , also cause the periodic variation of  $U_{sc}$  which is shown in Fig. 2. As the oscillations in capillary rise height are lower than  $\pm 0.1\%$  of the capillary rise height, we assume that the simulations have converged reasonably.  $h_s$  obtained when using  $C_{sh} = 0.5$  matches the capillary rise height reported by Vachaparambil and Einarsrud (2019a) using SSF model. It is also worth pointing out that  $U_{sc}$  obtained using  $C_{sh} = 0.0$  is an order larger than spurious velocities obtained with other values of sharpening coefficients, see Table 2 and Fig. 2.

#### 4.2 Millimeter sized stationary bubble

The Laplace pressure in a 2D bubble can be theoretically calculated using the Young–Laplace equation as

$$\Delta p_T = \frac{\sigma}{R} \quad (14)$$

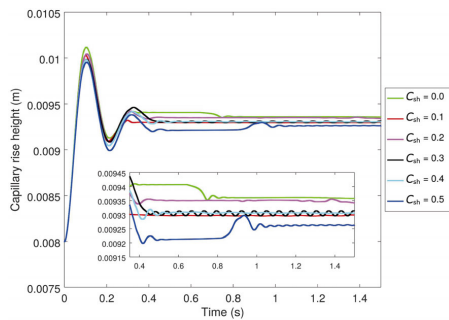


**Fig. 1** Temporal evolution of capillary rise height, calculated based on Eq. (13), for various values of sharpening coefficients ( $C_{sh}$ ).

**Table 2** Variation of capillary rise height with sharpening coefficients

$C_{sh}$	$U_{sc}  _{t=1.5s}$ (m/s)	$h_s$ (mm)	$E(h) = (h_T - h_s) / h_T$
0.0	0.1810	9.36	0.056
0.1	0.0098	9.30	0.062
0.2	0.0097	9.34	0.057
0.3	0.0050	9.30	0.061
0.4	0.0041	9.31	0.061
0.5	0.0031	9.26	0.065

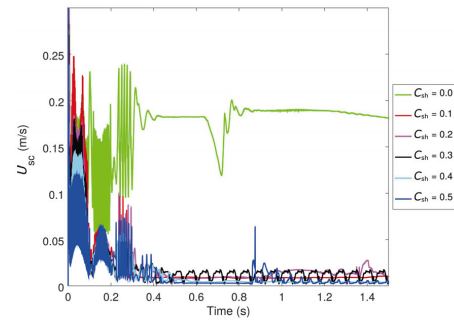


**Fig. 2** Temporal evolution of spurious velocities ( $U_{sc}$ ) during capillary rise simulations for various values of sharpening coefficients ( $C_{sh}$ ).

which for the bubble radius of 2.5 mm in the simulation is equal to 28 Pa. For simulations, the Laplace pressure in the bubble is calculated as

$$\Delta p_s = \frac{\int_V \alpha_2 p dV}{\int_V \alpha_2 dV} - p_0 \quad (15)$$

where  $p_0$  is the operating pressure (equal to 101,325 Pa). The mesh resolution and the time step constraints (calculated based on Eq. (11)) used in the simulations are summarized in Table 3.

The stationary millimeter bubble has been modelled with the three meshes as well as for a range of sharpening coefficients between 0 and 0.5, see Table 4 and Fig. 3. Spurious velocities are observed on both sides of the interface for all the cases modelled, as illustrated in Fig. 3. The use of larger sharpening coefficients seems to reduce the error in calculating Laplace pressure as well as spurious velocities in the simulations, see Table 4. Decreasing the mesh size does not always exacerbate spurious velocities which is contrast to the increasing  $U_{sc}$  observed with CSF model in the work by Deshpande et al. (2012) and Vachaparambil and Einarsrud (2019a). The variation between  $U_{sc}$  reported in Table 4 and the work by Vachaparambil and

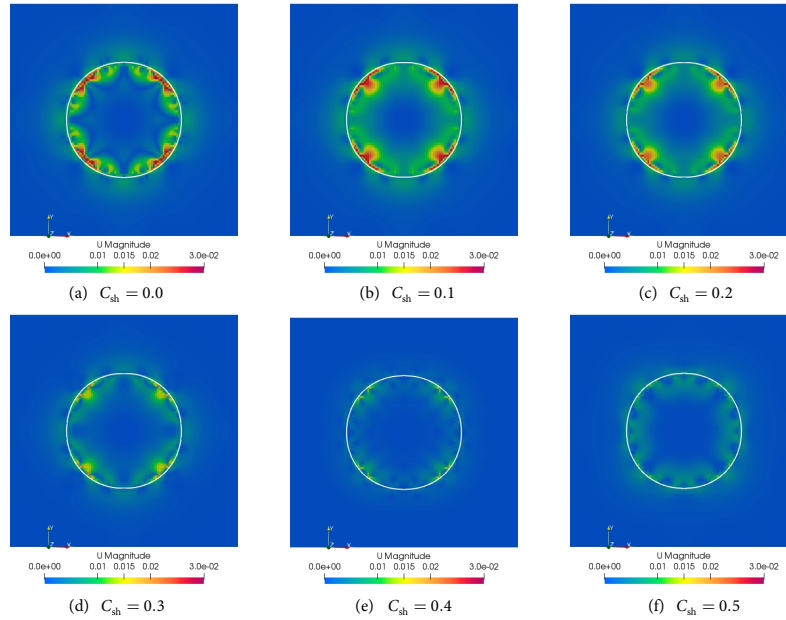


**Fig. 3** Magnitude of velocity (m/s) at  $t = 0.05$  s observed in the simulations of millimeter sized bubble for mesh M3 for various values of  $C_{sh}$ . The white contour represents the interface at  $\alpha_1 = 0.5$ .

**Table 3** Details of mesh and the associated maximum time step, calculated based on Eq. (11), used for stationary bubble simulations

Mesh	Mesh resolution (mm <sup>2</sup> )	Total number of cells	$2R / \delta x^*$	Maximum time step (s)
M1	0.25×0.25	1600	20	$3 \times 10^{-5}$
M2	0.125×0.125	6400	40	$1 \times 10^{-5}$
M3	0.083×0.083	14400	60	$6 \times 10^{-6}$

\*  $2R / \delta x$  is the ratio of the bubble diameter (equal to 5 mm) and the cell size.

Einarsrud (2019a) is due to the difference in the  $C_{sh}$  and solver setting, in Table 1, used for the simulations.

### 4.3 Sub-millimeter sized stationary bubble

A value of  $2R / \delta x$  around 50–60 is typically used in thermal and supersaturation driven phase change processes (Samkhaniani and Ansari, 2016). Consequently, a sub-millimeter bubble, of radius equal to 0.25 mm, is initialized in a 1 mm<sup>2</sup> domain that is meshed by 120×120 cells and the corresponding maximum time step, calculated

**Table 4** Variation of the time averaged spurious velocities (m/s), Laplace pressure (Pa), and associated error, calculated as  $E(\overline{\Delta p_s}) = (\Delta p_T - \overline{\Delta p_s}) / \Delta p_T$ , with sharpening coefficients and meshes

$C_{sh}$	Mesh M1			Mesh M2			Mesh M3		
	$\overline{U}_{sc}$	$\overline{\Delta p_s}$	$E(\overline{\Delta p_s})$	$\overline{U}_{sc}$	$\overline{\Delta p_s}$	$E(\overline{\Delta p_s})$	$\overline{U}_{sc}$	$\overline{\Delta p_s}$	$E(\overline{\Delta p_s})$
0.0	0.110	24.008	0.143	0.075	25.096	0.104	0.061	25.596	0.086
0.1	0.077	24.173	0.137	0.051	25.111	0.103	0.054	25.651	0.084
0.2	0.070	24.644	0.120	0.044	25.118	0.103	0.048	25.679	0.083
0.3	0.065	24.784	0.115	0.039	25.123	0.103	0.042	25.676	0.083
0.4	0.060	24.822	0.113	0.036	25.123	0.103	0.037	25.668	0.083
0.5	0.056	24.845	0.113	0.034	25.132	0.102	0.034	25.700	0.082



based on Eq. (11), is set at  $0.6 \mu\text{s}$ .

The Laplace pressure in the sub-millimeter bubble, equal to 280 Pa, is compared to the corresponding value obtained from simulations in Table 5. The sub-millimeter bubble could be modelled with  $C_{sh} \leq 0.3$ , see Fig. 4 and Fig. 5, but for sharpening coefficient of 0.4 and 0.5 the bubble numerically drifts. For  $C_{sh} \leq 0.2$ , the interface undergoes slight periodic deformation which is reflected in the oscillations in  $U_{sc}$  observed in Fig. 6. This deformation is not substantial enough to observe a noticeable deviation from the circular bubble shape, see Fig. 4. At  $t = 0.05$  s, the simulations using  $C_{sh} = 0.3$  seems to have very low spurious velocities on both sides of the interface when compared to other sharpening coefficients, see Fig. 5.

## 5 Conclusions

The effect of sharpening coefficient used in Sharp Surface Force model, developed in the work by Vachaparambil and Einarsrud (2019a), is investigated for capillary rise and stationary bubbles of radii equal to 0.25 and 2.5 mm. The solver ensures force balance between pressure gradient, surface tension, and gravitational force due to discretization

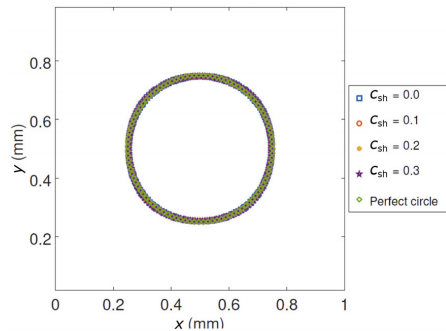


**Fig. 4** Bubble morphology, represented by  $\alpha_1 = 0.5$ , at  $t = 0.05$  s for values of sharpening coefficients compared with a theoretically perfect 2D bubble of radius equal to 0.25 mm.

**Table 5** Time averaged spurious velocities, Laplace pressure, and associated error (calculated as  $E(\Delta p_s) = (\Delta p_T - \overline{\Delta p_s}) / \Delta p_T$ ) while modelling a sub-millimeter bubble

$C_{sh}$	$\overline{U}_{sc}$ (m/s)	$\overline{\Delta p_s}$ (Pa)	$E(\Delta p_s)$
0.0	0.061	254.285	0.092
0.1	0.039	254.294	0.092
0.2	0.028	255.350	0.088
0.3	0.011	255.279	0.088
0.4	Bubble numerically drifts from the original position		
0.5	Bubble numerically drifts from the original position		

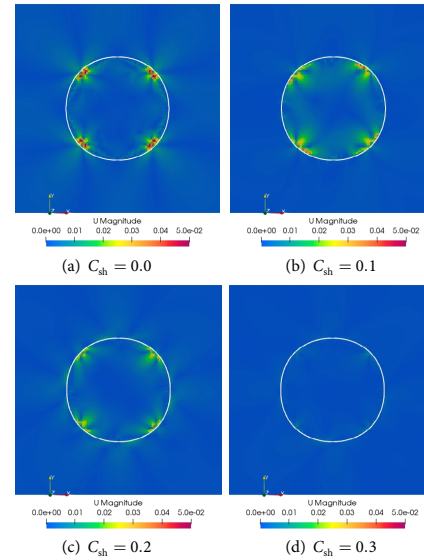


**Fig. 5** Magnitude of velocity (m/s) at  $t = 0.05$  s observed in the simulations of sub-millimeter sized bubble for various values of  $C_{sh}$ . The white contour represents the interface at  $\alpha_1 = 0.5$ .

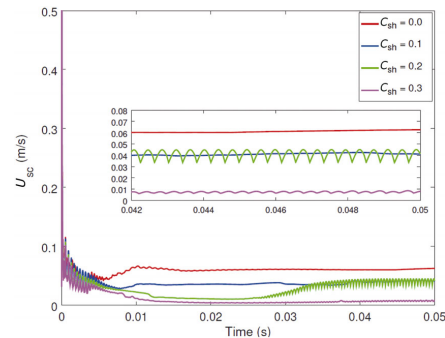


**Fig. 6** Temporal evolution of spurious velocities during simulations of bubble with radius equal to 0.25 mm for various values of  $C_{sh}$ .

and iterative procedure used to solve for  $p_{rgb}$  as recommended by Deshpande et al. (2012). In order to prevent the growth of spurious velocities, time step constraint based on fluid viscosity and density as well as mesh size, in Eq. (11), proposed by Deshpande et al. (2012) is used. The simulations for a range of value of sharpening coefficients,  $0 \leq C_{sh} \leq 0.5$ , shows that

- The use of a larger value of  $C_{sh}$  generally reduces the spurious velocities in capillary rise and stationary bubble simulations.
- The mesh refinement does not always exacerbate

spurious velocities, see Table 4, unlike while using CSF model (Deshpande et al., 2012; Vachaparambil and Einarsrud, 2019a).

- The millimeter sized bubble can be modelled with  $0 \leq C_{sh} \leq 0.5$  and the three meshes. Using the finest M3 mesh and  $C_{sh}$  equal to 0.5 provides the lowest spurious velocities as well as the most accurate prediction of Laplace pressure.
- The sub-millimeter bubble can be modelled with  $C_{sh} \leq 0.3$  but the lowest spurious velocities and error in Laplace pressure are observed when  $C_{sh} = 0.3$ .
- The capillary rise simulations show a non-linear variation of  $h_s$  with  $C_{sh}$  albeit the decrease in spurious velocities. The reduced spurious velocities and error in the capillary rise height is obtained when using  $C_{sh} = 0.2$ .

Although this paper investigated the effect of  $C_{sh}$  for a few flow scenarios, the results show the importance of choosing an optimized value of the sharpening coefficient for future applications of SSF model to simulate two-phase flow phenomena.

### Acknowledgements

This work was funded by the Department of Materials Science and Engineering at Norwegian University of Science and Technology (NTNU). The authors would also like to thank NTNU HPC and UNINETT Sigma2 for providing necessary computational resources through grant NN9741K. This paper is an extension of the poster, Vachaparambil and Einarsrud (2019b), which was presented at the 17th Multiphase Flow Conference & Short Course and subsequently invited for publication at this journal.

### Funding note

Open access funding provided by NTNU Norwegian University of Science and Technology (incl St. Olavs Hospital - Trondheim University Hospital).

### References

- Brackbill, J. U., Kothe, D. B., Zemach, C. 1992. A continuum method for modeling surface tension. *J Comput Phys*, 100: 335–354.
- Bullard, J. W., Garboczi, E. J. 2009. Capillary rise between planar surfaces. *Phys Rev E*, 79: 011604.
- Cifani, P., Michalek, W. R., Priems, G. J. M., Kuerten, J. G. M., van der Geld, C. W. M., Geurts, B. J. 2016. A comparison between the surface compression method and an interface reconstruction method for the VOF approach. *Comput Fluids*, 136: 421–435.
- Deshpande, S. S., Anumolu, L., Trujillo, M. F. 2012. Evaluating the performance of the two-phase flow solver interFoam. *Comput Sci Disc*, 5: 014016.
- Greenshields, C. J. 2019. OpenFOAM User Guide version 7. OpenFOAM Foundation Ltd.
- Maes, J., Soulaire, C. 2018. A new compressive scheme to simulate species transfer across fluid interfaces using the Volume-Of-Fluid method. *Chem Eng Sci*, 190: 405–418.
- Pavuluri, S., Maes, J., Doster, F. 2018. Spontaneous imbibition in a microchannel: Analytical solution and assessment of volume of fluid formulations. *Microfluid Nanofluid*, 22: 90.
- Popinet, S. 2018. Numerical models of surface tension. *Ann Rev Fluid Mech*, 50: 49–75.
- Raeni, A. Q., Blunt, M. J., Bijeljic, B. 2012. Modelling two-phase flow in porous media at the pore scale using the volume-of-fluid method. *J Comput Phys*, 231: 5653–5668.
- Samkhaniani, N., Ansari, M. 2016. Numerical simulation of bubble condensation using CF-VOF. *Prog Nucl Energy*, 89: 120–131.
- Saufi, A., Frassoldati, A., Faravelli, T., Cuoci, A. 2019. Droplet-SMOKE++: A comprehensive multiphase CFD framework for the evaporation of multidimensional fuel droplets. *Int J Heat Mass Trans*, 131: 836–853.
- Soh, G. Y., Yeoh, G. H., Timchenko, V. 2016. Numerical investigation on the velocity fields during droplet formation in a microfluidic T-junction. *Chem Eng Sci*, 139: 99–108.
- Vachaparambil, K. J., Einarsrud, K. E. 2019a. Comparison of surface tension models for the volume of fluid method. *Processes*, 7: 542.
- Vachaparambil, K. J., Einarsrud, K. E. 2019b. Spurious velocities in the volume of fluid method: Modeling a sub-millimeter bubble. In: Proceedings of the 17th Multiphase Flow Conference & Short Course.
- Vachaparambil, K. J., Einarsrud, K. E. 2020. Numerical simulation of bubble growth in a supersaturated solution. *Appl Math Model*, 81: 690–710.
- Yamamoto, T., Okano, Y., Dost, S. 2017. Validation of the S-CLSVOF method with the density-scaled balanced continuum surface force model in multiphase systems coupled with thermocapillary flows. *Int J Numer Method Fluids*, 83: 223–244.

**Open Access** This article is licensed under a Creative Commons Attribution 4.0 International License, which permits use, sharing, adaptation, distribution and reproduction in any medium or format, as long as you give appropriate credit to the original author(s) and the source, provide a link to the Creative Commons licence, and indicate if changes were made.

The images or other third party material in this article are included in the article's Creative Commons licence, unless indicated otherwise in a credit line to the material. If material is not included in the article's Creative Commons licence and your intended use is not permitted by statutory regulation or exceeds the permitted use, you will need to obtain permission directly from the copyright holder.

To view a copy of this licence, visit <http://creativecommons.org/licenses/by/4.0/>.



*Appended paper C*

**Numerical simulation of bubble growth in a supersaturated solution**

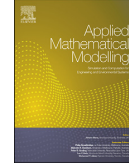
Kurian J. Vachaparambil and Kristian Etienne Einarsrud  
Published in *Applied Mathematical Modelling*





Contents lists available at ScienceDirect

## Applied Mathematical Modelling

journal homepage: [www.elsevier.com/locate/apm](http://www.elsevier.com/locate/apm)

# Numerical simulation of bubble growth in a supersaturated solution



Kurian J. Vachaparambil\*, Kristian Etienne Einarsrud

Department of Materials Science and Engineering, Norwegian University of Science and Technology (NTNU), Trondheim 7491, Norway

## ARTICLE INFO

## Article history:

Received 13 March 2019

Revised 12 December 2019

Accepted 8 January 2020

Available online 15 January 2020

## Keywords:

Bubble growth

Supersaturation

VOF

Interfacial mass transfer

## ABSTRACT

In this paper, a Volume of Fluid (VOF) based approach to simulate the growth of a pre-existing bubble in a supersaturated solution is developed and implemented in OpenFOAM®. The model incorporates the Compressive Continuous Species Transfer approach to describe the transport of dissolved gas and surface tension is treated using the Sharp Surface Force method. The driving force for bubble growth is defined using Fick's 1<sup>st</sup> law and a Sherwood number based correlation. The source terms for the governing equations are implemented by extending the work by Hardt and Wondra, J. Comp. Phys. 227 (2008) 5871–5895. The predictions of the proposed solver is compared against theoretical models for bubble growth in supersaturated solutions. The effect of spurious currents, which are generated while modelling surface tension, on bubble growth is also investigated. The proposed approach is used to model the growth of a rising bubble in the supersaturated solution.

© 2020 The Author(s). Published by Elsevier Inc.  
This is an open access article under the CC BY license.  
(<http://creativecommons.org/licenses/by/4.0/>)

## 1. Introduction

The growth of gas bubbles in supersaturated solutions occurs when the amount of dissolved gas ( $\bar{C}$ ) is higher than the saturation concentration ( $\bar{C}_{sat}$ ) in the liquid given by Henry's law [1]. Some processes where this phenomena is relevant are effervescence in beer [2], champagne [3] and carbonated beverages [4], decompression sickness [5], and electrochemical systems like electrolysis of water [6] and chloralkaline processes [7].

Bubble evolution in supersaturated solutions consists of nucleation of the bubble, which is an atomistic event, whereas bubble dynamics and the associated convection are continuum scale events [8]. Different modes by which nucleation can occur in a supersaturated solution has been proposed by Jones et al. [9], Vachaparambil and Einarsrud [10] and the critical radius ( $R_c$ ) required is

$$R_c = \frac{2\sigma}{\left(\frac{\bar{C}}{\bar{C}_{sat}} - 1\right)P}, \quad (1)$$

where  $\bar{C}/\bar{C}_{sat}$  indicates the supersaturation ratio ( $S$ ),  $\sigma$  is the surface tension and  $P$  is the operating pressure [11]. The current paper delves into the continuum scale phenomena of bubble evolution in supersaturated systems, but not atomistic scale

\* Corresponding author.

E-mail address: [kurian.j.vachaparambil@ntnu.no](mailto:kurian.j.vachaparambil@ntnu.no) (K.J. Vachaparambil).

<https://doi.org/10.1016/j.apm.2020.01.017>

0307-904X/© 2020 The Author(s). Published by Elsevier Inc. This is an open access article under the CC BY license.  
(<http://creativecommons.org/licenses/by/4.0/>)

events. The works by [8,11–13] provides a brief overview of various aspects of research in atomistic scale events relevant in bubble evolution.

The literature that has investigated bubble growth in supersaturated solutions can be divided into theoretical, experimental and numerical approaches. The two landmark theoretical papers are those by Epstein–Plesset [14] and Scriven [15]. Epstein and Plesset [14] studied the evolution of the bubble radius at various supersaturation levels when the effect of convection associated with the bubble growth is neglected. Scriven [15] considered the effect of this convection and obtained an asymptotic expression for the evolution of bubble radius. To account for the growth of bubble from a pre-existing bubble, Scriven's asymptotic solution is extended in [16]. On the other hand, experimental studies has reported the bubble radius to evolve as  $R = At^x$  where  $A$  and  $x$  are growth and time coefficients, respectively [15,17–19]. A value of  $x$  approximately equal to 0.5, derived by Scriven [15], indicates that the rate determining step is the diffusion of dissolved gas across the interface [17]. When rate determining step for bubble growth is the electrochemical reactions,  $x$  has been reported to be equal to 1/3 [18,19]. The effect of bubble growth on rise velocities of bubbles is studied in works like [20].

Computational Fluid Dynamics (CFD) is a widely used numerical approach to model continuum scale processes like bubble evolution. The main multiphase approaches used in CFD are Euler–Euler (EE), Euler–Lagrange (EL) and Volume of Fluid (VOF) methods. Although EE [21–26] and EL [8,25,27–31] approaches have been used to model gas evolution in supersaturated systems, they rely on the so called closure laws to model the interaction between the phases [32]. Compared to EE and EL approaches, the VOF method advects the volume fractions of the phases without using any approximation for the shape of the interface [32], which provides a versatile method to study the bubble evolution. In the work by Liu et al. [33], evolution of a single hydrogen bubble from the electrode surface has been modelled using the VOF approach and validated by comparison against evolution of bubble radius obtained from experiments. Other studies have used the VOF approach to model large carbon dioxide bubbles but the smaller bubble (which are below the mesh resolution) are described using a population balance model [34–36] and EL method [37,38] which are then validated using experimental data on electrical potential and bubble thickness respectively. Interestingly, these previous works [33–38] are developed based on a commercial solvers like FLUENT®. The VOF based approaches typically use a Sherwood number ( $Sh$ ) based correlation to describe the mass transfer across the interface [33–36]. Modelling mass transfer based on  $Sh$  can lead to erroneous results as these correlations are dependent on both the bubble shape and local velocity field [39,40]. A more universal approach is to use the Fick's 1<sup>st</sup> law of diffusive mass transfer instead [5,41,42].

Although considerable progress has been made in stimulating of bubble evolution driven by supersaturation, certain aspects of the phenomena such as bubble dynamics, mass transfer and momentum exchange between the phases are usually modelled rather than resolved to reduce the computational costs and are often suitable for very specific applications. To the best knowledge of the authors, there is a lack of generic solvers that can model bubble dynamics in supersaturated solutions and are validated using theoretical benchmarks. To further improve the computational approaches used, insights from the simulating boiling can be relevant. A review of the various computational approaches used for simulating boiling and condensation phenomena is available in [43]. One such approach, reported in the study by [44], developed a VOF based model for evaporation by using a continuum-field representation of source terms in FLUENT® which was subsequently implemented in OpenFOAM® 1.5.x [45] as 'evapVOFHardt' [46,47]. Apart from evapVOFHardt, other approaches developed using OpenFOAM® to model phase change driven by temperature are [48,49] and 'phaseChangeHeatFoam' [50,51].

In this paper, we propose a VOF based solver to model the bubble evolution in a supersaturated solution. The proposed solver is based on interFOAM (available in OpenFOAM® 6 [52]) and the mass transfer approach, developed for evaporation by Hardt and Wondra [44] as well as Kunkelmann and co-workers [46,47], is extended and implemented for the bubble growth driven by supersaturation of dissolved gases. The driving force for the bubble growth is modelled using both the Fick's 1<sup>st</sup> law and a correlation using  $Sh$ . The transport of the dissolved gas is modelled using a Compressive Continuous Species Transfer (C-CST) model [53] and the surface tension force is modelled using the Sharp Surface Force approach [54]. Following the derivation of the governing equations and its implementation in OpenFOAM®, the mass transfer model in the proposed solver is validated against theoretical models like the approximate solution of Epstein–Plesset [14], asymptotic solution of Scriven [15] and the extended Scriven model [16]. Spurious currents, produced due to modelling surface tension, and its effects on bubble growth are investigated. Finally, the proposed model is used to simulate the growth of a rising bubble in a supersaturated solution.

## 2. Governing equations and its implementation

The VOF method uses a scalar function to represent the interface and individual phases as

$$\alpha_1(\vec{x}, t) = \begin{cases} 0 & \text{(within Phase 2)} \\ 0 < \alpha_1 < 1 & \text{(at the interface)} \\ 1 & \text{(within Phase 1)}. \end{cases} \quad (2)$$

In the proposed solver,  $\alpha_1$  represents the volume fraction of Phase 1 (or liquid) and the volume fraction of Phase 2 (or bubble) can be written as  $\alpha_2 = 1 - \alpha_1$ .

Fluid properties like density ( $\rho$ ) and viscosity ( $\mu$ ) are determined using the volume fraction as a weighting function:

$$\chi = \chi_1\alpha_1 + \chi_2\alpha_2 \text{ where } \chi \in [\rho, \mu]. \quad (3)$$

The continuity equation for a growing bubble is written as

$$\nabla \cdot \vec{U} = \frac{\dot{m}}{\rho}, \quad (4)$$

where  $\dot{m} = \dot{m}_1\alpha_1 + \dot{m}_2\alpha_2$ , with  $\dot{m}_1$  and  $\dot{m}_2$  representing source/sink terms for Phase 1 and Phase 2, are defined in Eq. (24).

The continuity equation (Eq. (4)) can be used to derive a corresponding equation to describe the volume fraction as shown below

$$\frac{\partial(\alpha_1 + \alpha_2)}{\partial t} + \nabla \cdot ((\alpha_1 + \alpha_2)\vec{U}) = \frac{\dot{m}}{\rho}(\alpha_1 + \alpha_2). \quad (5)$$

Based on Eqs. (4) and (5), the evolution of  $\alpha_1$  can be computed as

$$\frac{\partial\alpha_1}{\partial t} + \nabla \cdot (\alpha_1\vec{U}) = \alpha_1\nabla \cdot \vec{U}, \quad (6)$$

which is analogous to the volume fraction equation described in [46,47]. In order to render a sharp interface, the advection term in Eq. (6) is modified to include a compressive flux as

$$\frac{\partial\alpha_1}{\partial t} + \nabla \cdot (\alpha_1\vec{U}) + \nabla \cdot (\alpha_1(1 - \alpha_1)\vec{U}_r) = \alpha_1\nabla \cdot \vec{U}, \quad (7)$$

where  $\vec{U}_r$  is compressive velocity defined in Eq. (8).

$$\vec{U}_r = C_\alpha \frac{\phi}{|S_f|} \frac{\nabla\alpha_1}{|\nabla\alpha_1| + \delta}, \quad (8)$$

where  $\phi$ , is volume flux that is computed based on velocity and  $S_f$  is cell face area vector,  $C_\alpha$  and  $\delta$  are velocity flux, cell surface area, a user-defined compression factor and a small non-zero value which is calculated as  $10^{-8} / \left(\frac{\sum V_i}{N}\right)^{1/3}$ , respectively.  $C_\alpha$  controls the interface smearing and is typically set to a value between zero and four [55].

In order to efficiently compute the pressure boundary condition and density jump at the interface, the solver uses a modified pressure ( $p_{rgh}$ ), defined as

$$p_{rgh} = p - \rho\vec{g} \cdot \vec{x}, \quad (9)$$

which is explained in [56]. Due to the use of modified pressure,  $-\nabla p + \rho\vec{g}$  can be written as

$$-\nabla p + \rho\vec{g} = -\nabla p_{rgh} - \vec{g} \cdot \vec{x}\nabla\rho. \quad (10)$$

The momentum equation, which is solved to obtain the velocity field in both the phases, is calculated as

$$\frac{\partial\rho\vec{U}}{\partial t} + \nabla \cdot (\rho\vec{U}\vec{U}) = -\nabla p + \left(\nabla \cdot (\mu\nabla\vec{U}) + \nabla\vec{U} \cdot \nabla\mu\right) + \rho\vec{g} + \vec{F}_{ST}, \quad (11)$$

where last term represents the surface tension force which in this solver is computed based on the Sharp Surface Force (SSF) model [54]. Substituting Eq. (10) in Eq. (11) gives the momentum equation as implemented in OpenFOAM<sup>®</sup>,

$$\frac{\partial\rho\vec{U}}{\partial t} + \nabla \cdot (\rho\vec{U}\vec{U}) = -\nabla p_{rgh} + \left(\nabla \cdot (\mu\nabla\vec{U}) + \nabla\vec{U} \cdot \nabla\mu\right) - \vec{g} \cdot \vec{x}\nabla\rho + \vec{F}_{ST}. \quad (12)$$

The SSF formulation used to describe the surface tension force can be defined as

$$\vec{F}_{ST} = \sigma\kappa_{final}\nabla\alpha_{sh}, \quad (13)$$

where  $\kappa_{final}$  is curvature of the interface obtained using a three step procedure described in [54] and  $\alpha_{sh}$  is a sharpened volume fraction of liquid defined as

$$\alpha_{sh} = \frac{1}{1 - C_{sh}} \left[ \min\left(\max\left(\alpha_1, \frac{C_{sh}}{2}\right), 1 - \frac{C_{sh}}{2}\right) - \frac{C_{sh}}{2} \right], \quad (14)$$

where  $C_{sh}$  is a sharpening coefficient. If  $C_{sh}=0$ ,  $\alpha_{sh}$  is equivalent to  $\alpha_1$  whereas when  $C_{sh}=1$  describes a very sharp interface that is numerically unstable [54]. Based on preliminary simulations, SSF model is preferred over the commonly used Continuum Surface Force model [57] because of its ability to reliably simulate a sub-millimeter bubble.

As the bubble growth is driven by supersaturation, the dissolved gas concentration ( $C_i$ ) can be represented as

$$C_i = \bar{C} - \bar{C}_{sat}. \quad (15)$$

Eq. (15) represents a concentration of dissolved gas that causes bubble growth when  $C_i > 0$  as it represents concentration greater than  $\bar{C}_{sat}$ . Assuming that the interface of a bubble growing is saturated, the interface is represented by  $C_i$  equal to zero, based on Eq. (15). The governing equation for the transport of  $C_i$  is based on the Compressive Continuous Species Transfer (C-CST) model, proposed by Maes and Soulaire [53], as

$$\frac{\partial C_i}{\partial t} + \nabla \cdot (\vec{U}C_i) = \nabla \cdot \left(\hat{D}_i\nabla C_i - \hat{D}_i\mathfrak{B}C_i\nabla\alpha_1\right) - \nabla \cdot \left(\mathfrak{B}\alpha_1\alpha_2\vec{U}_rC_i\right) + S_i, \quad (16)$$



where  $\mathfrak{B}$  is equal to  $(1 - He_i)/(\alpha_1 + \alpha_2 He_i)$ ,  $S_i$  is the sink term for the dissolved gas in the liquid at the interface (described in Eq. (25)),  $\bar{U}_r$  is the compressive velocity (defined in Eq. (8)) and  $\hat{D}_i$  is the harmonic interpolation of the diffusion coefficients [53]:

$$\hat{D}_i = \frac{D_{i,1}D_{i,2}}{D_{i,2}\alpha_1 + D_{i,1}\alpha_2}, \tag{17}$$

where  $D_{i,1}$  is the diffusion coefficient of dissolved gas in Phase 1 and  $D_{i,2}$  is the self-diffusion coefficient of the gas [58]. In Eq. (16),  $He_i$  represents dimensionless Henry's constant that accounts for the jump in  $C_i$  across the interface that is expressed as  $C_{i,2} = He_i C_{i,1}$ . In order to obtain the saturation condition of the interface when  $C_i$  is defined based on Eq. (15),  $He_i$  should be equal to zero. The concentration of the dissolved gas ( $C_i$ ) represents the  $\alpha_1 C_{i,1} + \alpha_2 C_{i,2}$ .

The mass transfer across the interface is described using two approaches: Fick's 1<sup>st</sup> law and Sherwood number based correlation. Fick's 1<sup>st</sup> law, which is applicable for any arbitrary flow scenario, is implemented as

$$j = M_i D_{i,1} |\nabla C_i|, \tag{18}$$

where  $M_i$  is the molar mass of the species  $i$ . The alternative method, which is typically implemented in practical applications, utilizes a Sherwood number correlation which can be written as

$$j = M_i k (\bar{C} - \bar{C}_{sat}) = M_i k C_i, \tag{19}$$

where  $k$  is the mean mass transfer coefficient defined as  $k = D_{i,1} Sh / 2R$ , where the mean Sherwood number ( $Sh$ ) is derived from Fick's 1<sup>st</sup> law for the mass transfer at interface for a spherical bubble in creeping flow [39] as

$$Sh = \frac{2Rk}{D_{i,1}} = 2 + 0.6515 \sqrt{ReSc}, \text{ where } Re = \frac{U_\infty 2R}{\nu_1} \text{ and } Sc = \frac{\nu_1}{D_{i,1}}. \tag{20}$$

In Eq. (20),  $U_\infty$  is calculated as  $(R - R^{n-1})/\Delta t$ , where  $R - R^{n-1}$  is the difference between the radius of the bubble at the current time step and the previous time step and  $\Delta t$  is the time step used by the solver. Equivalently, the mean mass transfer coefficient can be determined based on Eq. (20) as

$$k = \frac{D_{i,1}}{2R} \left( 2 + 0.6515 \sqrt{ReSc} \right). \tag{21}$$

The local mass transfer rate ( $\psi_0$ ) can be written based on  $j$  (defined in Eqs. (18) and (19)) as

$$\psi_0 = N j \alpha_1 |\nabla \alpha_1|, \tag{22}$$

where  $N$  is a normalization factor is defined in Eq. (26). The term  $\alpha_1$  is multiplied Eq. (22) to ensure that the mass flux that drives the bubble growth is based only on the supersaturation of the liquid.

In order to increase numerical stability,  $\psi_0$  is smeared over a few computational cells by solving

$$D \Delta t \nabla^2 \psi = \psi - \psi_0, \tag{23}$$

where  $\psi$  describes the smeared  $\psi_0$  at every time step [44]. In Eq. (23),  $D \Delta t$  is a product of a diffusion constant and parameter with dimension of time which controls the amount of smearing in Eq. (23) [44].

The source term of the continuity equation (Eq. (4)),  $\dot{m} = \dot{m}_1 \alpha_1 + \dot{m}_2 \alpha_2$  reduces to  $\dot{m} = \dot{m}_2 \alpha_2$  because liquid is not consumed when during bubble growth due to supersaturation. Based on the value of  $\psi$ , source term  $\dot{m}$  (in Eq. (4)) can be calculated as

$$\dot{m} = A \alpha_2 \psi, \tag{24}$$

where  $A$  is a normalization factor defined in Eq. (26). The source term  $\dot{m}$ , which is defined in Eq. (24), is calculated in the region where  $\alpha_1 < 0.001$  by artificially moving them away from the interface based on volume fraction of the liquid (further described in [44,47]).

The sink term in dissolved gas transport ( $S_i$ ), in Eq. (16), which represents the dissolved gas lost into the bubble due to mass transfer across the interface is calculated as

$$S_i = - \frac{N \alpha_1 (j |\nabla \alpha_1|)}{M_i}, \tag{25}$$

where  $N$  is the normalization factor defined in Eq. (26) and  $\alpha_1$  in Eq. (25) ensures that  $S_i$  is non-zero only at the liquid side of the interface. The normalization factors used in the solver can be defined as

$$A = \frac{\int_\Omega \psi_0 dV}{\int_\Omega \alpha_2 \psi dV} \text{ and } N = \frac{\int_\Omega |\nabla \alpha_1| dV}{\int_\Omega \alpha_1 |\nabla \alpha_1| dV}, \tag{26}$$

where  $\Omega$  is the domain for the flow computation.

The overall algorithm used to solve the governing equations (Eqs. (4), (7), (12), (16) and (23)) is summarized in Fig. 1. The volume fraction equation (Eq. (7)) is solved the Multidimensional Universal Limiter with Explicit Solution (MULES) method [57]. The Pressure Implicit with Splitting of Operator (PISO) algorithm is used to solve the momentum (Eq. (12)) and continuity (Eq. (4)) equations [56,57,59]. The PISO algorithm recasts the continuity equation into a pressure Poisson equation (or 'pressure correction equation') which is solved and then used to update the predicted velocity fields [56,57].

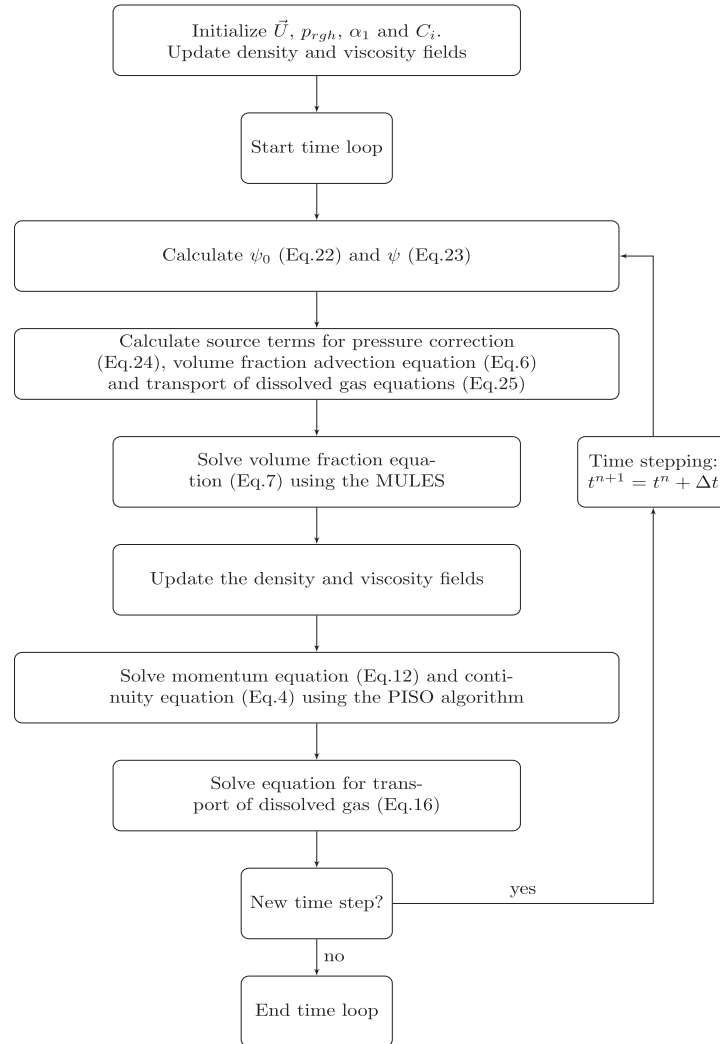


Fig. 1. Schematic of the solution procedure implemented in the proposed solver.

### 3. Computational setup

The computational domain is a square of dimensions  $3\text{ cm} \times 3\text{ cm}$  with a pre-existing bubble of radius equal to  $250\text{ }\mu\text{m}$  located at the center of the geometry. The boundaries are set to zero gradient conditions for  $\vec{U}$ ,  $\psi$ ,  $C_i$  and  $\alpha_1$  while  $p_{rgh}$  is equal to  $101,325\text{ Pa}$ . The phenomena modelled in this paper corresponds to a pre-existing bubble of radius equal to  $250\text{ }\mu\text{m}$  growing in a solution supersaturated by carbon dioxide. The saturation concentration of dissolved carbon dioxide in water is calculated using Henry's law at  $25\text{ }^\circ\text{C}$  and  $101,325\text{ Pa}$  to be  $33.44\text{ mol/m}^3$  [60]. The initial bulk concentration of carbon dioxide in water is set to  $C_i = 200.64\text{ mol/m}^3$ , corresponding to a supersaturation ratio (defined as  $\bar{C}/\bar{C}_{sat}$ ) equal to seven. To validate the mass transfer model implemented in the proposed solver, some of the simulations neglect the gravity and surface tension. When gravity and surface tension are treated in selected simulations,  $\vec{g}$  is assigned as  $(0\text{ } -9.81\text{ } 0)\text{ m/s}^2$  and  $\sigma$  equal to  $0.0468\text{ N/m}$  [31], respectively.

The settings used in the simulations are described in Table 1 and internal fields used for the simulations is tabulated in Table 2. Values for  $D\Delta t$  and  $He_i$  are set equal to  $10^{-6}\text{ m}^2$  and  $10^{-4}$  respectively and the maximum Courant number ( $Co_{max}$ ) is set equal to 0.05. In simulations where surface tension is neglected, the maximum time step is allowed to adjust

**Table 1**  
Fluid properties at 25 °C and 101325 Pa.

Fluid properties	Dimensions	Liquid (Phase 1)	Bubble (Phase 2)
Density	kg/m <sup>3</sup>	997.0751 [67]	1.81 [68]
Kinematic viscosity	m <sup>2</sup> /s	8.92 × 10 <sup>-7</sup> [67]	8.228 × 10 <sup>-6</sup> [68]
Diffusion coefficient	m <sup>2</sup> /s	1.94 × 10 <sup>-9</sup> [69]	9.18 × 10 <sup>-6</sup> [58]

**Table 2**  
Initial internal field of parameters used for the simulations.

	Dimensions	Liquid (Phase 1)	Bubble (Phase 2)
$\alpha_1$	–	1	0 (Pre-existing bubble, $R_0 = 250 \mu\text{m}$ )
$C_i$	mol/m <sup>3</sup>	200.64	0
$p_{\text{gh}}$	Pa	101,325	101,325
$\vec{U}$	m/s	(0 0 0)	(0 0 0)
$\psi$	kg/m <sup>3</sup> s	0	0

**Table 3**  
Discretisation schemes.

Modelling term	Keyword	Scheme	Remarks
Time derivatives	ddtSchemes	Euler	First order implicit method [70]
Divergence term	$\nabla \cdot (\rho \vec{U} \vec{U})$	vanLeerV	Modified vanLeer for vector fields [70]
	$\nabla \cdot (U \alpha_1)$ , $\nabla \cdot (U C_i)$	vanLeer	[71]
	$\nabla \cdot (U_r \alpha_1 (1 - \alpha_1))$	interfaceCompression	Used in [50,57]
	$\nabla \cdot (\hat{D}_i \mathfrak{B} C_i \nabla \alpha_1)$	vanLeer	[53]
	$\nabla \cdot (\mathfrak{B} \alpha_1 \alpha_2 U_r C_i)$	vanLeer	[53]
Gradient term	gradSchemes	Linear	Operator with $\nabla$
Laplacian term	laplacianSchemes	Linear corrected	Operator with $\nabla^2$
Other	snGradSchemes interpolationSchemes	Corrected Linear	Surface normal gradients Interpolates values

**Table 4**  
Solvers used for the discretised equation.

Equation	Linear solver	Smoother/preconditioner	Tolerance
Pressure correction equation	PCG	GAMG	10 <sup>-20</sup>
Momentum equation (Eq. (12))	smoothSolver	symGaussSeidel	10 <sup>-10</sup>
Volume fraction equation (Eq. (7))	smoothSolver	symGaussSeidel	10 <sup>-10</sup>
Species transport equation (Eq. (16))	PBiCGStab	Diagonal	10 <sup>-10</sup>
Smearing of mass transfer rate (Eq. (23))	PBiCGStab	Diagonal	10 <sup>-10</sup>

automatically based on the  $Co_{max}$ . When surface tension is considered, the time step constraint, which is required to prevent the temporal growth of spurious currents, is calculated as

$$\Delta t \leq \frac{1}{2} \left( C_2 \tau_\mu + \sqrt{(C_2 \tau_\mu)^2 + 4C_1 \tau_\rho^2} \right) \text{ and } \Delta t \leq \max \left( C_2 \tau_\mu, 10C_1 \tau_\rho \right), \quad (27)$$

where  $\tau_\mu$  and  $\tau_\rho$  are time scales which are defined as  $\mu_{avg} \Delta x / \sigma$  and  $\sqrt{\rho_{avg} (\Delta x)^3 / \sigma}$  respectively,  $\mu_{avg}$  and  $\rho_{avg}$  are defined as the average dynamic viscosity and density between the phases whereas  $\Delta x$  is the mesh resolution which is equal to 7.5  $\mu\text{m}$  [57]. The values of  $C_1$  and  $C_2$  has been reported to be equal to 0.01 and 10, respectively [57]. For the M4 mesh used in the simulations, the constraint on the time step is calculated, based on Eq. (27), to be equal to  $7.2 \times 10^{-7}$  s. A parametric study to the investigate the effect of pre-existing bubble size,  $D\Delta t$  and  $He_i$  on the solution is discussed later in the paper.

The governing equations (Eqs. (4), (7), (12), (16) and (23)) are discretised using schemes as mentioned in Table 3 with the relevant settings summarized in Tables 4 and 5. The tolerance criteria while solving the pressure correction equation is set to 10<sup>-20</sup> to reduce the force imbalance (between surface tension and pressure forces) which is generated due to the iterative procedure used in the solution algorithm [57]. The maximum number of iterations while solving the governing equations are set such that the tolerance criteria set in Table 4 is met at every time step.

#### 4. Convergence studies

The convergence of the simulations is studied using the Fick's 1<sup>st</sup> law as the driving force (in Eq. (18)) for bubble growth and neglecting gravity. The surface tension is also neglected in these simulations as the spurious currents generated are

**Table 5**  
Other parameters used in solving the discretised equations.

Parameter	Value	Notes
nAlphaCorr	2	Number of $\alpha_1$ correction; usually set equal to 1 or 2 for time-dependent flows [72].
nAlphaSubCycles	1	Represents the number of sub-cycles within $\alpha_1$ equation [70].
cAlpha ( $C_c$ )	1	Used for interface compression in Eq. (8).
MULESCorr	yes	Switches on semi-implicit MULES [73].
nLimiterIter	3	Number of MULES iterations over the limiter [73].
momentumPredictor	no	Controls solving of the momentum predictor; typically set to 'no' for multiphase and low Reynolds number flows [70].
nOuterCorrectors	1	PISO algorithm is selected by setting this parameter equal to unity in PIMPLE algorithm [70].
nCorrectors	3	The number of times the PISO algorithm solves the pressure and momentum equation in each step; usually set to 2 or 3 [70].
nNonOrthogonalCorrectors	0	Used when meshes are non-orthogonal [70].
relaxationFactors	1	Specifies the under-relaxation factors; set equal to one for transient simulations [54].
$C_{sh}$	0.3	Sharpening coefficient in Eq. (14); to model a reliable pre-existing bubble of radius 250 $\mu\text{m}$ [74].

**Table 6**  
Mesh convergence studies.

Mesh	Total number of cells	Mesh resolution ( $\Delta x$ )	$2R_0/\Delta x^a$	Radius normalized growth rate ( $\phi$ ) <sup>b</sup>	Relative error (%) <sup>c</sup>
M0	1000,000	$3.00 \times 10^{-5}$ m	16.67	$8.2248 \times 10^{-10}$	–
M1	1999,396	$2.12 \times 10^{-5}$ m	23.57	$8.5821 \times 10^{-10}$	4.34
M2	4000,000	$1.50 \times 10^{-5}$ m	33.33	$8.7887 \times 10^{-10}$	2.41
M3	7997,584	$1.06 \times 10^{-5}$ m	47.13	$8.8682 \times 10^{-10}$	0.90
M4	16,000,000	$7.50 \times 10^{-6}$ m	66.67	$8.9308 \times 10^{-10}$	0.71
M5	31,990,336	$5.30 \times 10^{-6}$ m	94.27	$8.9513 \times 10^{-10}$	0.23

<sup>a</sup> $2R_0/\Delta x$  represents the number of cells that resolve the pre-existing bubble diameter. <sup>b</sup>Radius normalized growth rate ( $\text{kg m}^{-1} \text{s}^{-1}$ ) is calculated at  $t=4.5$  s as  $\int \psi_0 dV/R$ . <sup>c</sup>Relative error is calculated as  $(\phi_{M_{i+1}} - \phi_{M_i}) \times 100 / \phi_{M_i}$  where  $i = 0, 1, 2, 3$  and 4.

dependent on the mesh resolution and a 'true' mesh convergence is difficult to achieve especially for capillary dominant flows [54,61,62]. The convergence is analyzed based on three criteria: independence of solution from the mesh, conservation of phases and dissolved gas, effect of domain size of the solution, and monitoring supersaturation/pressure data away from the bubble.

The grid convergence is analyzed using six different hexahedral meshes, as shown in Table 6, based on the radius normalized growth rates at  $t = 4.5$  s. The growth rates and bubble radii for various meshes, shown in Fig. 2, at  $t = 4.5$  s show a relative deviation of nearly 2% between the M4 and M5 meshes. This discrepancy is due to the discontinuous initial condition of  $C_i$  (in Table 2) which leads to a larger initial growth rate, offsetting the bubble radius for further time steps, see Fig. 2(a). The radius normalized growth rate, equivalent to the mass flux in 2D, is not influenced by this offset. As the relative change of the radius normalized growth rate at  $t = 4.5$  s between two finest meshes is lower than 0.25%, see Table 6, M4 has been used for simulations in the paper.

The imbalance in the phases, illustrated in Fig. 3, is lower than 0.1% of the volume of the liquid initially in the system. Calculated based on the amount of dissolved gas which is numerically in the bubble, the imbalance in the dissolved gas is lower than 0.1% of initial amount of dissolved gas in the system as shown in in Fig. 4.

The region far stream from the bubble growth should have a constant concentration and pressure as it is not effect by the bubble growth. Monitoring a point away from the interface shows that  $C_i$  and  $p_{rgh}$  remains equal to 200.64 mol/m<sup>3</sup> and 101,325 Pa, respectively for the duration of the simulation.

Using smaller domain for the simulations has been observed to affect the radially symmetric nature of the velocity field as shown in Fig. 5. In order reduce the effect of this error, the domain used in the simulations is nearly twelve times the bubble diameter at  $t=10$ s i.e. 3 cm  $\times$  3 cm, which has been showed in Fig. 5(c).

## 5. Validation

In this section, the proposed solver is validated by comparing against two theoretical cases i.e. the approximate solution of Epstein-Plesset [14], the asymptotic solution of Scriven [15] and Extended Scriven [16]. It is worth pointing out that surface tension is neglected in the simulations discussed in this section unless explicitly specified. The simulations used for comparison can be divided based on the description of driving force that drives the mass transfer across the interface as

- Constant driving force: The definition of  $j$  based on  $Sh$  correlation (Eq. (19)) is modified to account for driving force for bubble growth that is dependent on the bulk concentration of the supersaturated solution ( $\bar{C}_\infty$ ) which is expressed as
 
$$j = M_i k (\bar{C}_\infty - \bar{C}_{sat}). \quad (28)$$
- Local driving force: Eq. (19) provides a  $Sh$  correlation based definition of driving force that is dependent on the local concentration of the dissolved gas around the interface.

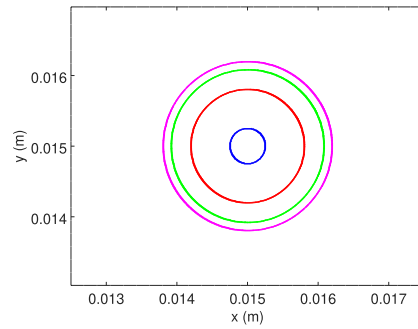
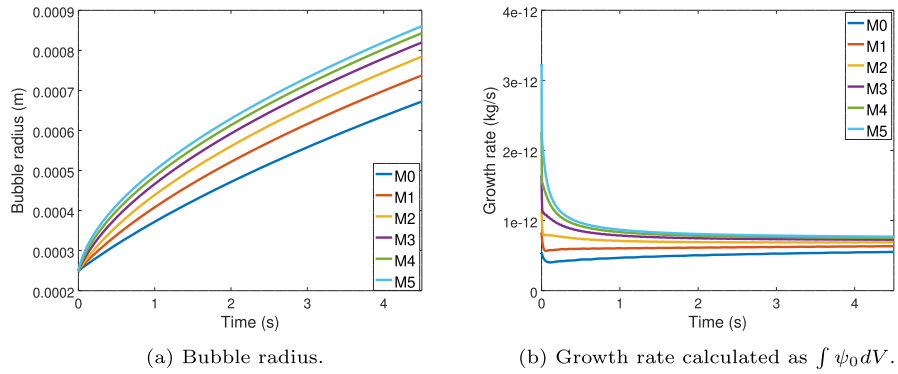


Fig. 2. Effect of mesh on the temporal changes in bubble radius and growth rates.

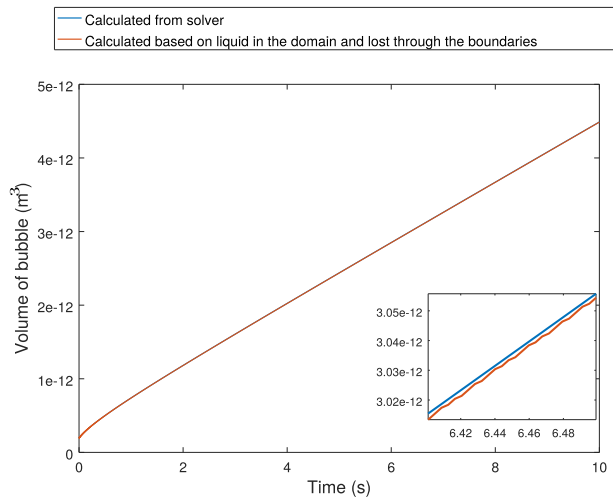


Fig. 3. Comparison of the bubble volume obtained from the solver and calculated based on the volume of liquid adjusted for the amount lost through the boundaries to calculate the imbalance of the phases in the system.

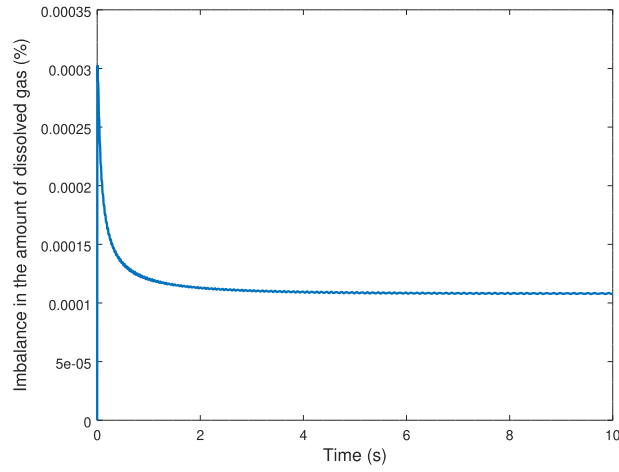


Fig. 4. The temporal variation in the imbalance of the dissolved gas during the simulation.

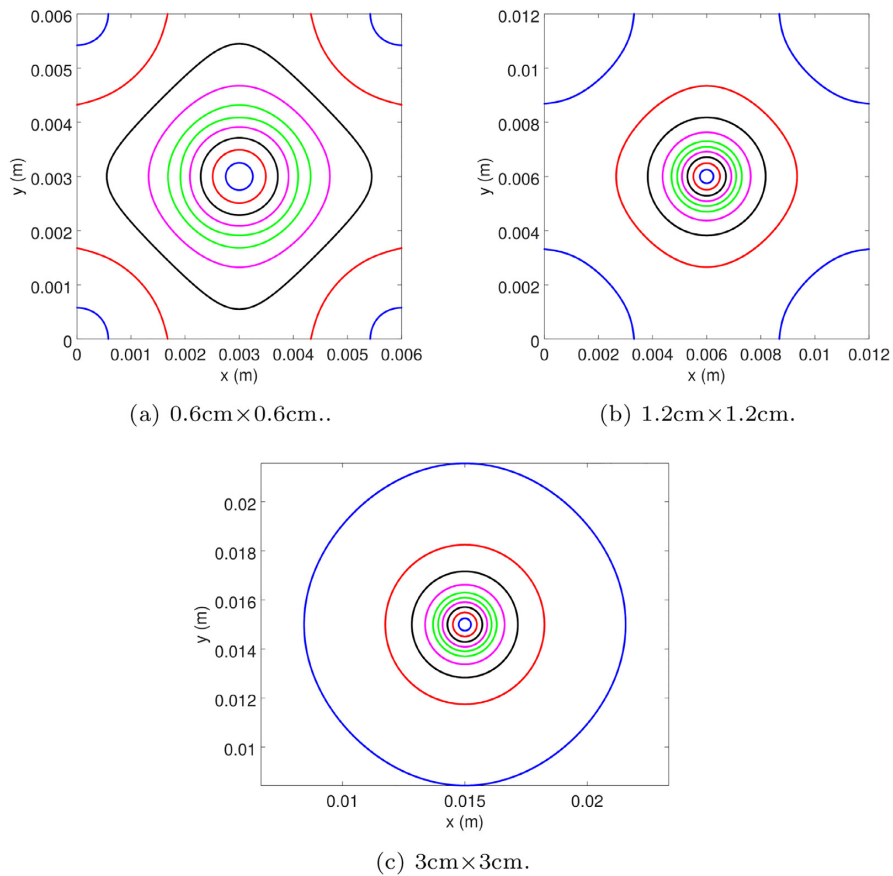
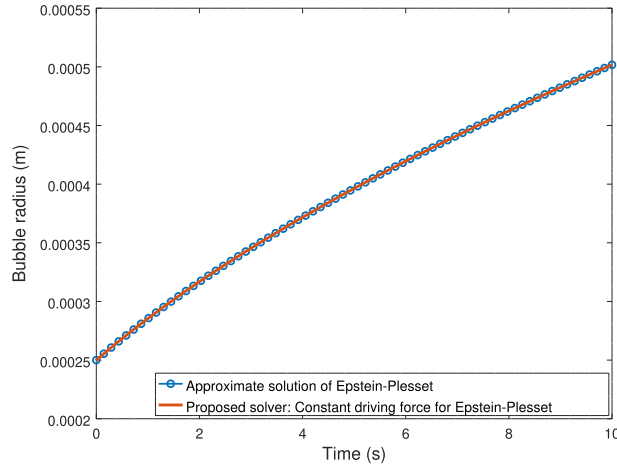


Fig. 5. Comparison of the velocity field, at  $t = 10$  s, analyzed through  $|U|$  contours plotted at  $1 \times 10^{-5}$  m/s (●),  $2 \times 10^{-5}$  m/s (●),  $3 \times 10^{-5}$  m/s (●),  $4 \times 10^{-5}$  m/s (●) and  $5 \times 10^{-5}$  m/s (●) with different computational domains used for the simulations.



**Fig. 6.** Comparison of the temporal evolution of bubble radius predicted by the proposed solver, using the constant driving force and  $k$  as defined in Eq. (33), with the approximate solution of Epstein–Plesset (Eq. (32)).

- Fick’s 1<sup>st</sup> law: Described in Eq. (18), Fick’s 1<sup>st</sup> law, provides a generic driving force for the bubble growth that is applicable for any flow scenario.

5.1. When convection of species concentration is neglected

The simulations consider a two dimensional growing bubble, a rate of bubble that is growing can be described as

$$\rho_2 \left( 2\pi R \frac{dR}{dt} \right) = 2\pi R j, \tag{29}$$

where  $R$  is the radius of the bubble and  $j$  is the constant driving force that causes the bubble growth (described in Eq. (28)), i.e.

$$\rho_2 \left( \frac{dR}{dt} \right) = M_i k (\bar{C}_\infty - \bar{C}_{sat}), \text{ where } k = \frac{D_{i,1}}{2R} \left( 2 + 0.6515\sqrt{ReSc} \right). \tag{30}$$

When the convection caused by bubble growth is neglected, i.e.  $Re = 0$ , the above equation can be written as

$$\rho_2 \left( \frac{dR}{dt} \right) = M_i k (\bar{C}_\infty - \bar{C}_{sat}), \text{ where } k = \frac{D_{i,1}}{R}. \tag{31}$$

Integrating the above equation from  $R_0$  at  $t = 0s$  to  $R$  at  $t$  gives

$$\left( \frac{R}{R_0} \right)^2 = 1 + \frac{2M_i D_{i,1} (\bar{C}_\infty - \bar{C}_{sat})}{\rho_2 R_0^2} t. \tag{32}$$

which is the ‘approximate solution of Epstein–Plesset’ [14] when the effect of surface tension and convection is neglected. Eq. (32) provides bubble growth when the bubble growth is driven by a the bulk concentration of the dissolved gas.

As the effect of convection on the bubble growth is neglected in the theoretical benchmark, the solver is modified by implementing the mass transfer coefficient as

$$k = \frac{D_{i,1}}{R}. \tag{33}$$

Using the mass transfer across the interface that is governed by Eqs. (33) and (28) in the proposed solver provides a prediction of bubble growth that is equivalent to the Epstein–Plesset solution as shown in Fig. 6. The predictions from the proposed solver marginally under-predicts the final radius of the bubble by less than 0.01%. The concentration of the dissolved gas, interface and velocity distribution in the domain for bubble growth driven by a constant driving force (using mass transfer coefficient described in Eq. (33)) is illustrated in Fig. 7.

5.2. When convection of species concentration is considered

The asymptotic solution of bubble growth in a supersaturated solution, proposed by Scriven [15], when convection is considered, is given by

$$R_{Scriven} = 2\beta \sqrt{D_{i,1} t} \tag{34}$$

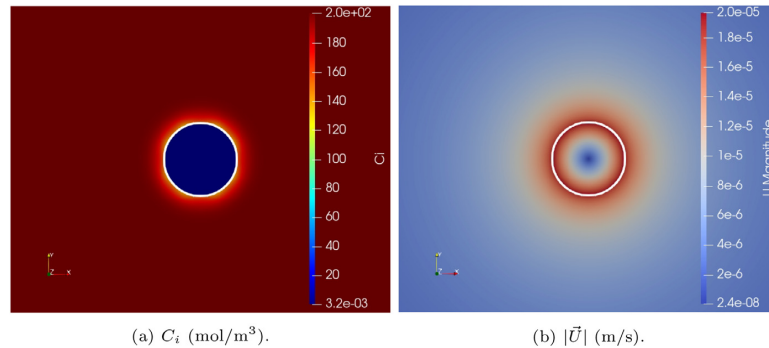


Fig. 7. Simulated concentration field and velocity at  $t=10$  s using a constant driving force with  $k$  defined in Eq. (33). The interface is represented with a white contour corresponding to  $\alpha_1 = 0.5$ .

where  $\beta$  is the growth parameter, valid only for diffusion controlled growth of spherical bubble in an unbounded medium. Based on the work by [16], an 'Extended Scriven model' that modifies Eq. (34) to account for the growth from a pre-existing bubble of radius  $R_0$  can be described as

$$R_{\text{Scriven-ext}} = 2\beta \sqrt{D_{i,1} \left( t + \frac{R_0^2}{4D_i\beta^2} \right)}. \quad (35)$$

Previous works by Wang and others [4,9,19], reported an analytical expression to determine  $\beta$  for a spherical bubble as

$$\beta_{3D} = \frac{a + \sqrt{a^2 + 2a}}{2} \quad \text{where } a = \frac{M_i(\bar{C}_\infty - \bar{C}_{\text{sat}})}{\rho_2}. \quad (36)$$

which has been shown to agree with the predictions by Scriven [15]. The formulations proposed in [4,9,15,19] to calculate  $\beta$  is derived for a spherical bubbles which is different from the 2D bubbles simulated in the current paper. For direct comparison to the simulations,  $\beta_{2D}$ , derived in Appendix A based on the work by Wang et al. [19], can be calculated as

$$\beta_{2D} = \frac{a + \sqrt{a^2 + 4a}}{2\sqrt{2}}, \quad (37)$$

where  $a$  is defined the same as Eq. (36). For the phenomena modelled in this paper,  $\beta_{3D}$  and  $\beta_{2D}$  can be calculated, using Eqs. (36) and (37), are equal to 5.3346 and 4.0509, respectively.

The velocity, concentration of dissolved gas and interface position is compared for Fick's 1<sup>st</sup> law (Eq. (18)) and local driving force (Eqs. (19) and (21)) in Fig. 8. The temporal evolution of bubble size from simulations are compared to the Scriven's asymptotic (Eq. (34)) and Extended Scriven (Eq. (35)) in Fig. 9. As expected, the bubble growth predicted by the Scriven's asymptotic expression and Extended Scriven theories using  $\beta_{2D}$  provides a better representation than  $\beta_{3D}$ . The driving force based on the  $Sh$  correlation under predicts the bubble radius by nearly a factor of 2 at  $t = 10$  s while Fick's 1<sup>st</sup> law provides a better agreement to the theoretical predictions using  $\beta_{2D}$ , with an error less than 2.5% at  $t = 10$  s. The discrepancy between the simulations can be explained using the growth rate in Fig. 10, where the growth rate is nearly 6.5 times smaller for the  $Sh$  correlation. Although the growth rate predicted by the driving force described by Fick's 1<sup>st</sup> law is initially different from the corresponding theory, it seems to asymptotically match the theoretical prediction. The initial discrepancy between the two is due to the discontinuous nature of concentration while initializing, see Table 2.

### 5.3. Influence of surface tension

Due to small length scales associated with bubble growth, surface tension dominates the flow physics. Modelling surface tension has its own challenges, namely the generation of spurious currents around the interface [44,50,54,57]. Due to the time step constraint, described in Eq. (27), the simulations are run only until 2 ms.

The spurious currents ( $U_{sc}$ ), calculated as  $\max(|\vec{U}|)$ , are observed on both sides of the interface as illustrated in Fig. 11 and its temporal variation plotted in Fig. 12(a). The convection that is generated by spurious currents seems to remove the dissolved gas at the interface which results in the reduction of the growth rate (calculated as volume integral of  $\psi_0$  in the computational domain) observed in Fig. 12(c). Due to the generation of large magnitude of spurious currents initially, there is a substantially drop in the growth rate of the bubble in the first few time steps as seen in Fig. 12(c). The average growth rate of the bubble during 2 ms reduces by approximately 32% compared to when surface tension is not treated. The reduction in the growth rate is also reflected in the temporal variation of bubble radius, as shown in Fig. 12(b). At  $t = 0.002$  s, the bubble radius differs by nearly 0.15% from the bubble radius when surface tension is not treated.



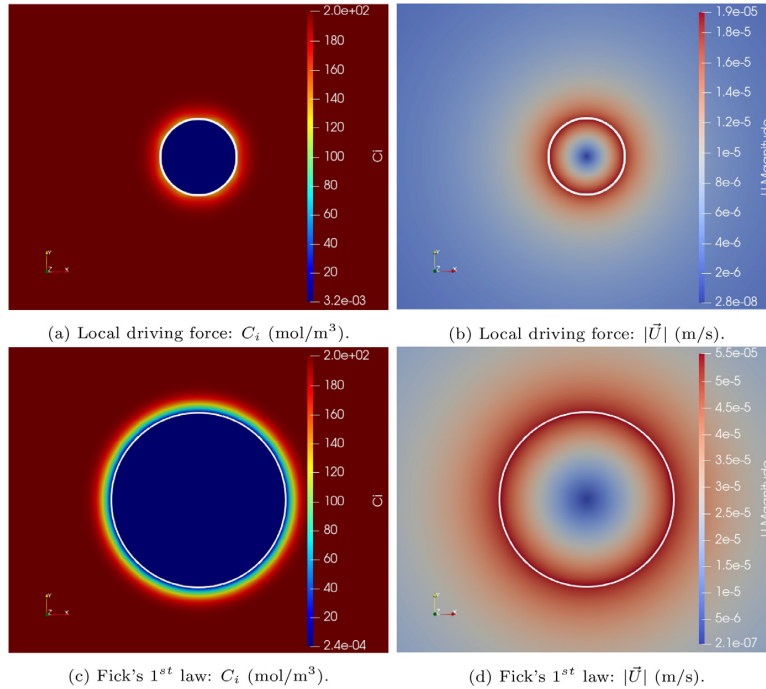


**Fig. 8.** Simulated concentration field and velocity at  $t=10$  s using a local driving force and Fick's 1<sup>st</sup> law. The interface is represented with a white contour corresponding to  $\alpha_1 = 0.5$ .

The Laplace pressure in the bubble obtained from the simulations ( $\Delta p_c$ ) is calculated as

$$\Delta p_c = \frac{\int_{\Omega} \alpha_2 p dV}{\int_{\Omega} \alpha_2 dV} - p_0, \quad (38)$$

where  $p_0$  is the operating pressure is equal to 101,325 Pa. For the two-dimensional bubble, the Laplace pressure in the bubble is calculated based on the Young-Laplace equation ( $\Delta p_c^* = \sigma/R$ ). The error associated with predicting the Laplace pressure can be calculated based on  $(\Delta p_c - \Delta p_c^*)/\Delta p_c^*$  and its temporal variation is plotted in Fig. 13. Although there is large initial discrepancy, the absolute error quickly reduces to values lower than 0.1, in Fig. 13.

## 6. Growth of a rising bubble in a supersaturated solution

The computational domain for modelling the growth and rise of a two-dimensional bubble is 3 mm  $\times$  9 mm. The pre-existing bubble of radius equal to 250  $\mu$ m is initialized such that its center is at a distance of 1mm from the bottom boundary and equidistant from the side boundaries. The dissolved carbon dioxide in the water is set at 200.64 mol/m<sup>3</sup>. Both gravity and surface tension are treated in this simulation. The four boundaries are described using a zero gradient conditions for  $\alpha_1$ ,  $C_i$ ,  $\vec{U}$  and  $\psi$  whereas a Dirichlet condition (equal to 101,325 Pa) is used for  $p_{\text{rgh}}$ . The mesh used in the simulation has a grid resolution ( $\Delta x$ ) and  $R_0/\Delta x$  equal to 7.5  $\mu$ m and 33.33, corresponding to the M4 mesh in Table 6. The simulation is terminated at 0.04s but the maximum time step, calculated based on Eq. (27), and maximum Courant number permitted are set to  $7.2 \times 10^{-7}$ s and 0.05 respectively. The driving force for bubble growth is described using Fick's 1<sup>st</sup> law as it provides a more realistic growth rate than  $Sh$  based correlation as shown in Fig. 9. The imbalance in the phases and dissolved gas in the simulation of the growth of the rising bubble is lower than 0.1% of the amount present initially in the system.

The changes in the bubble morphology along with its position in the computational domain as it evolves is illustrated in Fig. 14. The distribution of the dissolved gas around the bubble and velocity in the domain due to the rising bubble at  $t=0.04$ s is illustrated in Fig. 15(a) and (b), respectively. As the growing bubble grows and rises, the dissolved gas at rear of the rising bubble gets depleted before the mass transfer by convection and diffusion can replenish it. On the other hand, the incoming supersaturated liquid always replenishes the depleted dissolved gas. This variation in the concentration of the

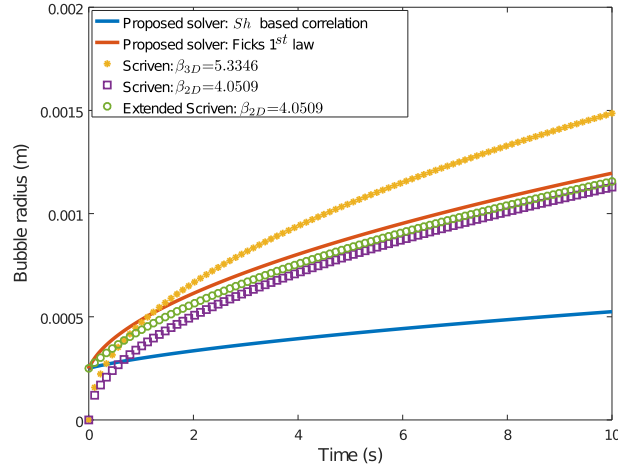


Fig. 9. Comparison between the simulated bubble radii using different driving forces ( $Sh$  based Local driving force and Fick's 1<sup>st</sup> law) and theoretical models (Eqs. (34) and (35)).

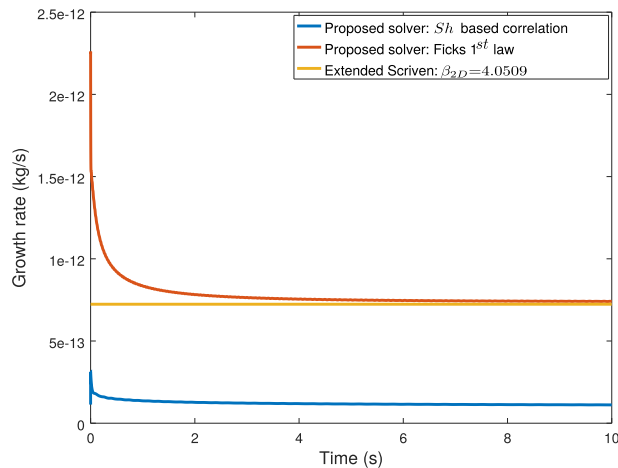


Fig. 10. Comparison of the growth rate predicted by the proposed solver using different driving forces for mass transfer across the interface to the Extended Scriven model. The growth rate of the bubble from the simulations and theory are calculated as  $\int_{\Omega} \psi_0 dV$  and Eq. (A.1), respectively.

dissolved gas around the interface leads to larger local mass transfer rate, calculated based on Eq. (22), in front of the bubble in comparison to its rear as shown in Fig. 15(c).

In order to understand the effect of bubble growth on rising, its rise velocity is compared to a bubble that is just rising without any growth. The rise velocity of the bubble is computed as the bubble volume averaged vertical component of the velocity vector [54]. The bubble rising without any growth is implemented by setting the dissolved gas concentration to zero in the simulation. Fig. 16(a) shows that, for 0.04s simulated, there is no substantial change in the rise velocity due to growth of the bubble by mass transfer across the interface. The corresponding growth of the rising bubble is illustrated through the increase in area of the bubble with time in Fig. 16(b). The insignificant change in the rise velocity indicates that the change in buoyancy force experienced by the bubble does not change as a result of the growth, which agrees with a previous experimental study [20].

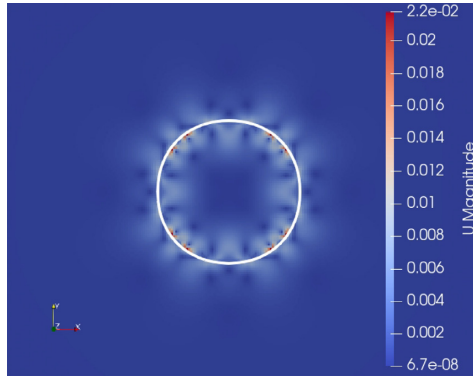


Fig. 11.  $U_{sc}$  (m/s), at  $t = 2$  ms, while modelling surface tension when the bubble growth is modelled based on the Fick's 1<sup>st</sup> law and  $\alpha_1 = 0.5$  is represented by a white contour.

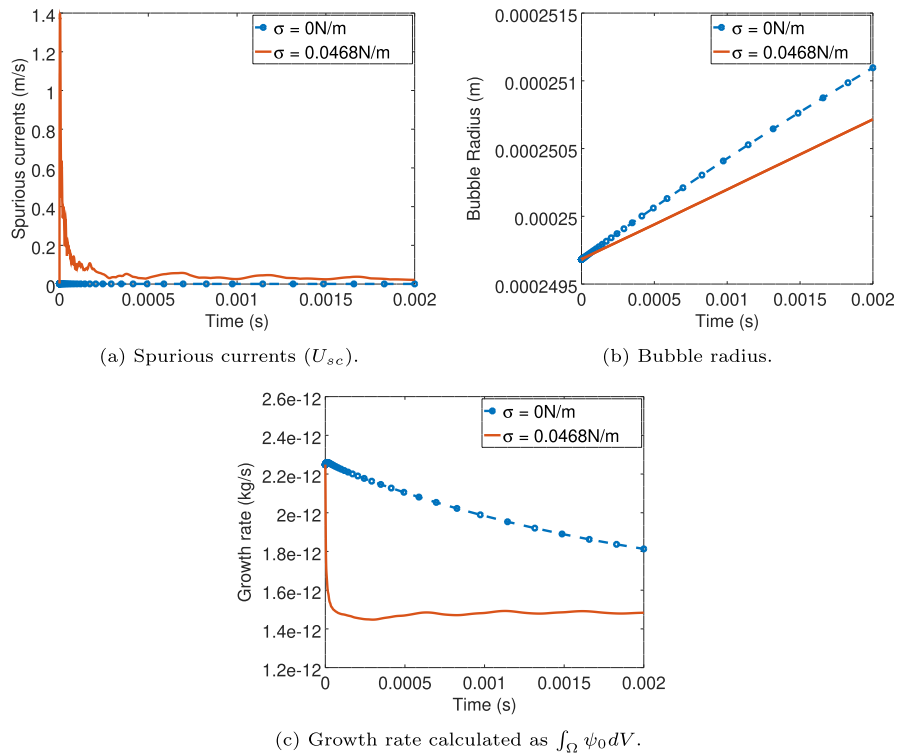


Fig. 12. Effect of modelling surface tension on the bubble growth.

### 7. Influence of user defined parameters

In this section, the effect of user defined parameters, like  $He_t$ ,  $D\Delta t$  and size of pre-existing bubble, are investigated using the the setup described in the validation studies i.e. neglecting surface tension and gravity while using Fick's 1<sup>st</sup> law as driving force for bubble growth.

Smearing of  $\psi_0$  to obtain  $\psi$ , using Eq. (23), relies on a user defined  $D\Delta t$  and ideally the solution should be independent of the effect of this parameter. As  $\psi$  is used to compute the source term required for bubble growth (i.e.  $\dot{m}$  which is defined

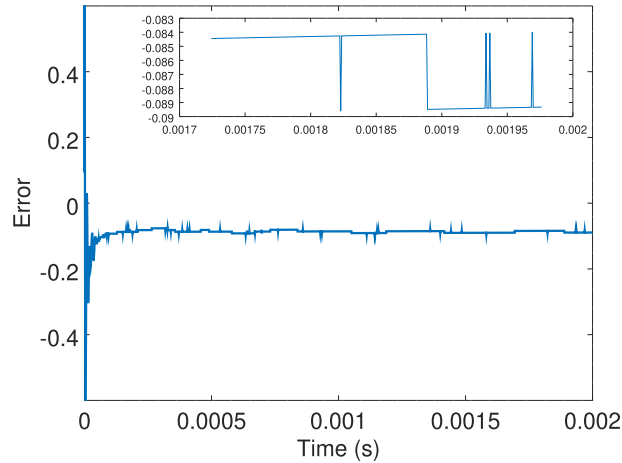


Fig. 13. Error in calculating the Laplace pressure in the growing bubble.

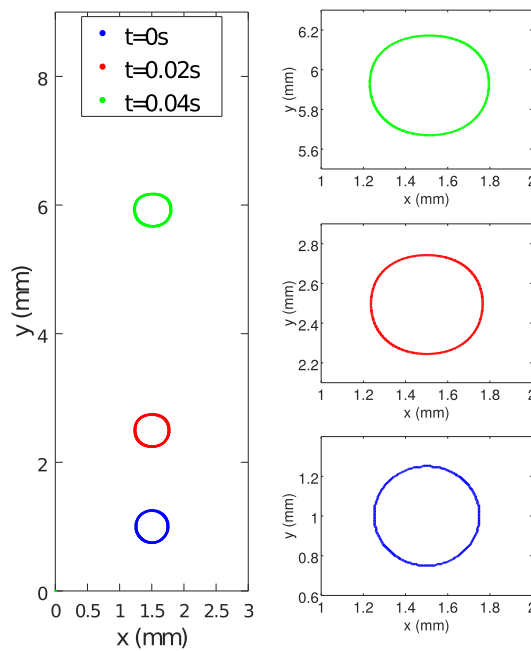


Fig. 14. Growth of a bubble rising through a supersaturated solution. The interface is represented by  $\alpha_1 = 0.5$ .

in Eq. (24), the evolution of the bubble radius can be used to study the effect of  $D\Delta t$ . The parameter,  $D\Delta t$ , is set equal to  $10^{-6}\text{m}^2$ ,  $10^{-7}\text{m}^2$ ,  $10^{-8}\text{m}^2$  and  $10^{-9}\text{m}^2$  which corresponds to a length scale for smearing the  $\psi_0$  equal to nearly 0.001 m, 0.00032 m, 0.0001 m and 0.00003 m, respectively (calculated as  $\sqrt{D\Delta t}$  [44]). The effect of  $D\Delta t$  on the growth rate of bubble is shown in Fig. 17 and the solution becomes nearly independent of  $D\Delta t$  when using larger values (i.e.  $10^{-6}\text{m}^2$  and  $10^{-7}\text{m}^2$ ).

The parameter  $He_i$ , which is used to model concentration jump across the interface, should theoretically be set equal to zero to model the transport of the dissolved gas and describe the interface as saturated. When  $He_i$  is set equal to zero the denominator in  $\mathfrak{B}$  (in Eq. (16)) becomes infinity for  $\alpha_1 = 0$ . Although  $He_i$  cannot be set equal to zero, the saturated condition of the interface can be reasonably reproduced by using a low enough value of  $He_i$ . So  $He_i$  is set to a non-zero number

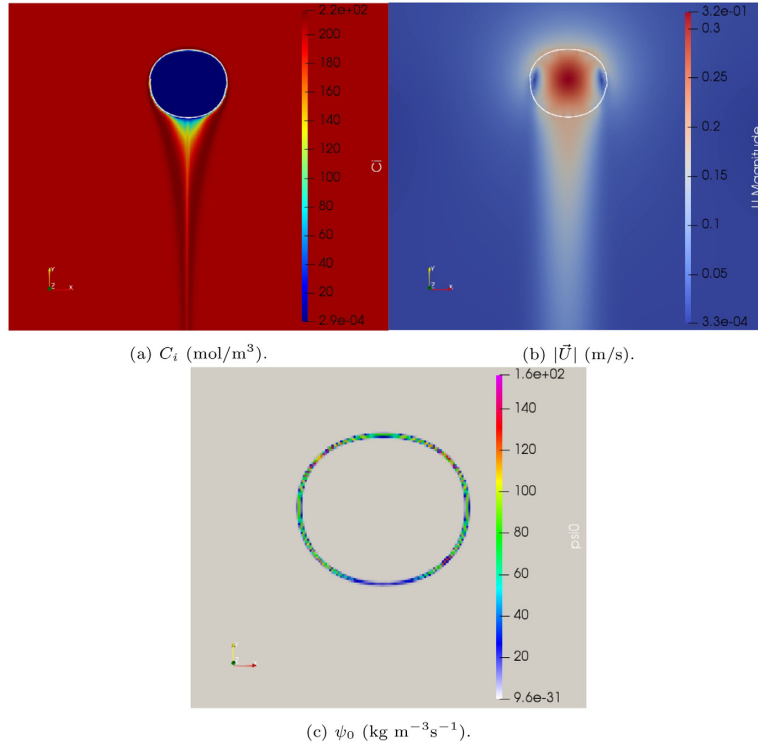


Fig. 15. Contours of velocity, concentration of dissolved gas and local mass transfer rate plotted at  $t = 0.04$  s. The interface is represented with a white contour at  $\alpha_1 = 0.5$ .

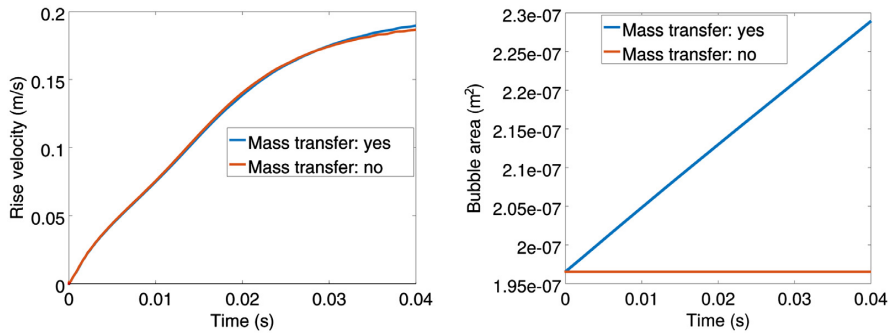


Fig. 16. The effect of bubble growth as the bubble rises up in a supersaturated liquid.

(i.e.  $10^{-4}$ ,  $10^{-3}$ ,  $10^{-2}$ ,  $10^{-1}$  and one) and its influence on the concentration distribution of dissolved gas and associated bubble growth is compared in Figs. 18 and 19, respectively. When  $He_i$  is equal to  $10^{-3}$  or  $10^{-4}$ , both bubble growth and concentration of dissolved gas in bubble becomes nearly independent of  $He_i$  which indicates that the saturation condition of the interface has been nearly reproduced. It is also worth pointing out that setting  $He_i$  to  $10^{-3}$  or  $10^{-4}$ , introduces some temporal unboundedness in the beginning of the simulation in the value of  $C_i$ . As the mass balance of the dissolved gas is not affected due to this temporal unboundedness of  $C_i$ , we consider effect of this error to be rather negligible.

The effect of the size of pre-existing bubbles (radii equal to 250  $\mu\text{m}$  and 500  $\mu\text{m}$ ) on the bubble growth is investigated in Fig. 20. The computational domain and the mesh resolution used in these simulations has been changed to make the

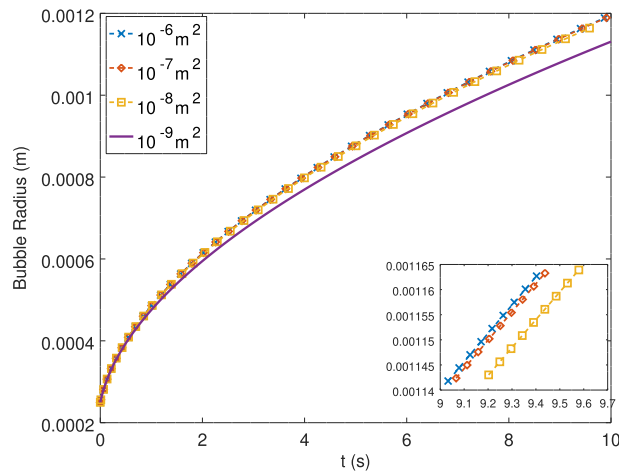


Fig. 17. Comparison of the evolution of bubble radius for various  $D\Delta t$ .

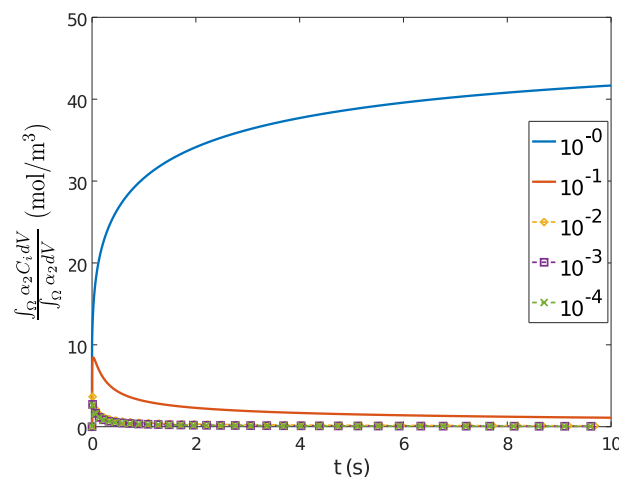


Fig. 18. The temporal variation of the concentration of dissolved gas numerically present in the bubble, due to the use of a non-zero  $He_i$ .

relative number of mesh elements equal in both simulations. The growth of the bubbles, in Fig. 20, shows that smaller the bubble higher the growth rate.

Although size of the pre-existing bubble (250  $\mu\text{m}$ ) used in the simulations is much larger than the critical radius, calculated using Eq. (1), it is in the same order as the radii of the pre-existing bubbles used in the theoretical work like [14] but larger than the cavity size reported in experiments, which is typically around 50–200  $\mu\text{m}$  [4]. These micrometer sized bubble are very difficult to model due the presence of spurious currents that can sometimes be large enough enough to render simulations inaccurate [63]. As lower limit to the size of the pre-existing bubble is dictated by the spurious currents, implementation of more advanced surface tension models are required to model micrometer size bubbles. It is also worth pointing out that boiling studies performed using OpenFOAM® [46,64] and condensation studies [50] typically use pre-existing bubbles radius in the same range as the ones used in this paper but other solvers, which use more advanced interface reconstruction algorithms, like Piecewise-Linear Interface Calculation (PLIC) scheme [44], and/or surface tension approach, using height functions [65], enables modelling even smaller pre-existing bubbles (in the order of few micrometers) due to the lower spurious current [44,66].

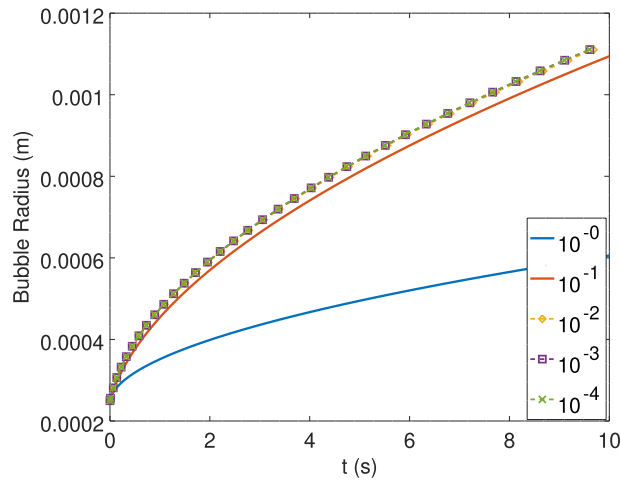


Fig. 19. Effect of  $He_i$  on the growth of the bubble.

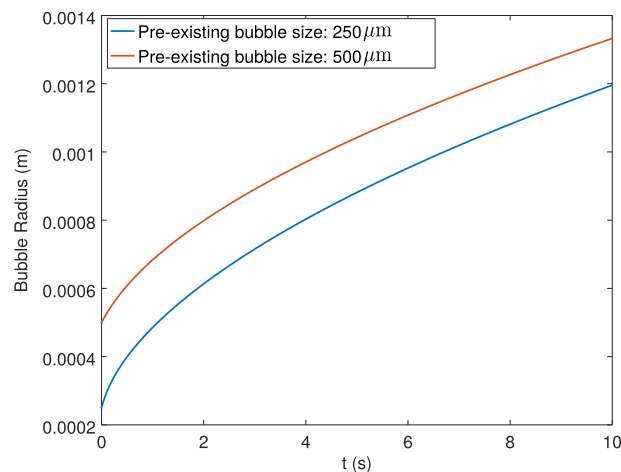


Fig. 20. Comparison of the evolution of bubble radius based on the size of the pre-existing bubble when the effect of both gravity and surface tension are neglected.

## 8. Conclusions

In this paper, a new VOF based solver to model bubble evolution in supersaturated systems is implemented in OpenFOAM 6. The proposed solver is created by adding dissolved gas transport equation (C-CST model [53]), surface tension (SSF [54]) model, driving force for bubble growth (Fick's 1<sup>st</sup> law and a  $Sh$  based correlation) and the relevant source terms are implemented, by extending the work of [44,46,47], in interFOAM.

The mass transfer models applied in the proposed solver are validated based on theoretical models like Epstein–Plesset [14] which do not consider the effect of convection, and Scriven [15] as well as Extended Scriven [16] which accounts for the effect of radial bubble growth. The proposed solver utilizing a driving force based on Eqs. (28) and (33), matches well with the approximate solution of Epstein–Plesset [14] as shown in Fig. 6. A driving force based on Fick's 1<sup>st</sup> law provides a better agreement to Scriven [15] and Extended Scriven [16] models than a  $Sh$  correlation as shown in Figs. 9 and 10. The modelling of the growth of the rising bubble using Fick's 1<sup>st</sup> law shows that the proposed solver, for the duration of 0.04 s, predicted the negligible effect of the bubble growth on rise velocity. Further remarks about the proposed solver are:

- Spurious currents, generated while modelling surface tension, introduces numerical convection near the interface that reduces the growth rate of the bubble by advecting away the dissolved gas at the interface.
- As expected, the solver is able to predict higher growth rate of smaller bubbles compared to larger bubbles and the increase in local mass transfer rate at the front of the bubble than its rear when a bubble is rising.
- The simulations also shows that the bubble growth is sensitive to the value of  $D\Delta t$  but the solution becomes nearly independent of the parameter at larger values.
- The use of  $He_i$  equal to  $10^{-4}$  in the C-CST has been shown to describe the transport of dissolved gas as well as the saturation condition at the interface reasonably well.

### Acknowledgment

The authors would like to acknowledge the Department of Material Science and Engineering, NTNU, for funding this research and the NTNU HPC for providing the required computing infrastructure. We would also like to thank the reviewers for the suggestions on improving the paper.

### Appendix A

Based on the derivation of expression to determine  $\beta_{3D}$ , i.e. Eq. (36) which is described in [19], we use the same approach to obtain a formulation for  $\beta_{2D}$  that describes a 2D bubble growing in a supersaturated solution. The growth rate of the bubble can be calculated as

$$\rho_2 2\pi Rh \frac{dR}{dt} = M_i (J_1 + J_2), \quad (\text{A.1})$$

where first term describes the rate of increase of the bubble volume,  $h$  describes a unit grid thickness which is set equal to  $10^{-6}$  m which is used in the simulations, and  $J_1 + J_2$  corresponds to the sum of mass transfer across the interface (Eq. (A.3)) and effect of convection generated by bubble growth (Eq. (A.4b)) [19]. The theoretical distribution of dissolved gas ( $\bar{C}$ ), once concentration boundary layer is developed, can be expressed as a sigmoid function, based on simulations as shown in Fig. 8(c), like

$$\bar{C} = \frac{2(\bar{C}_\infty - \bar{C}_{sat})}{1 + e^{-m(r-R)/R}} + 2\bar{C}_{sat} - \bar{C}_\infty, \quad (\text{A.2})$$

that satisfies the following boundary conditions

$$r = R, \bar{C} = \bar{C}_{sat},$$

$$r \rightarrow \infty, \bar{C} \rightarrow \bar{C}_\infty,$$

where  $m$  is a constant that is defined in Eq. (A.6). The diffusive mass transfer across the interface can be described as

$$J_1 = (2\pi Rh) D_{i,1} \left. \frac{\partial \bar{C}}{\partial r} \right|_{r=R} = 2\pi Rh D_{i,1} \frac{m(\bar{C}_\infty - \bar{C}_{sat})}{2R}. \quad (\text{A.3})$$

The effect of convection established by the increase in bubble radius on the growth rate is treated as

$$J_2 = A \sqrt{D_{i,1} \frac{dA/dt}{A}} (\bar{C}_\infty - \bar{C}_{sat}), \quad (\text{A.4a})$$

where  $A$  is the interface surface area that is equal to  $2\pi Rh$  which can be used to reduce the above equation as

$$J_2 = 2\pi Rh D_{i,1} (\bar{C}_\infty - \bar{C}_{sat}) \sqrt{\frac{1}{RD_{i,1}} \frac{dR}{dt}}. \quad (\text{A.4b})$$

Substituting Eqs. (A.3) and (A.4b) in Eq. (A.1) gives

$$\frac{dR}{dt} = \frac{M_i}{\rho_2} \left( D_{i,1} \frac{m(\bar{C}_\infty - \bar{C}_{sat})}{2R} + D_{i,1} (\bar{C}_\infty - \bar{C}_{sat}) \sqrt{\frac{1}{RD_{i,1}} \frac{dR}{dt}} \right). \quad (\text{A.5})$$

When  $J_2$  is neglected, the above equation must reduce to Eq. (31), which shows that

$$m = 2. \quad (\text{A.6})$$

As bubble radius in 2D also evolve as described by Eqs. (34) and (35), bubble radius evolution can be described as  $R = 2\beta_{2D} \sqrt{D_{i,1} t + B}$ , where  $B = R_0^2 / (4\beta_{2D}^2)$  it can be substituted in the above equation to obtain

$$\frac{\beta_{2D} D_{i,1}}{\sqrt{D_{i,1} t + B}} = \frac{M_i}{\rho_2} D_{i,1} (\bar{C}_\infty - \bar{C}_{sat}) \left( \frac{1}{2\beta_{2D} \sqrt{D_{i,1} t + B}} + \sqrt{\frac{1}{D_{i,1} 2\beta_{2D} \sqrt{D_{i,1} t + B}} \frac{\beta_{2D} D_{i,1}}{\sqrt{D_{i,1} t + B}}} \right), \quad (\text{A.7})$$



which can be further simplified to a quadratic equation for  $\beta_{2D}$  as

$$2\sqrt{2}\beta_{2D}^2 - 2a\beta_{2D} - \sqrt{2}a = 0, \quad (\text{A.8})$$

where  $a$  is defined in Eq. (36). Based on Eq. (A.8),  $\beta_{2D}$  can be calculated as

$$\beta_{2D} = \frac{a + \sqrt{a^2 + 4a}}{2\sqrt{2}}. \quad (\text{A.9})$$

## References

- [1] W. Henry, iii. experiments on the quantity of gases absorbed by water, at different temperatures, and under different pressures, *Phil. Trans. R. Soc. Lond.* 93 (1803) 29–274, doi:10.1098/rstl.1803.0004.
- [2] N.E. Shafer, R.N. Zare, Through a beer glass darkly, *Phys. Today* 44 (10) (1991) 48–52, doi:10.1063/1.881294.
- [3] G. Liger-Belair, R. Marchal, B. Robillard, M. Vignes-Adler, A. Maujean, P. Jeandet, Study of effervescence in a glass of champagne: Frequencies of bubble formation, growth rates, and velocities of rising bubbles, *Am. J. Enol. Viticult.* 50 (3) (1999) 317–323.
- [4] G. Barker, B. Jefferson, S. Judd, The control of bubble size in carbonated beverages, *Chem. Eng. Sci.* 57 (4) (2002) 565–573, doi:10.1016/S0009-2509(01)00391-8.
- [5] J. Solano-Altamirano, S. Goldman, The lifetimes of small arterial gas emboli, and their possible connection to inner ear decompression sickness, *Math. Biosci.* 252 (2014) 27–35, doi:10.1016/j.mbs.2014.03.008.
- [6] D. Fernández, P. Maurer, M. Martine, J.M.D. Coey, M.E. Möbius, Bubble formation at a gas-evolving microelectrode, *Langmuir* 30 (43) (2014) 13065–13074, doi:10.1021/la500234r.
- [7] S. Lakshmanan, T. Murugesan, The chlor-alkali process: Work in progress, *Clean Technol. Environ. Policy* 16 (2) (2014) 225–234, doi:10.1007/s10098-013-0630-6.
- [8] A. Taqieeddin, M.R. Allshouse, A.N. Alshawabkeh, Editors' choice-critical review-mathematical formulations of electrochemically gas-evolving systems, *J. Electrochem. Soc.* 165 (13) (2018) E694–E711, doi:10.1149/2.0791813jes.
- [9] S. Jones, G. Evans, K. Galvin, Bubble nucleation from gas cavities—a review, *Adv. Colloid Interface Sci.* 80 (1) (1999) 27–50, doi:10.1016/S0001-8686(98)00074-8.
- [10] K.J. Vachaparambil, K.E. Einarsrud, Explanation of bubble nucleation mechanisms: A gradient theory approach, *J. Electrochem. Soc.* 165 (10) (2018) E504–E512, doi:10.1149/2.1031810jes.
- [11] S.D. Lubetkin, Why is it much easier to nucleate gas bubbles than theory predicts? *Langmuir* 19 (7) (2003) 2575–2587, doi:10.1021/la0266381.
- [12] G. Liger-Belair, R. Marchal, P. Jeandet, Close-up on bubble nucleation in a glass of champagne, *Am. J. Enol. Viticult.* 53 (2) (2002) 151–153.
- [13] A. Perret, D.A. Bonhommeau, G. Liger-Belair, T. Cours, A. Alijah, CO<sub>2</sub> diffusion in champagne wines: A molecular dynamics study, *J. Phys. Chem. B* 118 (7) (2014) 1839–1847, doi:10.1021/jp410998f.
- [14] P.S. Epstein, M.S. Plesset, On the stability of gas bubbles in liquid–gas solutions, *J. Chem. Phys.* 18 (11) (1950) 1505–1509, doi:10.1063/1.1747520.
- [15] L. Scriven, On the dynamics of phase growth, *Chem. Eng. Sci.* 10 (1) (1959) 1–13, doi:10.1016/0009-2509(59)80019-1.
- [16] S.J. Hashemi, J. Abedi, Advances in modeling of new phase growth, *Energy Fuels* 21 (4) (2007) 2147–2155, doi:10.1021/ef060643l.
- [17] G. Sakuma, Y. Fukunaka, H. Matsushima, Nucleation and growth of electrolytic gas bubbles under microgravity, *Int. J. Hydrog. Energy* 39 (15) (2014) 7638–7645, doi:10.1016/j.ijhydene.2014.03.059.
- [18] H. Matsushima, D. Kiuchi, Y. Fukunaka, K. Kuribayashi, Single bubble growth during water electrolysis under microgravity, *Electrochem. Commun.* 11 (8) (2009) 1721–1723, doi:10.1016/j.elecom.2009.07.009.
- [19] Y. Wang, X. Hu, Z. Cao, L. Guo, Investigations on bubble growth mechanism during photoelectrochemical and electrochemical conversions, *Colloids Surf. A Physicochem. Eng. Aspects* 505 (2016) 86–92, doi:10.1016/j.colsurfa.2016.01.004.
- [20] G. Liger-Belair, R. Marchal, B. Robillard, T. Dambrouck, A. Maujean, M. Vignes-Adler, P. Jeandet, On the velocity of expanding spherical gas bubbles rising in line in supersaturated hydroalcoholic solutions: Application to bubble trains in carbonated beverages, *Langmuir* 16 (4) (2000) 1889–1895, doi:10.1021/la990653x.
- [21] A. Alexiadis, M. Dudukovic, P. Ramachandran, A. Cornell, J. Wanngrd, A. Bokkers, Liquid gas flow patterns in a narrow electrochemical channel, *Chem. Eng. Sci.* 66 (10) (2011) 2252–2260, doi:10.1016/j.ces.2011.02.046.
- [22] G. Li, X. Yang, G. Dai, CFD simulation of effects of the configuration of gas distributors on gas–liquid flow and mixing in a bubble column, *Chem. Eng. Sci.* 64 (24) (2009) 5104–5116, doi:10.1016/j.ces.2009.08.016.
- [23] L. Liu, W. Cai, Y. Chen, Y. Wang, Fluid dynamics and mass transfer study of electrochemical oxidation by CFD prediction and experimental validation, *Indust. Eng. Chem. Res.* 57 (18) (2018) 6493–6504, doi:10.1021/acs.iecr.7b04226.
- [24] W. El-Askary, I. Sakr, K. Ibrahim, A. Balabel, Hydrodynamics characteristics of hydrogen evolution process through electrolysis: Numerical and experimental studies, *Energy* 90 (2015) 722–737, doi:10.1016/j.energy.2015.07.108.
- [25] R. Hreiz, L. Abdelouahed, D. Fünfschilling, F. Lapique, Electrogenerated bubbles induced convection in narrow vertical cells: A review, *Chem. Eng. Res. Des.* 100 (2015) 268–281, doi:10.1016/j.cherd.2015.05.035.
- [26] A. Cubeddu, V. Nandana, U. Janoske, A numerical study of gas production and bubble dynamics in a Hall–Héroult reduction cell, in: C. Chesonis (Ed.), *Light Metals 2019*, Springer International Publishing, Cham, 2019, pp. 605–613.
- [27] M. Philippe, H. Jérôme, B. Sebastien, P. Gérard, Modelling and calculation of the current density distribution evolution at vertical gas-evolving electrodes, *Electrochim. Acta* 51 (6) (2005) 1140–1156, doi:10.1016/j.electacta.2005.06.007.
- [28] R. Hreiz, L. Abdelouahed, D. Fünfschilling, F. Lapique, Electrogenerated bubbles induced convection in narrow vertical cells: PIV measurements and euler–lagrange CFD simulation, *Chem. Eng. Sci.* 134 (2015) 138–152, doi:10.1016/j.ces.2015.04.041.
- [29] T. Nierhaus, H. Van Parys, S. Dehaeck, J. van Beeck, H. Deconinck, J. Deconinck, A. Hubin, Simulation of the two-phase flow hydrodynamics in an irde reactor, *J. Electrochem. Soc.* 156 (9) (2009) P139–P148, doi:10.1149/1.3155423.
- [30] A. Battistella, S.S.C. Aelen, I. Roghair, M. van Sint Annaland, Euler–lagrange modeling of bubbles formation in supersaturated water, *ChemEngineering* 2 (3) (2018) 39, doi:10.3390/chemengineering2030039.
- [31] F. Beaumont, C. Popa, G.L. Belair, G. Polidori, Numerical modeling of bubble-induced flow patterns in champagne glasses, *Int. J. Numer. Methods Heat Fluid Flow* 24 (3) (2014) 563–578, doi:10.1108/HFF-03-2012-0063.
- [32] M. Sommerfeld, *Numerical Methods for Dispersed Multiphase Flows*, Springer International Publishing, Cham, pp. 327–396. doi:10.1007/978-3-319-60282-0\_6.
- [33] H. Liu, L.-M. Pan, J. Wen, Numerical simulation of hydrogen bubble growth at an electrode surface, *Canad. J. Chem. Eng.* 94 (1) (2016) 192–199, doi:10.1002/cjce.22378.
- [34] K.E. Einarsrud, A Treatise on Interpolar Transport Phenomena, Norwegian University of Science and Technology (NTNU), Trondheim, 2012 Ph.D. thesis. <https://books.google.no/books?id=L5FnNllaGfC>.
- [35] K.E. Einarsrud, I. Eick, W. Bai, Y. Feng, J. Hua, P.J. Witt, Towards a coupled multi-scale, multi-physics simulation framework for aluminium electrolysis, *Appl. Math. Modell.* 44 (2017) 3–24, doi:10.1016/j.apm.2016.11.011.
- [36] K.E. Einarsrud, S.T. Johansen, Modelling of bubble behaviour in aluminium reduction cells, *Progr. Comput. Fluid Dyn. Int. J.* 12 (2–3) (2012) 119–130, doi:10.1504/PCFD.2012.047455.

- [37] M. Sun, B. Li, L. Li, A multi-scale mathematical model of growth and coalescence of bubbles beneath the anode in an aluminum reduction cell, *Mater. Trans. B* 49 (5) (2018) 2821–2834, doi:10.1007/s11663-018-1311-y.
- [38] M. Sun, B. Li, L. Li, Multiscale simulation of bubble behavior in aluminum reduction cell using a combined discrete-bubble-model volume-of-fluid magnetohydrodynamical method, *Indust. Eng. Chem. Res.* 58 (8) (2019) 3407–3419, doi:10.1021/acs.iecr.8b05109.
- [39] R. Bird, W. Stewart, E. Lightfoot, *Transport Phenomena: Revised Second Edition*, Wiley, New York, 2007.
- [40] D. Deising, D. Bothe, H. Marschall, Direct numerical simulation of mass transfer in bubbly flows, *Comput. Fluids* 172 (2018) 524–537, doi:10.1016/j.compfluid.2018.03.041.
- [41] C.G. Bisperink, A. Prins, Bubble growth in carbonated liquids, *Colloids Surf. A Physicochem. Eng. Aspects* 85 (2) (1994) 237–253, doi:10.1016/0927-7757(94)02744-7.
- [42] Y. Li, Z. Yao, Z. Hua Chen, K. Cao, S. long Qiu, F. jun Zhu, C. Zeng, Z. ming Huang, Numerical simulation of polypropylene foaming process assisted by carbon dioxide: Bubble growth dynamics and stability, *Chem. Eng. Sci.* 66 (16) (2011) 3656–3665, doi:10.1016/j.ces.2011.04.035.
- [43] C.R. Kharangate, I. Mudawar, Review of computational studies on boiling and condensation, *Int. J. Heat Mass Transf.* 108 (2017) 1164–1196, doi:10.1016/j.ijheatmasstransfer.2016.12.065.
- [44] S. Hardt, F. Wondra, Evaporation model for interfacial flows based on a continuum-field representation of the source terms, *J. Comput. Phys.* 227 (11) (2008) 5871–5895, doi:10.1016/j.jcp.2008.02.020.
- [45] OpenCFD Ltd (ESI Group), (<https://openfoam.com/>). [Online; accessed 18-September-2019].
- [46] C. Kunkelmann, P. Stephan, Cfd simulation of boiling flows using the volume-of-fluid method within openfoam, *Numer. Heat Transf. Part A Appl.* 56 (8) (2009) 631–646, doi:10.1080/10407780903423908.
- [47] C. Kunkelmann, Numerical Modeling and Investigation of Boiling Phenomena, Technische Universität, Darmstadt, 2011 Ph.D. thesis. <http://tuprints.ulb.tu-darmstadt.de/2731/>.
- [48] A.S. Rattner, S. Garimella, Simple Mechanistically consistent formulation for volume-of-fluid based computations of condensing flows, *J. Heat Transf.* 136 (7) (2014), 071501, doi:10.1115/1.4026808.
- [49] M. Bahreini, A. Ramiar, A.A. Ranjbar, Numerical simulation of bubble behavior in subcooled flow boiling under velocity and temperature gradient, *Nuclear Eng. Des.* 293 (2015) 238–248, doi:10.1016/j.nucengdes.2015.08.004.
- [50] N. Samkhaniani, M. Ansari, Numerical simulation of bubble condensation using CF-VOF, *Progr. Nuclear Energy* 89 (2016) 120–131, doi:10.1016/j.pnucene.2016.02.004.
- [51] N. Samkhaniani, M.R. Ansari, The evaluation of the diffuse interface method for phase change simulations using openfoam, *Heat Transf. Asian Res.* 46 (8) (2017) 1173–1203, doi:10.1002/htj.21268.
- [52] The OpenFOAM Foundation, (<https://openfoam.org/>). [Online; accessed 18-September-2019].
- [53] J. Maes, C. Soulaire, A new compressive scheme to simulate species transfer across fluid interfaces using the volume-of-fluid method, *Chem. Eng. Sci.* 190 (2018) 405–418, doi:10.1016/j.ces.2018.06.026.
- [54] K.J. Vachaparambil, K.E. Einarsrud, Comparison of surface tension models for the volume of fluid method, *Processes* 7 (8) (2019) 542, doi:10.3390/pr7080542.
- [55] M. Aboukhedr, A. Georgoulas, M. Marengo, M. Gavaises, K. Vogiatzaki, Simulation of micro-flow dynamics at low capillary numbers using adaptive interface compression, *Comput. Fluids* 165 (2018) 13–32, doi:10.1016/j.compfluid.2018.01.009.
- [56] H. Rusche, Computational fluid dynamics of dispersed two-phase flows at high phase fractions, Imperial College London (University of London), 2003 PhD thesis. <http://hdl.handle.net/10044/1/8110>.
- [57] S.S. Deshpande, L. Anumolu, M.F. Trujillo, Evaluating the performance of the two-phase flow solver interFoam, *Comput. Sci. Discov.* 5 (1) (2012) 014016, doi:10.1088/1749-4699/5/1/014016.
- [58] E.B. Winn, The temperature dependence of the self-diffusion coefficients of argon, neon, nitrogen, oxygen, carbon dioxide, and methane, *Phys. Rev.* 80 (1950) 1024–1027, doi:10.1103/PhysRev.80.1024.
- [59] R. Issa, Solution of the implicitly discretised fluid flow equations by operator-splitting, *J. Comput. Phys.* 62 (1) (1986) 40–65, doi:10.1016/0021-9991(86)90099-9.
- [60] R. Sander, Compilation of Henry's law constants (version 4.0) for water as solvent, *Atmosph. Chem. Phys.* 15 (8) (2015) 4399–4981, doi:10.5194/acp-15-4399-2015.
- [61] T. Yamamoto, Y. Okano, S. Dost, Validation of the s-clsvof method with the density-scaled balanced continuum surface force model in multiphase systems coupled with thermocapillary flows, *Int. J. Numer. Methods Fluids* 83 (3) (2017) 223–244, doi:10.1002/ld.4267.
- [62] J. Klostermann, K. Schaake, R. Schwarze, Numerical simulation of a single rising bubble by vof with surface compression, *Int. J. Numer. Methods Fluids* 71 (8) (2013) 960–982, doi:10.1002/ld.3692.
- [63] A. Saufi, A. Frassoldati, T. Faravelli, A. Cuoci, Dropletsmoke++: A comprehensive multiphase CFD framework for the evaporation of multidimensional fuel droplets, *Int. J. Heat Mass Transf.* 131 (2019) 836–853, doi:10.1016/j.ijheatmasstransfer.2018.11.054.
- [64] E.J. Owoeye, D. Schubring, Cfd analysis of bubble microlayer and growth in subcooled flow boiling, *Nuclear Eng. Des.* 304 (2016) 151–165, doi:10.1016/j.nucengdes.2016.04.027.
- [65] Z. Guo, D.F. Fletcher, B.S. Haynes, Implementation of a height function method to alleviate spurious currents in CFD modelling of annular flow in microchannels, *Appl. Math. Modell.* 39 (16) (2015) 4665–4686, doi:10.1016/j.apm.2015.04.022.
- [66] J. Murallidharan, G. Giustini, Y. Sato, B. Niemo, V. Badalassi, S.P. Walker, Computational fluid dynamic simulation of single bubble growth under high-pressure pool boiling conditions, *Nuclear Eng. Technol.* 48 (4) (2016) 859–869, doi:10.1016/j.net.2016.06.004.
- [67] J. Kestin, M. Sokolov, W.A. Wakeham, Viscosity of liquid water in the range –8 °C to 150 °C, *J. Phys. Chem. Ref. Data* 7 (3) (1978) 941–948, doi:10.1063/1.555581.
- [68] H. Iwasaki, M. Takahashi, Viscosity of carbon dioxide and ethane, *J. Chem. Phys.* 74 (3) (1981) 1930–1943, doi:10.1063/1.441286.
- [69] A. Tamimi, E.B. Rinker, O.C. Sandall, Diffusion coefficients for hydrogen sulfide, carbon dioxide, and nitrous oxide in water over the temperature range 293–368 K, *J. Chem. Eng. Data* 39 (2) (1994) 330–332, doi:10.1021/je00014a031.
- [70] C.J. Greenshields, Openfoam user guide version 6, <http://foam.sourceforge.net/docs/Guides-a4/OpenFOAMUserGuide-A4.pdf>.
- [71] B. van Leer, Towards the ultimate conservative difference scheme. ii. monotonicity and conservation combined in a second-order scheme, *J. Comput. Phys.* 14 (4) (1974) 361–370, doi:10.1016/0021-9991(74)90019-9.
- [72] K. Maki, Ship resistance simulations with openfoam, 6th OpenFOAM Workshop, The Pennsylvania State University State College, PA, USA, 13-16 June 2011.
- [73] C. Greenshields, Openfoam 2.3.0: Multiphase modelling, 2014, (<https://openfoam.org/release/2-3-0/multiphase/>). [Online; accessed 12-August-2019].
- [74] K.J. Vachaparambil, K.E. Einarsrud, in: Spurious velocities in the volume of fluid method: modeling a sub-millimeter bubble, *Proceedings of the 17th Multiphase Flow Conference & Short Course*, Dresden, Germany, 11-15 November 2019.



*Appended paper D*

**Modeling interfacial mass transfer driven bubble growth in supersaturated solutions**

Kurian J. Vachaparambil and Kristian Etienne Einarsrud  
Published in *AIP Advances*



# Modeling interfacial mass transfer driven bubble growth in supersaturated solutions

Cite as: AIP Advances 10, 105024 (2020); doi: 10.1063/5.0020210

Submitted: 29 June 2020 • Accepted: 26 September 2020 •

Published Online: 15 October 2020



Kurian J. Vachaparambil<sup>a)</sup>  and Kristian Etienne Einarsrud<sup>b)</sup> 

## AFFILIATIONS

Department of Materials Science and Engineering, Norwegian University of Science and Technology (NTNU), Trondheim 7491, Norway

<sup>a)</sup>Author to whom correspondence should be addressed: kurian.j.vachaparambil@ntnu.no and kurian\_jomy@hotmail.com

<sup>b)</sup>Electronic mail: kristian.e.einarsrud@ntnu.no

## ABSTRACT

A commonly encountered phenomenon in chemical processes is bubble evolution driven by supersaturation. On the continuum scale, this essentially involves interfacial mass transfer resulting in the growth of bubbles and their subsequent detachment from a surface. Analytical approaches to study this phenomenon typically involve estimating the driving force for interfacial mass transfer based on Sherwood number ( $Sh$ ) correlations and the bulk concentration of dissolved gas. This is often not practical since the bulk concentration is often unknown and  $Sh$  correlations are sometimes not available to provide an accurate description of the associated flow fields. With the use of interface-resolved simulations to model these processes, the local distribution of dissolved gas can be obtained by solving for the concentration field. The driving force for interfacial mass transfer can be computed based on  $Sh$  correlations (which can be adopted for specific flows and are typically used in “engineering” applications) or the universally applicable Fick’s first law. This paper compares the predictions of these approaches for the well-studied case of a two-dimensional bubble growing in an unbounded supersaturated solution for three different levels of supersaturation. The equivalent two-dimensional simulations are run in a previously developed volume of fluid framework on OpenFOAM® [K. J. Vachaparambil and K. E. Einarsrud, Appl. Math. Model. **81**, 690–710 (2020)]. The results show that the choice of an appropriate  $Sh$  correlation can provide a reasonable estimate of bubble growth. In a more universal approach, which is relevant when the flow being simulated cannot be captured by a single  $Sh$  correlation (e.g., bubble growth/coalescence and detachment) or when existing  $Sh$  correlations are not applicable, Fick’s first law can be used to compute the driving force for bubble growth, provided that the concentration boundary layer can be resolved.

© 2020 Author(s). All article content, except where otherwise noted, is licensed under a Creative Commons Attribution (CC BY) license (<http://creativecommons.org/licenses/by/4.0/>). <https://doi.org/10.1063/5.0020210>

## I. INTRODUCTION

Bubble evolution in supersaturated solutions is a process initiated by nucleation, followed by interfacial mass transfer driven growth and eventually detachment from the surface.<sup>1</sup> This phenomenon is relevant to processes such as electrolysis of water and electrolytic reduction of alumina, as well as to the opening of champagne bottles. As the presence of bubbles reduces the efficiency of electrochemical systems,<sup>2</sup> it is important to efficiently remove them. The bubble growth can be divided into two main regimes: inertial (which lasts for less than a second for very small bubbles of the order of tens of micrometers in size) and diffusion-controlled (the interfacial mass transfer driven regime relevant for continuum scale bubbles).<sup>2</sup> Apart from these two regimes, in electrochemical systems, the

heterogeneous reactions that result in supersaturation of the liquid can also affect the bubble growth.<sup>2</sup> Consequently, the continuum-scale bubble growth driven by interfacial mass transfer in supersaturated solutions is an important topic that has been investigated using analytical, numerical, and experimental approaches.

Seminal analytical studies were carried out by Epstein and Plesset<sup>11</sup> and by Scriven<sup>7</sup> in the 1950s. Epstein and Plesset<sup>11</sup> derived an approximate solution for the temporal changes in bubble size starting from a pre-existing bubble, although they neglected the effect of convection induced by the bubble growth. The effect of convection induced by the radially symmetric bubble growth was subsequently treated by Scriven<sup>7</sup> who derived an asymptotic solution describing the bubble growth controlled by interfacial mass transfer. Bruman and Jameson<sup>8</sup> derived a Sherwood number ( $Sh$ ) correlation (see

**TABLE I.** Some examples of Sherwood number ( $Sh$ ) correlations reported in the literature.

$Sh$ correlation	Applicable flow scenario	References
$Sh = 2$	$Re = 0$ flow around a spherical bubble	3
$Sh = 2 + 0.6515(Re Sc)^{1/2}$	$Re \ll 1$ flow around a bubble	4
$Sh = 2 + 0.6Re^{1/2}Sc^{1/3}$	$2 < Re < 200$ flow around a droplet	5 and 6
$Sh = 4\beta^2/\mathfrak{A}^3$	Bubble growth based on the work of Scriven <sup>7</sup>	8
$Sh = 0.332Re^{1/2}Sc^{1/3}$	Laminar flow over a flat plate	9
$Sh = 1.26Re^{1/3}Sc^{1/3}$	Rising bubble in champagne	10

<sup>a</sup> $\beta$  and  $\mathfrak{A}$  are dimensionless numbers that are defined in Eqs. (16) and (17), respectively.

Table I) based on the bubble growth scenario described by Scriven. The growth of rising bubbles in champagne was also described using a  $Sh$  correlation by Liger-Belair *et al.*<sup>10</sup> In these works based on  $Sh$  correlations, the analytical driving force ( $j_a$ ) for interfacial mass transfer is computed as

$$j_a = M \frac{D Sh}{L} (C_\infty - C_{sat}), \quad (1)$$

where  $M$  and  $D$  are the molar mass and the diffusion coefficient of the dissolved gas, respectively,  $L$  is a characteristic length scale, and  $C_\infty - C_{sat}$  is the difference between the concentration of dissolved gas in the bulk and at the interface (which is assumed to be at saturation). The supersaturation is represented by  $S$ , which is calculated as  $C_\infty/C_{sat}$ . Additionally, these analytical models assume that the bubbles are present in the bulk and are surrounded by an unbounded uniformly supersaturated solution.

In contrast to these analytical models, which present a greatly simplified view of the process, experimental studies have revealed the complex nature of bubble growth, including its dependence on surface wettability and the inhomogeneous distribution of supersaturation around the bubble.<sup>2</sup> Owing to the inhomogeneous distribution of supersaturation, as a result of convection or heterogeneous reactions, the driving force for interfacial mass transfer must be computed based on the local value of the dissolved gas concentration near the interface.

Numerical approaches, especially interface-resolved multiphase models such as the Volume of Fluid (VOF) method, can provide an adequate framework to resolve and study the growth of individual bubbles as well as to solve for the dissolved gas transport to determine its distribution and even treat heterogeneous reactions. However, owing to the difficulty in modeling transport of dissolved gas in multiphase flows and coupling this to the bubble growth, advances in numerical modeling of the latter phenomenon have been made only relatively recently. The transport of dissolved gas in multiphase flows requires treatment of the interface conditions that account for the jump in concentration and that of the continuity of the diffusive fluxes that accounts for interfacial mass transfer.<sup>12</sup> The ways in which these interfacial conditions

have been addressed in the literature can be broadly grouped as follows:

- two-field approaches,<sup>12–14</sup> which use individual transport equations for the dissolved species in each phase and in which interfacial conditions are applied as boundary conditions for each phase; and
- single-field approaches,<sup>15–17</sup> which use a single governing equation (which accounts for the interfacial conditions) to describe the transport of dissolved gas in both phases.

Although interfacial mass transfer can be simulated by both types of approaches, the two-field approach has a greater computational requirement owing to the larger number of governing equations that have to be solved, as well as the requirement for the sharp representation of the interface (obtained using geometrical reconstruction in VOF methods).<sup>15</sup> This information about the local concentration of the dissolved gas can be used to obtain a driving force for the interfacial mass transfer and bubble growth, which is computed in one of the following ways:

- Fick's first law provides an accurate representation of interfacial mass transfer for any given flow scenario, but it is computationally expensive owing to the need to resolve concentration gradients at the interface.
- The use of Sherwood number correlations is computationally cheaper and circumvents the need for gradient calculations by means of flow-specific approximations for "engineering" applications. As a result of these approximations,  $Sh$  correlations can be adopted for specific flow scenarios (see Table I) and can be generally expressed as  $Sh = 2 + aRe^bSc^c$ , where  $a$ ,  $b$ , and  $c$  are case-specific constants,  $Re$  is the Reynolds number (the ratio of inertial to viscous forces), and  $Sc$  is the Schmidt number (the ratio of the kinematic viscosity to the diffusion coefficient).<sup>16</sup> The associated driving force is computed based on the  $Sh$  correlations and the local concentration of the dissolved gas near the interface.

A summary of studies that have implemented these methods for determining driving forces and have simulated bubble growth by interfacial mass transfer is presented in Table II. Although the use of a driving force based on Fick's first law provides an accurate and generic representation of bubble growth for any flow scenario,  $Sh$  correlations are typically used for engineering applications.

The aim of this paper is to compare the bubble growth predictions using driving forces based on Fick's first law and two  $Sh$  correlations for a bubble growing in an unbounded solution that is supersaturated for a range of values. These driving forces are implemented in a VOF-based framework on OpenFOAM<sup>®</sup> 6 proposed in our recent work.<sup>21</sup> This flow scenario, which has been thoroughly investigated analytically, is chosen because of the availability of the exact solutions that can be used for the verification of the computational model. The results from the simulations show that carefully chosen  $Sh$  correlations can provide reasonably predictions that match analytical models. For flow scenarios that cannot be described by a single  $Sh$  correlation, such as bubble evolution (which includes growth, coalescence, and detachment), Fick's first law should be used to compute the driving force for interfacial mass transfer. Finally, when

**TABLE II.** Summary of the literature on bubble evolution driven by interfacial mass transfer.

Reference	Interfacial mass transfer	Transport	Concentration treated <sup>a</sup>	VOF scheme <sup>b</sup>
19	<i>Sh</i> correlation	Two-field	L <sup>c</sup>	Geometric
20	Fick's first law	Two-field	L + I + G	Geometric
21	Fick's first law	Single-field	L + I	Algebraic
22	Fick's first law	Single-field	L + I + G	Algebraic

<sup>a</sup>This refers to the regions to which the dissolved gas transport model applies: the liquid phase (L), the interfacial region where the jump conditions are treated (I), and the gas phase (G).

<sup>b</sup>Geometric VOF methods employ interface reconstruction within each cell, whereas algebraic VOF methods, which are computationally cheaper, generate an interface based on algebraic techniques (e.g., interface compression), which results in the interface being smeared over a few computational cells.<sup>18</sup>

<sup>c</sup>Interface jump conditions are not described in Ref. 19.

Fick's first law is used, the concentration boundary layer must always be resolved. This paper shows that using the appropriate *Sh* correlation can provide reliable results, which is beneficial for obtaining computationally cheaper simulations in engineering applications. As the effect of gravity has been studied in our previous work,<sup>21</sup> it will not be investigated again here. This paper will also ignore surface tension, since its modeling can lead to the well-known problem of spurious velocities,<sup>18,23-25</sup> which has been reported to alter interface mass transfer.<sup>21</sup>

## II. GOVERNING EQUATIONS AND SOLUTION ALGORITHM

The solver used in this paper, proposed in Ref. 21, is based on the algebraic VOF method used by OpenFOAM<sup>®</sup> 6 (in the interFoam solver<sup>18</sup>) along with a single-field dissolved gas transport model [the Compressive-Continuous Species Transfer (C-CST) model<sup>17</sup>] and a continuum field representation of source terms that was adapted based on the work of Hardt and Wondra<sup>26</sup> and Kunkelmann.<sup>27</sup> An overview of the governing equation and the overall solution algorithm of the solver is provided in this section; for further details and the derivation of the governing equations, see Ref. 21.

The first step of the solver is advection of the volume fraction of liquid. The volume fraction of liquid, denoted by  $\alpha_1$ , is a scalar used in the VOF method to distinguish between the phases.  $\alpha_1 = 1$  indicates the liquid (phase 1),  $\alpha_1 = 0$  indicates the gas/bubble (phase 2), and  $0 < \alpha_1 < 1$  indicates the interfacial region. To preserve the sharpness of the interface,  $\alpha_1$  is advected using the interface compression method (which belongs to the algebraic VOF approach), which is described as follows:

$$\frac{\partial \alpha_1}{\partial t} + \nabla \cdot (\alpha_1 \vec{U}) + \nabla \cdot [\alpha_1 (1 - \alpha_1) \vec{U}_r] = \alpha_1 \nabla \cdot \vec{U}, \quad (2)$$

where the first two terms on the left-hand side are the temporal and convection terms, while the third term, which is nonzero only in the interfacial region, compresses the interface depending on the relative velocity between the phases,  $\vec{U}_r$ .<sup>18</sup> The term on the right-hand side is associated with the source term that results in the bubble growth.<sup>21</sup> Equation (2) is solved using the semi-implicit multi-dimensional limiter for explicit solution (MULES) to ensure that  $\alpha_1$  remains bounded.<sup>28</sup> The volume fraction of phase 2,  $\alpha_2$ , is calculated as  $1 - \alpha_1$ . The fluid properties such as density  $\rho$  and viscosity

$\nu$  are computed using volume fraction based algebraic averaging as  $\chi = \alpha_1 \chi_1 + \alpha_2 \chi_2$ , where  $\chi \in [\rho, \nu]$ .

Once  $\alpha_1$  has been advected, the driving force for interfacial mass transfer is calculated. The solver computes the transport only to the dissolved gas (see Table II) and determines only the concentration  $C_i$  above the saturation condition. These simplifications allow the saturation concentration on the gas side of the interface to be described as  $0 \text{ mol/m}^3$ , and correspondingly, the driving force can be computed based on one of the following approaches:

- Fick's first law in the form

$$j = M_i D_{i,1} |\nabla C_i|, \quad (3)$$

where  $M_i$  is the molar mass of dissolved gas ( $i$ ) and  $D_{i,1}$  is the diffusion coefficient of the dissolved gas in the liquid. Equation (3) is based on the assumption that the gradient of concentration of the dissolved gas at the interface in the tangential direction is negligible in comparison with the normal component, as discussed by Deising *et al.*<sup>15</sup>

- *Sh* correlation 1:  $Sh = 2 + 0.6515 \sqrt{Re Sc}$ , which is applicable for low solubility/small mass transfer rates from the interface to liquid for a bubble in a creeping flow.<sup>4</sup> In this case,

$$j = M_i k_{Sh1} C_i, \quad (4)$$

with  $k_{Sh1}$  given by

$$k_{Sh1} = \frac{D_{i,1}}{2R} Sh = \frac{D_{i,1}}{2R} (2 + 0.6515 \sqrt{Re Sc}), \quad (5)$$

where  $R$  is the bubble radius,  $Re$  is given by  $2RU_\infty/\nu_1$  (where  $U_\infty$  is computed as the rate of increase in the bubble radius), and  $Sc = \nu_1/D_{i,1}$ .

- *Sh* correlation 2:  $Sh = 4\beta^2 \rho_2 / (M_i C_i)$ , which is applicable for the bubble growth driven by supersaturation (derived in Appendix A). In this case,

$$j = M_i k_{Sh2} C_i = \left( \frac{D_{i,1}}{2R} \frac{4\beta^2 \rho_2}{M_i C_i} \right) M_i C_i = 4\beta^2 \rho_2 \frac{D_{i,1}}{2R}, \quad (6)$$

where  $\beta$  is the growth coefficient used in Scriven's model<sup>7</sup> and is estimated using Eq. (16).



Based on  $j$ , the local mass transfer rate is computed at the liquid side of the interface as

$$\psi_0 = Nj\alpha_1|\nabla\alpha_1|, \quad (7)$$

where  $N$  is a normalization factor calculated as  $\int_{\Omega} |\nabla\alpha_1| dV / \int_{\Omega} \alpha_1 |\nabla\alpha_1| dV$ . To improve numerical robustness, the calculated local mass transfer rate is smeared at the interface, according to the method of Hardt and Wondra,<sup>26</sup> using a user-defined value  $D\Delta t$  as follows:

$$D\Delta t \nabla^2 \psi = \psi - \psi_0. \quad (8)$$

For the simulations reported in this paper,  $D\Delta t$  is set equal to  $10^{-6} \text{ m}^2$  based on the parametric study reported in our previous work.<sup>21</sup> For numerical stability, the source term for the continuity equation, which is redistributed in the region where  $\alpha_1 < 10^{-3}$  using a Heaviside function (as described by Kunkelmann<sup>27</sup>), is expressed as

$$\dot{m} = A\alpha_2\psi, \quad (9)$$

where  $A$  is a normalization factor equal to  $\int_{\Omega} \psi_0 dV / \int_{\Omega} \alpha_2 \psi dV$ . The sink term in the transport of the dissolved gas is computed at the liquid side of the interface as

$$S_i = -\frac{N\alpha_1(j|\nabla\alpha_1|)}{M_i}, \quad (10)$$

where  $N$  is the normalization factor used in Eq. (7).

The momentum equation, using a modified pressure ( $p_{\text{rgh}} = p - \rho\vec{g} \cdot \vec{x}$ ) and a single-field velocity field ( $\vec{U}$ ), is written as

$$\begin{aligned} \frac{\partial \rho \vec{U}}{\partial t} + \nabla \cdot (\rho \vec{U} \vec{U}) = & -\nabla p_{\text{rgh}} + \nabla \cdot (\mu \nabla \vec{U}) + \nabla \vec{U} \\ & \cdot \nabla \mu - \vec{g} \cdot \vec{x} \nabla \rho + \vec{F}_{\text{ST}}, \end{aligned} \quad (11)$$

where  $\nabla \cdot (\mu \nabla \vec{U}) + \nabla \vec{U} \cdot \nabla \mu$  are the viscous terms of the momentum equation.<sup>18</sup> As the surface tension effects are not simulated in this paper,  $\vec{F}_{\text{ST}}$ , which is the volumetric surface tension force, will not be considered here. As the densities of the individual phases are assumed to be constant, mass conservation can be described using the continuity equation as

$$\nabla \cdot \vec{U} = \frac{\dot{m}}{\rho}, \quad (12)$$

where  $\dot{m}$  is the source term for phase 2 computed in Eq. (9). The momentum and continuity equations are solved together using the pressure implicit with splitting of operator (PISO) algorithm.<sup>18,21</sup>

Finally, the C-CST model<sup>17</sup> for the transport of the dissolved gas is solved,

$$\begin{aligned} \frac{\partial C_i}{\partial t} + \nabla \cdot (\vec{U} C_i) = & \nabla \cdot (\hat{D}_i \nabla C_i) - \nabla \cdot \left( \hat{D}_i \frac{1 - He_i}{\alpha_1 + \alpha_2 He_i} C_i \nabla \alpha_1 \right) \\ & - \nabla \cdot \left( \frac{1 - He_i}{\alpha_1 + \alpha_2 He_i} \alpha_1 \alpha_2 \vec{U}_r C_i \right) + S_i, \end{aligned} \quad (13)$$

where  $S_i$  is computed using Eq. (10),  $He_i$  describes the interfacial jump in concentration, which is set to  $10^{-4}$  to reliably model just the dissolved gas,<sup>21</sup>  $\vec{U}_r$  is the relative velocity between the phases that appears in Eq. (2), and  $\hat{D}_i$  is the harmonic average of the diffusion coefficients of the phases.<sup>17</sup>

TABLE III. Settings used to solve the governing equations.

Equation	Linear solver	Smoother/preconditioner	Tolerance
$p_{\text{rgh}}$	PCG	GAMG	$10^{-20}$
$\vec{U}$	smoothSolver	symGaussSeidel	$10^{-10}$
$\alpha_1$	smoothSolver	symGaussSeidel	$10^{-10}$
$C_i$	PBiCGStab	Diagonal	$10^{-10}$
$\psi$	PCG	DIC	$10^{-10}$

### A. Numerical settings

The governing equations are discretized with the first- and second-order schemes in time and space,<sup>21</sup> respectively, and computed using the iterative solvers listed in Table III. Other OpenFOAM<sup>®</sup> specific numerical settings, such as MULESCorr and momentumPredictor, are set as described in our previous work.<sup>21</sup> The maximum time step is set by applying an upper limit on the Courant number equal to 0.05. The iterative solver used to solve for  $\psi$ , given in Table III, is used instead of the settings used in our previous work,<sup>21</sup> namely, PBiCGStab–diagonal, to reduce the computational time required, as described in Appendix B.

## III. RESULTS AND DISCUSSION

### A. Problem description

The computational domain and boundary/initial conditions used in the simulations are presented in Fig. 1. The fluid properties used in the simulations, adapted from our previous work,<sup>21</sup> are listed in Table IV. The supersaturation levels used in the simulations

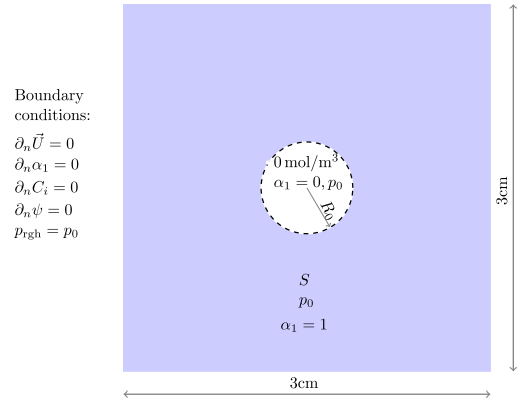


FIG. 1. Computational domain and boundary/initial conditions used in the simulations. The operating pressure ( $p_0$ ) and the pre-existing bubble radius ( $R_0$ ) used in the simulations are equal to 101 325 Pa and 250  $\mu\text{m}$ , respectively. The concentration of the dissolved gas at  $t = 0$  s is set based on the various levels of supersaturation  $S$ .

**TABLE IV.** Fluid properties used for the simulations (adapted from Ref. 21).

Property	Phase 1 (liquid)	Phase 2 (bubble)
Density (kg/m <sup>3</sup> )	997.0751 (Ref. 29)	1.81 (Ref. 30)
Viscosity (m <sup>2</sup> /s)	$8.92 \times 10^{-7}$ (Ref. 29)	$8.228 \times 10^{-6}$ (Ref. 30)
Diffusion coefficient (m <sup>2</sup> /s)	$1.94 \times 10^{-9}$ (Ref. 31)	$9.18 \times 10^{-6}$ (Ref. 32)
Molar mass (kg/mol)	$44 \times 10^{-3}$ (Ref. 21)	

are 2.5, 4, and 7, which correspond to the initialized concentrations of dissolved gas  $C_i$  equal to 50.16 mol/m<sup>3</sup>, 100.32 mol/m<sup>3</sup>, and 200.64 mol/m<sup>3</sup>, respectively (with a saturation concentration equal to 33.44 mol/m<sup>3</sup>). It should be noted that the initialized uniform distribution of the dissolved gas does not take account of any concentration boundary layer, the implications of which will be explored later in the discussion of the results. Again, both surface tension and gravity are neglected in the simulations, but we have investigated the influence of these parameters on growth previously.<sup>21</sup> The mesh used for all the simulations presented in this paper had a uniform hexahedral grid of  $16 \times 10^6$  cells based on grid convergence studies

performed for the bubble growth associated with  $S = 7$  and a driving force based on Fick's first law in our previous work.<sup>21</sup>

## B. Choice of analytical model

As the Epstein-Plesset model<sup>11</sup> ignores the effect of bubble growth on interfacial mass transfer, Scriven's asymptotic solution<sup>7</sup> provides the most reliable description of bubble growth via interfacial mass transfer, as was also noted by Burman and Jameson.<sup>8</sup> According to Scriven,<sup>7</sup> the increase in bubble radius can be described as

$$R_{\text{Scriven}} = 2\beta\sqrt{D_{i,1}t}, \quad (14)$$

where  $\beta$  is the growth coefficient. To treat the interfacial mass transfer driven growth of a pre-existing bubble, Scriven's solution was extended by Hashemi and Abedi<sup>33</sup> (in what we will refer to here as the "extended Scriven model") where the evolution of the bubble radius is described by

$$R_{\text{Scriven-ext}} = 2\beta\sqrt{D_{i,1}\left(t + \frac{R_0^2}{4D_{i,1}\beta^2}\right)}, \quad (15)$$

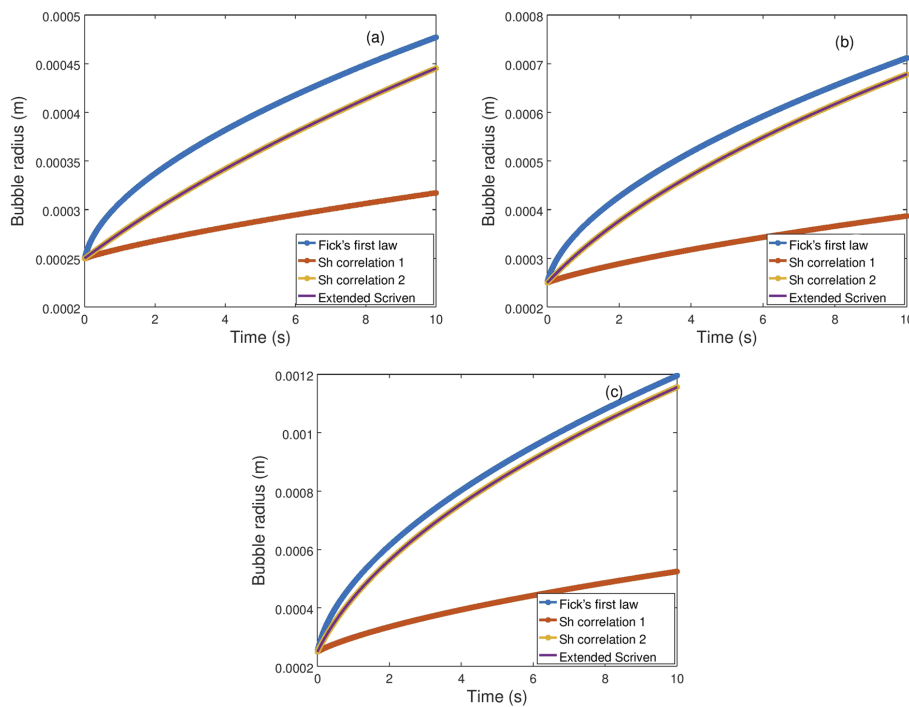


**FIG. 2.** Comparison of the results of simulations of bubble radius evolution using the driving forces based on Fick's first law [Eq. (3)] and on Sh correlations [Eqs. (4) and (6)] with the results of the extended Scriven model (with  $\beta_{2D}$ ) for various levels of supersaturation: (a) 2.5, (b) 4.0, and (c) 7.0.

where  $R_0$  is the radius of the pre-existing bubble. Our previous work<sup>21</sup> has shown that Eq. (15) provides a better representation of the process of interfacial mass transfer driven bubble growth from a pre-existing bubble when compared to Eq. (14).

The growth coefficient for two-dimensional bubbles should be calculated as<sup>21</sup>

$$\beta_{2D} = \frac{\mathfrak{A} + \sqrt{\mathfrak{A}^2 + 4\mathfrak{A}}}{2\sqrt{2}}, \quad (16)$$

where  $\mathfrak{A}$  is calculated as

$$\mathfrak{A} = \frac{M_i \Delta C}{\rho_2}, \quad (17)$$

with  $\Delta C$  being the concentration of the dissolved gas in the bulk above the saturation condition. As the simulations in this paper deal with the growth of a two-dimensional bubble from a pre-existing bubble, the theoretical model used to verify the simulations is the extended Scriven model [Eq. (15)] with the growth coefficient determined based on Eq. (16). As  $\Delta C$  in the simulations is set to 50.16 mol/m<sup>3</sup>, 100.32 mol/m<sup>3</sup>, and 200.64 mol/m<sup>3</sup>, the corresponding values of  $\beta_{2D}$  are 1.3230, 2.2632, and 4.0509, respectively.

### C. Verification of the simulations

As the simulations predict bubble growth due to uniform supersaturation, the velocity and concentration of the dissolved gas around the bubble are radially symmetric (as reported in our previous work<sup>21</sup>). Figure 2 compares the increase in bubble radius predicted by simulations using a driving force for interfacial mass transfer based on Fick's first law and on  $Sh$  correlations with the prediction by the analytical solution of the extended Scriven model for various supersaturation levels. The simulations using a driving force based on  $Sh$  correlation 1 underpredict the bubble size compared with the analytical model for all three supersaturation levels. Interestingly, the simulation using a driving force based on Fick's first law appears to agree with the analytical model at larger supersaturation, whereas the simulations using a driving force based on  $Sh$  correlation 2 exhibits good agreement with the extended Scriven model for all three supersaturation levels.

As the interfacial mass transfer is proportional to the surface area of the bubble (which in the case of a two-dimensional bubble is proportional to the bubble radius), a normalized growth rate based on the bubble radius, which is computed as  $\int \psi_0 dV/R$ , is used to account for the different bubble sizes.<sup>21</sup> In the extended

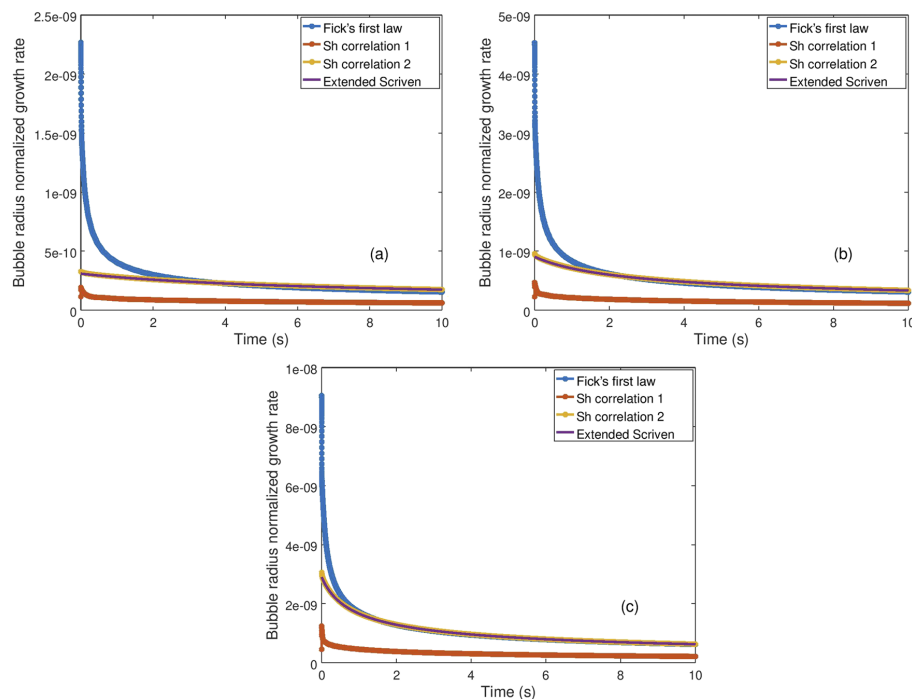


**FIG. 3.** Comparison of the results of simulations of bubble radius normalized growth rates ( $\text{kg m}^{-1} \text{s}^{-1}$ ) based on Fick's first law [Eq. (3)] or on  $Sh$  correlations [Eqs. (4) and (6)] with the results of the extended Scriven model (with  $\beta_{2D}$ ) for various levels of supersaturation: (a) 2.5, (b) 4.0, and (c) 7.0.

Scriven model, the radius normalized growth rate is computed as the rate of change in the mass of the bubble divided by the bubble radius based on the analytical model, i.e., Eq. (15). The discrepancies between the temporal change in bubble radius computed using a driving force based on Fick's first law or on  $Sh$  correlations and that computed using the analytical extended Scriven model can be explained based on the bubble radius normalized growth rate (see Fig. 3). The driving force based on  $Sh$  correlation 1 used for the simulations appears to underpredict the radius normalized growth rate (see Fig. 3) compared with the analytical model, which results in the bubble being smaller (see Fig. 2). On the other hand, the evolution of the bubble radius predicted using a driving force based on  $Sh$  correlation 2 agrees reasonably well with the analytical model, since the normalized growth rates from the two methods match, with an absolute deviation of less than 1% for all three cases at  $t = 10$  s (see Figs. 2 and 3). As the initialized distribution of the dissolved gas does not take account of the concentration boundary layer, the local value of  $C_i$ , which is used to calculate  $j$  based on Eq. (4), is close to the bulk supersaturation, which causes the initial spike in the normalized growth rate observed in Fig. 3. As the simulation proceeds over time, a concentration boundary layer develops, and the local  $C_i$  becomes lower than the bulk supersaturation. Although for  $Sh$  correlations,  $j$  is calculated to be proportional to  $C_i$ , Fick's first law computes  $j$  based on the gradient of the local concentration [see Eq. (3)]. As a result of this gradient-based calculation, the use of  $j$  from Fick's first law leads to a large normalized growth rate that is greater than the analytical solution, as observed in Fig. 3. As the concentration boundary layer becomes fully developed, the simulated radius normalized growth rate matches the analytical solution for all three supersaturation levels. This initial larger growth rate in the simulations causes the bubble radius to increase more rapidly than expected, which results in the discrepancy observed in Fig. 2.

#### IV. CONCLUSIONS

In this paper, the VOF-based approach proposed previously<sup>21</sup> has been used to simulate the interfacial mass transfer driven growth of a bubble in a unbounded and uniformly supersaturated solution (for  $S = 2.5, 4, \text{ and } 7$ ). As an analytical solution is available for this flow scenario, the results of simulations with the driving forces computed based on Fick's first law and on two  $Sh$  correlations have been compared with the theoretical results to assess the predictions of bubble growth. The results reveal the following:

- If a  $Sh$  correlation that is appropriate for the specific flow being simulated is chosen to compute the driving force for interfacial mass transfer, a reasonably accurate prediction of bubble growth can be obtained. In the case of radially symmetric bubble growth driven by supersaturation,  $Sh$  correlation 2 [Eq. (6)] is better suited than  $Sh$  correlation 1 [Eq. (4)].
- If  $Sh$  correlations are not available to describe a flow scenario or if a single correlation cannot capture a complex phenomenon (such as bubble growth, coalescence, and detachment), the driving force should be computed based on Fick's first law, since it provides a better representation of the flow than a single  $Sh$  correlation with limited applicability.

- The driving force computed using Fick's first law has been shown to be able to handle bubble growth for a range of supersaturation levels, provided that the concentration boundary layer has been resolved, even at  $t = 0$  s.
- The driving forces based on  $Sh$  correlations and Fick's first law are proportional to the local concentration and the gradient of  $C_i$ . This means that the computational requirements (with respect to mesh resolution) needed with  $Sh$  correlations are lower than when Fick's first law is used, since the latter requires the resolution of concentration gradients near the interface.

Future work within this framework will utilize a driving force computed based on the local concentration to model the bubble growth driven by heterogeneous reactions such as electrochemical gas evolution.

#### ACKNOWLEDGMENTS

This work was funded by the Department of Materials Science and Engineering at NTNU, and the required computational resources were provided by UNINETT Sigma2 through Grant NN9741K.

#### APPENDIX A: DERIVATION OF $Sh$ CORRELATION 2

In this appendix, based on the original work by Burman and Jameson,<sup>8</sup> we extend their approach to derive  $Sh$  correlation that is used in simulations.

For a two-dimensional bubble as simulated in this paper, the growth rate can be expressed as

$$\rho_2 \frac{dV}{dt} = jA, \quad (\text{A1})$$

where  $V = \pi R^2 h$ ,  $A = 2\pi R h$ , and  $j = M_i k C_i$ , with  $h$  being the unit cell thickness used to define the two-dimensional domains in OpenFOAM®, which in this paper is set to  $1 \mu\text{m}$ . Substituting the expressions for  $V$ ,  $A$ , and  $j$ , we get

$$\rho_2 \frac{dR}{dt} = M_i k C_i. \quad (\text{A2})$$

The rate of change in the radius can be calculated based on Eq. (15) as

$$\frac{dR}{dt} = \frac{2\beta^2 D_{i,1}}{R}. \quad (\text{A3})$$

Substituting Eq. (A3) into Eq. (A2), we get

$$\frac{2\beta^2 D_{i,1}}{R} = \frac{M_i k C_i}{\rho_2}. \quad (\text{A4})$$

This equation can be rearranged and multiplied by 2 on both sides to give

$$k = \frac{D_{i,1}}{2R} \frac{4\beta^2 \rho_2}{M_i C_i}, \quad (\text{A5})$$

and the corresponding  $Sh$  is defined as  $4\beta^2 \rho_2 / (M_i C_i)$ . In the work by Burman and Jameson,<sup>8</sup> the value of  $C_i$  is written in terms of the

bulk concentration of the dissolved gas under the assumption of diffusion-limited mass transfer through the liquid film. This leads to  $Sh$  being defined as  $4\beta^2\rho_2/(M_i\Delta C)$ , where  $\Delta C$  is defined as in Eq. (17). At a very low supersaturation, when  $Re$  is approximately zero and  $\beta$  is small, Burman and Jameson<sup>8</sup> showed that  $Sh \approx 2$ , as expected for the case of diffusive mass transfer in the absence of convection (see Table I).

#### APPENDIX B: CHOICE OF LINEAR SOLVER AND PRECONDITIONER

To reduce the computational time required for the simulations, the effect of the iterative solver used to smear  $\psi_0$  [Eq. (8)], which is the bottleneck in the simulation at each time step, is investigated in this appendix. Bubble growth driven by supersaturation  $S = 7$  is chosen as the flow scenario to be simulated, with the convergence criterion for Eq. (8) set at  $10^{-10}$ . The first case corresponds to the setting used in this paper, i.e., Eq. (8) is solved using PCG (linear solver)–DIC (preconditioner). The second case corresponds to the setting used in our previous work,<sup>21</sup> i.e., Eq. (8) is solved using PBiCGStab (linear solver)–diagonal (preconditioner).

Although the bubble growths predicted by the two simulations are in very close agreement (see Fig. 4), the number of iterations required for the convergence of Eq. (8) is reduced by almost half at every time step, as observed in the log file obtained from the solver during the run:

- For the PCG–DIC solver setting:
  - At  $t = 0$  s: DICPCG: Solving for psi, Initial residual = 1, Final residual =  $9.88185e - 11$ , No Iterations 1842
  - At  $t = 10$  s: DICPCG: Solving for psi, Initial residual = 0.0132484, Final residual =  $9.94304e - 11$ , No Iterations 1218
- For the PBiCGStab–diagonal solver setting:

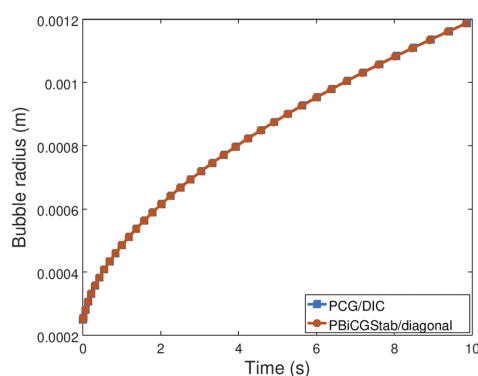


FIG. 4. Bubble size simulated using the various solvers for Eq. (8). The bubble evolution for the PBiCGStab/diagonal setting is obtained from the data reported in our previous work.<sup>21</sup>

- At  $t = 0$  s: diagonalPBiCGStab: Solving for psi, Initial residual = 1, Final residual =  $4.55196e - 11$ , No Iterations 4020
- At  $t = 10$  s: diagonalPBiCGStab: Solving for psi, Initial residual = 0.0131794, Final residual =  $9.72418e - 11$ , No Iterations 2904

#### DATA AVAILABILITY

The data that support the findings of this study are available within the article.

#### REFERENCES

- <sup>1</sup>S. Jones, G. Evans, and K. Galvin, “Bubble nucleation from gas cavities—A review,” *Adv. Colloid Interface Sci.* **80**, 27–50 (1999).
- <sup>2</sup>G. Sakuma, Y. Fukunaka, and H. Matsushima, “Nucleation and growth of electrolytic gas bubbles under microgravity,” *Int. J. Hydrogen Energy* **39**, 7638–7645 (2014).
- <sup>3</sup>J. Villadsen, J. Nielsen, and G. Lidén, *Bioreaction Engineering Principles* (Springer, 2011).
- <sup>4</sup>R. Bird, W. Stewart, and E. Lightfoot, *Transport Phenomena* (Wiley, 2006).
- <sup>5</sup>W. E. Ranz and W. R. Marshall, “Evaporation from drops,” *Chem. Eng. Prog.* **48**, 141–146 (1952), available at <http://dns2.asia.edu.tw/~ysho/YSHO-English/1000%20CE/PDF/Che%20Eng%20Pro48,%20141.pdf>.
- <sup>6</sup>C. Crowe, J. Schwarzkopf, M. Sommerfeld, and Y. Tsuji, *Multiphase Flows with Droplets and Particles* (CRC Press, 2011).
- <sup>7</sup>L. E. Scriven, “On the dynamics of phase growth,” *Chem. Eng. Sci.* **10**, 1–13 (1959).
- <sup>8</sup>J. Burman and G. Jameson, “Diffusional mass transfer to a growing bubble,” *Chem. Eng. Sci.* **31**, 401–403 (1976).
- <sup>9</sup>G. Brenn, “Mass transfer,” in *Analytical Solutions for Transport Processes: Fluid Mechanics, Heat and Mass Transfer* (Springer, 2017), pp. 239–270.
- <sup>10</sup>G. Liger-Belair, M. Vignes-Adler, C. Voisin, B. Robillard, and P. Jeandet, “Kinetics of gas discharging in a glass of champagne: The role of nucleation sites,” *Langmuir* **18**, 1294–1301 (2002).
- <sup>11</sup>P. S. Epstein and M. S. Plesset, “On the stability of gas bubbles in liquid–gas solutions,” *J. Chem. Phys.* **18**, 1505–1509 (1950).
- <sup>12</sup>D. Bothe and S. Fleckenstein, “A volume-of-fluid-based method for mass transfer processes at fluid particles,” *Chem. Eng. Sci.* **101**, 283–302 (2013).
- <sup>13</sup>P. S. Weber, H. Marschall, and D. Bothe, “Highly accurate two-phase species transfer based on ALE interface tracking,” *Int. J. Heat Mass Transfer* **104**, 759–773 (2017).
- <sup>14</sup>M. Falcone and H. Marschall, “Explicit radial-basis-function-based finite-difference method for interfacial mass-transfer problems,” *Chem. Eng. Technol.* **40**, 1385–1390 (2017).
- <sup>15</sup>D. Deising, H. Marschall, and D. Bothe, “A unified single-field model framework for volume-of-fluid simulations of interfacial species transfer applied to bubbly flows,” *Chem. Eng. Sci.* **139**, 173–195 (2016).
- <sup>16</sup>D. Deising, D. Bothe, and H. Marschall, “Direct numerical simulation of mass transfer in bubbly flows,” *Comput. Fluids* **172**, 524–537 (2018).
- <sup>17</sup>J. Maes and C. Soullaine, “A new compressive scheme to simulate species transfer across fluid interfaces using the volume-of-fluid method,” *Chem. Eng. Sci.* **190**, 405–418 (2018).
- <sup>18</sup>S. S. Deshpande, L. Anumolu, and M. F. Trujillo, “Evaluating the performance of the two-phase flow solver interFoam,” *Comput. Sci. Discovery* **5**, 014016 (2012).
- <sup>19</sup>H. Liu, L.-M. Pan, and J. Wen, “Numerical simulation of hydrogen bubble growth at an electrode surface,” *Can. J. Chem. Eng.* **94**, 192–199 (2016).
- <sup>20</sup>S. Fleckenstein and D. Bothe, “A volume-of-fluid-based numerical method for multi-component mass transfer with local volume changes,” *J. Comput. Phys.* **301**, 35–58 (2015).

- <sup>21</sup>K. J. Vachaparambil and K. E. Einarsrud, "Numerical simulation of bubble growth in a supersaturated solution," *Appl. Math. Modell.* **81**, 690–710 (2020).
- <sup>22</sup>J. Maes and C. Soulaire, "A unified single-field volume-of-fluid-based formulation for multi-component interfacial transfer with local volume changes," *J. Comput. Phys.* **402**, 109024 (2020).
- <sup>23</sup>J. Klostermann, K. Schaake, and R. Schwarze, "Numerical simulation of a single rising bubble by VOF with surface compression," *Int. J. Numer. Methods Fluids* **71**, 960–982 (2013).
- <sup>24</sup>K. J. Vachaparambil and K. E. Einarsrud, "Comparison of surface tension models for the volume of fluid method," *Processes* **7**, 542 (2019).
- <sup>25</sup>K. J. Vachaparambil and K. E. Einarsrud, "On sharp surface force model: Effect of sharpening coefficient," *Exp. Comput. Multiphase Flow* (published online 2020).
- <sup>26</sup>S. Hardt and F. Wondra, "Evaporation model for interfacial flows based on a continuum-field representation of the source terms," *J. Comput. Phys.* **227**, 5871–5895 (2008).
- <sup>27</sup>C. Kunkelmann, "Numerical modeling and investigation of boiling phenomena," Ph.D. thesis, Technische Universität, Darmstadt, 2011.
- <sup>28</sup>C. Greenshields, See <https://openfoam.org/release/2-3-0/multiphase/> for Predictor-corrector semi-implicit MULES, 2014; accessed on 17 June 2020.
- <sup>29</sup>J. Kestin, M. Sokolov, and W. A. Wakeham, "Viscosity of liquid water in the range  $-8^{\circ}\text{C}$  to  $150^{\circ}\text{C}$ ," *J. Phys. Chem. Ref. Data* **7**, 941–948 (1978).
- <sup>30</sup>H. Iwasaki and M. Takahashi, "Viscosity of carbon dioxide and ethane," *J. Chem. Phys.* **74**, 1930–1943 (1981).
- <sup>31</sup>A. Tamimi, E. B. Rinker, and O. C. Sandall, "Diffusion coefficients for hydrogen sulfide, carbon dioxide, and nitrous oxide in water over the temperature range 293–368 K," *J. Chem. Eng. Data* **39**, 330–332 (1994).
- <sup>32</sup>E. B. Winn, "The temperature dependence of the self-diffusion coefficients of argon, neon, nitrogen, oxygen, carbon dioxide, and methane," *Phys. Rev.* **80**, 1024–1027 (1950).
- <sup>33</sup>S. J. Hashemi and J. Abedi, "Advances in modeling of new phase growth," *Energy Fuels* **21**, 2147–2155 (2007).



## *Appended paper E*

### **On modelling electrochemical gas evolution using the Volume of Fluid method**

Kurian J. Vachaparambil and Kristian Etienne Einarsrud

Under-peer review in *14th International Conference on Computational Fluid Dynamics In the Oil & Gas, Metallurgical and Process Industries (CFD2020)*, Trondheim





## ON MODELLING ELECTROCHEMICAL GAS EVOLUTION USING THE VOLUME OF FLUID METHOD

Kurian J. VACHAPARAMBIL<sup>1\*</sup>, Kristian Etienne EINARSRUD<sup>1†</sup>

<sup>1</sup>Department of Materials Science and Engineering, Norwegian University of Science and Technology (NTNU), Trondheim 7491, Norway

\* E-mail: kurian.j.vachaparambil@ntnu.no

† E-mail: kristian.e.einarsrud@ntnu.no

### ABSTRACT

In this work we describe the various building block relevant in simulating electrochemical gas evolution using Volume of Fluid (VOF) method. These building blocks are implemented in the VOF solver available in OpenFOAM® and its predictions are compared to the theoretical models reported in literature. The fully coupled solver to model electrochemical gas evolution is used to model the case of a bubble evolving on a vertical electrode under constant potential condition to showcase its ability.

**Keywords:** VOF, Surface tension modelling, Interfacial mass transfer, Bubble growth, Gauss's law, Dissolved gas transport, Electrochemical systems .

### NOMENCLATURE

#### Greek Symbols

- $\rho$  Density, [ $kg/m^3$ ]
- $\mu$  Dynamic viscosity, [ $kg/ms$ ]
- $\nu$  Kinematic viscosity, [ $m^2/s$ ]
- $\sigma$  Surface tension, [ $N/m$ ]
- $\kappa$  Interfacial curvature, [ $1/m$ ]
- $\alpha$  Volume fraction, [-]
- $\phi$  Potential, [V]
- $\beta$  Growth coefficient, [-]
- $\mathcal{F}$  Fraction of electrode area covered by bubble, [-]

#### Latin Symbols

- $D$  Diffusion coefficient, [ $m^2/s$ ].
- $\vec{g}$  Acceleration due to gravity, [ $m/s^2$ ].
- $k$  Conductivity, [ $S/m$ ].
- $p$  Pressure, [Pa].
- $C$  Molar concentration, [ $mol/m^3$ ].
- $\vec{x}$  Position vector, [ $m$ ].
- $\vec{U}$  Velocity vector, [ $m/s$ ].
- $\vec{i}$  Current density vector, [ $A/m^2$ ].
- $\vec{S}$  Individual cell face surface area vector, [ $m^2$ ].
- $He$  Jump condition across the interface, [-].
- $f$  Void fraction, [-].
- $R$  Bubble radius, [ $m$ ].
- $I$  Current when no bubbles are present, [A].
- $d$  Interelectrode distance, [ $m$ ].
- $A$  Total electrode area, [ $m^2$ ].
- $M$  Molar mass, [ $kg/mol$ ].
- $F$  Faraday's constant ( $=96485$ ), [ $As/mol$ ].

#### Sub/superscripts

- 1 Liquid or phase 1.
- 2 Bubble or phase 2.
- $i$  Dissolved gas species.
- 0 Operating condition.
- $s$  Saturation condition.
- $e$  Averaged or effective value.
- $'$  Initial/starting condition.
- $m$  Modified.
- $\infty$  At bulk.
- $\wedge$  Harmonic average.

### INTRODUCTION

Electrochemical gas evolution is relevant in a variety of industrial processes such as water-splitting, chloralkaline and Hall-Héroult. Bubble evolution in these systems involve nucleation, growth, coalescence and detachment from electrode. The dynamic behaviour of bubbles causes overpotential changes due to supersaturation, ohmic resistance and electrode screening, as well as enhanced mass transfer (Zhao *et al.*, 2019). Due to the complex and coupled nature of electrochemical gas evolution (Taqieddin *et al.*, 2018), numerical modelling of the system is an ideal way to understand its physics and develop strategies to efficiently remove these bubbles.

In literature, the numerical models used to simulate the continuum scale processes in electrochemical gas evolution can be broadly divided into dispersed and interface-resolving approaches. The dispersed approaches, like Euler-Euler, Mixture and Euler-Lagrange models, relies on a priori knowledge of flow to select interphase closure terms (Hreiz *et al.*, 2015). These approaches do not resolve the dispersed bubbles and are typically used to simulate industrial scale electrochemical systems (Hreiz *et al.*, 2015). On the other hand, interface-resolving approaches, like Volume of Fluid (VOF) (Einarsrud and Johansen, 2012; Einarsrud *et al.*, 2017; Sun *et al.*, 2018) and phase-field (Zhang *et al.*, 2020), resolve individual bubbles and is typically used to study in detail the dynamic behaviour of few bubbles. Although these studies have provided knowledge relevant to simulate the multiphysics nature of electrochemical gas evolution, there is still a lack research that addresses the coupled multiphysics as well as the multiscale nature of the process as highlighted by Taqieddin *et al.* (2018)

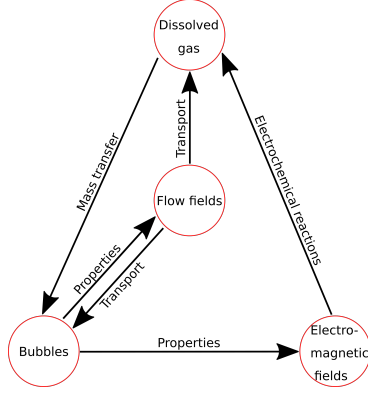


**Figure 1:** Schematic of the coupling between various modules of the proposed solver proposed to model electrochemical gas evolution.

In this work, we highlight various modules required to simulate electrochemical gas evolution, see Fig.1, to partly address the knowledge gap highlighted by Taqieddin *et al.* (2018). The decoupled modules are developed on the VOF solver available on OpenFOAM<sup>®</sup> 6, interFoam (Deshpande *et al.*, 2012). These modules are individually verified by comparison to relevant theoretical models available in literature and finally the potential of the fully coupled solver is discussed.

## THE DECOUPLED MODEL DESCRIPTION

In this section, we introduce the various modules that are relevant in modelling electrochemical gas evolution: reliable small (sub-millimeter) bubbles, transport of dissolved gas, supersaturation driven bubble growth and ohmic resistance associated with bubble evolution. Before these individual modules are described, the VOF model as implemented in interFoam is introduced, for further details please refer Deshpande *et al.* (2012). The VOF model uses a scalar function known as volume fraction of liquid ( $\alpha_1$ ) which takes a value equal to unity in the liquid, zero in the gas phase and  $0 < \alpha_1 < 1$  in the interface. The volume fraction of gas is calculated as  $\alpha_2 = 1 - \alpha_1$ . The advection of the volume fraction of liquid is computed as

$$\frac{\partial \alpha_1}{\partial t} + \nabla \cdot (\alpha_1 \vec{U}) + \nabla \cdot (\alpha_1 (1 - \alpha_1) \vec{U}_r) = 0, \quad (1)$$

where  $\vec{U}$  is the velocity in domain and  $\vec{U}_r$  is the compressive velocity computed based on a user-defined compression factor ( $C_\alpha$ ), see Deshpande *et al.* (2012). The fluid properties, like density ( $\rho$ ) and viscosity ( $\mu$ ), are computed as  $\chi = \alpha_1 \chi_1 + \alpha_2 \chi_2$ . The mass conservation equation of the phases, described using continuity equation, is

$$\nabla \cdot \vec{U} = 0. \quad (2)$$

The momentum equation is written using a modified pressure,  $p_m = p - \rho \vec{g} \cdot \vec{x}$ , as

$$\frac{\partial \rho \vec{U}}{\partial t} + \nabla \cdot (\rho \vec{U} \vec{U}) = \nabla \cdot (\mu \nabla \vec{U}) + \nabla \vec{U} \cdot \nabla \mu + \vec{F}_{ST} - \nabla p_m - \vec{g} \cdot \vec{x} \nabla \rho, \quad (3)$$

where  $\vec{F}_{ST}$  is the surface tension force is treated using the Continuum Surface Force (CSF) model (Brackbill *et al.*, 1992) and viscous term, usually written as  $\nabla \cdot \mu (\nabla \vec{U} + \nabla \vec{U}^T)$  can be expressed as  $\nabla \cdot (\mu \nabla \vec{U}) + \nabla \vec{U} \cdot \nabla \mu$  using Eq.2, see Deshpande *et al.* (2012).

## Modelling sub-millimeter bubbles

One of the main well known problems associated with VOF approach is the errors in determining the local curvature used in surface tension modelling. These errors generate spurious velocities near the interface that can cause non-physical flow in the computational domain (Popinet, 2018; Vachaparambil and Einarsrud, 2019). The spurious velocities tend to become stronger with smaller length scales or lower Capillary number and it can sometimes be strong enough to generate nonphysical random walk of the bubbles. One of the approaches to reduce spurious velocities is to replace the commonly used CSF model with the Sharp Surface Force (SSF) model, proposed by Raeyni *et al.* (2012), other advances has been reviewed in Popinet (2018). The work by Vachaparambil and Einarsrud (2019), has shown the ability of SSF to successfully simulate capillary rise and rising bubbles as well as reduce spurious velocities compared to CSF model.

The SSF model, based on the work of Raeyni *et al.* (2012); Vachaparambil and Einarsrud (2019), describes  $\vec{F}_{ST}$  as

$$\vec{F}_{ST} = \sigma \kappa_{final} \nabla \alpha_{sh}, \quad (4)$$

where  $\kappa_{final}$  is obtained using a three step smoothing of curvature and  $\alpha_{sh}$  is calculated as

$$\alpha_{sh} = \frac{1}{1 - C_{sh}} \left[ \min \left( \max \left( \alpha_1, \frac{C_{sh}}{2} \right), 1 - \frac{C_{sh}}{2} \right) - \frac{C_{sh}}{2} \right], \quad (5)$$

where  $C_{sh}$  is the user-defined sharpening coefficient which must satisfy  $0 \leq C_{sh} < 1$ . To model sub-millimeter bubble, the sharpening coefficient is set to 0.3 (Vachaparambil and Einarsrud, 2020b).

## Transport of dissolved gas

Compared to single phase flows, the transport of species in a two phase flow requires the treatment of the interfacial conditions i.e. concentration jump across the interface and continuity of diffusive fluxes, see Maes and Soulaïne (2018) or Deising *et al.* (2018). These interfacial conditions are incorporated into a single unified transport equation which solves for the concentration field in both liquid and the gas in the Compressive Continuous Species Transfer (CCST) model, developed by Maes and Soulaïne (2018). The governing equation for  $C_i$ , in CCST model, is

$$\frac{\partial C_i}{\partial t} + \nabla \cdot (\vec{U} C_i) = \nabla \cdot (\hat{D}_i \nabla C_i - \hat{D}_i B C_i \nabla \alpha_1) - \nabla \cdot (B \alpha_1 \alpha_2 \vec{U}_r C_i), \quad (6)$$

where  $\vec{U}_r$  is the compressive velocity (used in Eq.1),  $B$  is the defined as  $(1 - He)/(\alpha_1 + \alpha_2 He)$ , where  $He$  describes the concentration jump across the interface (also known as partition coefficient), and  $\hat{D}_i$  is the harmonic averaging of the diffusion coefficients, see Maes and Soulaïne (2018) for further details. Inorder to simulate the transport of dissolved

gas, which should only be in the liquid, we use  $He$  equal to a value near zero (like  $10^{-4}$ ), to minimize the transport of dissolved gas into the bubble which is accounted for by the CCST model based on the defined value of  $He$  (Maes and Soulaire, 2018; Vachaparambil and Einarsrud, 2020b). As  $He$  is a small number ( $10^{-4}$ ),  $C_i$  obtained from Eq.6 can be interpreted as  $\bar{C}_i = \bar{C}_i - \bar{C}_s$ , where  $\bar{C}_i$  is the actual concentration and  $\bar{C}_s$  represents the saturation concentration, based on Vachaparambil and Einarsrud (2020a,b).

### Supersaturation driven bubble growth

When modelling interfacial mass transfer phenomena and the associated bubble growth, Sherwood number based correlations are widely used in CFD simulations (Einarsrud and Johansen, 2012; Einarsrud *et al.*, 2017). The drawback of these correlations is its limited applicability, due to its dependence on the bubble shape and relevant Reynolds and Schmidt number (Deising *et al.*, 2018). A more universal approach is to use the Fick's 1<sup>st</sup> law, which is the governing equation used in deriving Sherwood number correlations (Bird *et al.*, 2007). To the best of the authors knowledge there are only two very recent works that has used Fick's 1<sup>st</sup> law to model bubble evolution: Vachaparambil and Einarsrud (2020a,b) and Maes and Soulaire (2020).

In order to model the growth of bubble driven by the supersaturated electrolyte, we use the approach proposed by Vachaparambil and Einarsrud (2020a,b). In this work, the phenomenological Fick's 1<sup>st</sup> law, the driving force for bubble growth, is coupled to CCST, described based on Eq.6, with relevant source terms for species transport (Eq.6), advection of  $\alpha_1$  (Eq.1) and continuity (Eq.2) equations is implemented by extending the work of Hardt and Wondra (2008). For information about the relevant governing equations and source terms, please refer to Vachaparambil and Einarsrud (2020b).

### Modelling electromagnetic effects

To model the electromagnetic effects, we use Gauss's law which can be described mathematically as

$$\nabla \cdot \vec{i} = 0, \quad (7)$$

where the current density ( $\vec{i}$ ) can be expressed using the gradient of potential ( $\phi$ ) as

$$\vec{i} = -k\nabla\phi, \quad (8)$$

where  $k$  is the conductivity, calculated as an algebraic averaging of conductivities, i.e.  $\alpha_1 k_1 + \alpha_2 k_2$ . This approach has been used in literature to describe the evolution of carbon dioxide bubbles in aluminum reduction process (Einarsrud and Johansen, 2012).

### SOLVER SETTINGS

Due to the coupled nature of momentum and pressure equations, the equations are computed using the PISO algorithm, see Deshpande *et al.* (2012). The governing equations are discretized with first order schemes for time and second order schemes in space, for details please refer to Vachaparambil and Einarsrud (2020b). The convergence criterion used solve governing equations for  $p_{rgh}$  and other variables (like  $\phi$ ,  $\vec{U}$ ,  $C_i$  and others) are  $10^{-20}$  and  $10^{-10}$  respectively. When surface tension is relevant in the simulations,

a constraint on time step constraint described in Deshpande *et al.* (2012); Vachaparambil and Einarsrud (2019) is used to prevent the growth of spurious velocities.

### VERIFICATION OF THE DECOUPLED SOLVER

In this section, we verify the individual modules implemented in interFoam using theoretical models described in literature.

#### On sub-millimeter bubbles

The ability of the SSF model to reliably simulate sub-millimeter bubbles is demonstrated by a simulation of a stationary bubble. Without body forces, i.e. gravity, in the domain, any velocities present in the simulation can be attributed to spurious velocities. As electrochemically generated bubbles can be present on both the electrode surface and in the bulk (after detachment), it is necessary to reliably simulate sub-millimeter bubbles for both cases.

The properties of the liquid and gas used in the simulation are  $\rho_1 = 1000\text{kg/m}^3$ ,  $\rho_2 = 1\text{kg/m}^3$ ,  $\nu_1 = 10^{-6}\text{m}^2/\text{s}$ ,  $\nu_2 = 1.48 \times 10^{-5}\text{m}^2/\text{s}$  and  $\sigma = 0.07\text{N/m}$ . Two test cases, where the bubble is available in the bulk (SBC1) and attached to the electrode surface (SBC2), where the stationary bubble has a diameter ( $2R$ ) of 0.5mm are simulated in a 2D domain of dimensions  $4R \times 4R$ . Both SBC1 and SBC2 are meshed using a hexahedral grid with  $120 \times 120$  cells. For SBC1, all the boundaries are assigned zeroGradient for both  $\vec{U}$  and  $\alpha_1$  but the  $p_{rgh}$  is assigned fixedValue of 101325Pa. In the case of SBC2, where the left and right boundaries are defined as walls,  $\vec{U}$  uses no-slip condition at the walls and zeroGradient at the other boundaries along with  $\alpha_1$  uses zeroGradient on all boundaries (with a default contact angle of  $90^\circ$  at the walls) and  $p_{rgh}$  as fixedValue (equal to 0Pa) at the top wall and fixedFluxPressure (Greenshields, 2019) on the other boundaries. Due to the surface tension, the maximum time step allowed is manually limited to  $0.6\mu\text{s}$  (see Deshpande *et al.* (2012); Vachaparambil and Einarsrud (2019)) and the simulations are run until 0.05s.

The accuracy of these simulations are estimated using Laplace pressure and magnitude spurious velocities, like in Vachaparambil and Einarsrud (2019). The Laplace pressure in a 2D bubble can be calculated based on Young-Laplace equation as  $\Delta p_c = \sigma/R$  and the spurious velocities ( $\vec{U}_{sc}$ ) is estimated as  $\max(|\vec{U}|)$ . The Laplace pressure in the bubble, from the simulations, is calculated as

$$\Delta p = \frac{\int_V \alpha_2 p dV}{\int_V \alpha_2 dV} - p_0, \quad (9)$$

where  $p_0$  is the operating pressure used in the simulations. The associated error in Laplace pressure ( $E$ ) is calculated as  $(\overline{\Delta p} - \Delta p_c)/\Delta p_c$ , where the overbar indicates the averaged value over the simulation time.

**Table 1:** Time averaged values of spurious velocities, Laplace pressure and its error obtained while simulating a stationary sub-millimeter bubble.

Case	$\overline{U}_{sc}$ (m/s)	$\overline{\Delta p}$ (Pa)	E
SBC1	0.0108	255.35	-0.088
SBC2	0.0198	253.91	-0.093

As shown in Fig.2, the spurious velocities generated are present on both sides of the interface (for both TC1 and

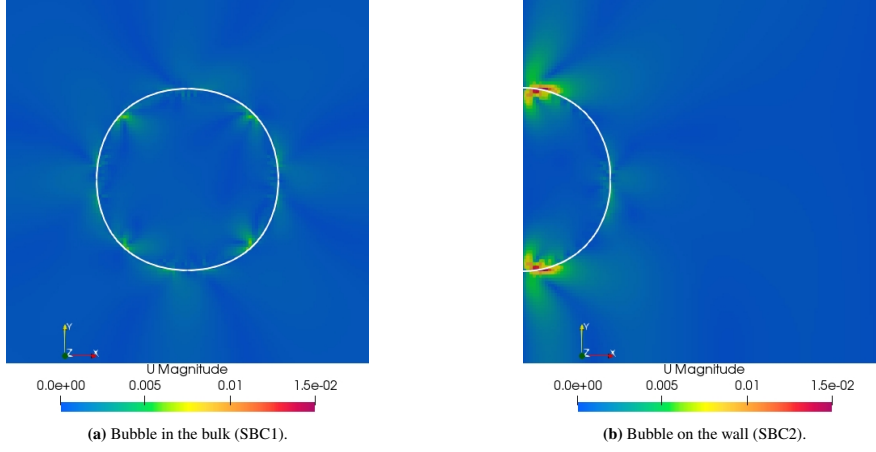


**Figure 2:** Comparison of the spurious velocities (m/s) generated while modelling stationary bubbles at  $t = 0.05s$  with interface (at  $\alpha_1 = 0.5$ ) represented by the white contour.

TC2). Interestingly, the spurious velocities generated are quite different in both TC1 and TC2, with the latter generating strong spurious velocities near the foot of the bubble. These time averaged spurious velocities and error in estimating the Laplace pressure of the bubble quantified in Table.1.

### On the transport of dissolved gas

In order to show that Eq.6 with  $He = 10^{-4}$  can model the transport of dissolved gas reasonably well, we take a hypothetical case where a rising bubble moves through a region of supersaturation. The fluid properties used in the simulations, which are adapted from Hysing *et al.* (2009), are  $\rho_1 = 1000\text{kg/m}^3$ ,  $\rho_2 = 1\text{kg/m}^3$ ,  $\nu_1 = 0.01\text{m}^2/\text{s}$ ,  $\nu_2 = 0.1\text{m}^2/\text{s}$ ,  $\sigma = 1.96\text{N/m}$  and  $|\vec{g}| = 0.98\text{m/s}^2$  along with  $D_1 = 10^{-9}\text{m}^2/\text{s}$  and  $D_2 = 10^{-5}\text{m}^2/\text{s}$ . A bubble of diameter  $0.5\text{m}$  is initialized such that its center is  $0.5\text{m}$  from the bottom and side boundaries in a domain of dimensions  $1\text{m} \times 2\text{m}$ . The simulation is run with hexahedral mesh with  $160 \times 320$  cells. The region of supersaturation,  $C_i = 10\text{mol/m}^3$ , is initialized in an area of  $1\text{m} \times 0.7\text{m}$  from a distance of  $0.8\text{m}$  from the bottom wall. All four boundaries are assigned the zeroGradient condition for  $C_i$  and  $\alpha_1$ . The boundary conditions for  $\vec{U}$  are assigned slip conditions at the side walls and remaining walls are set as no-slip. For  $p_{rgh}$ , the top wall is assigned the fixedValue (equal to zero) but the other walls are described using fixedFluxPressure (Greenshields, 2019).

The spatial distribution of the dissolved gas as the bubble rises and deforms is illustrated in Fig.3. The convection induced by the rising bubble does not advect the dissolved gas into the bubble. Due to the use of a non-zero  $He$ , to prevent  $B$  in Eq.6 from becoming infinity, dissolved gas does numerically drift into the bubble but this is negligible (lower than  $0.01\%$  of the amount of dissolved gas).

### On supersaturation driven bubble growth

Adapted from Vachaparambil and Einarsrud (2020a,b), the fluid properties used in the simulation are  $\rho_1 = 997.08\text{kg/m}^3$ ,  $\rho_2 = 1.81\text{kg/m}^3$ ,  $\nu_1 = 8.92 \times 10^{-7}\text{m}^2/\text{s}$ ,  $\nu_2 = 8.228 \times 10^{-6}\text{m}^2/\text{s}$ ,  $D_1 = 1.94 \times 10^{-9}\text{m}^2/\text{s}$ ,  $D_2 = 9.18 \times 10^{-6}\text{m}^2/\text{s}$  and  $M = 44 \times 10^{-3}\text{kg/mol}$ . Both surface tension and gravity are neglected in the simulations. The parameters used in the solver are defined based on the work by Vachaparambil and Einarsrud (2020b). The domain used for the computation is  $3\text{cm} \times 3\text{cm}$  which is meshed with  $4000 \times 4000$  cells, the pre-existing bubble (of diameter equal to  $0.5\text{mm}$ ) is initialized at the center of the domain. The liquid phase is initialized with a concentration of dissolved gas at  $200.64\text{mol/m}^3$ . The boundary conditions used are described in Vachaparambil and Einarsrud (2020b).

The approach to describe the growth of a pre-existing bubble in a supersaturated solution can be verified by the Extended Scriven model proposed by Hashemi and Abedi (2007) (based on the work by Scriven (1959)):

$$R = 2\beta \sqrt{D_1 \left( t + \frac{R'^2}{4D_1\beta^2} \right)}, \quad (10)$$

where  $\beta$  is the growth coefficient and  $R'$  is the radius of the pre-existing bubble. The growth coefficient for 2D bubbles, derived in Vachaparambil and Einarsrud (2020b), is

$$\beta_{2D} = \frac{a + \sqrt{a^2 + 4a}}{2\sqrt{2}}, \quad (11)$$

where  $a$  is equal to  $M\Delta C/\rho_2$  and  $\Delta C$  is equal to the concentration of the dissolved gas that is over the saturation condition (equal to  $200.64\text{mol/m}^3$ ). Fig.4 shows that the evolution of bubble radius predicted by the model agrees reasonably with the Extended Scriven with  $\beta_{2D}$ . The discrepancy between the simulation and the Extended Scriven model can be explained by the discontinuous nature of dissolved gas concentration at  $t = 0s$  (Vachaparambil and Einarsrud, 2020a,b).

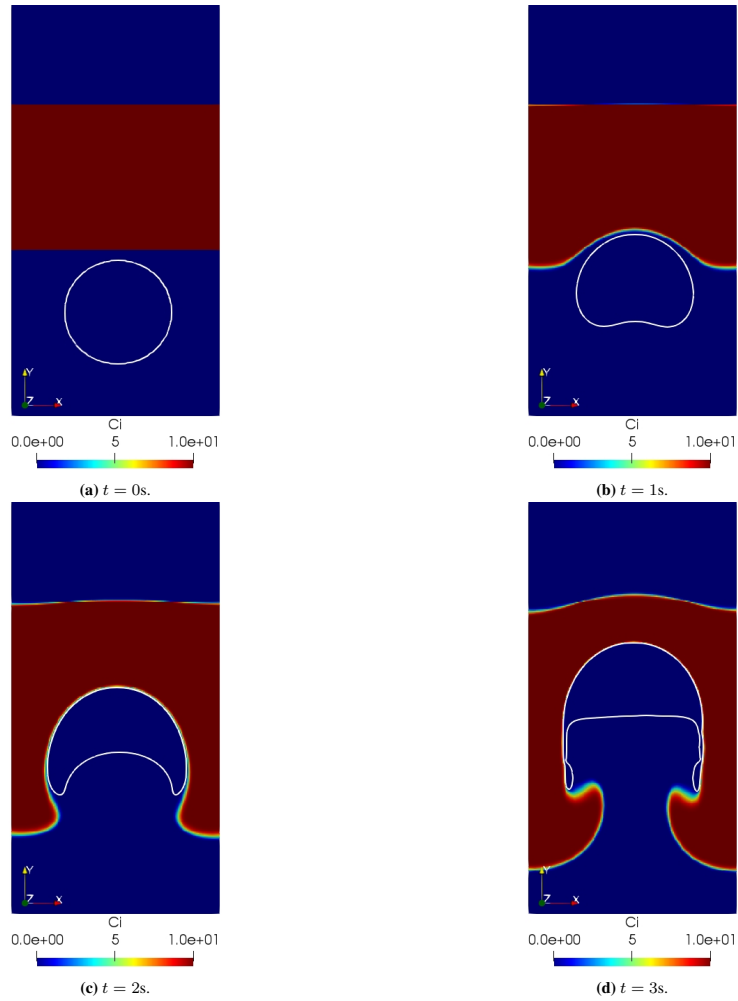


**Figure 3:** The concentration of dissolved gas ( $\text{mol/m}^3$ ) around a rising bubble (interface, at  $\alpha_1 = 0.5$ , is represented by white contour) modelled based on Eq.6.

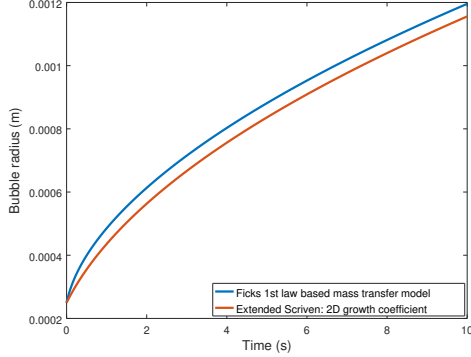


**Figure 4:** Comparison of the bubble growth predicted by Fick's 1<sup>st</sup> law based model (based on the work by Vachaparambil and Einarsrud (2020b)) and the Extended Scriven model (Eq.10) using  $\beta_{2D} = 4.0509$ .

### On electromagnetism and its effects

In the case of constant potential difference across the electrodes, the current varies due to the bubble evolution. The effect of bubbles can be divided based on its position, i.e. in the bulk and attached to the electrode, which is investigated in this subsection.

The fluid parameters used for these simulations are  $\rho_1 = 1000\text{kg/m}^3$ ,  $\rho_2 = 1\text{kg/m}^3$ ,  $\nu_1 = 10^{-6}\text{m}^2/\text{s}$ ,  $\nu_2 = 1.48 \times 10^{-5}\text{m}^2/\text{s}$ ,  $k_1 = 100\text{S/m}$  and  $k_2 = 10^{-13}\text{S/m}$ . Both gravity and surface tension are neglected in these simulations. Assuming that the electrolyte is bubble free, for an inter-electrode gap of 1cm and the difference in potential between the electrode is 0.01V corresponds to a current density of  $100\text{A/m}^2$ . Any change in current density can be attributed to the presence of bubbles in the computational domain.

#### When bubbles are attached on the electrode surface

When bubbles are present on the electrode surface, it increases the resistance in the system due to volume of the bubble and electrode screening. If an area of 2D bubble, which is present in the bulk, is redistributed on the surface such that the effective area is the same, the current reduces due to the increase in effective resistance at the electrode (due to electrode screening). This is showcased by considering two cases: EC1 (bubble is present in the bulk) and EC2 (bubble is attached to the electrode), see Fig.5.

The computational domain, of dimensions  $1\text{cm} \times 1\text{cm}$ , is meshed by  $200 \times 200$  cells. The left and right boundaries, which are the electrodes, are assigned as no-slip conditions for velocity and fixedFluxPressure (Greenshields, 2019) for pressure. The top and bottom boundaries are assigned fixed-Value (equal to 0Pa) for  $p_{rgh}$  and zeroGradient for velocity. All the boundaries are assigned zeroGradient for  $\alpha_1$ . For  $\phi$ , left and right walls are assigned 0V and 0.01V respectively, whereas the remaining boundaries are set as zeroGradient. The initial conditions for the  $\alpha_1$ , are set as described in Fig.5.

The reduction of the current due to the presence of the bubble on the electrode surface is shown in Table.2.

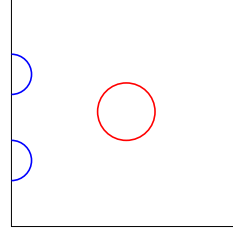


**Figure 5:** Illustration of the cases, EC1 and EC2, considered to showcase the effect electrode screening. EC1, represented by  $\bullet$ , considers a bubble of radius 1mm at the center of domain. EC2, represented by  $\bullet$ , considers two equally sized bubbles (semicircles with radii equal to 1mm) whose centers are 2.5mm and 6.5mm away from the bottom wall.

**Table 2:** Reduction of current due to the presence of bubble on the electrode.

Case	$\mathcal{F}^a$	Area of 2D bubbles ( $\text{m}^2$ )	Current <sup>b</sup> (A)
EC1	1	$3.16 \times 10^{-6}$	$9.384 \times 10^{-7}$
EC2	0.6	$3.16 \times 10^{-6}$	$9.306 \times 10^{-7}$

<sup>a</sup>  $\mathcal{F}$  represents the fraction of the left electrode area in contact with electrolyte, <sup>b</sup> Current is calculated as  $\sum \vec{i} \cdot \vec{S}$  where  $\vec{S}$  is the face surface area of individual cell on the left electrode.

#### When bubbles are present in the bulk

The 2D simulations use the a domain, of size  $1\text{cm} \times 1\text{cm}$ , which is meshed with  $200 \times 200$  cells. The left and right boundaries use no-slip, fixedFluxPressure (Greenshields, 2019) and fixedValue (equal to 0V and 0.01V) for  $\vec{U}$ ,  $p_{rgh}$  and  $\phi$  respectively. The other boundaries are assigned zeroGradient for both  $\vec{U}$  and  $\phi$  whereas  $p_{rgh}$  use fixedValue (equal to 0V). For  $\alpha_1$ , all the boundaries are assigned the zeroGradient condition. For 3D simulations, the domain of size  $1\text{cm} \times 1\text{cm} \times 1\text{cm}$  is meshed with  $200 \times 200 \times 200$  cells. The left and right boundaries are set according to the analogous conditions for 2D simulations whereas the remaining boundaries are treated like the top/bottom boundaries used in 2D simulations. The initial conditions used for  $\alpha_1$  is chosen so that bubble, with a range of sizes, are randomly placed in the bulk, as shown in Fig.A1 and Fig.A2 for 2D and 3D simulations respectively.

The bubbles change the effective conductivity of the electrolyte ( $k_e$ ) which can be theoretically estimated using the Bruggemann's correlation (valid for polydispersed spherical bubbles (Bruggeman, 1935)) as

$$k_e/k_1 = (1 - f)^{1.5}, \quad (12)$$

where  $f$  is the void fraction (calculated as the ratio of total volume of the bubble to the volume of the domain). Once the  $k_e$  is computed, the resistance is computed as  $d/(k_e A)$ , where  $d$  is the interelectrode distance (equal to 1cm) and  $A$  is the area of the 3D electrode (equal to  $0.01 \times 0.01\text{m}^2$ ), and current in the system and current density are determined based on Ohm's law with cell voltage computed as the difference between the right and left boundary conditions for  $\phi$  (equal to 0.01V). As expected, Fig.6 shows that 3D simulations provides a better agreement to the current density obtained from Bruggemann correlations than the 2D simulations. Further the solver successfully predicts the

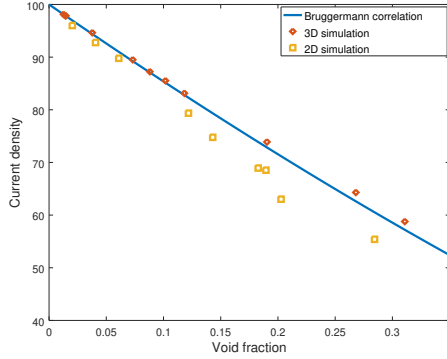


**Figure 6:** Comparison of the current density ( $A/m^2$ ) reduction with increase in void fraction of bubbles (in bulk) predicted by the simulations (for 2D and 3D) and Bruggemann's correlation.

reduction of current density with the increase in the void fraction of bubbles.

#### ON THE FULLY COUPLED SOLVER

For the fully coupled solver, the solution is obtained by solving the volume fraction equation, then calculating the relevant source terms, the coupled momentum and continuity equations, then the Gauss' law and finally the transport of dissolved gas using CCST model at each time step.

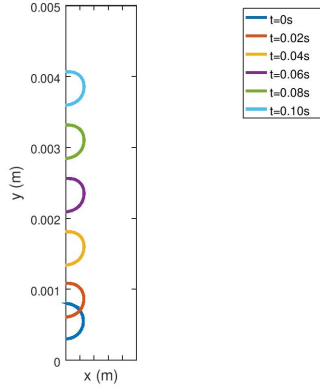


**Figure 7:** Comparison interface morphology and position with time in the computational domain.

In order to showcase the ability of the solver, we simulate the growth of a pre-existing bubble due to electrochemical reactions occurring at a vertical electrode-electrolyte interface. The occurrence of pre-existing bubbles at surface imperfections, for instance from previous nucleation events, can reduce the energy required for nucleation to values as low as zero (Vachaparambil and Einarsrud, 2018). This approximation, which is physically reasonable as bubble has been observed to generate from the same site on the electrode

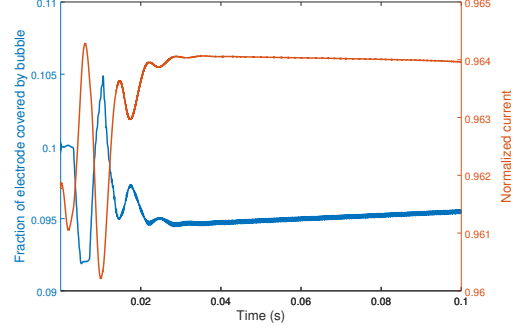


**Figure 8:** Comparison change in footprint of the bubble on the electrode (fraction of bubble covered electrode) and the associated change in normalized current (calculated as  $(\sum \vec{i} \cdot \vec{S}) / (I)$ , where  $I$  is the current when no bubbles are present, i.e.  $100A/m^2 \times (5 \times 10^{-9}m^2)$ ) with time.

for a range of current densities (Westerheide and Westwater, 1961; bo Liu *et al.*, 2019), enables direct modelling of the growth of the bubble without the need to treat bubble nucleation. In order to treat bubble nucleation in a CFD framework, algorithms like the one proposed by Damme *et al.* (2010) are required.

The computational domain used for the simulation is  $1mm \times 5mm$  which is meshed by  $200 \times 1000$  cells. The left and right boundaries are set as walls and the boundary conditions are described based on the individual modules in the decoupled solver except for the the  $C_i$  at the left wall which is computed using the Faraday's law of electrolysis, as  $\partial_n C_i = |\vec{j}| \alpha_i / (2FD_1)$ , and  $\phi$  is assigned a fixed Value of 0V and  $10^{-3}V$  at left and right walls respectively. The pre-existing bubble, of radius equal to 0.25mm, is initialized as that its center is on the left wall at a distance of 0.55mm from the lower boundary. The fluid properties used in the proof of concept simulation are:  $\rho_1 = 1000kg/m^3$ ,  $\rho_2 = 1kg/m^3$ ,  $\nu_1 = 10^{-6}m^2/s$ ,  $\nu_2 = 1.48 \times 10^{-5}m^2/s$ ,  $D_1 = 10^{-9}m^2/s$ ,  $D_2 = 10^{-5}m^2/s$ ,  $\sigma = 0.003N/m$ ,  $M = 44 \times 10^{-3}kg/mol$ ,  $k_1 = 100S/m$ ,  $k_2 = 10^{-13}S/m$  and  $|\vec{g}| = 9.81m/s^2$ . Due to the use of surface tension, the maximum time step allowed is manually limited to  $8\mu s$  (see Deshpande *et al.* (2012); Vachaparambil and Einarsrud (2019)) and the simulations are run until 0.1s.

The concentration distribution of the dissolved gas generated by the electrochemical reactions and the current density distribution around the rising bubble attached to the electrode at  $t = 0.1s$  is shown in Fig.9. As the bubble rises up, the growth rate and the effective radius of the bubble increases as seen in Fig.10 which is associated with the increase in the bubble footprint after the initial transient behaviour of the bubble, see Fig.8. The change in current obtained directly correlates with the footprint and size of the bubble, see Fig.8 and Fig.10.

#### CONCLUSION

We implemented the individual models relevant in modelling an electrochemical gas evolution in the VOF solver available in OpenFOAM® 6. The modules added into interFoam are: SSF (for surface tension modelling), C-CST



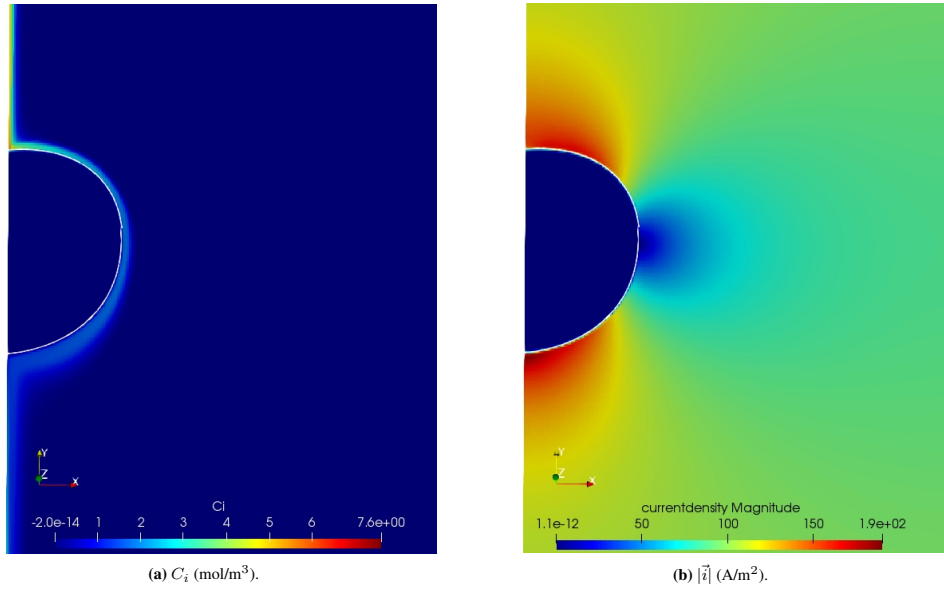


**Figure 9:** Comparison of the distribution of dissolved gas and current density (magnitude) around the bubble (whose interface, at  $\alpha_1 = 0.5$ , is represented by the white contour) at  $t = 0.1s$ .

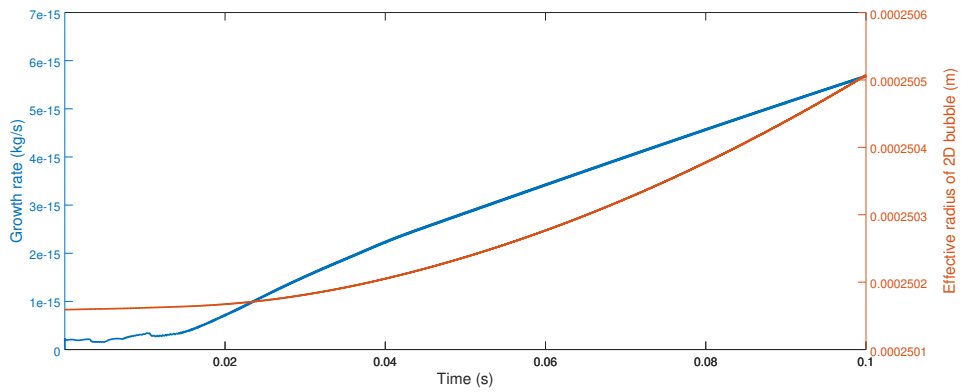


**Figure 10:** Comparison of the growth rate and the effective radius of the bubble as it evolves.

(transport of dissolved gas), supersaturation driven bubble growth model and Gauss's law. The predictions from these decoupled modules agree quite reasonably with relevant theoretical models available in literature. The bubble evolution, under constant potential condition, as predicted by the fully coupled solver is also discussed to showcase the ability of the proposed solver to handle electrochemical gas evolution. The proposed fully coupled solver, unlike other works reported in literature, can 'theoretically' be applied to simulate a variety of flow configuration (current density and electrode orientations) as well as the impact of bubble detachment in electrochemical systems due to the use of phenomenological models.

## ACKNOWLEDGEMENTS

This work was funded by the Department of Materials Science and Engineering at NTNU. The authors would also like to thank UNINETT Sigma2 for providing necessary computational resources through grant NN9741K.

## REFERENCES

- BIRD, R., STEWART, W. and LIGHTFOOT, E. (2007). *Transport Phenomena: Revised Second Edition*. Wiley, New York.
- BO LIU, H., HU, Q., MING PAN, L., WU, R., LIU, Y. and ZHONG, D. (2019). "Electrode-normal magnetic field facilitating neighbouring electrochemical bubble release from hydrophobic islets". *Electrochimica Acta*, **306**, 350 – 359.
- BRACKBILL, J., KOTHE, D. and ZEMACH, C. (1992). "A continuum method for modeling surface tension". *Journal of Computational Physics*, **100**(2), 335 – 354.
- BRUGGEMAN, D.A.G. (1935). "Berechnung verschiedener physikalischer konstanten von heterogenen substanzen. i. dielektrizitätskonstanten und leitfähigkeiten der mischkörper aus isotropen substanzen". *Annalen der Physik*, **416**(7), 636–664.
- DAMME, S.V., MACIEL, P., PARYS, H.V., DECONINCK, J., HUBIN, A. and DECONINCK, H. (2010). "Bubble nucleation algorithm for the simulation of gas evolving electrodes". *Electrochemistry Communications*, **12**(5), 664 – 667.
- DEISING, D., BOTHE, D. and MARSCHALL, H. (2018). "Direct numerical simulation of mass transfer in bubbly flows". *Computers & Fluids*, **172**, 524 – 537.
- DESHPANDE, S.S., ANUMOLU, L. and TRUJILLO, M.F. (2012). "Evaluating the performance of the two-phase flow solver interFoam". *Computational Science & Discovery*, **5**(1), 014016.
- EINARSRUD, K.E. and JOHANSEN, S.T. (2012). "Modelling of bubble behaviour in aluminium reduction cells". *Progress in Computational Fluid Dynamics, an International Journal*, **12**(2-3), 119–130.
- EINARSRUD, K.E., EICK, I., BAI, W., FENG, Y., HUA, J. and WITT, P.J. (2017). "Towards a coupled multi-scale, multi-physics simulation framework for aluminium electrolysis". *Applied Mathematical Modelling*, **44**, 3 – 24.
- GREENSHIELDS, C.J. (2019). "Openfoam user guide version 7". URL <http://foam.sourceforge.net/docs/Guides-a4/OpenFOAMUserGuide-A4.pdf>.
- HARDT, S. and WONDRA, F. (2008). "Evaporation model for interfacial flows based on a continuum-field representation of the source terms". *Journal of Computational Physics*, **227**(11), 5871 – 5895.
- HASHEMI, S.J. and ABEDI, J. (2007). "Advances in modeling of new phase growth". *Energy & Fuels*, **21**(4), 2147–2155.
- HREIZ, R., ABDELOUAHED, L., FÜNFSCILLING, D. and LAPICQUE, F. (2015). "Electrogenerated bubbles induced convection in narrow vertical cells: A review". *Chemical Engineering Research and Design*, **100**, 268 – 281.
- HYSING, S., TUREK, S., KUZMIN, D., PAROLINI, N., BURMAN, E., GANESAN, S. and TOBISKA, L. (2009). "Quantitative benchmark computations of two-dimensional bubble dynamics". *International Journal for Numerical Methods in Fluids*, **60**(11), 1259–1288.
- MAES, J. and SOULAINÉ, C. (2018). "A new compressive scheme to simulate species transfer across fluid interfaces using the volume-of-fluid method". *Chemical Engineering Science*, **190**, 405 – 418.
- MAES, J. and SOULAINÉ, C. (2020). "A unified single-field volume-of-fluid-based formulation for multi-component interfacial transfer with local volume changes". *Journal of Computational Physics*, **402**, 109024.
- POPINET, S. (2018). "Numerical models of surface tension". *Annual Review of Fluid Mechanics*, **50**(1), 49–75.
- RAEINI, A.Q., BLUNT, M.J. and BIJELJIC, B. (2012). "Modelling two-phase flow in porous media at the pore scale using the volume-of-fluid method". *Journal of Computational Physics*, **231**(17), 5653 – 5668.
- SCRIVEN, L. (1959). "On the dynamics of phase growth". *Chemical Engineering Science*, **10**(1), 1 – 13.
- SUN, M., LI, B. and LI, L. (2018). "A multi-scale mathematical model of growth and coalescence of bubbles beneath the anode in an aluminum reduction cell". *Metallurgical and Materials Transactions B*, **49**(5), 2821–2834.
- TAQIEDDIN, A., ALLSHOUSE, M.R. and AL-SHAWABKEH, A.N. (2018). "Editors' choice—critical review—mathematical formulations of electrochemically gas-evolving systems". *Journal of The Electrochemical Society*, **165**(13), E694–E711.
- VACHAPARAMBIL, K.J. and EINARSRUD, K.E. (2018). "Explanation of bubble nucleation mechanisms: A gradient theory approach". *Journal of The Electrochemical Society*, **165**(10), E504–E512.
- VACHAPARAMBIL, K.J. and EINARSRUD, K.E. (2019). "Comparison of surface tension models for the volume of fluid method". *Processes*, **7**(8), 542.
- VACHAPARAMBIL, K.J. and EINARSRUD, K.E. (2020a). "Modeling interfacial mass transfer driven bubble growth in supersaturated solutions". *AIP Advances*, **10**(10), 105024.
- VACHAPARAMBIL, K.J. and EINARSRUD, K.E. (2020b). "Numerical simulation of bubble growth in a supersaturated solution". *Applied Mathematical Modelling*, **81**, 690 – 710.
- WESTERHEIDE, D.E. and WESTWATER, J.W. (1961). "Isothermal growth of hydrogen bubbles during electrolysis". *AIChE Journal*, **7**(3), 357–362.
- ZHANG, Z., LIU, W. and FREE, M.L. (2020). "Phase-field modeling and simulation of gas bubble coalescence and detachment in a gas-liquid two-phase electrochemical system". *Journal of The Electrochemical Society*, **167**(1).
- ZHAO, X., REN, H. and LUO, L. (2019). "Gas bubbles in electrochemical gas evolution reactions". *Langmuir*, **35**(16), 5392–5408.

## APPENDIX A

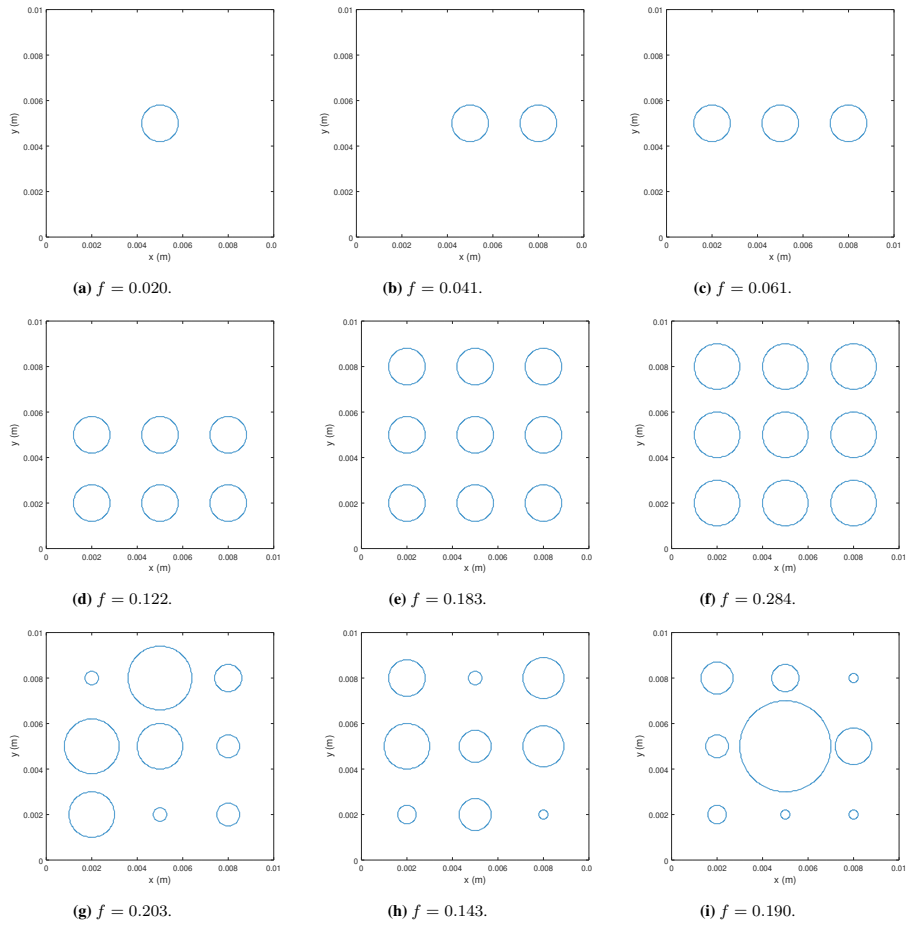
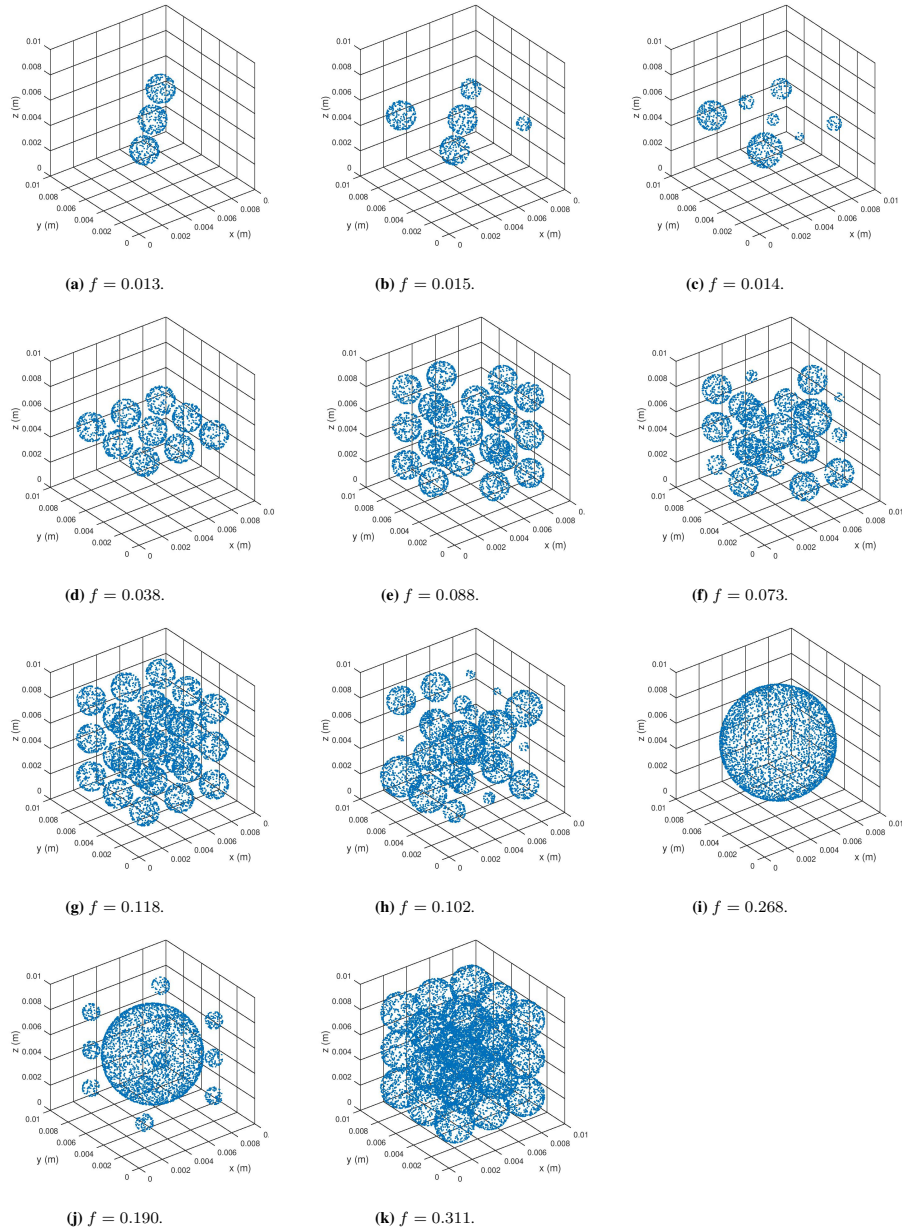


Figure A1: The distribution of the 2D bubbles in the computational domain.



**Figure A2:** The distribution of the 3D bubbles in the computational domain.



*Appended paper F*

**Numerical simulation of continuum scale electrochemical hydrogen bubble evolution**

Kurian J. Vachaparambil and Kristian Etienne Einarsrud  
Submitted to *Applied Mathematical Modelling*



# Numerical simulation of continuum scale electrochemical hydrogen bubble evolution

Kurian J. Vachaparambil, Kristian Etienne Einarsrud\*

*Department of Materials Science and Engineering, Norwegian University of Science and Technology (NTNU), Trondheim 7491, Norway*

---

## Abstract

One of the important aspects in improving the efficiency of electrochemical processes, such as water electrolysis, is the efficient removal of bubbles which evolve from the electrodes. Numerical modelling based on Computational Fluid Dynamics (CFD) can describe the process, provide insights into its complexity, elucidate the underlying mechanisms of how bubbles evolve and their effect as well as aid in developing strategies to reduce the impact of the bubble.

In this paper, a Volume of Fluid (VOF) based simulation framework to study the evolution of hydrogen bubbles in the order of few hundred micrometers, referred to as continuum scale bubbles, is proposed. The framework accounts for the multiphase nature of the process, electrochemical reactions, dissolved gas transport, charge transport, interfacial mass transfer and associated bubble growth. The proposed solver is verified by comparison to analytical solution of bubble growth in supersaturated solutions and qualitative analysis based on experimental observations of the variations in current based on static simulations. The proposed solver is used to simulate the evolution of a single bubble under various wetting conditions of the electrode as well as the coalescence driven evolution of two bubbles. The results show that as the bubbles detach, the surface of the bubble oscillates and as it rises it reaches a stable shape determined by the balance between drag force and surface tension. These surface oscillations,

---

\*Corresponding author

*Email address:* `kristian.e.einarsrud@ntnu.no` (Kristian Etienne Einarsrud)



which causes the bubble to get flattened and elongated, results in temporal variation of the electrical current. The reduction of current due to bubble growth is visible only when these surface oscillations have reduced. The simulations also show the current as a function of the position of the bubble in the interelectrode gap. The framework also predicts the increase in current as a result of bubbles leaving the surface which is larger when the process is coalescence driven. The simulations indicate that bubble coalescence is the underlying mechanism for continuum scale bubble detachment.

*Keywords:* Volume of Fluid, Multiphysics simulations, Electrochemical bubble evolution

---

## 1. Introduction

One of the potential ways to address the intermittencies in energy production via renewable sources is to convert surplus energy into hydrogen using water electrolysis. This hydrogen can be used as an energy vector which would reduce the dependence on fossil fuels, reduce carbon footprint and foster the move to the environmentally-benign hydrogen economy [1]. In order to enable this transition, the cost of hydrogen production from water electrolysis must be reduced, with cheaper electricity from renewable sources on energy (as electricity can account upto 70% of the costs [1]) and more efficient water electrolyzers. On going research into making efficient water electrolyzers has been focused primarily on the development of active and durable electrocatalysts for the water splitting reactions, see [2, 3, 4]. Another aspect to improve the efficiency of the electrolyzer is to remove bubbles, which reduce the area of the electrode in contact with electrolyte as well as the effective electrolyte conductivity, see [5, 6]. Additionally, convection associated with bubble evolution has been reported to increase mass transfer rates in the electrochemical systems [6]. As efficient removal of bubbles during water electrolysis can result in saving 10-25% of the energy supplied [5], understanding the dynamics of bubble evolution can aid in developing strategies to improve the efficiency of the water electrolyzers.

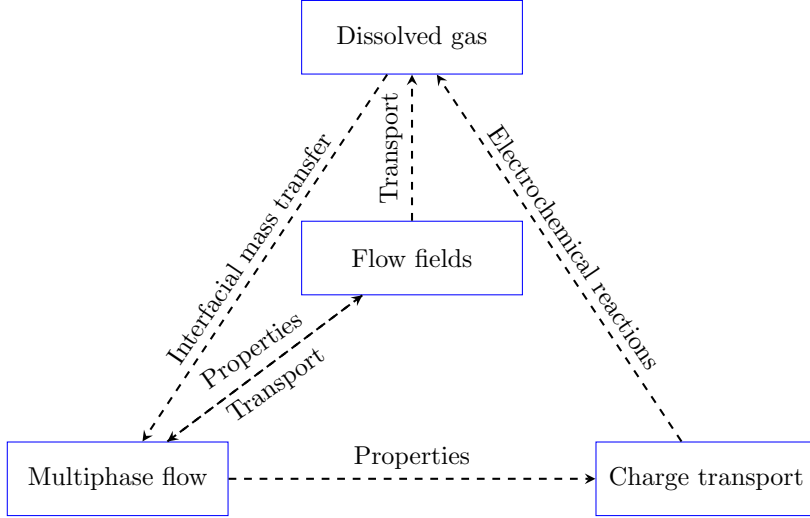


Figure 1: Illustration of the coupled nature of electrochemical gas evolution.

Although experimental works have provided substantial insights into the physics underlying the electrochemical gas evolution, [7, 8, 9, 10], numerical simulations can provide a fundamental understanding of the coupled nature of the process as well as the temporal and spatial variations of the flow parameters as bubbles evolve. As electrochemical gas evolution is a multiphysics-multiscale process, the choice of numerical simulations employed depends on the phenomena of interest, see [11]. Broadly speaking, atomistic process like the electrochemical reactions and the bubble nucleation are typically studied using molecular dynamic simulations [12] whereas continuum scale process (which are few hundred micrometer or larger) like bubble growth and detachment can be studied using Computational Fluid Dynamics (CFD) [13] and the intermediate scales relevant for ion migration and continuous bubble evolution can be investigated using meso-scale models like Lattice Boltzmann method [14, 15]. This paper delves into the evolution of continuum scale hydrogen bubbles, which are few hundred micrometers in radius, observed in experimental works like [7, 9], which are studied using multiphase-multiphysics CFD approaches.

In order to study the dynamics of continuum scale electrochemical bubble

evolution it is necessary to simulate the relevant multiphysics, summarized in Fig. 1. The numerical modelling of *multiphase flows* can be divided into dispersed phase and interface resolved modelling [16]. Dispersed phase modelling (which includes Euler-Euler, Mixture and Euler-Lagrange approaches) requires closure models to describe the momentum transfer between the phases as the individual bubbles are below the mesh resolution. These momentum closure terms relies on the assumption of a bubble size which is typically set based on experimentally observed detachment diameter, see [17]. The dispersed phase modelling approaches, which are used in majority of the numerical simulation of the electrochemical gas evolution, see the review by [17], are typically employed to study the dynamics of industrial scale electrolyzers where the larger flow features are of interest. On the other hand interface resolved modelling approaches, like the Volume of Fluid (VOF), are typically used to study the detailed behaviour of the interface without using any approximations for momentum transfer. As a result of resolving the bubble, VOF provides an ideal framework to study the details of evolution of bubbles which are of interest in this work. The VOF model uses a scalar, the volume fraction of liquid ( $\alpha_1$ ), to identify the bubble, liquid and interface which corresponds to  $\alpha_1$  equal to zero, unity and (0, 1) respectively [16]. The interface is captured by advecting  $\alpha_1$  and the sharpness of the interface is ensured by using either the computationally cheap algebraic VOF, see [18], or the sharper but computationally more demanding geometric VOF, see [19]. A drawback of the algebraic VOF method<sup>1</sup> is the smeared nature of the interface which generates numerical artifacts known as 'spurious velocities' when simulating surface tension dominant flows, which is very well studied in literature [19, 18, 20, 21]. Some of the approaches proposed to reduce the spurious velocities are the Sharp Surface Force and Smoothed CSF models proposed by [22] and [23] respectively. Readers interested in the source

---

<sup>1</sup>It should be noted geometric VOF methods also generate spurious velocities but they are several orders of magnitude smaller than the ones produces in algebraic VOF methods, see [18, 19].

of these spurious velocities and review of on going research to address them are referred to works like [20].

Another relevant feature in electrochemical gas evolution of continuum scale bubble is the transport of the *dissolved gas* which requires treatment of interfacial jump conditions for diffusive fluxes and concentration across the interface, see [24]. Two ways to simulate the dissolved gas transport are single and two field approaches. The two field approach, described by [24, 25], uses individual transport equations for dissolved gas in each phase and the interfacial jump conditions are treated like boundary conditions for each phase. The single field approach, described by [26, 27], uses a unified governing equation that accounts for the interfacial jump conditions to describe the transport of dissolved gas in both phases. Although dissolved gas transport can be simulated by both these approaches, two and single field approaches are recommended to be used with geometric and algebraic VOF methods respectively, see [26]. Once the dissolved gas distribution is known, the *interfacial mass transfer* and the associated *bubble growth* can be computed based on universally valid Fick's 1<sup>st</sup> law (see [28, 29]) or with flow scenario based Sherwood number based correlations (see [30]). As Sherwood number correlations are applicable for a specific flow scenario, bubble evolution, which is associated with complex flow patterns as well as interface deformation, cannot be accurately described by a single Sherwood number correlation to the best of the authors' knowledge.

Another aspect of simulating electrochemical gas evolution is the *charge transport*, which drives the electrochemical reactions as it is proportional to the current density, based on Faraday's law of electrolysis. The commonly used approach to simulate it is based on charge conservation using Gauss's law, one of the four Maxwell's equations for electromagnetism, and current density expressed based on the Ohm's law analogous to works like [31, 32].

Due to the coupled multiphysics relevant in electrochemical gas evolution, literature which employs interface resolved simulations to study the dynamics of electrochemically generated bubbles are quite limited to the best of the knowledge of the authors. These works can be divided into pure and hybrid VOF

methods. In 'pure' VOF methods, like [30], the evolution of a single hydrogen bubble was studied by simulating the growth driven by interfacial mass transfer (based on Sherwood number) without accounting for the charge transport. In 'hybrid' VOF approaches, like [31, 32, 33], VOF was coupled with sub-grid bubbles treated via dispersed modelling approaches and the resolved bubble were assumed to grow only via coalescence. These hybrid VOF, typically used to simulate the carbon dioxide evolution at the anode during aluminium production, is used to simulate bubble evolution on an whole electrode. [31, 32] reported the transient evolution of voltage (under constant current condition) as result of bubble evolution from the electrode whereas [33] did not simulate the current distribution nor the transport of dissolved gas generated from the electrochemical reactions. Apart from these studies, other simplified studies have employed interface resolved simulations to investigate the behaviour of the interface without considering any multiphysics effects like [34]. Although the previous works have provided substantial knowledge into the modelling of evolution of electrochemically generated bubbles, there is still a lack of computational models that treat the complexity associated with the multiphysics and multiscale nature of the process as highlighted in the recent review by [11]. Additionally, another review on the hydrodynamics of electrochemical gas evolution, by [35], highlights the lack of CFD studies that consider the effect of bubble coalescence and detachment.

In this paper, we attempt to partly address this lack of knowledge by developing a coupled multiphysics solver that can handle the continuum scale hydrogen bubble evolution during water electrolysis. The proposed solver is based on the algebraic VOF framework available in OpenFOAM<sup>®</sup> 6 which is modified to account for transport of dissolved gas [27] along with the associated supersaturation driven bubble growth (based on [28]) and charge transport (based on Gauss's law and Ohm's law, see [31]) which are coupled based on electrochemical reaction defined based on Faraday's law of electrolysis. In order to reduce the complexity of the process, the proposed solver is subject to the following simplifications:

- The bubble evolution and the electrochemical reactions occurs only at the cathode and the anode/counter-electrode is assumed to not affect the process,
- The proposed model treats the evolution of only continuum scale bubbles, which are in the order of few hundred micrometers,
- The liquid and the bubble are assumed to be have a constant density and viscosity,
- The flow is assumed to be isothermal and laminar,
- The interface is assumed to be always saturated and saturation concentration is assumed to be constant with the variation of hydrostatic pressure and Laplace pressure in sub-millimeter sized bubbles as it evolves,
- The system is assumed to be under constant potential difference, so the bubble evolution leads to changes in current. The proposed solver accounts for the current variation as a result of the ohmic contribution of the bubbles present in the bulk and on the surface. The change in current due to the contributions from the surface and concentration overpotentials, see [36], as a result of bubble evolution is neglected in this paper.

The ability of the proposed solver is showcased via 2D simulations of the evolution of the single hydrogen bubble from cathode for various wetting condition at the electrode. In addition to single bubble simulations, the evolution of bubble driven by coalescence is also investigated. The temporal change in the current as bubble evolves is analyzed for these cases.

## 2. Governing equations and solution algorithm

The proposed solver is developed based on OpenFOAM<sup>®</sup> 6 with VOF framework for interface capturing. The VOF framework is modified, based on works

like [28] and [31], to treat multiphysics nature of the process. The overall solution algorithm along with the implemented governing equations can be summarized as:

1. The volume fraction of electrolyte ( $\alpha_1$ ) is computed based on

$$\frac{\partial \alpha_1}{\partial t} + \nabla \cdot (\alpha_1 \vec{U}) + \nabla \cdot (\alpha_1 (1 - \alpha_1) \vec{U}_r) = \dot{S}_\alpha, \quad (1)$$

where  $\dot{S}_\alpha = \alpha_1 \nabla \cdot \vec{U}$  is the source term for bubble growth and the single field formulation of velocity is represented by  $\vec{U}$ . The third term in Eq. 1 represents the interface compression method which belongs to the algebraic VOF method [37], acting only in the interfacial region to render a sharp interface based on the compressive velocity, determined as:

$$\vec{U}_r = C_\alpha \left| \frac{\phi}{|\vec{S}_f|} \right| \vec{n}, \quad (2)$$

where  $\vec{n}$  is the unit normal to the interface,  $\vec{S}_f$  is the area vector of the cell face,  $\phi$  is the volumetric flux which is calculated as  $\vec{U} \cdot \vec{S}_f$ , and  $C_\alpha$  is the user defined compression factor which is usually set in the order of unity (between values of zero and four). As Eq. 1 relies on interface compression method which belong to the algebraic VOF (over the more accurate sub-cell level interface reconstruction known as geometric VOF), it produces an interface which is smeared over two-three cells [18]. Eq. 1 is solved using the semi-implicit Multidimensional Universal Limiter with Explicit Solution (MULES) method which uses a implicit predictor and explicit corrector steps to ensure the boundedness of  $\alpha_1$  between zero and unity [38]. Once  $\alpha_1$  is computed, the volume fraction of phase 2 or bubble ( $\alpha_2$ ) is computed as  $\alpha_2 = 1 - \alpha_1$ .

2. Once the interface is known at the current time step, fluid properties, like density ( $\rho$ ) and viscosity ( $\nu$ ), are updated based on  $\chi = \alpha_1 \chi_1 + \alpha_2 \chi_2$  where  $\chi \in [\rho, \nu]$ . The subscripts 1 and 2 indicate the fluid property related to Phase 1 and 2 respectively.

3. The driving force for interfacial mass transfer is then computed based on the universally applicable Fick's 1<sup>st</sup> law as

$$j = M_i D_{i,1} |\nabla C_i|, \quad (3)$$

where  $M_i$  is the molar mass of hydrogen ( $i$ ) and  $D_{i,1}$  is the diffusion coefficient of the hydrogen in the liquid. Based on Eq. 3, the local mass transfer rate is computed at the liquid side of the interface as

$$\psi_0 = N j \alpha_1 |\nabla \alpha_1|, \quad (4)$$

where  $N$  is normalization factor computed as  $\int_{\Omega} |\nabla \alpha_1| dV / \int_{\Omega} \alpha_1 |\nabla \alpha_1| dV$ .

4. In order to improve the numerical stability,  $\psi_0$  is smeared using an inhomogeneous Helmholtz equation as proposed by [39]:

$$D \Delta t \nabla^2 \psi = \psi - \psi_0, \quad (5)$$

where  $D \Delta t$  is the user defined term which controls the extent of smearing.

5. Using  $\psi$ , the source term for the continuity equation which accounts only for the bubble growth, is redistributed in the region where  $\alpha_1 < 0.001$  as

$$\dot{m} = A \alpha_2 \psi, \quad (6)$$

where  $A$  is a normalization factor computed as  $\int_{\Omega} \psi_0 dV / \int_{\Omega} \alpha_2 \psi dV$ . This procedure to define  $\dot{m}$  based on a heavyside function, is based on the work by [40], enables the interface to get advected just by the velocity field, without being influenced by the source term. The sink term for the dissolved hydrogen to account for the interfacial mass transport is computed at the liquid side of the interface as

$$S_i = -\frac{N \alpha_1 (j |\nabla \alpha_1|)}{M_i}, \quad (7)$$

where  $N$  is the normalization factor used in Eq.4.

6. The surface tension force is computed based on Sharp Surface Force (SSF) as implemented in [21], based on the work by [22]. The SSF model is preferred over the commonly used Continuum Surface Force (CSF) model



(proposed by [41]) as it has been shown to reduce spurious velocities and reliably simulate a range of surface tension dominant flow scenarios [22, 21]. The pressure gradient, surface tension force computed by SSF, gravitational force as well as volumetric flux ( $\phi$ ) are computed at cell faces to ensure force balance to reduce spurious velocities due to inconsistent discretization of these terms, as recommended by [18]. SSF, in summary, consists of four steps: smoothening operation on  $\alpha_1$ ; obtain an initial estimate of the interfacial curvature based on the smoothed  $\alpha_1$  which is subsequently smoothed away from the interface; then the final curvature ( $\kappa_{final}$ ) is estimated; and the surface tension force is computed as

$$\vec{F}_{st} = \sigma \kappa_{final} \nabla \alpha_{sh}, \quad (8)$$

where  $\alpha_{sh}$  is the sharpened volume fraction of phase 1, equal to

$$\alpha_{sh} = \frac{1}{1 - C_{sh}} \left[ \min \left( \max \left( \alpha_1, \frac{C_{sh}}{2} \right), 1 - \frac{C_{sh}}{2} \right) - \frac{C_{sh}}{2} \right], \quad (9)$$

where  $C_{sh}$  is a sharpening coefficient  $C_{sh} \in [0, 1)$ . It should be pointed out that surface tension is computed explicitly as it is determined based on the advected  $\alpha_1$  in Eq.1.

7. Now momentum and continuity equations are solved using Pressure Implicit with Splitting of Operators (PISO) algorithm [42]. This can be briefly summarized as iterative procedure in which predicted velocity field is corrected based on pressure correction equation [18]. The momentum equation is

$$\frac{\partial \rho \vec{U}}{\partial t} + \nabla \cdot (\rho \vec{U} \vec{U}) = -\nabla p_{rgh} + \nabla \cdot (\mu \nabla \vec{U}) + \nabla \vec{U} \cdot \nabla \mu - \vec{g} \cdot \vec{x} \nabla \rho + \vec{F}_{ST}, \quad (10)$$

where  $p_{rgh}$ , the modified pressure, is equal to  $p - \rho \vec{g} \cdot \vec{x}$  and  $\nabla \cdot (\mu \nabla \vec{U}) + \nabla \vec{U} \cdot \nabla \mu$  are the viscous terms of the momentum equation, see [18]. The continuity equation is

$$\nabla \cdot \vec{U} = \frac{\dot{m}}{\rho}, \quad (11)$$

where  $\dot{m}$  is computed based on Eq. 6.

8. Charge conservation is solved based on Gauss's law as

$$\nabla \cdot \vec{i} = 0, \quad (12)$$

where  $\vec{i}$  is the local current density is expressed based on Ohm's law as equal to

$$\vec{i} = -\Gamma \nabla \Phi \quad (13)$$

where  $\Gamma$  is the volume fraction weighted average electrical conductivity, i.e.  $\Gamma = \alpha_1 \Gamma_1 + \alpha_2 \Gamma_2$ , and  $\Phi$  is the electrical potential.

9. The transport of the dissolved hydrogen is based on the single field Compressive Continuous Species Transfer model, which was proposed by [27],

:

$$\frac{\partial C_i}{\partial t} + \nabla \cdot (\vec{U} C_i) = \nabla \cdot \left( \hat{D}_i \nabla C_i - \hat{D}_i \mathcal{B} C_i \nabla \alpha_1 - \mathcal{B} \alpha_1 \alpha_2 \vec{U}_r C_i \right) + S_i, \quad (14)$$

where  $S_i$  is computed in Eq. 7,  $\mathcal{B}$  is equal to  $(1 - He_i)/(\alpha_1 + \alpha_2 He_i)$ ,  $He_i$  describes the interfacial jump in concentration of the dissolved gas,  $\vec{U}_r$  is the compressive velocity defined in Eq. 2, and  $\hat{D}_i$  is the harmonic average of the diffusion coefficients of the phases. As the dissolved gas distribution is of interest to simulate the bubble growth and assuming that the interface is always saturated,  $C_i$  can be understood as the concentration of dissolved hydrogen which is over the saturation condition [28]. Subsequently  $He_i$  can be set to a value close to zero, see Table. 3, to reliably model the saturation condition at the interface and simulate the transport of only the dissolved hydrogen as shown by [28]. Electrochemical reactions which are dependent on the local value of current density are added as boundary conditions (further described in Section. 3.1).

10. Now the solver moves to the next time step. Adaptive time stepping is used in the simulations to allow for computing the time step such that maximum Courant number, which is defined by the user, is always satisfied. If a maximum time step is defined, the solver takes the minimum of the user defined maximum time step and the time step associated with the Courant number [37].

Table 1: Discretisation schemes used, see [37] for information about the schemes.

Modelling term	Keyword	Scheme
Time derivatives	ddtSchemes	Euler
Divergence term	$\nabla \cdot (\rho \vec{U} \vec{U})$	vanLeerV
	$\nabla \cdot (\vec{U} \alpha_1), \nabla \cdot (\vec{U} C_i)$	vanLeer
	$\nabla \cdot (\vec{U}_r \alpha_1 (1 - \alpha_1))$	interfaceCompression
	$\nabla \cdot (\hat{D}_i \mathcal{B} C_i \nabla \alpha_1)$	vanLeer
	$\nabla \cdot (\mathcal{B} \alpha_1 \alpha_2 \vec{U}_r C_i)$	vanLeer
Gradient term	gradSchemes	linear
Laplacian term	laplacianSchemes	linear corrected
Other	snGradSchemes	corrected
	interpolationSchemes	linear

All the variables are stored at the cell center like in a collocated arrangement but computations are performed at the cell faces (which was initially proposed by [43]) to prevent checkerboard type errors. The Finite Volume Method is employed to solve the governing equations with spatial and temporal terms discretized based on Table. 1. The discretized governing equations are solved with iterative solvers with the relevant preconditioners/smoothers tabulated in Table. 2. The maximum number of iterations is set such that the solution of flow variable converges and satisfies the tolerance criterion defined in Table. 2. A summary of the parameters used in the solution algorithm is provided in Table. 3. Unless otherwise noted, the time step taken by the proposed solver is based on the maximum Courant number which is set equal to 0.05.

Table 2: Solvers used for the discretised governing equations [37].

Flow variable	Linear solver	Smoother/preconditioner	Tolerance
$p_{rgh}$	PCG	GAMG	$10^{-10}$
$\vec{U}$	smoothSolver	symGaussSeidel	$10^{-10}$
$\alpha_1$	smoothSolver	symGaussSeidel	$10^{-10}$
$\Phi$	GAMG	DICGaussSeidel	$10^{-10}$
$C_i$	PBiCGStab	diagonal	$10^{-10}$
$\psi$	GAMG	DICGaussSeidel	$10^{-10}$

### 3. Definition of test cases

#### 3.1. Computational domain and boundary conditions

The two-dimensional computational domain used in the simulations is a rectangle, of length ( $L_e$ ) and height ( $L_{ac}$ ) equal to 10 mm and 5 mm respectively, as illustrated in Fig. 2. Although the simulations discussed in the paper are two-dimensional, OpenFOAM<sup>®</sup> requires a finite thickness with a single cell resolution in the third direction, represented by  $h$ , which is set to 1  $\mu\text{m}$ . These 'additional' boundaries are set to 'empty' boundary conditions to perform a 2D simulation. The area of each electrode,  $A$ , is computed as  $L_e \times h$  and the volume of the entire domain is equal to  $A \times L_{ac}$ . The left and right boundaries are assigned zero gradient for volume fraction of liquid ( $\alpha_1$ ), dissolved gas concentration ( $C_i$ ), local mass transfer rate ( $\psi$ ) and electrical potential ( $\Phi$ ) where as single field velocity ( $\vec{U}$ ) and modified pressure ( $p_{rgh}$ ) are set as inletOutlet (zero gradient for outflow but back flow into the domain is restricted by setting zero velocity) and fixed value (equal to 0 Pa). The top boundary is assigned zero gradient for  $\alpha_1$ , fixed value (equal to 0 mol/m<sup>3</sup>) for  $C_i$ , fixed value (of 0.2 V) for electrical potential ( $\Phi$ ), fixedFluxPressure for  $p_{rgh}$ , zero gradient for  $\psi$  and no-slip for velocity. The bottom boundary, referred to as electrode, is assigned zero gradient for  $\alpha_1$  along with the static contact angle ( $\theta$ ) condition at the electrode, fixed gradient (which is computed based on Faraday's law of

Table 3: Summary of the other settings used in the solution algorithm which is set based on [28] and OpenFOAM<sup>®</sup> recommendations [37].

Parameter	Value	Notes
<code>nAlphaCorr</code>	2	Number of $\alpha_1$ correction.
<code>nAlphaSubCycles</code>	1	Number of sub-cycles of $\alpha_1$ equation within each time step.
<code>cAlpha (<math>C_\alpha</math>)</code>	1	Used for interface compression in Eq.
<code>MULESCorr</code>	yes	Switches on semi-implicit MULES.
<code>nLimiterIter</code>	3	Number of MULES iterations over the limiter.
<code>momentumPredictor</code>	no	Controls solving of the momentum predictor.
<code>nOuterCorrectors</code>	1	PISO algorithm is selected by setting this parameter equal to unity in PIMPLE algorithm.
<code>nCorrectors</code>	3	The number of times the PISO algorithm solves the pressure and momentum equation in each time step.
<code>nNonOrthogonalCorrectors</code>	0	Used when meshes are non-orthogonal.
<code>relaxationFactors</code>	1	Specifies the under-relaxation factors used for fields and equations [21].
$C_{sh}$	0.3	Sharpening coefficient used in the Sharp Surface Force model to simulate a sub-millimeter bubble [44].
$D\Delta t$	$10^{-6}$	Smearing of the local mass transfer rate (based on sensitivity studies performed in [28]).
$He_i$	$10^{-4}$	Interfacial jump condition for concentration to simulated just the dissolved gas (based on parametric study in [28]).

electrolysis<sup>2</sup>) for the dissolved gas concentration ( $C_i$ ), fixed value (of 0.0 V) for  $\Phi$ , fixedFluxPressure for modified pressure, zero gradient for  $\psi$  and no-slip for velocity. The boundary conditions of electrical potential ( $\Phi$ ) are chosen such that the current density obtained from the system when bubbles are not present in the domain is calculated from Ohm's law, as  $\kappa_1(\Phi_{top} - \Phi_{electrode})/L_{ac}$ , to be equal to 1210.8 A/m<sup>2</sup> which is in the practical range (between 1000-3000 A/m<sup>2</sup>) used in commercially used alkaline electrolyzer systems, see [45].

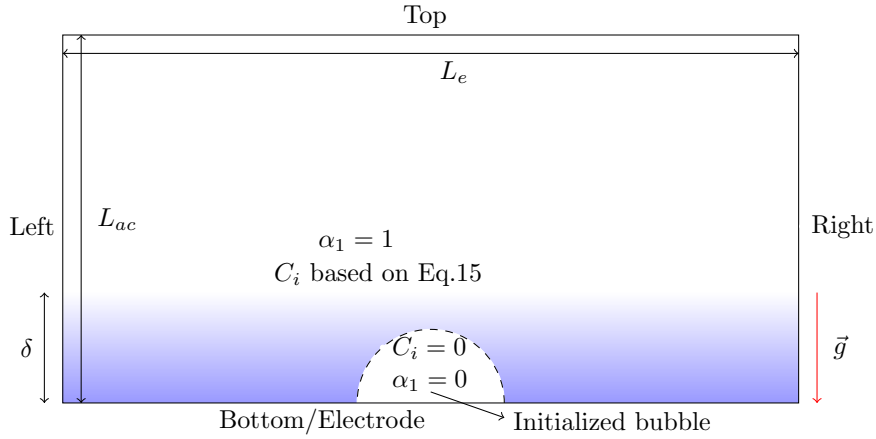


Figure 2: Illustration of computational domain used in the simulations and the initial conditions used in the simulations.

As  $C_i$  indicates the concentration of the dissolved gas which exceeds the saturation condition, which for hydrogen dissolved in water under 1 atm and 25 °C is 0.79 mol/m<sup>3</sup> [46], the concentration boundary layer at the electrode is initialized based on the vertical distance from the electrode ( $y$ ), as shown in

<sup>2</sup>The boundary condition for  $C_i$  at the electrode, which is computed based on Faraday's law of electrolysis, is  $\partial_n C_i = |\vec{v}| \alpha_1 / (nFD_{i,1})$ , where  $n$  is the number of electrons transferred for the electrochemical reaction to produce hydrogen (equal to 2),  $F$  is the Faraday's constant (equal to 96485 As/mol) and  $D_{i,1}$  is the diffusion coefficient of dissolved hydrogen in the liquid.

Table 4: The fluid properties, based on 1atm and 25°C, for Phase 1 (liquid/electrolyte) and Phase 2 (hydrogen bubble) used in the simulations.

Properties	Dimensions	Phase 1	Phase 2
Density ( $\rho$ )	kg/m <sup>3</sup>	1075.05	0.082
Viscosity ( $\nu$ )	m <sup>2</sup> /s	$9.89 \times 10^{-7}$	0.00011
Diffusion coefficient ( $D_i$ )	m <sup>2</sup> /s	$4.80 \times 10^{-9}$	$1 \times 10^{-5}$
Electrical conductivity ( $\Gamma$ )	S/m	30.27	$1 \times 10^{-13}$
Molar mass ( $M_i$ )	kg/mol		$2 \times 10^{-3}$
Surface tension ( $\sigma$ )	N/m		0.072

Fig. 2, such that

$$C_i = \begin{cases} C_{i,y=\delta} & (\text{when } y > \delta), \\ C_{i,y=0} + (C_{i,y=\delta} - C_{i,y=0})y/\delta & (\text{when } y \leq \delta), \end{cases} \quad (15)$$

where  $\delta$  is the concentration boundary layer thickness set to 0.5 mm (see Appendix D),  $C_{i,y=0}$  and  $C_{i,y=\delta}$  is the concentration at the electrode and distance of  $\delta$  (or larger) which is set equal to 125.66 mol/m<sup>3</sup> (based on supersaturation reported in [47]) and 0 mol/m<sup>3</sup> (which corresponds to saturation) respectively. It should be noted that the initialized concentration boundary layer does not account for the depleted concentration of the dissolved gas near the bubble due to interfacial mass transfer across the interface. The single bubble in the domain, which is initialized as in Fig. 2, is located such that its center is 5 mm from the left boundary and 0 mm from the bottom boundary ( $y_c$ ). In the case of two bubbles, used in coalescence studies, with radii equal to  $R_{2a}$  and  $R_{2b}$ , the bubbles are initialized as semicircles such that the centers of the bubbles are a distance of  $5 \times 10^{-3} - R_{2a}$  and  $5 \times 10^{-3} + R_{2b}$  from the left boundary. As the electrodes are horizontal with respect to gravity, which is set as  $|\vec{g}| = 9.81 \text{ m}^2/\text{s}$ , the evolution of the bubble would lead to detachment and subsequent vertical rise due to buoyancy. The fluid properties used in the simulations is described in Table. 4. The computational geometry is meshed by 1600×800 hexahedral cells based on the mesh convergence study in described in Appendix B.

### 3.2. Definition of parameters

Although visual comparison is a very useful tools to interpret the results, to compare various simulations and quantify its results, it is important and easier to use standardized parameters. The standardized parameters which are used in the paper for analyzing the results are defined in this section.

*Normalized bubble volume.* The volume of the bubble at any time ( $V$ ) is calculated as  $\int \alpha_2 dV$  and the corresponding area of the bubble is equal to  $V/h$ , where  $h$  is unit cell thickness. The normalized bubble volume is calculated as the fraction of the computational domain occupied by the bubble ( $f$ ) which is determined as

$$f = \frac{V}{A \times L_{ac}} \quad (16)$$

where  $A$  is the area of the electrode and  $L_{ac}$  is the inter-electrode distance. For the geometry used in the simulation  $A \times L_{ac}$  is equal to  $5 \times 10^{-11} \text{m}^{-3}$ , see Fig. 2.

*Rise velocity.* The mean velocity with which a bubble rises is computed as

$$U_{rise} = \frac{\int \vec{v} \alpha_2 dV}{\int \alpha_2 dV} \quad (17)$$

where  $\vec{v}$  is the vertical component of the velocity vector. The rise velocity, computed based on Eq.17, has been previously used in works like [48] and [21] to study the dynamics of single rising bubble.

*Bubble coverage of electrode.* The fraction of the area of the electrode covered by the bubble is computed as

$$\Theta = \frac{\sum \alpha_2 |\vec{S}|}{\sum |\vec{S}|}, \quad (18)$$

which is computed at the electrode boundary with  $|\vec{S}|$  representing the magnitude of the surface area of the individual mesh cell at the boundary and  $\sum |\vec{S}|$  is the area of the electrode ( $A$ ), which is equal to  $10^{-8} \text{m}^2$ . The fraction of the electrode area in contact with the electrolyte is equal to  $1 - \Theta$ . When the bubble has detached or when the whole electrode is in contact with the electrolyte,  $\Theta$  reduces to zero.



*Bubble detachment.* Based on the temporal variation of  $1 - \Theta$ , the bubble is considered to have detached when  $1 - \Theta > 0.999$  and the corresponding time, which is indicated by  $\tau_d$ , is considered as the detachment time of the bubble.

*Average current.* As the proposed solver computes local current density ( $\vec{i}$ ), the current obtained from the system ( $I$ ) is equal to

$$I = \sum \vec{i} \cdot \vec{S}, \quad (19)$$

which is the sum of dot product of local value of current density and cell area vector of individual mesh at the electrode boundary. For simplicity, a normalized average current ( $I/I_0$ ) is used in this paper which is determined as the ratio of  $I$  to  $I_0$  which is the current obtained when bubbles are absent in the system<sup>3</sup>.

*Bubble deformation.* As the bubble detaches from the surface, it undergoes deformation which is measured horizontally ( $\Delta x$ ) and vertically ( $\Delta y$ ). The horizontal deformation of the bubble at any time step is calculated as the difference between maximum and minimum x coordinates of the interface ( $\alpha_1 = 0.5$ ). Similarly  $\Delta y$  is the difference between maximum and minimum y coordinates of the interface.

#### 4. Verification of the proposed solver

Apart from the verification of the solution with respect to analytical solution for bubble growth in supersaturated solution and qualitative analysis of the variation in current, which is described in this section, the relevant imbalance (mass of liquid/bubble and dissolved gas), mesh and temporal convergence studies have also been performed in Appendix A, Appendix B and Appendix C respectively.

---

<sup>3</sup>Theoretically the current which can be obtained for the applied potential difference is when the system does not have any bubbles can be calculated by substituting relevant values in  $I_0 = \Gamma_1 A (\Phi_{topboundary} - \Phi_{electrode}) / L_{ac}$  which gives  $I_0$  equal to  $1.2108 \times 10^{-5} \text{A}$ .

#### 4.1. Bubble growth in a uniformly supersaturated solution

In order to verify the bubble growth predicted by the proposed solver, the domain, boundary and initial conditions along with the mesh as described in [28] is used. The fluid properties as well as the solution algorithm is based on details summarized in Table. 3 and Table. 4 but both gravity and surface tension effects are ignored. The computational setup describes the growth of hydrogen bubble, with radius equal to 0.25mm, due to the uniform supersaturation of 200.64 mol/m<sup>3</sup> in an unbounded medium. This setup allows for the verification of the result with exact analytical results which was earlier derived by [49] as an extension of the phenomenological work by [50] to account for the size of the pre-existing bubble at  $t = 0$  s. The evolution the bubble radius as it grows due to interfacial mass transfer is given by

$$R_{ext-scriven} = 2\beta \sqrt{D_{i,1} \left( t + \frac{R_0^2}{4D_{i,1}\beta^2} \right)}, \quad (20)$$

where  $\beta$  is the growth coefficient which was proposed by [50] and  $R_0$  is the radius of the bubble at  $t = 0$  s. The growth coefficient for 2D bubbles in a

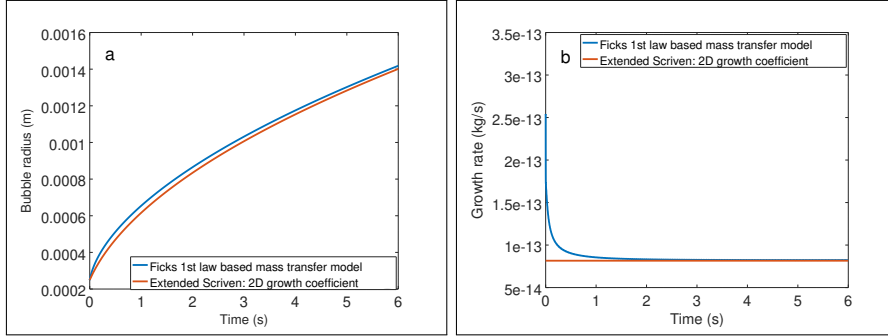


Figure 3: Comparison of the prediction of the proposed solver with the Extended-Scriven model to predict the bubble growth from a pre-existing bubble in a uniformly supersaturated solution: a) Bubble radius b) Growth rate.

uniformly supersaturated unbounded solution is given by

$$\beta_{2D} = \frac{a + \sqrt{a^2 + 4a}}{2\sqrt{2}}, \quad (21)$$

where  $a$  is calculated as

$$a = \frac{M_i \Delta C}{\rho_2}, \quad (22)$$

where  $\Delta C$  is the difference between the bulk concentration of the dissolved gas and the saturation concentration at the interface, equal to  $200.64 \text{ mol/m}^3$  for this case. The radius predicted by the proposed solver is calculated as  $R = \sqrt{V/(\pi h)}$  where  $V$  is defined as in Eq. 16 and growth rate is computed as  $\int \psi_0 dV$ . The bubble radius and growth rate predicted by the proposed solver and the analytical solution is compared in Fig. 3. The small discrepancy between the bubble radius predicted by the simulation and analytical solution is the result of the lack on concentration boundary layer around the interface in the initialized  $C_i$  used in the simulation which causes growth rate which is larger than the corresponding analytical value. This larger growth rate occurs till the concentration boundary layer is established and phenomena becomes diffusion limited, see [28].

#### 4.2. Effect of the bubble on current obtained

The current in a pure electrolyte between two parallel electrodes has vertical path lines. As the bubbles are non-conductive, the current path lines are deformed in its vicinity which causes the increase in resistance and decrease in current under constant potential difference [51]. In a homogeneous medium, the overall resistance is directly proportional to the  $l/A$  where  $l$  is the characteristic length which is equal to  $L_{ac}$  when bubbles are absent in the system. When a bubble is present in the bulk of the electrolyte, the increased resistance is a result of the deformed the path lines of current which causes an increase in  $l$ . Similarly, when bubble is present on the electrode, the electrode-electrolyte area is reduced to  $A(1 - \Theta)$  which results in larger resistance (if  $l$  is constant), than when the bubble is in the bulk. Experimental works, like [52], reported a decrease in current as the bubble grows on the electrode and an increase when the bubble has detached.

In order to showcase the variations in current, fourteen simplified cases with stationary circular (in bulk) and semicircular (on surface) bubbles are investi-

Table 5: The variation of normalised current ( $I/I_0$ ) for various static bubble simulations with positions of the center of the bubble denoted by  $x_c$  and  $y_c$ .

Case	$x_c$ (m)	$y_c$ (m)	$f$	$\Delta x$ (mm)	$\Delta y$ (mm)	$1 - \Theta$	$I/I_0$
TC1a	0.0050	0.0000	0.0051	0.813	0.406	0.92	0.98978
TC1b	0.0050	0.0000	0.0026	0.575	0.288	0.94	0.99487
TC1c	0.0053, 0.0047	0.0000,0.0000	0.0051	1.138	0.288	0.89	0.98329
TC2a	0.0050	0.0003	0.0051	0.575	0.575	1.00	0.99148
TC2b	0.0050	0.0006	0.0051	0.575	0.575	1.00	0.99032
TC2c	0.0050	0.0009	0.0051	0.575	0.575	1.00	0.99002
TC2d	0.0050	0.0012	0.0051	0.575	0.575	1.00	0.98992
TC2e	0.0050	0.0015	0.0051	0.575	0.575	1.00	0.98987
TC2f	0.0050	0.0018	0.0051	0.575	0.575	1.00	0.98985
TC2g	0.0050	0.0021	0.0051	0.575	0.575	1.00	0.98983
TC2h	0.0050	0.0024	0.0051	0.575	0.575	1.00	0.98983
TC3a	0.0050	0.0017	0.0051	0.575	0.575	1.00	0.98986
TC3b	0.0050	0.0017	0.0051	0.578	0.549	1.00	0.98961
TC3c	0.0050	0.0017	0.0102	0.813	0.813	1.00	0.98003

gated. These simulations differ in the initial conditions of  $\alpha_1$ , which are summarized in Table. 5. Except for the case of TC1c, which has two bubbles on the surface hence two coordinates for the centers, all other cases have a single bubble. All the boundaries are treated as described in Section. 3.1 with the exception of electrochemical reaction at the electrode which is replaced with a zero gradient condition to prevent addition of dissolved hydrogen to the electrolyte which can result in bubble growth. Additionally, both surface tension and gravitational forces are neglected in these simplified simulations to ensure stationary bubbles.

The variation of the current ( $I/I_0$ ) when bubbles is present in the bulk, the

smaller bubbles would indicate lesser distortion of the current path lines (giving a smaller value of  $l$ ) which results in larger current ( $I/I_0$ ). This is observed in TC3a when compared to TC3c, see Table. 5. When the bubble is horizontally deformed, which is indicated by larger  $\Delta x$  and smaller vertical deformation ( $\Delta y$ ), when compared to TC3a, the current path lines are further distorted as a result of the larger projected area of the bubble which reduces the current, as observed in TC3b. Interestingly, current increases closer the detached bubble is to the electrode but it reaches an asymptotic value near half of the inter-electrode distance, as observed in cases TC2a-h. This dependence of current on the location of bubble can be understood as the reduction of the effective distance traversed by the current path lines ( $l$ ) when the detached bubble is close to the electrode and shields a part of the electrode as deformed current path lines extends for several bubble radii [51], as seen in Fig. 4.

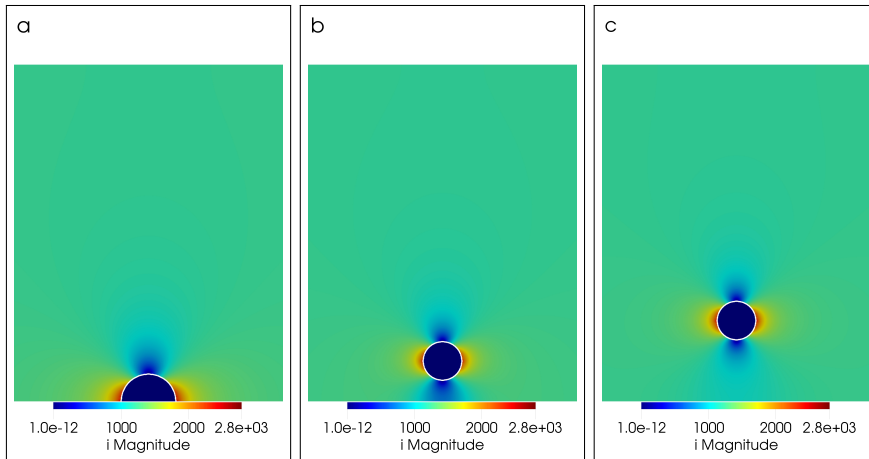


Figure 4: The distribution  $|i|$  for static bubble simulations: a) TC1a b) TC2b and c) TC2d.

When the bubble is attached to the electrode, in TC1a and TC1b, increase in the bubble footprint is observed to reduce the current as result of the covering the electrode (represented by  $A(1 - \Theta)$ ) and deforming the current path lines which has been observed in experiments like [52]. For the same equivalent volume of bubble, the presence of two bubbles, in TC1c, results in a larger fraction

of the electrode covered by the bubble and  $\Delta x$ , which results in reduction of current when compared to TC1a. As the bubble which has detached, TC2a-h, has the same volume as the bubble present on electrode, both TC1a and TC1c, the detachment is observed to result in increase in the current as observed in experimental works like [52].

## 5. Results and discussion

### 5.1. Single bubble evolution

*Effect of contact angle.* The contact angle is an important parameter which has been experimentally observed to effect the bubble detachment [5]. Larger the value of contact angle ( $\theta$ ), measured in the liquid, less hydrophilic the electrode surface becomes which leads to difficulty in the bubble detachment. The wetting condition at the electrode is investigated with three cases: SCT0, SCT1, and SCT2 which differ by the contact angle ( $\theta$ ) defined at the electrode which is equal to  $15^\circ$ ,  $30^\circ$  and  $45^\circ$  respectively.

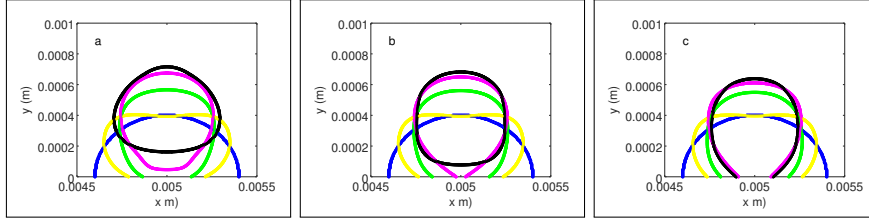


Figure 5: The evolution of the bubble (isosurface of  $\alpha_1 = 0.5$ ) at 0s (—),  $5 \times 10^{-4}$ s(—),  $1 \times 10^{-3}$ s(—),  $1.5 \times 10^{-3}$ s(—) and  $2 \times 10^{-3}$ s(—) for the various wetting condition at the electrode: (a)  $15^\circ$  in SCT0, (b)  $30^\circ$  in SCT1, and (c)  $45^\circ$  in SCT2.

As shown in Fig. 5, the bubble detaches in the cases of SCT0 and SCT1 whereas it remains adhered to the electrode for the case of SCT2. As the initialized bubbles for all three cases are of radius equal to  $400 \mu\text{m}$ , gravitational force can be ruled out as the reason for the observed detachment. The detachment, observed in the simulation, is a result of the momentum induced as a result of deformation wave travelling at the interface due to the difference between the contact angle of the initialized bubble and the equilibrium contact

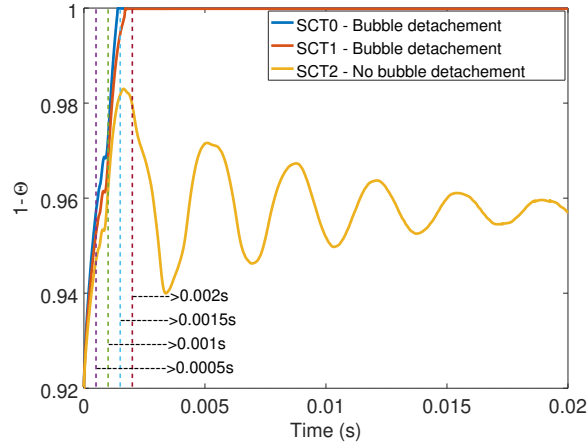


Figure 6: Temporal change in the fraction of area of the electrode in contact with the electrolyte ( $1 - \Theta$ ) as the bubble evolves in SCT0 ( $\theta = 15^\circ$ ), SCT1 ( $\theta = 30^\circ$ ) and SCT2 ( $\theta = 45^\circ$ ). The timesteps at which the isosurface of  $\alpha_1 = 0.5$  is extracted to plot Fig. 5 is illustrated using vertical dashed lines.

angle at the electrode. As all three simulations start with the same initial bubble of radius equal to  $400 \mu\text{m}$  and a contact angle of  $90^\circ$ , the momentum induced for SCT0 would be larger compared to the other two cases (as a result of larger deviation between the initial and equilibrium conditions). In the cases of SCT0 and SCT1, the bubble is able to detach as the initial momentum causes a 'lift' which overcomes adhesion due to surface tension. The initial momentum in SCT2 causes the bubble to deform and lift, until around  $0.0016 \text{ s}$  which is when  $1 - \Theta$  is minimum (see Fig. 6), but the bubble does not detach and subsequently surface tension pulls the bubble down in an attempt to reach the equilibrium shape based on the wetting condition. This dynamic process continues until the bubble reaches an equilibrium shape which is dictated by the surface tension and gravitational force which is observed in damping of  $1 - \Theta$  with time, observed in Fig. 6. Although bubble detachment is observed for both SCT0 and SCT1, the initial momentum imparted to the bubble is larger for the former which results in a smaller  $\tau_d$ , see Table. 6.

For the case of SCT0, the detachment of the bubble results in its deformation

Table 6: The variation of detachment time ( $\tau_d$ ) of the bubble from the electrode surface for various contact angles.

	SCT0 ( $\theta = 15^\circ$ )	SCT1 ( $\theta = 30^\circ$ )	SCT2 ( $\theta = 45^\circ$ )
$\tau_d$	0.00138 s	0.00169 s	No detachment

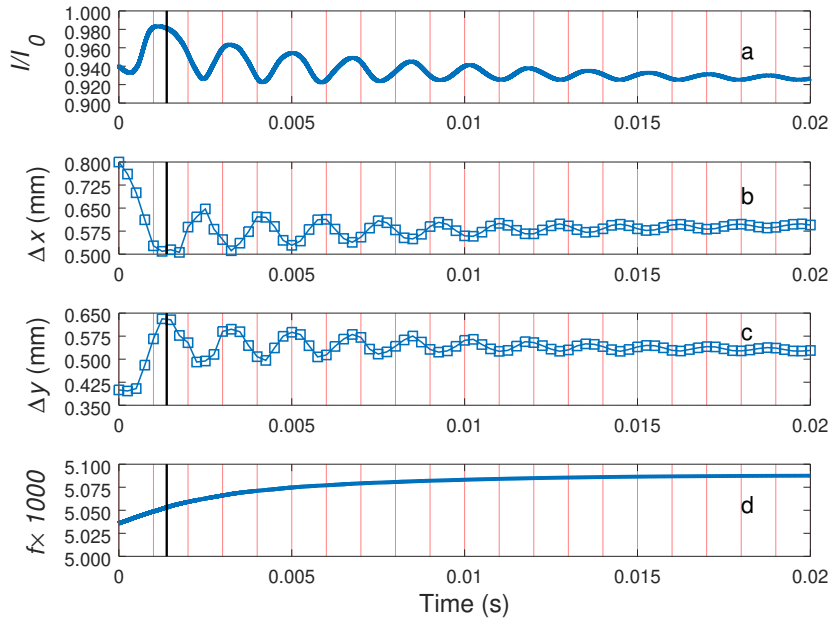


Figure 7: The temporal variation of various relevant parameters during bubble detachment in SCT0 ( $\theta = 15^\circ$ ): a) normalized current ( $I/I_0$ ), b) horizontal deformation ( $\Delta x$ ), c) vertical deformation ( $\Delta y$ ), d) normalized volume of bubble ( $f$ ). The vertical black line indicates the detachment time,  $\tau_d$ , and the vertical red lines are equidistant grid line at every 0.001s to enable comparison between the plots.



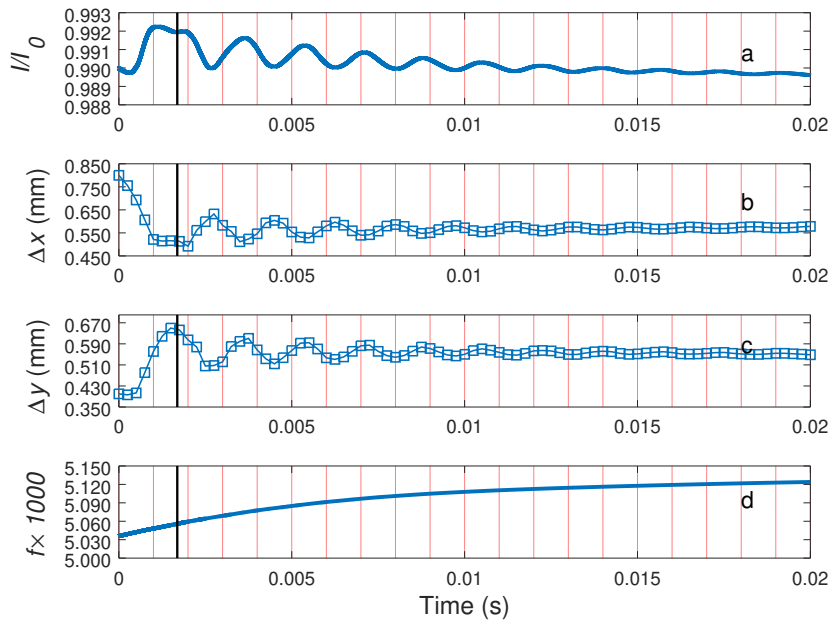


Figure 8: The temporal variation of various relevant parameters during bubble detachment in SCT1 ( $\theta = 30^\circ$ ): a) normalized current ( $I/I_0$ ), b) horizontal deformation ( $\Delta x$ ), c) vertical deformation ( $\Delta y$ ), d) normalized volume of bubble ( $f$ ). The vertical black line indicates the detachment time,  $\tau_d$ , and the vertical red lines are equidistant grid line at every 0.001s to enable comparison between the plots.

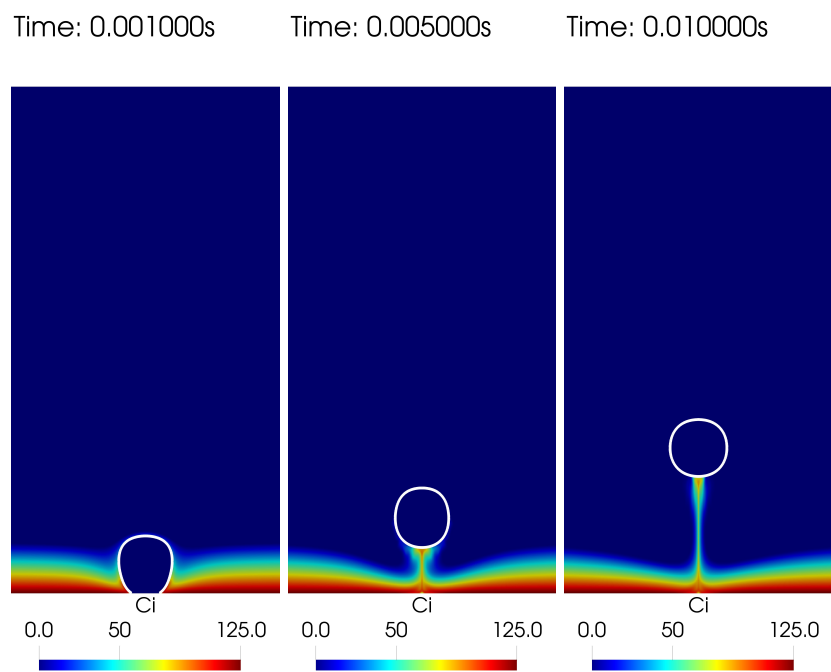


Figure 9: The change in the dissolved hydrogen concentration ( $\text{mol}/\text{m}^3$ ) as the bubble evolves in the case of SCT0. The white line represents the interface which is plotted at  $\alpha_1 = 0.5$ . See supplementary materials for more information.

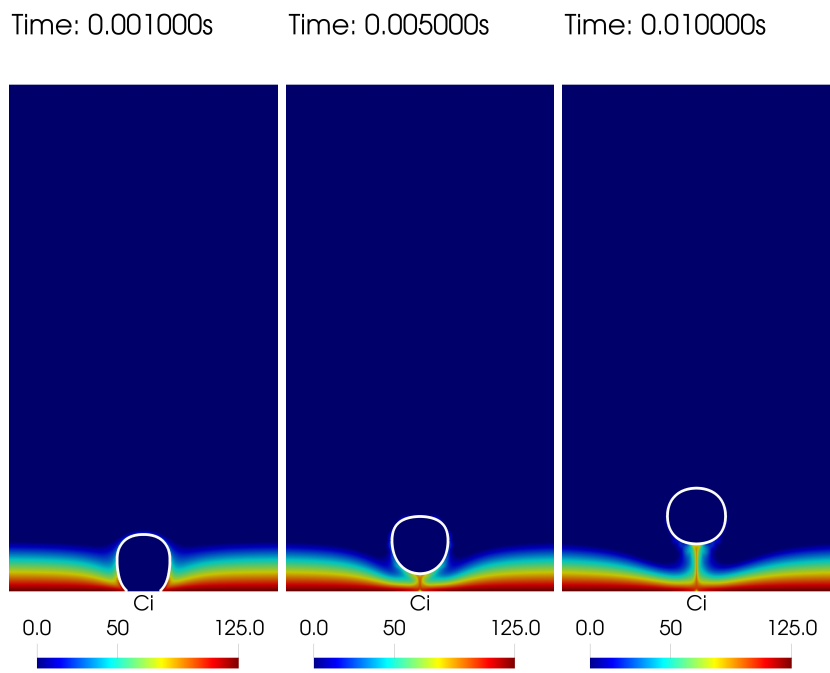


Figure 10: The change in the dissolved hydrogen concentration ( $\text{mol/m}^3$ ) as the bubble evolves in the case of SCT1. The white line represents the interface which is plotted at  $\alpha_1 = 0.5$ . See supplementary materials for more information.

and growth as it rises up through the concentration boundary layer, as shown in Fig. 5. This deformation and growth results in temporal variations of current, see Fig. 7. Before the bubble detaches, the bubble gets lifted and vertically elongated due to the initially imparted momentum, see Fig. 5, this results in increasing  $\Delta y$  and decreasing  $\Delta x$ . The increase in current before detachment is a direct consequence of the reduction of the electrode region covered by the bubble (indicated by  $1 - \Theta$ ) which reduces from the initial bubble diameter of 0.8mm to nearly half at detachment, see Fig. 7c. As a result of the bubble leaving the surface, the current increases by around 0.2% from  $t = 0$ s to the detachment. Once the bubble detaches, the bubble shape oscillates i.e. it first gets flattened (larger  $\Delta x$ ) and then gets elongated (larger  $\Delta y$ ), see Fig. 7b-c. These oscillations progressively gets damped as the bubble rises up. As the bubble gets flattened, the projection of the bubble on the electrode becomes larger which yields lower current in contrast to vertical elongation when projection is reduced and current increases, see Fig. 7b-c. The existence of surface oscillations as bubbles rise were also experimentally reported in detached bubble (in the order of few hundred micrometers) in the work by [53]. Similar trends, in the variation between bubble deformations and current, is also visible for the bubble evolving in SCT1 (see Fig. 8). Instead of the single peak in  $I/I_0$  near detachment observed for SCT0, SCT1 produces an additional peak around 0.002s which is a consequence of the detached bubble staying close to the electrode for longer than SCT0 due to the smaller rise velocity, see Fig. 11. The rise velocities of SCT0 and SCT1, see Fig. 11, show substantial difference after detachment due stronger surface tension force in the latter case. As a result, the bubble in SCT1 rises up mostly due to buoyancy where as in SCT0 the momentum 'left-over' after detachment also aids in the evolution. Apart from the variation of current due to bubble detachment and deformation, as the bubble rises, the current also reduces with the vertical distance from the electrode, which agrees with the observations in Table. 5. Although both SCT0 and SCT1 produce larger current at detachment, when compared to the current at  $t = 0$  s, the current reduces as a result of increase in the  $\Delta x$  and  $f$  once the bubble has detached, as well as the reduction

in current observed in vertical distance.

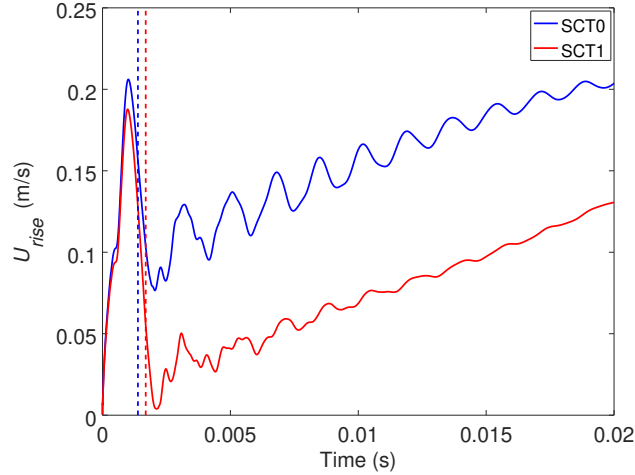


Figure 11: The temporal variation of the rise velocity for SCT0 ( $\theta = 15^\circ$ ) and SCT1 ( $\theta = 30^\circ$ ) with the detachment time ( $\tau_d$ ) represented using dashed lines (blue for SCT0 and red for SCT1).

Due to the quick ascent of the bubble in SCT0, through the concentration boundary layer, the increase in the volume of the bubble is larger for SCT1 when compared to SCT0, see Fig. 7d and Fig. 8d. Although the growth of the bubble occurs when it is within the concentration boundary layer, its effect on current is visible only when bubble surface oscillations have damped, see Fig.E.24a-b. Due to the larger rise velocity in SCT0 compared to SCT1, the drag force acting on the rising bubble in the former is larger which results in a bigger  $\Delta x$  and consequently a smaller current, see Table. 7. As the bubble detaches from the electrode surface, the convection established seems to drag the dissolved hydrogen in the concentration boundary layer in the wake of the rising bubble as observed in Fig. 9 and Fig. 10.

In the case of SCT2, the initially imparted momentum causes the bubble to deform and reach an equilibrium shape which influences the current. In this attempt to reach equilibrium shape,  $1 - \Theta$  increases and the effective radius of the bubble shielding the electrode (indicated by  $\Delta x$ ) effectively reduces causing

Table 7: Comparison of the time averaged bubble deformations and current obtained for SCT0 and SCT1.

Case	$\overline{\Delta x}$ (mm)	$\overline{\Delta y}$ (mm)	$\bar{I}/I_0$
SCT0	0.586	0.537	0.98996
SCT1	0.572	0.553	0.99046

current to increase, see Fig. 12a-b. The change in the bubble size is reflected in the transition of  $\Delta x$  from 0.8mm initially to a more elongated bubble towards the end of the simulation, reducing  $\Delta x$ . As the bubble remains within the concentration boundary layer, in this case, its growth is larger compared to SCT0 and SCT1 cases. In spite of the larger growth rate in SCT2, the effect on current is visible only towards the latter part of the simulation when the bubble deformations has damped, see Fig. E.24c. It should be noted that in the case of SCT2, as the bubble remains on the electrode, the convection in this case is different from SCT0 and SCT1 which is reflected in the concentration distribution of the dissolved gases, see Fig. 13.

*Effect of the initial concentration boundary layer thickness.* In order to study the influence of the concentration boundary layer thickness, set as  $\delta = 0.5\text{mm}$  in the previous simulations, three different cases which differ only by the values of  $\delta$  is used: SCT1 ( $\delta = 0.5\text{mm}$ ), SCT1BL- ( $\delta = 0.3\text{mm}$ ) and SCT1BL+ ( $\delta = 0.8\text{mm}$ ). The contact angle at the electrode as well as other computational setting are set based on SCT1. The initialized distribution of the dissolved gas concentration used in these three simulations is based on Eq. 15.

As the bubble travels through the concentration boundary layer, it grows due to interfacial mass transfer driven by local supersaturation. As larger concentration boundary layer thickness represents a greater region which is supersaturated, the largest growth is observed in SCT1BL+ (equal to 0.8mm) followed by SCT1 (equal to 0.5mm) and SCT1BL- (equal to 0.3mm) with an increase in bubble volume of around 4%, 1.5% and 0.5% of the initial bubble volume. The effect of the increase in the bubble volume on current is only visible when the

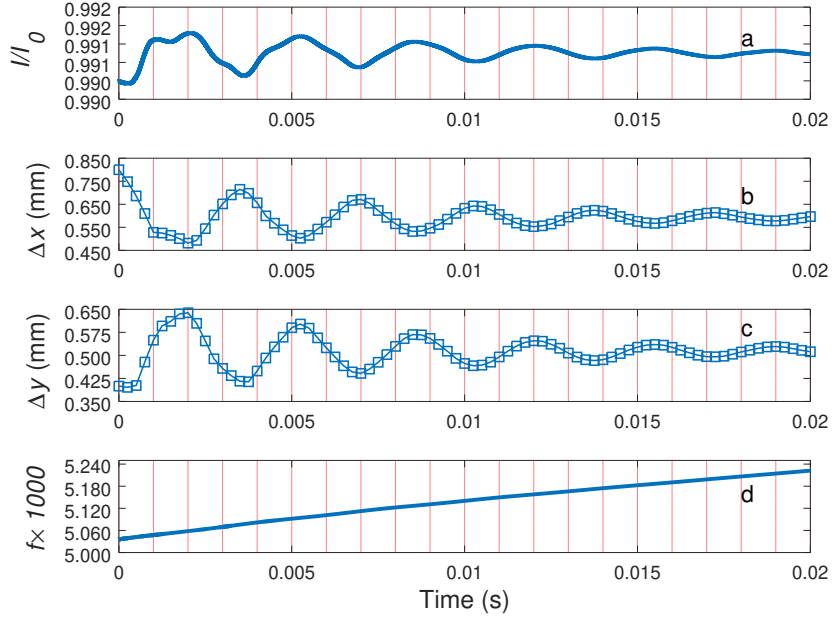


Figure 12: The temporal variation of a) normalized current ( $I/I_0$ ), b) horizontal deformation ( $\Delta x$ ), c) vertical deformation ( $\Delta y$ ), d) normalized volume of bubble ( $f$ ) for SCT2 ( $\theta = 45^\circ$ ) as the bubble deforms on the electrode surface. The vertical red lines are equidistant grid line at every 0.001s to enable comparison between the plots.

bubble deformations has damped, see Fig. 14a. Despite the increase in bubble volume, its effect on rise velocity of the bubble and detachment time is mostly negligible, see Fig. 14.

### 5.2. Coalescence driven bubble evolution

As observed in the static bubble simulations, the presence of two bubbles on the electrode which produces a single detached bubble provides a larger increase in current when compared to a single bubble of equivalent volume detaching, see Table. 5. In order to investigate the dynamic effect of the coalescence of continuum scale hydrogen bubbles, two cases, DC1 and DC2, in which bubbles are initialized based on Table. 8 such that the  $x_c$  of the bubbles are offset by

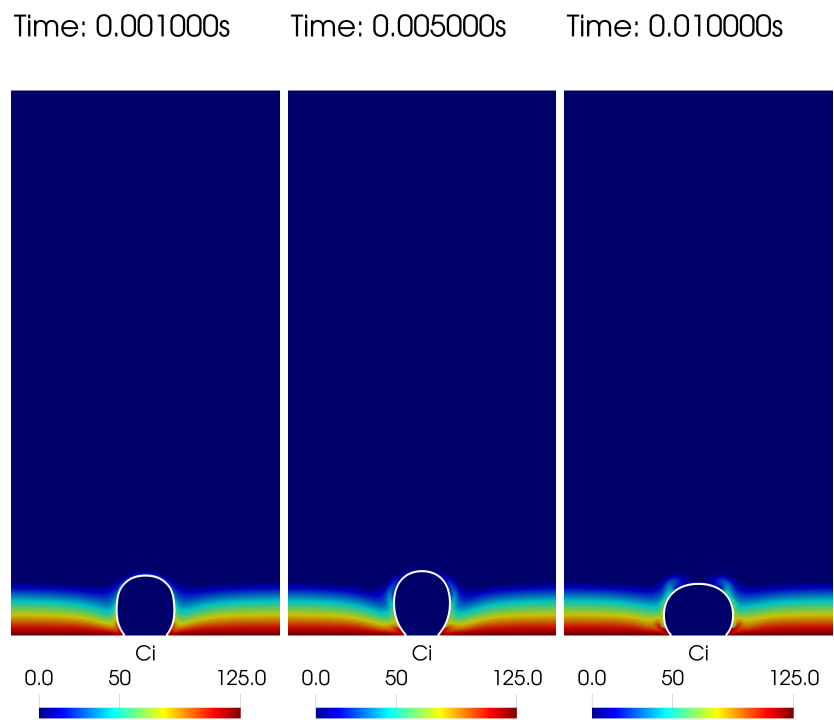


Figure 13: The change in the dissolved hydrogen concentration ( $\text{mol}/\text{m}^3$ ) as the bubble evolves in the case of SCT2. The white line represents the interface which is plotted at  $\alpha_1 = 0.5$ . See supplementary materials for more information.



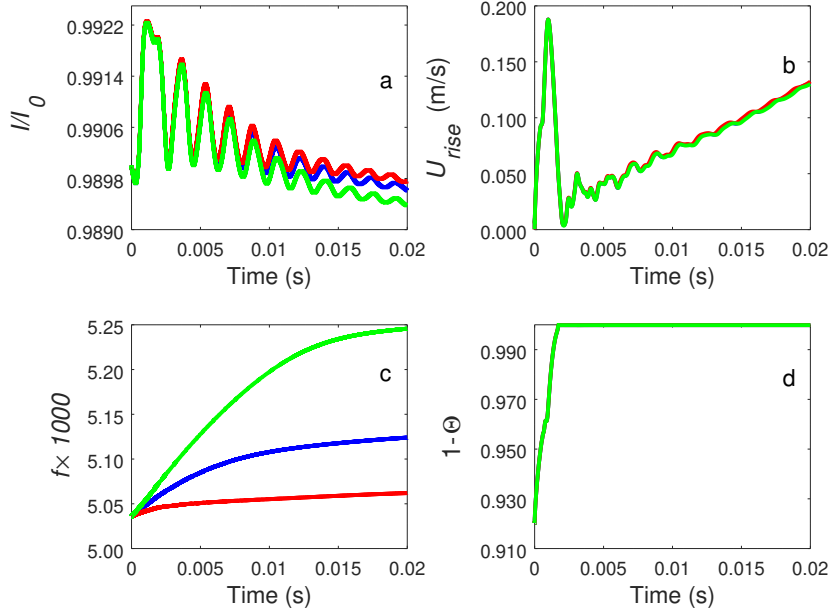


Figure 14: Comparison of a)  $I/I_0$ , b) rise velocity and c) normalized bubble volume ( $f$ ), d)  $1 - \Theta$  obtained for bubble evolution with a contact angle at the electrode set at  $30^\circ$  but the initialized concentration boundary layer thickness is varied from SCT1BL- ( $\delta = 0.3\text{mm}$  indicated with —), SCT1 ( $\delta = 0.5\text{mm}$  indicated with —) and SCT1BL+ ( $\delta = 0.8\text{mm}$  indicated with —).

the radius from  $x = 5\text{mm}$ . The boundary conditions are set analogous to single bubble evolution from the electrode with  $\theta = 45^\circ$ , i.e. SCT2.

Contrary to the single bubble in SCT2 which remained adhered to the surface, both DC1 and DC2, under identical wetting conditions at the electrode, show detachment of the coalesced bubble, see Fig. 15 and Fig. 16. Although the difference between the initialized contact angle of the bubble and the equilibrium wetting condition at the electrode provides some initial momentum, like the case of SCT2, the coalescence process of the bubbles is the driver of the bubble detachment. During coalescence, the surface tension acts to minimize the surface area of the bubbles, which results in dynamic changes in the interface

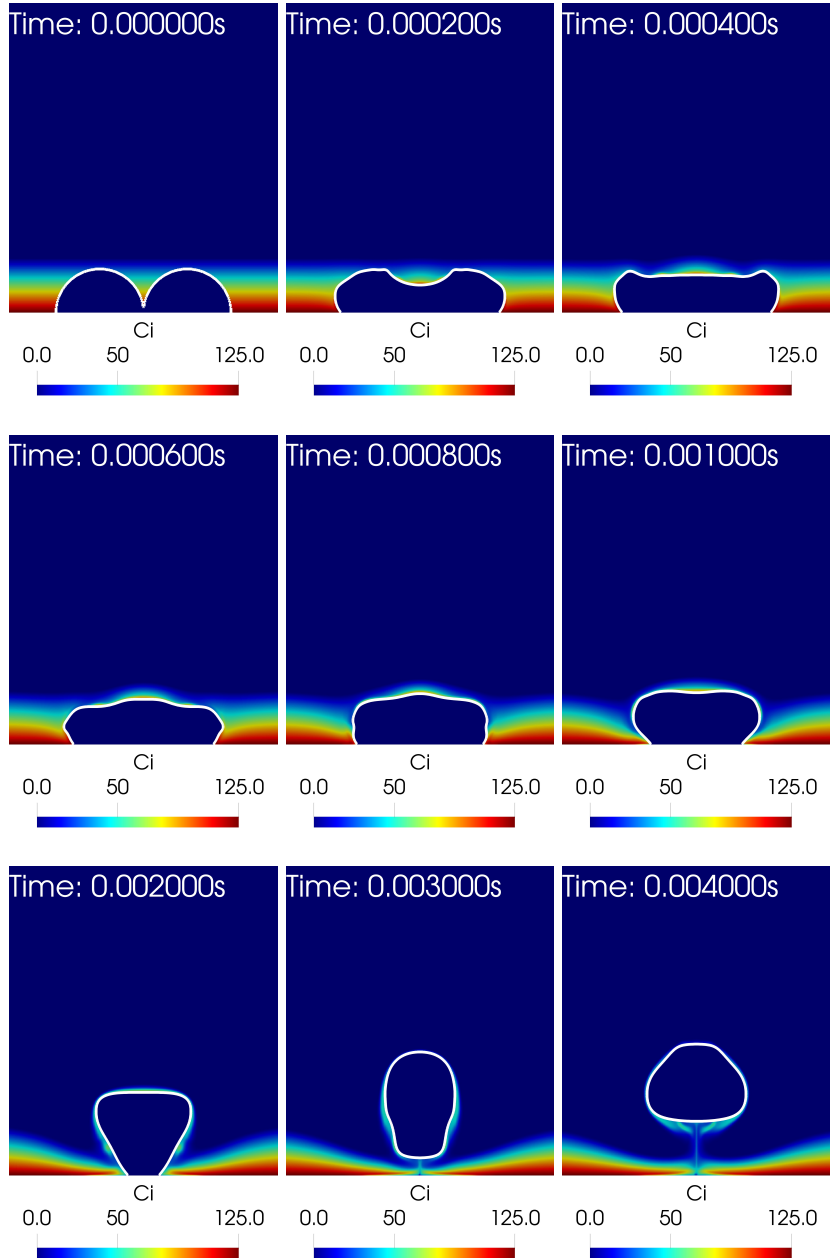


Figure 15: The evolution of the interface and the concentration of the dissolved gas ( $\text{mol/m}^3$ ) as the bubble coalescence and evolves in the case of DC1. Note the necking process (between 0s-0.4ms), propagation of deformation waves along the bubble interface which leads to the lifting of the bubble (between 0.6ms-2ms) and detachment as well as the oscillations of the bubble surface leading to elongation and flattening (2ms-4ms). The white line represents the interface which is plotted at  $\alpha_1 = 0.5$ . See supplementary materials for more information.

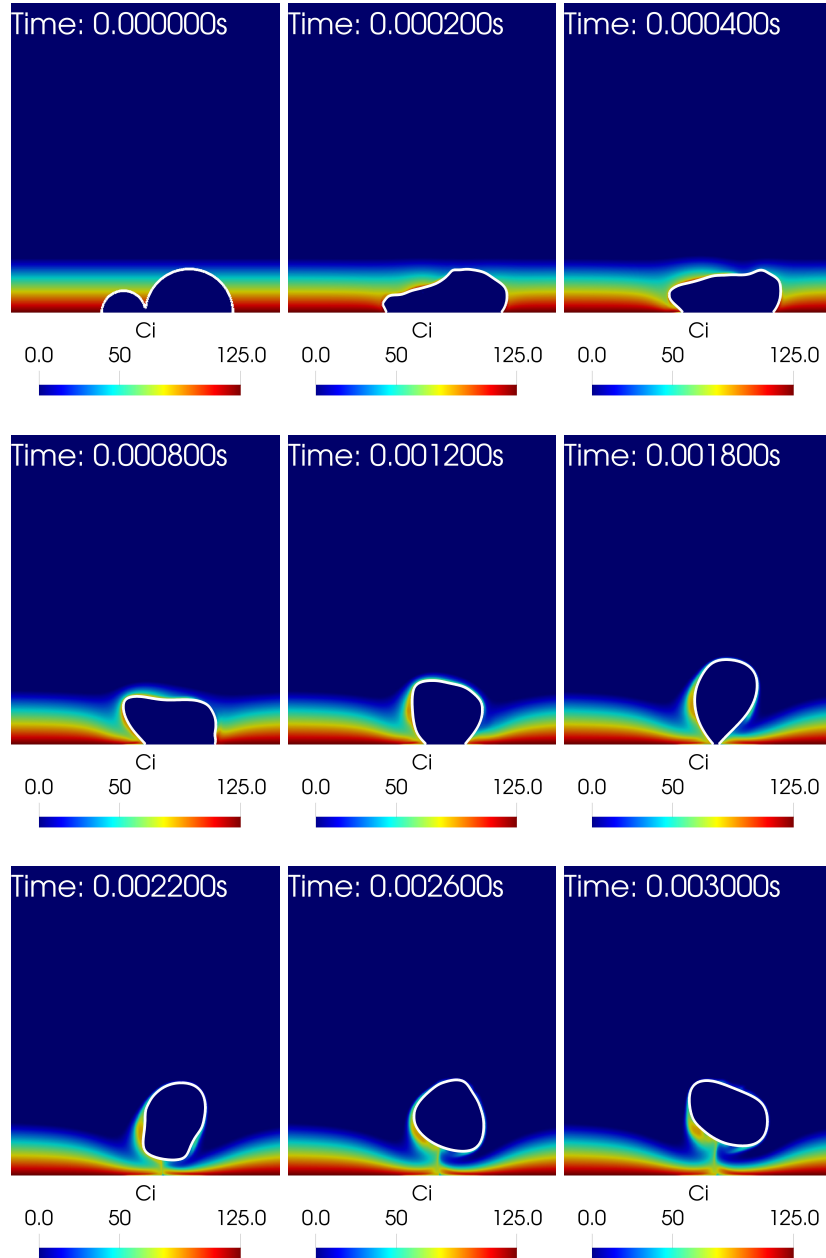


Figure 16: The evolution of the interface and the concentration of the dissolved gas ( $\text{mol/m}^3$ ) as the bubble coalescence and evolves in the case of DC2. Note the necking process (between 0s-0.2ms), propagation of deformation waves along the bubble interface which leads to the lifting of the bubble (between 0.4ms-1.2ms) and detachment as well as the oscillations of the bubble surface leading to elongation and flattening (1.8ms-3ms). The white line represents the interface which is plotted at  $\alpha_1 = 0.5$ . See [36](#) supplementary materials for more information.

Table 8: The initialized bubbles used in the coalescence simulations.

Case	Bubble 1		Bubble 2		$f$	$1 - \Theta$
	$x_c$ (mm)	$y_c$ (mm)	$x_c$ (mm)	$y_c$ (mm)		
DC1	0.0046	0.0000	0.0054	0.0000	0.0101	0.84
DC2	0.0048	0.0000	0.0054	0.0000	0.0063	0.88

which can be categorized into neck formation between the bubbles, deformation wave propagation at the interface which results in the lifting of the bubble, detachment of the bubble and the oscillations in bubble shape, see Fig. 15 and Fig. 16. These stages during coalescence has also been observed during the in the the experimental work by [53], using two equally sized bubbles of radii equal to 0.3mm. The deformation waves, which are qualitatively analogous to the ones observed in the second stage of the bubble coalescence in DC1 and DC2 in Fig. 15 and Fig. 16, are reported to be capillary waves in the work by [53]. In DC1, as these deformation waves are symmetric about  $x = 5\text{mm}$ , see Fig. 15, the detached bubble is also symmetric about the same axis. On the other hand, the asymmetric propagation of the deformation wave towards the smaller bubble in DC2, see Fig. 16, results in translation of the detached bubble along the electrode. Interestingly the deformation induced during coalescence in DC2 results in a quicker detachment of the final bubble compared to DC1 in spite of the larger bubble volume in the latter, see Fig. 17 and Fig. 18. The detachment of bubble in the DC1 and DC2 yields larger current when compared to when the two bubbles where present on the electrode, see Fig. 17a and Fig. 18a. Before detachment, as surface tension attempts to reduce the surface area of the bubble via coalescence,  $\Delta x$  reduces until detachment as shown in Fig. 15 and Fig. 16. The deformation of the detached bubble also has a substantial impact on the current obtained i.e. larger projection of the bubble on the electrode, indicated by larger  $\Delta x$ , results in lower current. It should also be pointed out that, during the coalescence driven bubble evolution in DC1 and DC2 the bubble grew by around 0.97% and 1.34% when compared to the initial bubble

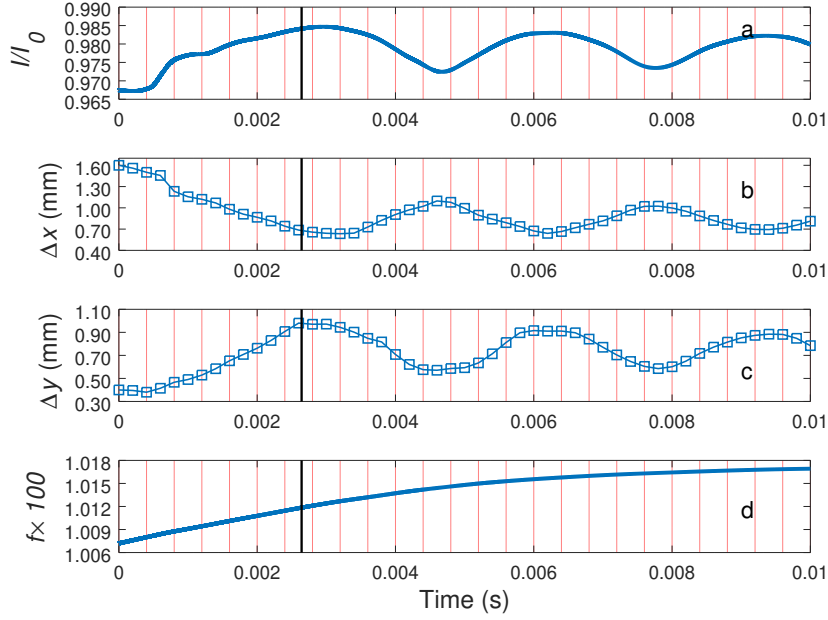


Figure 17: The temporal variation of various relevant parameters as two equally sized bubbles coalescence and detachment in DC1: a) normalized current ( $I/I_0$ ), b) horizontal deformation ( $\Delta x$ ), c) vertical deformation ( $\Delta y$ ), d) normalized volume of bubble ( $f$ ). The vertical black line indicates the detachment time,  $\tau_d$ , and the vertical red lines are equidistant grid line at every 0.0004s to enable comparison between the plots.

volume respectively. The difference in the growth rate between the two cases is a result of larger amount of dissolved gas which is present near the detached bubble in DC2, see Fig. 15 and Fig. 16, due the convection established during the coalescence and detachment.

## 6. Conclusion

In this paper, a new Volume of Fluid (VOF) based framework to study the continuum scale evolution of hydrogen bubble in an electrochemical system is presented. The proposed framework is based on the VOF framework available in OpenFOAM<sup>®</sup> 6, which uses an algebraic VOF method to capture the interface.

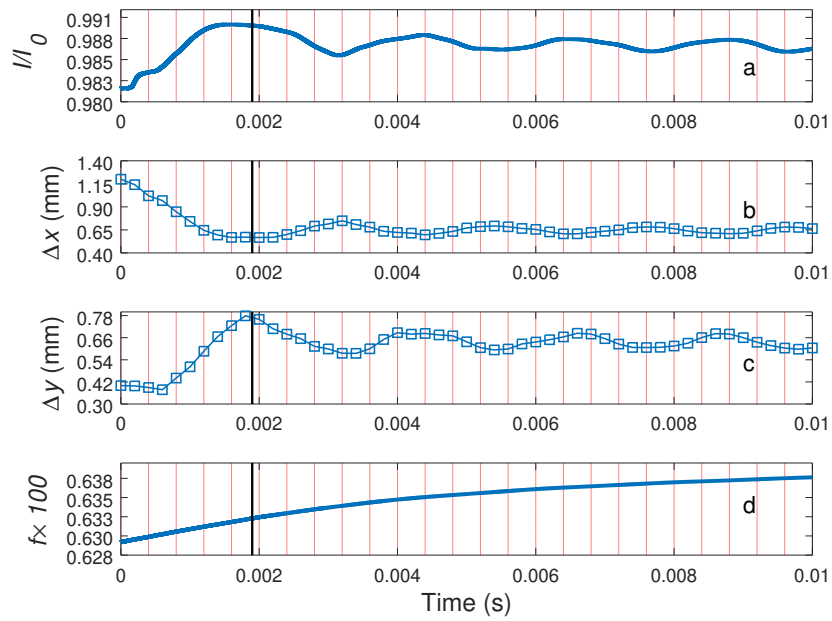


Figure 18: The temporal variation of various relevant parameters as two unequally sized bubbles coalescence and detachment in DC2: a) normalized current ( $I/I_0$ ), b) horizontal deformation ( $\Delta x$ ), c) vertical deformation ( $\Delta y$ ), d) normalized volume of bubble ( $f$ ). The vertical black line indicates the detachment time,  $\tau_d$ , and the vertical red lines are equidistant grid line at every 0.0004s to enable comparison between the plots.

The transport of the dissolved gas is based on the Compressive Continuous Species Transport model [27], the driving force for interfacial mass transfer is based on the phenomenological Fick's 1<sup>st</sup> law and relevant source terms are computed based on [28], charge conservation is ensured using Gauss's law and Ohm's law [31] and surface tension modelled as described by [21]. The proposed solver is verified by comparison to the analytical solution for bubble growth in a uniformly supersaturated unbounded medium by [49] which is based on the landmark work by [50]. Additionally the variation of the current predicted by the solver is compared qualitatively to reported observations in experiments like [52].

The single bubble simulations showed that the observed detachment of the bubble is a result of the deviation between the contact angle of the initialized bubble and the wetting condition at the horizontal electrode. In order to accurately simulate the process, hybrid VOF methods like [31, 32, 33] are required to generate larger bubbles which are consistent with the electrode wetting conditions. Regardless, single bubble simulations showed quicker bubble detachment with smaller contact angles as a result of the stronger hydrophilic nature of the surface. When the bubble is present on the surface, the reduction in the area of the bubble covering the electrode is observed to increase the current. At detachment, the current obtained is larger than at the initial state of the system. Once the bubble has detached, the surface of the bubble is observed to show oscillations which causes the bubble to flatten and elongate analogous to the experimental observations by [53]. These deformation of the bubble cause the variation in the current i.e. larger horizontal deformation ( $\Delta x$ ), which means larger projected area of the bubble, results in lower current due to the larger distortion of the current path lines. These distortions in the current pathlines are observed for several bubble radius as shown previously by [51]. Interestingly, the current is observed to decrease as it rises up, after the detachment. This can be explained as the result of the reducing the effective resistance by lowering the characteristic length experienced by the current pathlines as the detached bubble close to the electrode still shields part of the electrode, see Fig. 4.

As the bubble rises up, the bubble shape is dictated by the surface tension and drag forces which means that a bubble with higher rise velocity tends to be flatter or has a larger  $\Delta x$  which produces less current, see Table. 7. As the bubble evolves, in the cases it detaches, the convection established by the rising bubble also drags some dissolved gas up with it, see Fig. 9 and Fig. 10. Although the bubble drags the dissolved gas as it rises up, the bubble grows predominately within the concentration boundary layer. The effect of the bubble growth is not visible in detachment time and rise velocity but it has a noticeable effect on current evolution only when the bubble surface oscillations have damped, see Fig. 14 and Fig. E.24.

The coalescence driven bubble detachment shows an increase in current as bubble detaches and rises up, see Fig. 17 and Fig. 18, when compared to a single bubble simulations, see Fig. 7 and Fig. 8. This larger increase in current in coalesce driven detachment is a result of value of higher value of  $1 - \Theta$  at  $t = 0s$  when compared to single bubble simulations. In the coalescence driven case, the current is also observed to vary with the bubble deformation, see Fig. 17 and Fig. 18. Simulations considering the coalesce of two bubbles show three distinct regimes: necking, propagation of the deformation waves, and detachment of the bubble, which has also been reported in the work by [53]. The simulations also shows the existence of travelling deformation waves at the interface, observed by [53]. The propagation of these deformation waves is found to influence the detachment process, as observed in the quicker detachment of the DC2 which has a smaller bubble compared to DC1, as well as causes the translation of the detached bubble along the electrode. The simulations suggests that the bubble detachment, at least for continuum scale bubbles, are primarily driven by coalescence rather than bubble growth by interfacial mass transfer.

#### **Declaration of interest**

The authors declare that they have no known competing monetary/personal interests which would influence the work reported in this paper.



## Acknowledgement

The authors would like to acknowledge the Department of Material Science and Engineering, NTNU, for funding this research and UNINETT Sigma2 for providing necessary computational resources through grant NN9741K.

## Appendix A. Imbalance in liquid/bubble and dissolved gas

As the proposed framework treats the growth and evolution of a bubble, based on Eq.6, the volume of liquid should in principle remain constant in the simulation. Fig. A.19 shows the imbalance in the liquid/bubble during the simulation to be much lower than 0.1%. The imbalance in the amount of dissolved gas is due to the presence of dissolved gas in the bubble, this is lower than 0.1% of the dissolved gas in the computational domain (which is always around  $2.9 \times 10^{-10}$  mol despite the addition of dissolved gas via electrochemical reactions), see Fig. A.20.

## Appendix B. Spatial convergence

As the proposed framework, which is based on the Finite Volume Method, relies on the mesh to discretize the governing equations, it is important to ensure that the solution is not independent of these errors. In order to study the mesh convergence of the solution, for the case of SCT1, is studied using six different meshes:  $400 \times 200$ ,  $564 \times 282$ ,  $800 \times 400$ ,  $1128 \times 564$ ,  $1600 \times 800$  and  $2256 \times 1128$  which represents 32, 45, 64, 90, 128 and 180 cells across the diameter of the initialized bubble respectively. The grid convergence is studied by comparing the bubble shape ( $\alpha_1 = 0.5$ ) at 0.02s in Fig. B.21. As the variation between the bubble shapes for the finest two meshes are negligible,  $1600 \times 800$  is used in the simulations considered in the paper. Additionally, the difference in the current obtained between the two finest meshes,  $1600 \times 800$  and  $2256 \times 1128$ , at 0.02s is less than 0.01%.

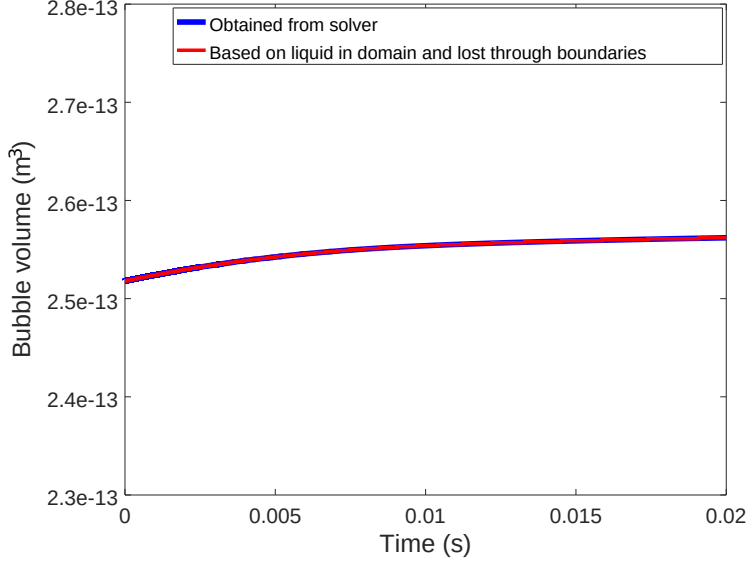


Figure A.19: Temporal variation of the mass imbalance in the system indicated as the bubble volume obtained from the solver (equal to  $\int \alpha_2 dV$ ) and the difference in the total volume of the domain and the volume of liquid present in the domain which is adjusted for the liquid lost through the boundaries.

### Appendix C. Temporal convergence

As surface tension is dominant in the electrochemical bubble evolution phenomena, its modelling can be influenced by the well known problem of spurious velocities in VOF based methods [18, 20, 21]. These spurious velocities which are numerical artifacts can result in non-physical flow velocities/deformations of the interface can reduce the accuracy of the simulation as observed in [54, 28, 44]. These spurious velocities are generated in the proposed solver due to inaccuracies in the curvature calculation used in surface tension modelling, see [44]. As the surface tension is treated explicitly in the proposed solver, the spurious current in the simulation can increase over time if an appropriate time step is not used which would lead to a dependence of the solution on time step [18, 21]. The most commonly used time step constraint which is used to prevent the

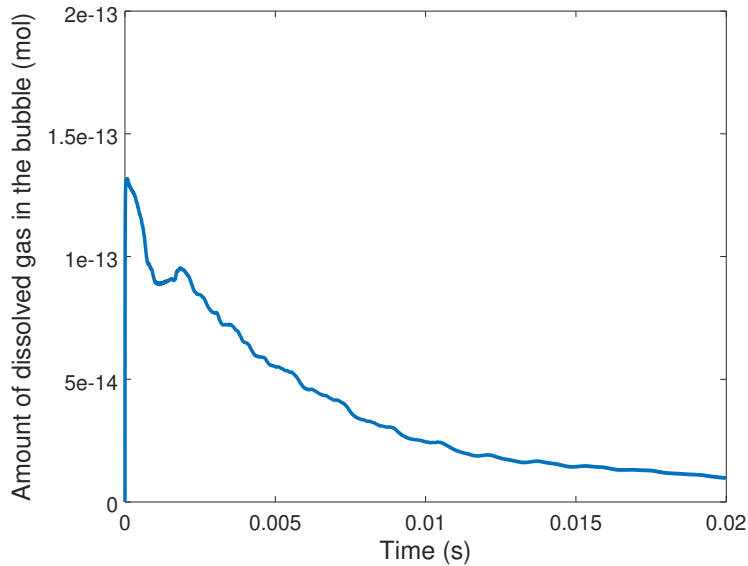


Figure A.20: Temporal variation of the amount of dissolved gas in the bubble which is calculated as  $\int C_i \alpha_2 dV$ .

growth of these spurious velocities, is the one proposed by [41]:

$$\Delta t < \sqrt{\frac{\rho_{avg} \Delta_x^3}{2\pi\sigma}}, \quad (\text{C.1})$$

where  $\Delta_x$  is the mesh cell size and  $\rho_{avg}$  is the average density between the two phases. In order to ensure the simulations discussed in the paper are not influenced by spurious velocities, the predictions of the proposed solver for SCT1 and SCT2 cases (due to the lower rise velocity when compared to SCT0) are compared with maximum time step based on Courant number of 0.05 and Eq. C.1, which is equal to  $5.25 \times 10^{-7}$  s.

Comparison of  $I/I_0$ , rise velocity, normalized bubble volume and bubble coverage for SCT1 and SCT2, see Fig. C.22 and Fig. C.23, shows that the time step resolution does not result in much change to these parameters for the duration of the simulation. This can be explained by understanding the velocity field induced by the motion of the interface to be much larger than the

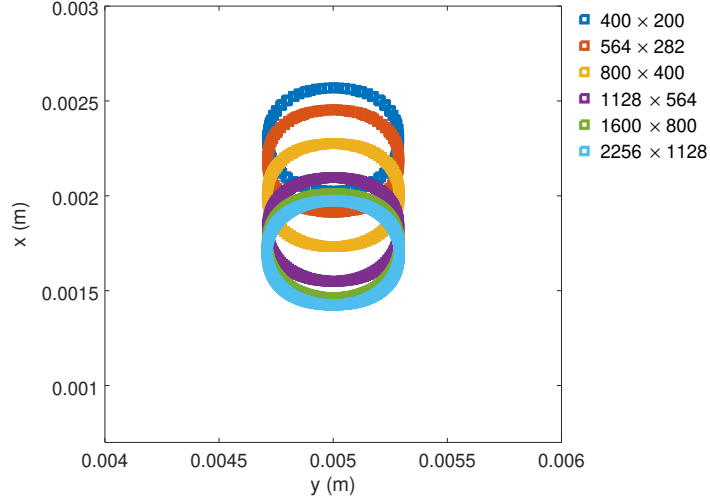


Figure B.21: The interface of the bubble at 0.02s for SCT1 for the six meshes considered in the convergence study.

nonphysical velocity field generated by the spurious velocities. As a result, in the case of SCT1, the time step constraint can be ignored to obtain reasonable results and to save the computational overhead imposed Eq. C.1. For the case of SCT2, it should be pointed out that in order to simulate the bubble reaching equilibrium shape on the electrode, when physically the velocity in the domain should reduce to zero, it would be necessary to suppress spurious velocities by using more advanced surface tension modelling approaches (most probably based on the geometric VOF [19]) and impose time step constraint to prevent the growth of these numerical artifacts.

#### Appendix D. Estimation of the initial concentration boundary layer thickness

The thickness of hydrodynamic boundary layer, for a laminar flow over a flat plate, according to [55], is equal to

$$\delta_H = 5\sqrt{\frac{\nu_1 x}{U_\infty}}. \quad (\text{D.1})$$

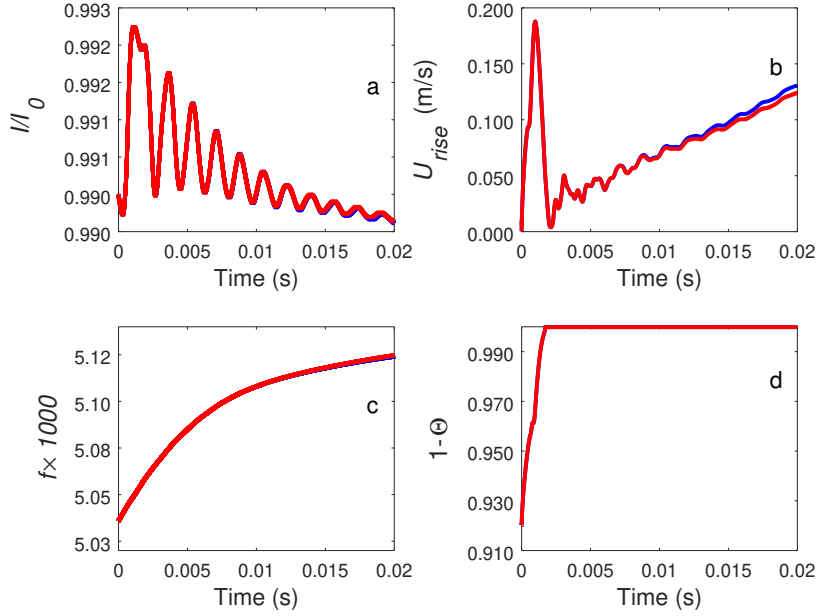


Figure C.22: Comparison of a)  $I/I_0$ , b) rise velocity and c) normalized bubble volume ( $f$ ), d)  $1 - \Theta$  obtained for bubble evolution for SCT1 (contact angle at the electrode set at  $30^\circ$ ) for simulations based on time step based on Courant number (—) and Brackbill time step constraint (—).

where  $x$  is the distance from the leading edge of the plate and  $U_\infty$  is the free stream flow velocity. The concentration boundary layer thickness ( $\delta_C$ ) can be expressed in terms of  $\delta_H$  as

$$\frac{\delta_C}{\delta_H} = \left( \frac{\nu_1}{D_{i,1}} \right)^{-1/3} = Sc^{-1/3}, \quad (\text{D.2})$$

where  $Sc$  is the non-dimensional Schmidt number. The above equation can be rearranged to get an expression of the concentration boundary layer thickness as

$$\begin{aligned} \delta_C &= \left( \frac{\nu_1}{D_{i,1}} \right)^{-1/3} 5 \sqrt{\frac{\nu_1 x}{U_\infty}} \\ &= 5 \nu_1^{1/6} D_{i,1}^{1/3} x^{1/2} U_\infty^{-1/2}. \end{aligned} \quad (\text{D.3})$$

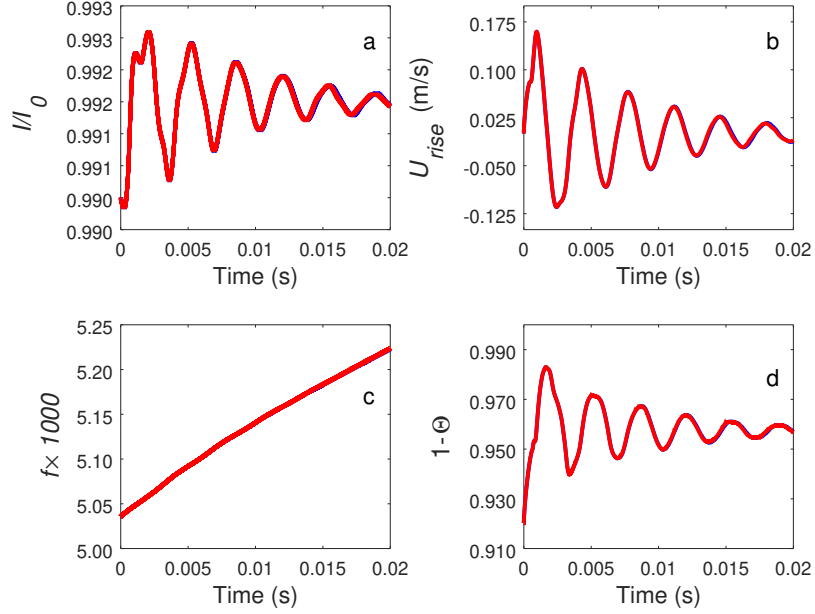


Figure C.23: Comparison of a)  $I/I_0$ , b) rise velocity and c) normalized bubble volume ( $f$ ), d)  $1 - \Theta$  obtained for bubble evolution for SCT2 (contact angle at the electrode set at  $45^\circ$ ) for simulations based on time step based on Courant number (—) and Brackbill time step constraint (—).

Eq. D.3 can be averaged over the length of the flat plate ( $L$ ) to get an average concentration boundary layer equal to

$$\bar{\delta}_C = \frac{1}{L} \int_0^L 5\nu_1^{1/6} D_{i,1}^{1/3} x^{1/2} U_\infty^{-1/2} dx \quad (\text{D.4})$$

$$\bar{\delta}_C = \frac{10}{3} \nu_1^{1/6} D_{i,1}^{1/3} U_\infty^{-1/2} L^{1/2} \quad (\text{D.5})$$

For electrode length scale ( $L$ ) equivalent to  $10^{-2}\text{m}$ ,  $\nu_1 = 9.89 \times 10^{-7}\text{m}^2/\text{s}$ ,  $D_{i,1} = 4.8 \times 10^{-9}\text{m}^2/\text{s}$  and  $U_\infty$  in the order of  $0.1\text{m/s}$  gives  $\bar{\delta}_C$  in the order of  $10^{-4}\text{m}$ . In order to simplify notation in the main body of the paper,  $\bar{\delta}_C$  is written as  $\delta$ .

### Appendix E. Comparison of current obtained with and without mass transfer driven bubble growth

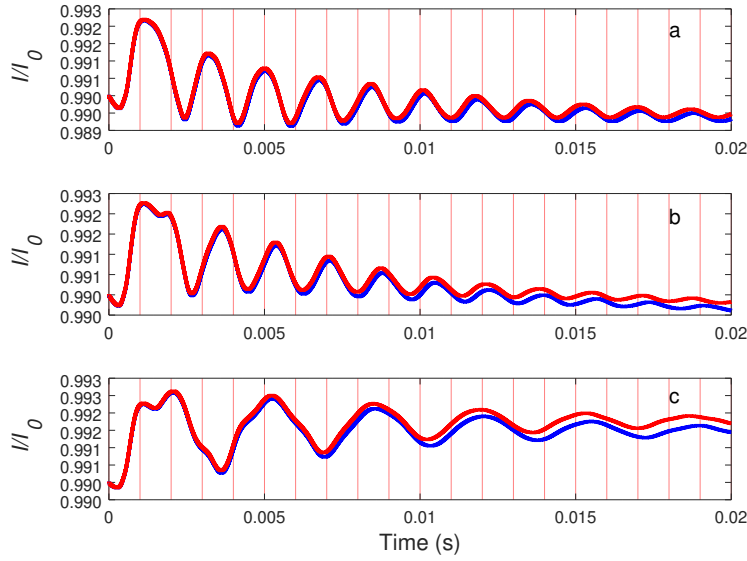


Figure E.24: Comparison of the normalized current ( $I/I_0$ ) for various contact angles with (—) and without (—) interfacial mass transfer driven bubble growth: a) SCT0, b) SCT1 and c) SCT2. The vertical red lines are equidistant grid line at every 0.001s to enable comparison between the plots.

In order to compare the effect of bubble growth on the current obtained, the cases without any mass transfer is simulated by using analogous setups to SCT0, SCT1 and SCT2 for the initial and boundary conditions except for the electrochemical reactions which was replaced with a zero gradient condition at the wall in addition to not initializing a concentration boundary layer. This prevent the growth of the bubble due to interfacial mass transfer driven by supersaturation. The comparison of the current obtained in SCT0, SCT1 and SCT2 with and without bubble growth is plotted in Fig. E.24.

## References

- [1] K. Scott, Chapter 1 introduction to electrolysis, electrolysers and hydrogen production, in: *Electrochemical Methods for Hydrogen Production*, The Royal Society of Chemistry, 2020, pp. 1–27. doi:10.1039/9781788016049-00001.
- [2] M. A. Khan, H. Zhao, W. Zou, Z. Chen, W. Cao, J. Fang, J. Xu, L. Zhang, J. Zhang, Recent progresses in electrocatalysts for water electrolysis, *Electrochemical Energy Reviews* 1 (4) (2018) 483–530. doi:10.1007/s41918-018-0014-z.
- [3] H. Jin, J. Joo, N. K. Chaudhari, S.-I. Choi, K. Lee, Recent progress in bifunctional electrocatalysts for overall water splitting under acidic conditions, *ChemElectroChem* 6 (13) (2019) 3244–3253. doi:10.1002/celec.201900507.
- [4] Z. Lei, T. Wang, B. Zhao, W. Cai, Y. Liu, S. Jiao, Q. Li, R. Cao, M. Liu, Recent progress in electrocatalysts for acidic water oxidation, *Advanced Energy Materials* 10 (23) (2020) 2000478. doi:10.1002/aenm.202000478.
- [5] G. B. Darband, M. Aliofkhazraei, S. Shanmugam, Recent advances in methods and technologies for enhancing bubble detachment during electrochemical water splitting, *Renewable and Sustainable Energy Reviews* 114 (2019) 109300. doi:https://doi.org/10.1016/j.rser.2019.109300.
- [6] X. Zhao, H. Ren, L. Luo, Gas bubbles in electrochemical gas evolution reactions, *Langmuir* 35 (16) (2019) 5392–5408. doi:10.1021/acs.langmuir.9b00119.
- [7] C. Brussieux, P. Viers, H. Roustan, M. Rakib, Controlled electrochemical gas bubble release from electrodes entirely and partially covered with hydrophobic materials, *Electrochimica Acta* 56 (20) (2011) 7194 – 7201. doi:https://doi.org/10.1016/j.electacta.2011.04.104.



- [8] D. Fernández, P. Maurer, M. Martine, J. M. D. Coey, M. E. Möbius, Bubble formation at a gas-evolving microelectrode, *Langmuir* 30 (43) (2014) 13065–13074. doi:10.1021/la500234r.
- [9] X. Yang, D. Baczyzmalski, C. Cierpka, G. Mutschke, K. Eckert, Marangoni convection at electrogenerated hydrogen bubbles, *Phys. Chem. Chem. Phys.* 20 (2018) 11542–11548. doi:10.1039/C8CP01050A.
- [10] A. Bashkatov, S. S. Hossain, X. Yang, G. Mutschke, K. Eckert, Oscillating hydrogen bubbles at pt microelectrodes, *Phys. Rev. Lett.* 123 (2019) 214503. doi:10.1103/PhysRevLett.123.214503.
- [11] A. Taqieddin, M. R. Allshouse, A. N. Alshawabkeh, Editors' choice- critical review—mathematical formulations of electrochemically gas-evolving systems, *Journal of The Electrochemical Society* 165 (13) (2018) E694–E711. doi:10.1149/2.0791813jes.
- [12] F. Hofbauer, I. Frank, Electrolysis of water in the diffusion layer: First-principles molecular dynamics simulation, *Chemistry – A European Journal* 18 (1) (2012) 277–282. doi:10.1002/chem.201002094.
- [13] L. F. Catañeda, F. F. Rivera, T. Pérez, J. L. Nava, Mathematical modeling and simulation of the reaction environment in electrochemical reactors, *Current Opinion in Electrochemistry* 16 (2019) 75 – 82, *electrochemical Materials and Engineering • Sensors and Biosensors*. doi:https://doi.org/10.1016/j.coelec.2019.04.025.
- [14] X. He, N. Li, Lattice boltzmann simulation of electrochemical systems, *Computer Physics Communications* 129 (1) (2000) 158 – 166. doi:https://doi.org/10.1016/S0010-4655(00)00103-X.
- [15] S. Gong, P. Cheng, Lattice boltzmann simulation of periodic bubble nucleation, growth and departure from a heated surface in pool boiling, *International Journal of Heat and Mass Transfer* 64 (2013) 122 – 132. doi:https://doi.org/10.1016/j.ijheatmasstransfer.2013.03.058.

- [16] M. Sommerfeld, Numerical Methods for Dispersed Multiphase Flows, Springer International Publishing, Cham, 2017, pp. 327–396. doi:10.1007/978-3-319-60282-0\_6.
- [17] R. Hreiz, L. Abdelouahed, D. Fünfschilling, F. Lopicque, Electrogenerated bubbles induced convection in narrow vertical cells: A review, Chemical Engineering Research and Design 100 (2015) 268 – 281. doi:<https://doi.org/10.1016/j.cherd.2015.05.035>.
- [18] S. S. Deshpande, L. Anumolu, M. F. Trujillo, Evaluating the performance of the two-phase flow solver interFoam, Computational Science & Discovery 5 (1) (2012) 014016. doi:10.1088/1749-4699/5/1/014016.
- [19] Y. Renardy, M. Renardy, Prost: A parabolic reconstruction of surface tension for the volume-of-fluid method, Journal of Computational Physics 183 (2) (2002) 400 – 421. doi:<https://doi.org/10.1006/jcph.2002.7190>.
- [20] S. Popinet, Numerical models of surface tension, Annual Review of Fluid Mechanics 50 (1) (2018) 49–75. doi:10.1146/annurev-fluid-122316-045034.
- [21] K. J. Vachaparambil, K. E. Einarsrud, Comparison of surface tension models for the volume of fluid method, Processes 7 (8) (2019) 542. doi:10.3390/pr7080542.
- [22] A. Q. Raeini, M. J. Blunt, B. Bijeljic, Modelling two-phase flow in porous media at the pore scale using the volume-of-fluid method, Journal of Computational Physics 231 (17) (2012) 5653 – 5668. doi:<https://doi.org/10.1016/j.jcp.2012.04.011>.
- [23] D. A. Hoang, V. [van Steijn], L. M. Portela, M. T. Kreutzer, C. R. Kleijn, Benchmark numerical simulations of segmented two-phase flows in microchannels using the volume of fluid method, Computers & Fluids 86

- (2013) 28 – 36. doi:<https://doi.org/10.1016/j.compfluid.2013.06.024>.
- [24] D. Bothe, S. Fleckenstein, A volume-of-fluid-based method for mass transfer processes at fluid particles, *Chemical Engineering Science* 101 (2013) 283 – 302. doi:<https://doi.org/10.1016/j.ces.2013.05.029>.
- [25] M. Falcone, H. Marschall, Explicit radial-basis-function-based finite-difference method for interfacial mass-transfer problems, *Chemical Engineering & Technology* 40 (8) (2017) 1385–1390. doi:[10.1002/ceat.201600536](https://doi.org/10.1002/ceat.201600536).
- [26] D. Deising, H. Marschall, D. Bothe, A unified single-field model framework for volume-of-fluid simulations of interfacial species transfer applied to bubbly flows, *Chemical Engineering Science* 139 (2016) 173 – 195. doi:<https://doi.org/10.1016/j.ces.2015.06.021>.  
URL <http://www.sciencedirect.com/science/article/pii/S0009250915004297>
- [27] J. Maes, C. Soullaine, A new compressive scheme to simulate species transfer across fluid interfaces using the volume-of-fluid method, *Chemical Engineering Science* 190 (2018) 405 – 418. doi:<https://doi.org/10.1016/j.ces.2018.06.026>.
- [28] K. J. Vachaparambil, K. E. Einarsrud, Numerical simulation of bubble growth in a supersaturated solution, *Applied Mathematical Modelling* 81 (2020) 690 – 710. doi:<https://doi.org/10.1016/j.apm.2020.01.017>.
- [29] J. Maes, C. Soullaine, A unified single-field volume-of-fluid-based formulation for multi-component interfacial transfer with local volume changes, *Journal of Computational Physics* 402 (2020) 109024. doi:<https://doi.org/10.1016/j.jcp.2019.109024>.
- [30] H. Liu, L.-m. Pan, J. Wen, Numerical simulation of hydrogen bubble growth

at an electrode surface, *The Canadian Journal of Chemical Engineering* 94 (1) (2016) 192–199. doi:10.1002/cjce.22378.

- [31] K. E. Einarsrud, S. T. Johansen, Modelling of bubble behaviour in aluminium reduction cells, *Progress in Computational Fluid Dynamics, an International Journal* 12 (2-3) (2012) 119–130. doi:10.1504/PCFD.2012.047455.
- [32] K. E. Einarsrud, I. Eick, W. Bai, Y. Feng, J. Hua, P. J. Witt, Towards a coupled multi-scale, multi-physics simulation framework for aluminium electrolysis, *Applied Mathematical Modelling* 44 (2017) 3 – 24. doi:<https://doi.org/10.1016/j.apm.2016.11.011>.
- [33] M. Sun, B. Li, L. Li, A multi-scale mathematical model of growth and coalescence of bubbles beneath the anode in an aluminum reduction cell, *Metallurgical and Materials Transactions B* 49 (5) (2018) 2821–2834. doi:10.1007/s11663-018-1311-y.
- [34] Z. Zhang, W. Liu, M. L. Free, Phase-field modeling and simulation of gas bubble coalescence and detachment in a gas-liquid two-phase electrochemical system, *Journal of The Electrochemical Society* 167 (1) (2020) 013532. doi:10.1149/2.0322001jes.
- [35] A. Taqieddin, R. Nazari, L. Rajic, A. Alshwabkeh, Review—physicochemical hydrodynamics of gas bubbles in two phase electrochemical systems, *Journal of The Electrochemical Society* 164 (13) (2017) E448–E459. doi:10.1149/2.1161713jes.
- [36] J. A. Leistra, Voltage components at gas evolving electrodes, *Journal of The Electrochemical Society* 134 (10) (1987) 2442. doi:10.1149/1.2100218.
- [37] C. J. Greenshields, *OpenFOAM User Guide version 7*, The OpenFOAM Foundation (2019).  
URL <http://foam.sourceforge.net/docs/Guides-a4/OpenFOAMUserGuide-A4.pdf>

- [38] C. Greenshields, Predictor-Corrector Semi-Implicit MULES, <https://openfoam.org/release/2-3-0/multiphase/>, [Online; accessed 6-July-2020] (2014).
- [39] S. Hardt, F. Wondra, Evaporation model for interfacial flows based on a continuum-field representation of the source terms, *Journal of Computational Physics* 227 (11) (2008) 5871 – 5895. doi:<https://doi.org/10.1016/j.jcp.2008.02.020>.
- [40] C. Kunkelmann, Numerical modeling and investigation of boiling phenomena, Ph.D. thesis, Technische Universität, Darmstadt (May 2011). URL <http://tuprints.ulb.tu-darmstadt.de/2731/>
- [41] J. Brackbill, D. Kothe, C. Zemach, A continuum method for modeling surface tension, *Journal of Computational Physics* 100 (2) (1992) 335 – 354. doi:[https://doi.org/10.1016/0021-9991\(92\)90240-Y](https://doi.org/10.1016/0021-9991(92)90240-Y).
- [42] R. Issa, Solution of the implicitly discretised fluid flow equations by operator-splitting, *Journal of Computational Physics* 62 (1) (1986) 40 – 65. doi:[https://doi.org/10.1016/0021-9991\(86\)90099-9](https://doi.org/10.1016/0021-9991(86)90099-9).
- [43] C. M. Rhie, W. L. Chow, Numerical study of the turbulent flow past an airfoil with trailing edge separation, *AIAA Journal* 21 (11) (1983) 1525–1532. doi:[10.2514/3.8284](https://doi.org/10.2514/3.8284).
- [44] K. J. Vachaparambil, K. E. Einarsrud, On sharp surface force model: Effect of sharpening coefficient, *Experimental and Computational Multiphase Flow* doi:[10.1007/s42757-020-0063-5](https://doi.org/10.1007/s42757-020-0063-5).
- [45] K. Zeng, D. Zhang, Recent progress in alkaline water electrolysis for hydrogen production and applications, *Progress in Energy and Combustion Science* 36 (3) (2010) 307 – 326. doi:<https://doi.org/10.1016/j.pecs.2009.11.002>.

- [46] R. Sander, Compilation of henry’s law constants (version 4.0) for water as solvent, *Atmospheric Chemistry and Physics* 15 (8) (2015) 4399–4981. doi:10.5194/acp-15-4399-2015.
- [47] H. Vogt, On the supersaturation of gas in the concentration boundary layer of gas evolving electrodes, *Electrochimica Acta* 25 (5) (1980) 527 – 531. doi:[https://doi.org/10.1016/0013-4686\(80\)87052-6](https://doi.org/10.1016/0013-4686(80)87052-6).
- [48] S. Hysing, S. Turek, D. Kuzmin, N. Parolini, E. Burman, S. Ganesan, L. Tobiska, Quantitative benchmark computations of two-dimensional bubble dynamics, *International Journal for Numerical Methods in Fluids* 60 (11) (2009) 1259–1288. doi:10.1002/flid.1934.
- [49] S. J. Hashemi, J. Abedi, Advances in modeling of new phase growth, *Energy & Fuels* 21 (4) (2007) 2147–2155. doi:10.1021/ef0606431.
- [50] L. Scriven, On the dynamics of phase growth, *Chemical Engineering Science* 10 (1) (1959) 1 – 13. doi:[https://doi.org/10.1016/0009-2509\(59\)80019-1](https://doi.org/10.1016/0009-2509(59)80019-1).
- [51] P. J. Sides, Primary potential and current distribution around a bubble on an electrode, *Journal of The Electrochemical Society* 127 (2) (1980) 288. doi:10.1149/1.2129657.  
URL <https://doi.org/10.1149%2F1.2129657>
- [52] X. Yang, F. Karnbach, M. Uhlemann, S. Odenbach, K. Eckert, Dynamics of single hydrogen bubbles at a platinum microelectrode, *Langmuir* 31 (29) (2015) 8184–8193. doi:10.1021/acs.langmuir.5b01825.
- [53] Á. Moreno Soto, T. Maddalena, A. Fraters, D. van der Meer, D. Lohse, Coalescence of diffusively growing gas bubbles, *Journal of Fluid Mechanics* 846 (2018) 143–165.  
URL <https://doi.org/10.1017/jfm.2018.277>

- [54] N. Samkhaniani, M. Ansari, Numerical simulation of bubble condensation using cf-vof, *Progress in Nuclear Energy* 89 (2016) 120 – 131. doi:<https://doi.org/10.1016/j.pnucene.2016.02.004>.
- [55] H. Schlichting, K. Gersten, *Boundary–Layer Equations in Plane Flow; Plate Boundary Layer*, Springer Berlin Heidelberg, Berlin, Heidelberg, 2017, pp. 145–164. doi:[10.1007/978-3-662-52919-5\\_6](https://doi.org/10.1007/978-3-662-52919-5_6).